# Photoelectrochemical Characterization of Dye-Sensitized Solar Cells Based on ZnO and Organic Dyes

**Dissertation**

zur Erlangung des Doktorgrades

der Naturwissenschaften

(Dr. rer. nat.)

vorgelegt dem Fachbereich 07

der Justus-Liebig-Universität Gießen

von

**Melanie Rudolph**

Gießen, September 2015

Advisor & First Referee: Prof. Dr. Derck Schlettwein

Second Referee: Prof. Dr. Jürgen Janek

# Abstract

Dye-sensitized solar cells (DSCs) based on electrodeposited mesoporous ZnO films present a low-temperature alternative to conventional DSCs built from high-temperature treated nanoparticulate $TiO_2$ films. Using a liquid iodide/triiodide electrolyte and the indoline dye D149 as photosensitizer, the highest efficiency reported for such cells is 5.6%, which is slightly less than half of that reached by titania-based systems. In the present work, the role of the dye layer at the interface between ZnO and electrolyte in determining cell performance was investigated. Optical spectroscopy and time- and frequency-resolved photoelectrochemical methods involving small or large electrical or illumination perturbations were employed to study light harvesting, charge separation, charge transport, and recombination in sandwich-type solar cells with systematically varied dye loadings, dye combinations, or dye/coadsorbate combinations. On the basis of analytical models considering an exponential distribution of band gap states in the semiconductor and nonlinear recombination to the electrolyte ($\beta$-recombination model), strategies to quantitatively detangle the microscopic factors that determine global device characteristics were introduced. It was shown that the relatively low fill factor in cells based on electrodeposited ZnO/D149 is strongly determined by D149 aggregates accelerating recombination at intermediate cell voltages. The beneficial effect of the coadsorbate cholic acid (CA) on device performance resulted from a suppression of the dye-related recombination by limiting the extent of D149 aggregation. Addressing the low short-circuit photocurrent densities of ZnO/D149-based DSCs with respect to standard $TiO_2$-based cells, an extension of the spectral light harvesting efficiency was achieved by co-sensitization of electrodeposited or screenprinted nanoparticulate ZnO with D149, the indoline dye D131, and a red-absorbing sensitizer, which was either the squaraine dye SQ2 or the partially sulfonated zinc(II) phthalocyanine $S_{1.15}$PcZn. The beneficial effect of panchromatic light harvesting was counteracted by significant voltage losses due to undesired dye/dye and dye/semiconductor interactions in the presence of the red absorbers, including downward shifts of the ZnO conduction band edge and formation of recombination-promoting surface trap states. On the basis of the specific properties of ZnO-based DSCs determined in this work, guidelines for the choice of alternative sensitizers and red-absorbing co-sensitizers were discussed.

# Kurzfassung

Farbstoffsolarzellen (DSCs) auf Basis elektrochemisch abgeschiedener poröser ZnO-Schichten bieten gegenüber konventionellen $TiO_2$-basierten Systemen den Vorteil, bei niedrigen Temperaturen hergestellt werden zu können. Derartige Zellen haben mit flüssigen Iodid/Triiodid-Elektrolyten und dem Indolinfarbstoff D149 bisher Wirkungsgrade von bis zu 5.6% erreicht, was noch deutlich unterhalb der Wirkungsgrade $TiO_2$-basierter Systeme liegt. In der vorliegenden Arbeit wurde der Einfluss der Farbstoffschicht an der Grenzfläche zwischen ZnO und Elektrolyt auf die Eigenschaften ZnO-basierter DSCs untersucht. Mittels optischer Spektroskopie sowie zeit- und frequenzaufgelöster photoelektrochemischer Methoden wurden Lichtabsorption, Ladungsträgerseparation, Ladungstransport, und Rekombination in planaren Testzellen mit systematisch variierten Farbstoffbeladungen, Farbstoffkombinationen, oder Farbstoff/Coadsorbat- Kombinationen analysiert. Analytische Modelle unter Einbezug exponentieller Fallenverteilungen im Halbleiter und nichtlinearer Rekombinationskinetik mit dem Elektrolyten ($\beta$-Rekombinationsmodell) wurden genutzt, um Auswertungsverfahren zur Quantifizierung der Einflüsse unterschiedlicher mikroskopischer Größen auf globale Zellcharakteristika zu entwickeln. Der vergleichsweise niedrige Füllfaktor elektrochemisch hergestellter ZnO/D149-Solarzellen wurde auf erhöhte Rekombination im Bereich niedrigerer Zellspannungen in Anwesenheit aggregierter D149-Moleküle zurückgeführt. Die bekannte Verbesserung der photovoltaischen Leistung durch Coadsorption von Cholsäure (CA) lag in einer verringerten Aggregationsneigung des Farbstoffes und der dadurch bedingten Reduktion der aggregatbedingten Rekombination begründet. Die spektrale Absorption in ZnO/D149-Solarzellen wurde mittels Co-Sensibilisierung mit D149, dem Indolinfarbstoff D131, und einem von zwei im roten Spektralbereich absorbierenden Farbstoffen (dem Squarainfarbstoff SQ2 oder dem teilsulfonierten Zink(II)-Phthalocyanin $S_{1.15}$PcZn) erweitert. Dabei traten unerwünschte Farbstoff/Farbstoff- und Farbstoff/Halbleiter-Wechselwirkungen wie z.B. eine ungünstige Verschiebung der ZnO-Leitungsbandkante sowie eine Bildung rekombinationsfördernder Fallenzustände zutage, welche dem positiven Effekt der verbesserten Lichtabsorption entgegenwirkten. Unter Berücksichtigung der in dieser Arbeit bestimmten spezifischen Eigenschaften ZnO-basierter DSCs wurden Richtlinien für die Auswahl alternativer Sensibilisatoren und Co-Sensibilisatoren diskutiert.

# Table of Contents

# Introduction

A 2010 advertisement by the oil and gas company Shell depicted a little girl who is reading in bed. The image was accompanied by the comment, "What sort of world will this little girl grow up in? [...] if we're going to keep the lights on for her, we will need to look at every possible energy source. [...] Let's Go."[1, 2] Clearly, Shell was addressing the fact that global reserves of fossil fuels like oil and gas are becoming scarce. One of the oil giant's approaches to tackle this problem was to plan a multi-billion dollar project to explore some of the Earth's last big reserves of fossil fuels in the Arctic Sea. Two years later, after a series of disconcerting technical issues and safety problems in the rough waters of the Arctic Ocean, Shell's 200 million dollar Arctic drill rig, the Kulluk, had run ashore on Sitkalidak Island in the Gulf of Alaska and eventually had to be scrapped.[1] Together with the increasing certainty among climate researchers that the global warming we are experiencing is largely caused by human combustion of fossil fuels,[3] accidents like this unambiguously suggest the conclusion that we must indeed, in Shell's own words, look at every possible energy source. However, in order to secure a clean and reliable supply of energy for future generations, it is inevitable that we focus on advancing efficient technologies to exploit *safe and sustainable* energy sources, such as wind, water and sunlight. These so-called renewables will make up an increasing share of the global energy mix of the future.[4] Exploitation of the vast amount of energy arriving every second at the upper atmosphere of the Earth in the form of solar radiation (174,000 TJ)[5] is expected to play a prominent role in that mix.[4] In fact, one of the future energy scenarios Shell presented in 2013 (*New Lens Scenarios*)[6] predicts that sunlight will be the dominant energy source by 2100, making up nearly 40% of the world's energy mix. In accordance with such scenarios, several established industrial companies such as Schott,[7] Sharp,[8] and Panasonic[9] have been investing in solar energy, and even the oil giants Shell and BP themselves were active in the solar market for several years.[10] Among solar energy technologies, photovoltaic cells, which convert incident sunlight directly into electric energy, represent an attractive, low-maintenance option that can be used to either feed electricity into the grid or function as island systems to provide electricity in remote areas far away from the grid.[11] In the interest of sustainability, it is essential to develop photovoltaic approaches that rely only on non-toxic and

earth-abundant materials as well as on energy-efficient production methods, avoiding unsustainable processing conditions such as high temperatures, high pressure, or (ultra-) high vacuum. If environmental and health-related hazards are monetized,[12] increasing sustainability also significantly contributes to achieving high cost-efficiency, which in turn increases commercial attractiveness. Conventional bulk Si solar cells, which nowadays still dominate the market,[13] require processing temperatures above 1000 °C[14] and, thus, are not satisfying the demand for low-energy fabrication. With present power conversion efficiencies of up to 13%[15] and the prospect of low-energy production,[16] dye-sensitized solar cells (DSCs) present one of the most promising systems among alternative photovoltaics trying to meet the above criteria for sustainability. One new concept that has developed out of dye-sensitized cells has gained particularly high attention over the past few years: Perovskite-based solar cells, which have reached efficiencies above 20%.[17] While exhibiting highly competitive performance, the success of Perovskite-based solar cells currently relies on the use of lead halide compounds for the light-absorbing material, which raises concerns regarding toxicity.[18] Therefore, from a point of view of sustainability it is clearly necessary to continue and intensify research efforts in the field of classical ("Grätzel"-type) dye-sensitized solar cells, which typically consist of a nanostructured metal oxide electrode to which a photosensitizing dye is adsorbed, a counter electrode, and a liquid redox electrolyte or solid hole conductor in between the two electrodes.[19] While the most efficient DSCs today are fabricated from nanoparticulate $TiO_2$ films that require high-temperature post-treatment to ensure good electronic conductivity,[19, 20] the semiconductor ZnO offers a variety of possibilities to be deposited as nanostructured films at significantly lower temperatures.[21] Low preparation temperatures not only directly translate into a reduced amount of energy required for cell fabrication, but also contribute to increased sustainability by allowing the replacement of energy-intensive[16] glass substrates by flexible and light-weight plastic substrates.[22-25] One particularly attractive low-cost method to prepare mesoporous ZnO electrodes for dye-sensitized solar cells is electrodeposition in the presence of molecular templates such as eosin Y, which proceeds at temperatures as low as 70°C and has been successfully transferred to plastic substrates.[25, 26] This technique yields thin films with columnar, sponge-like structures with pore sizes in the range of ~20 nm,[27] which have been found to exhibit favorable electron transport properties even without any high-temperature post-treatments.[28] As regards the photosensitizer, DSCs have originally

relied on Ru(II)-bipyridyl complexes to achieve competitive efficiencies,[29] but over the last decade numerous groups have focused on the development of alternative sensitizers, including high-extinction coefficient metal-free sensitizers that can be obtained via simple synthesis routes. This has resulted in remarkable efficiencies of up to 10.3% using the fully organic dye C219 in combination with $TiO_2$.[30] For solar cells based on electrodeposited porous ZnO electrodes, the best power conversion efficiency reported was ~5.6% and was, in fact, achieved with a metal-free sensitizer, the indoline dye D149, in combination with the coadsorbate cholic acid.[25] As the photovoltaic performance of this materials system remains clearly below that of $TiO_2$ cells, additional research efforts are essential in order to deepen the understanding of this sustainable, non-toxic, and prospectively cost-efficient alternative to titania-based DSC structures and thereby develop systematic strategies for further improvement of their efficiency.

The studies discussed in the present thesis were designed to contribute to this objective by elucidating how systematic changes to the dye layer at the interface between electrodeposited ZnO and a liquid iodide/triiodide redox electrolyte impact microscopic charge transport and transfer processes and, ultimately, solar cell device characteristics. A major goal was to deepen the understanding of the role of D149 in limiting the efficiency of ZnO/D149 solar cells and to clarify the detailed mechanism by which coadsorption of cholic acid (CA) with D149 improves cell performance with respect to cells without coadsorbate. The experimental strategy chosen to approach this goal was to prepare and characterize solar cells from electrodeposited ZnO films that had been loaded with different amounts of D149 by systematic variation of the immersion time in dye or mixed dye/coadsorbate solutions. Combination of current-voltage characterization and electrochemical impedance spectroscopy allowed attributing characteristic differences in the photovoltaic parameters of cells with different dye loadings and with or without coadsorbate to changes in the extent of D149 aggregation and resulting variations in the energy-dependence of interfacial recombination. A further key aim of this work was to extend the spectral light harvesting efficiency of DSCs based on electrodeposited ZnO with respect to ZnO/D149 cells. This was achieved by co-sensitizing the ZnO with combinations of D149 and one or more other dyes showing absorption spectra complementary to that of D149. The co-sensitizers were selected based on the following criteria: (1) successful combination with D149 on ZnO in a previous study (blue-absorbing indoline dye D131),[31] (2) efficient sensitization of $TiO_2$ as individual dye or co-

sensitizer in previous reports (red-absorbing squaraine dye SQ2),[32, 33] or (3) availability within a collaboration with industry (red-absorbing partially sulfonated zinc(II) phthalocyanine $S_{1.15}$PcZn). The characterization of the co-sensitized cells and of reference cells with individual sensitizers offered detailed insights into the effect of different dye-dye and dye-semiconductor interactions on the density and distribution of electronic states in the semiconductor, charge injection from the dye(s) to the semiconductor, as well as recombination kinetics. To expand the understanding of how the type of semiconductor matrix affects the solar cell performance, a comparative study of devices based on nanoparticulate ZnO films prepared by screen printing was performed. Finally, a number of different types of cells prepared as part of the thesis work were characterized multiple times over different periods of time of up to several months in order to gain information about their short- and long-term stability.

The thesis is arranged as follows. Chapter 1 provides a foundation for the discussion of the results by addressing the basics of dye-sensitized solar cell operation, the theoretical description of DSCs, and the fundamentals of the characterization methods employed to analyze the cells in this work. In chapter 2, the experimental procedures used to prepare and characterize the solar cells are described. Chapter 3 gives an overview of the film morphology and thickness within the set of electrodeposited ZnO samples used to fabricate DSCs. In chapters 5 through 9, the results of the different experimental studies outlined above are presented and discussed. In chapter 10, the thesis is concluded with a final discussion considering all results, and with an outlook on future research in the field of dye-sensitization of electrodeposited ZnO as it appears useful in view of the present results.

# 1 Basic Concepts

## 1.1 Dye-Sensitized Solar Cells (DSCs)

### 1.1.1 Structure and Operation Principle

The main component of a classical dye-sensitized solar cell of the type introduced by Grätzel and O'Regan in 1991[19] is a mesoporous film of a wide-band gap semiconductor, which is deposited on a glass substrate coated with a transparent conductive oxide (TCO) such as FTO (fluorine-doped tin oxide), cf. ***Figure 1***. A monolayer of dye molecules is adsorbed to the surface of the semiconductor as photosensitizer and the semiconductor/dye film is permeated by an electrolyte containing a redox couple. The DSC is completed by a counter electrode, which typically consists of TCO/glass coated with a catalytic platinum layer.[19, 34] Under illumination, the dye molecules absorb part of the incident light and are thereby electronically excited. Appropriate energy level alignment provided, electrons are rapidly injected from the excited states of the dye into the conduction band of the semiconductor and are transported through the mesoporous structure to the back contact (substrate). The oxidized photosensitizer is regenerated by electron transfer from the reduced species of the redox couple. The oxidized species of the redox electrolyte diffuses[35, 36] to the counter electrode, where it is reduced. In the case of the commonly used $I^-/I_3^-$ (iodide/triiodide) redox couple, a Grotthus-like mechanism may contribute to the transport of positive charges to the counter electrode, as observed in ionic liquid-based electrolytes at high iodide concentrations.[37]

In the original Grätzel cell,[19] the porous semiconductor film was a layer of $TiO_2$ nanoparticles that had been sintered to interconnect the particles and form a conductive network. While such $TiO_2$-based DSCs presently still deliver the highest efficiencies and therefore constitute the most common approach,[15, 34, 38, 39] other metal oxide semiconductors have been widely investigated and have been found to be advantageous for certain applications or cell configurations.[22, 40-42] Most studies investigating alternative semiconductors for DSCs - including the present work - have focused on ZnO, which offers the beneficial possibility of creating a variety of different nanostructures even at

low temperatures.[21, 22, 25, 43, 44] Chapters 1.3.1 and 1.3.2 will give a detailed introduction on DSCs based on ZnO photoelectrodes.

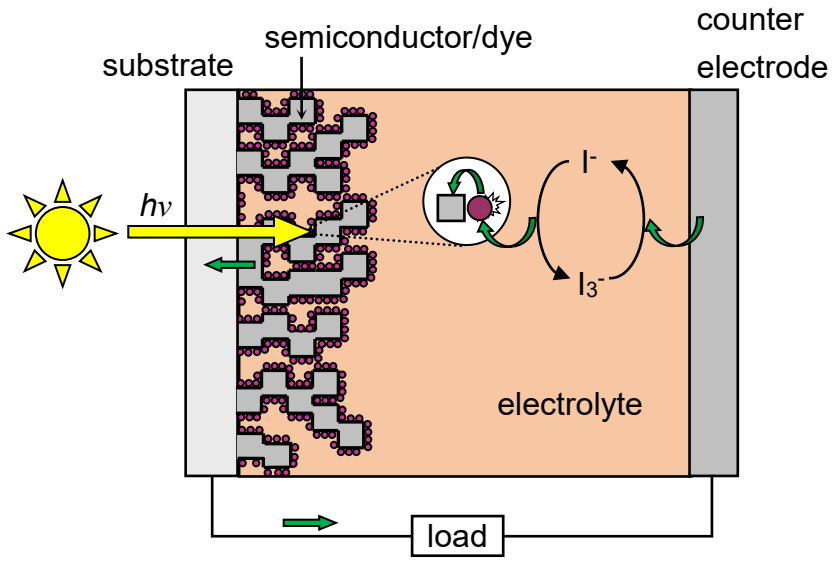


***Figure 1**: Schematic representation of structure and operation principle of a dye-sensitized solar cell with substrate-side illumination. Green arrows indicate the flow of electrons. The circular blow-up illustrates the desired charge transfer processes at the semiconductor/dye/electrolyte interface following photoexcitation of the dye.*

The first DSCs employed ruthenium(II) polypyridyl complexes such as N3 as photosensitizers.[19, 29, 45] As is the case for most other DSC dyes, the adsorption of these molecules to the inner surface of the porous oxide semiconductor is based on the formation of a covalent bond via their carboxylic acid groups.[45] DSCs using Ru(II) sensitizers continued to yield the best conversion efficiencies among $TiO_2$-based devices for almost 20 years, reaching up to 11.5 % in 2009.[46, 47] In 2011, however, a new record was attained using the *porphyrin*-based dye YD2-*o*-C8 on $TiO_2$, without ($\eta$ = 11.9%) or with ($\eta$ = 12.3%) the metal-free dye Y123 as co-sensitizer.[34] This was followed by a record cell with a conversion efficiency of 13.0% in 2014,[15] which was based on $TiO_2$ with SM315, a porphyrin sensitizer with improved light harvesting and electrolyte compatibility. Fully organic absorber molecules like the above-mentioned Y123 have also been successfully used as individual photosensitizers, albeit resulting in somewhat lower efficiencies.[48-51] Compared to rare metal complexes, they have typically higher molar absorptivities, offer the prospect of lower-cost synthesis and their molecular structure can be easi-

ly modified to suit the needs of different cell concepts.[52] Moreover, organic dyes have been successfully used as sensitizers for semiconductor structures that were found to show low efficiencies with the typical Ru(II) dyes, such as the electrodeposited porous ZnO structures[25] used in this work. Chapter 1.3.4 will address this group of photosensitizers for dye-sensitized solar cells in more depth.

The most commonly used electrolyte consists of the $I^-/I_3^-$ redox shuttle in combination with liquid organic solvents like acetonitrile.[35] It was already used in the early DSC studies by Grätzel et al.[19] and has remained the preferred choice because it yields highly efficient and stable cells.[47, 53] The main advantage of the $I^-/I_3^-$ mediator is that oxidation of $I^-$ and hence dye regeneration is fast whilst reduction of $I_3^-$ by electrons from the porous semiconductor (recombination, cf. section 1.1.2 and 1.2.3) is kinetically hindered.[54] On the other hand, several drawbacks such as the relatively high redox potential of $I^-/I_3^-$ (posing an upper limit on the output voltage of the cell)[35, 55] and potential corrosiveness towards the counter electrode Pt layer[56] triggered studies focusing on the development of alternative redox couples.[34, 57, 58] The most successful alternative found so far is the Co(II/III) polypyridyl couple,[15, 34] which was employed in the record cell using the sensitizers YD2-*o*-C8/Y123 and SM315 (see above). However, the applicability of this redox mediator is limited to select photosensitizers: with standard Ru(II) complex dyes, for example, fast recombination between semiconductor and Co(II/III)-based electrolyte was found to lead to inferior efficiencies compared with the $I^-/I_3^-$electrolyte.[59] As the use of liquid electrolytes in general comes along with certain practical challenges such as the need for an effective cell sealing to prevent leakage or evaporation of the electrolyte, extensive research is also being performed in the field of solid or quasi-solid DSC hole transporters.[60] The non-volatility and high temperature stability of solid-state hole transporting materials renders them the most promising candidates for practical applications, but they currently show relatively low conversion efficiencies due to incomplete filling of the pores with the hole conductor[61] and significantly higher rates of recombination as compared to liquid electrolyte cells.[62] In the studies presented in this thesis, a standard liquid $I^-/I_3^-$ electrolyte has been deliberately chosen in spite of the drawbacks with respect to practical applicability. This is, first, because the dyes utilized in this work have shown optimum efficiencies in combination with the $I^-/I_3^-$ redox couple (see chapter 1.3.4) and, second, because the pore filling issues of solid hole conductors would have interfered with the aim of a systematic and quantitative interpretation of

recombination data, which relies on assuming the same contact surface between dye-sensitized semiconductor and electrolyte/hole transporter in all samples under comparison.

### 1.1.2 Overview of Energy Levels and Electron Transfer Processes

***Figure 2*** presents a basic energy level diagram of semiconductor, dye and electrolyte in a dye-sensitized solar cell and illustrates various desired and undesired processes of excitation, relaxation, transfer, and transport of charge carriers.

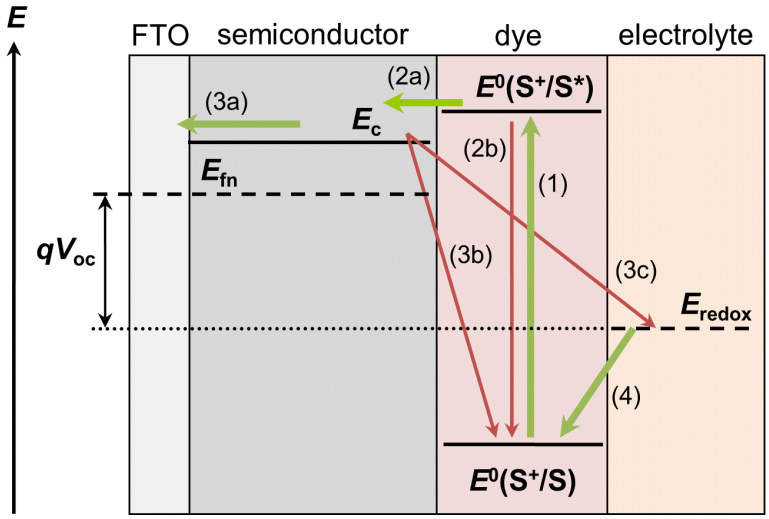


***Figure 2****: Energy levels in different components of a dye-sensitized solar cell at open-circuit conditions under illumination, with arrows representing charge flow and loss processes. The valence band of the semiconductor is outside the scale of the scheme. Note that the diagram represents free (e.g., $E_{fn}$) and internal (e.g. $E_c$) energies using one common scale.*

An accurate description of the energetic structure of the DSC must also include the distributions of electronic states (density of states $g(E)$) in the different cell components, which are explicitly represented in ***Figure 3***. The electronic structure of the mesoporous semiconductor is typically characterized via the position of the conduction band edge, $E_c$, the density of states in the conduction band, $g^{cb}(E)$, and a distribution of trap states in the band gap, $g^{t}(E)$. In the vicinity of the conduction band edge, where the band can be described by a parabola in $k$-space, the density of states in the conduction band of a

bulk semiconductor is expected to follow the relationship $g^{cb}(E) \propto (E\text{-}E_c)^{1/2}$, as indicated in ***Figure 3***.[63]

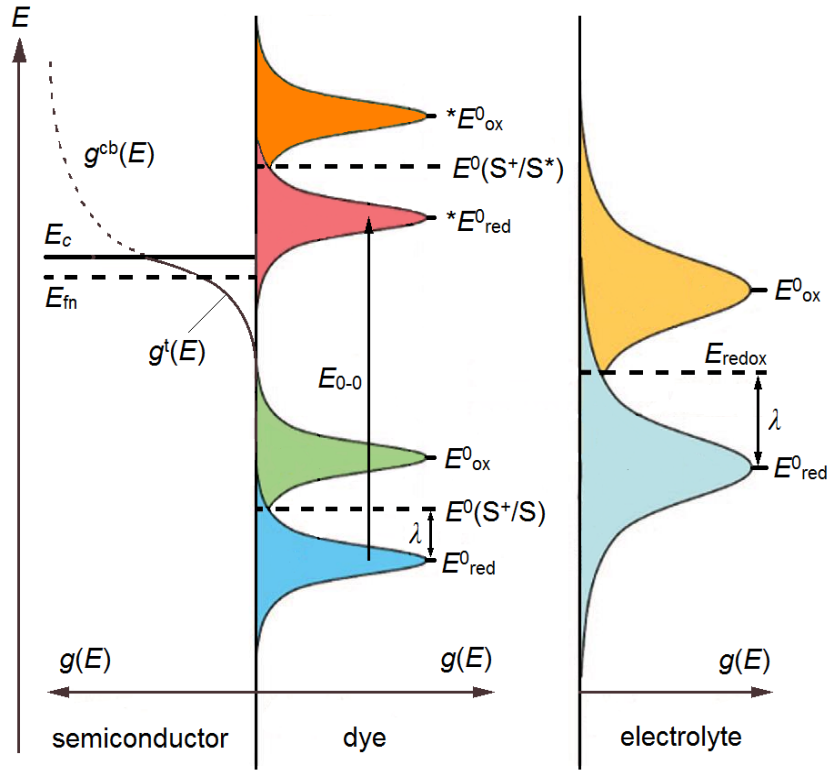


***Figure 3****: Distribution of electronic states in semiconductor, dye, and electrolyte. The density of states in the conduction band of the semiconductor is shown for the example of a bulk material without quantum confinement effects. The distributions of occupied states in dye and electrolyte are highlighted in blue, pink, and light blue, while the corresponding distributions of unoccupied states are presented in green, orange, and yellow. Adapted from Figure 11 of ref.* [38] *with additions and modifications.*

However, if quantum confinement in one or more dimensions plays a role, the density of states takes on significantly different shapes.[64] The distribution of trap states in nanostructured semiconductors usually shows an exponential increase towards $E_c$ (cf. section 1.2.2). Due to this so called tailing of the conduction band, some authors have pointed out that it is more appropriate to speak about a mobility edge (defined as the energy separating localized and delocalized states in a disordered semiconductor)[65] than about a conduction band edge in a strict sense.[66] In the present work, the expression "conduction band edge" and the symbol $E_c$ will be used in terms of a mobility edge and "shifts of the conduction band edge" will refer to energetic shifts of that mobility edge

and the density of states around it. The position of the semiconductor energy levels as well as the density of trap states at the surface are influenced by molecular adsorbates such as dyes or coadsorbates:[67-70] Surface-bound molecules can entail a reduction of the density of surface traps by attachment to coordinatively unsaturated surface atoms, and surface charges or dipolar fields of adsorbates can lead to shifts of $E_c$. The probability of population of the electronic states in the semiconductor is reflected in the quasi-Fermi level[I] (electrochemical potential) of electrons, $E_{fn}$.[63] It is related to the electron density $n_c$ in the conduction band via[63]

$$E_{fn} = E_c + kT \cdot \ln\left(\frac{n_c}{N_c}\right) \tag{1}$$

where $N_c$ is the effective density of states at the conduction band edge. In the dark, $E_{fn}$ is in equilibrium with the electrochemical potential of electrons in the electrolyte, which on the energy scale is often referred to as the redox level, or Fermi level of electrons in the electrolyte, $E_{redox}$.[38, 71] The redox level separates unoccupied and occupied electronic states in the electrolyte and according to the Nernst equation depends on the ratio of the concentrations of oxidized and reduced species.[72] The occupied and unoccupied states, represented as yellow and light blue areas in ***Figure 3***, show Gaussian distributions that intersect at $E_{redox}$. The maxima of the distributions, $E^0_{ox}$ and $E^0_{red}$, correspond to the most probable energies for the occupied and empty states, respectively.[73] $E^0_{ox}$ and $E^0_{red}$ differ from $E_{redox}$ by the reorganization energy $\lambda$, which is the energy required to transform the nuclear configurations in the reactant (inner reorganization energy) and in the surrounding solvent (outer reorganization energy) to those of the product state created in the oxidation or reduction reaction.[71, 74, 75] In a DSC under illumination, $E_{redox}$ remains stationary while $E_{fn}$ in the porous semiconductor is shifted upwards (towards $E_c$) as a result of the increase in electron density through electron injection from the dye. Under open-circuit conditions (zero current), the quasi-Fermi level in the semiconductor is spatially homogeneous and the split of Fermi levels $E_{fn} - E_{redox}$ determines the open-circuit photovoltage $V_{oc}$, as indicated in ***Figure 2***.[71] The sensitizer energy levels most relevant for DSC operation are the Fermi levels corresponding to the oxidation potentials of the dye in its ground and excited (*) state, $E^0(S^+/S)$ and $E^0(S^+/S^*)$,[38, 71] which are

[I] *quasi* here refers to the fact that $E_{fn}$ is the Fermi level of electrons under non-equilibrium conditions (i.e., under illumination) as opposed to the dark equilibrium Fermi level.

indirectly related to the energies $E_{LUMO}$ and $E_{HOMO}$ of the lowest unoccupied molecular orbital (LUMO) and the highest occupied molecular orbital (HOMO) of an isolated dye molecule.[76] In analogy to the states in the electrolyte, occupied and unoccupied states in the ground state and the excited state of the dye are described by Gauss functions intersecting at $E^0(S^+/S)$ and $E^0(S^+/S^*)$, characterized by reorganization energies $\lambda$ and by maxima located at $E^0_{ox}$ and $E^0_{red}$ and $^*E^0_{ox}$ and $^*E^0_{red}$, respectively.[71] The blue and pink areas in ***Figure 3*** represent occupied states of the ground and excited state, and the green and orange areas indicate the corresponding unoccupied states. $E_{0\text{-}0}$ corresponds to the energy of the transition between the lowest vibrational levels in the ground and excited states.[71]

Light harvesting, electron transfer, and electron transport in the dye-sensitized solar cell depend on the energy levels and distributions of states discussed above. In ***Figure 2***, the green arrows represent desired processes in the cell, while the red arrows indicate reactions connected to loss processes. Note that, although in the simplified representation of this picture some of the interfacial charge transfer processes are illustrated by diagonal arrows between the Fermi levels of the two phases involved in the transfer, such processes are generally isoenergetic in nature, i.e., they occur between occupied states of a donor and unoccupied states of an acceptor that are located at the same energy level.[71, 74, 77] Following excitation of electrons in the dye by absorption of incident light, (1), electrons are injected into the conduction band of the semiconductor, (2a), or recombine with the ground state (excited state decay), (2b). The efficiency of process (1) is called the light harvesting efficiency $\eta_{lh}$ (cf. chapter 1.4.1) and is a wavelength-dependent quantity determined by the molar absorptivity of the dye, the concentration of dye molecules in the film, and the film thickness (see eq. (24), eq. (26), and eq. (27)).[78] The quantum efficiency of charge transfer from the dye to the semiconductor is the electron injection efficiency $\eta_{inj}$. It is defined as $\eta_{inj} = k_{inj}/(k_{inj}+k_{decay})$, where $k_{inj}$ and $k_{decay}$ are the rate constants of electron injection, (2a), and excited state decay, (2b), i.e., it corresponds to the fraction of photoexcited electrons injected. According to the Gerischer theory for electron transfer from an excited molecule to a semiconductor electrode,[71, 77, 79] a high rate of electron injection results from a large energetic overlap of the density of occupied states in the excited dye and the density of unoccupied states in the semiconductor (cf. corresponding distributions in ***Figure 3***) as well as from a short distance between the dye molecules and the semiconductor. Therefore, efficient injection is pro-

moted by the excited state levels of the dye being located above $E_c$, which ensures a large energetic overlap of the involved occupied and unoccupied states, and by a direct and strong attachment of the dye molecules to the surface, which minimizes the distance between electron donor and acceptor.[79] A directionality in the excited states of the dye, meaning that the LUMO orbitals are localized at or close to its anchoring group, has been found to be of tremendous benefit for injection.[80, 81] In the case of standard Ru(II) dyes adsorbed to $TiO_2$, electron injection happens on a time scale of $10^{-12}$ – $10^{-13}$ s while excited state lifetimes of such dyes are in the range of $10^{-8}$ s.[82] As a result, $\eta_{inj}$ is generally high in standard DSCs.[82] For some other systems, however, it has been suggested that electron injection is slow enough for excited state decay and injection to compete.[83]

Following injection, electrons are transported through the semiconductor and ideally extracted at the back contact, (3a). In a real DSC, transport and extraction compete with recombination of electrons with the oxidized dye or with oxidized species in the electrolyte, (3b/c). Because of shielding effects, a space charge cannot build up in the semiconductor and, hence, electron transport through the mesoporous structure occurs primarily by diffusion. This part of the cell operation is influenced by the presence of band gap states[84] and will be discussed in detail in section 1.2.2. As a result of the influence of the traps, the diffusion coefficient of electrons in DSC photoelectrodes as measured by time- or frequency-modulated measurement techniques is orders of magnitude smaller than in bulk semiconductors[84] and is generally referred to as the effective (i.e., trap-influenced) diffusion coefficient $D_n$.[84, 85] Because of the fact that the occupation of trap states depends on the quasi-Fermi level, $D_n$ and thus the time needed for electrons to diffuse to the back contact vary strongly with $E_{fn}$.[84, 86]

Under AM1.5G[II] illumination and short-circuit conditions (zero voltage), efficient cells show a $D_n$ of the order $10^{-5}$ $cm^2s^{-1}$,[87, 88] and the time scale of electron diffusion through the porous film is ~$10^{-3}$ s.[89] The recombination reactions (3b) and (3c) can either occur directly from the conduction band of the semiconductor or via surface trap states.[90] Electrons may also recombine between substrate (e.g., FTO) and electrolyte. This reaction is not shown in the Figure, because it is efficiently suppressed by deposition of a

[II] AM 1.5G (air mass 1.5 global) conditions correspond to illumination by the sun shining through the atmosphere to sea level, with oxygen and nitrogen absorption, at an oblique angle 48.2° from the zenith (J. Nelson, *The physics of solar cells*, 2005).

compact metal oxide blocking layer on the substrate in most cells.[91, 92] A parameter commonly used to characterize the time scale of recombination is the effective (trap-influenced) electron lifetime $\tau_n$ obtained by time- or frequency-modulated characterization methods,[84, 90] which will be addressed in depth together with further aspects of recombination in chapter 1.2.3. Like $D_n$, the effective electron lifetime shows a strong dependence on the quasi-Fermi level in the semiconductor.[84] For an efficient cell under open-circuit conditions and AM1.5G illumination, it is of the order $10^{-2}$ s.[87] In most cases $\tau_n$ reflects the time scale of recombination with the electrolyte, because under standard operating conditions recombination with the oxidized dye is often negligible (see below).[93] However, if the dye is not regenerated quickly enough, $\tau_n$ may reflect the combined effect of the two different recombination paths.[94, 95] In studies specifically investigating recombination with oxidized dye molecules in the absence of a redox couple it was found that this reaction takes place on a time scale of ~$10^{-4}$ s.[96]

The experimental parameters $D_n$ and $\tau_n$ can be used to calculate the diffusion length[86, 97]

$$L_n = \sqrt{D_n \tau_n} \tag{2}$$

which is a measure of the efficiency of extraction of charges at the back contact, i.e., of the charge collection efficiency $\eta_{cc}$.[98, 99] Calculations have shown that in a standard $TiO_2$-based DSC the charge collection efficiency approaches 100% if the diffusion length is three times the film thickness.[87]

As indicated above, in a well-functioning cell recombination between semiconductor and oxidized dye is intercepted by regeneration of the latter by $I^-$ ions in the electrolyte, (4).

It has been proposed both for Ru(II) sensitizers[100] as well as for organic dyes[101] that dye regeneration occurs in several reaction steps involving intermediate formation of dye-iodide complexes such as (dye$\cdots I_2^{-\bullet}$). After dissociation of the complex, $I_2^{-\bullet}$ disproportionates into $I^-$ and $I_3^-$. The quantum efficiency of process (4) is the dye regeneration efficiency defined as $\eta_{reg} = k_{reg}/(k_{reg}+k_{rec,dye})$, where $k_{reg}$ and $k_{rec,dye}$ are the rate constants of dye regeneration and recombination with the oxidized dye, respectively. Regeneration kinetics is dependent on the energetic structure of the sensitizer as well as on the composition of the electrolyte.[100, 102] In order to ensure efficient regeneration, the thermodynamic driving force, i.e. the energetic difference between $E_{redox}$ and $E^0(S^+/S)$ of the

dye, should be around 0.5 – 0.6 eV.[38, 100, 103] In $TiO_2$-based cells with liquid $I^-/I_3^-$ electrolytes and with different metal-organic and organic dyes, regeneration was found to happen on a time scale of $10^{-5}$ s or shorter,[100, 104, 105] which is fast enough to prevent undesired recombination between semiconductor and oxidized dye. Nevertheless, for DSCs based on some materials combinations it was reported that their performance appeared to be limited by dye regeneration.[106, 107]

## 1.2 Theoretical Description of Processes Relevant for the Operation of DSCs

### 1.2.1 The Continuity Equation

The theoretical description of electron transport and recombination in the nanostructured photoelectrode of a DSC commonly uses a continuity equation for electrons as a starting point. This type of conservation equation describes the time-dependent change of the electron density $n$ resulting from carrier generation, local changes in electron flux, and recombination. The continuity equation for electrons in conduction band states, $n_c$, is[108, 109]

$$\frac{\partial n_c(x,t)}{\partial t} = G_n + \frac{1}{q}\frac{\partial J}{\partial x} - U_n \tag{3}$$

where $x$ is the position along an axis perpendicular to the substrate, $t$ is the time, $G_n$ is volume rate of electron generation, $q$ is the electron charge, $J$ is the current density, and $U_n$ is the volume rate of recombination.

The electron generation rate is controlled by light absorption by the dye molecules and by the electron injection efficiency $\eta_{inj}$ (section 1.1.2). Typically, a homogenous distribution of the dye within the porous semiconductor film is assumed and the spatial variation of the photon flux within the film is described by the Beer-Lambert law (cf. eq. (24) in chapter 1.4.1). $G_n$ can then be written as:[94]

$$G_n = \eta_{inj}\alpha_{abs}(\lambda)\phi \cdot e^{-\alpha_{abs}(\lambda)x} \tag{4}$$

where $\phi$ is the incident photon flux density and $\alpha_{abs}(\lambda)$ is the absorption coefficient.

As for the electric current $J$, it can generally be driven by electric fields (drift current) or by electron density gradients (diffusion current). In dye-sensitized nanostructured semi-

conductors in contact with redox electrolytes, electric fields are generally negligible[97, 110] (see details in the following section) and $J$ is described by Fick's law of diffusion:[88]

$$\frac{\partial J}{\partial x} = \frac{\partial}{\partial x}\left( qD_0 \frac{\partial n_c(x)}{\partial x} \right) = qD_0 \frac{\partial^2 n_c(x)}{\partial x^2} \tag{5}$$

where $D_0$ is the diffusion coefficient of electrons in the conduction band assuming that transport is not affected by the presence of trap states in the band gap. A discussion of the influence of traps on the electron diffusion coefficient will follow in section 1.2.2.

Assuming that recombination with the oxidized dye is negligible (cf. chapter 1.1.2), that the concentration of acceptor species in the electrolyte (mainly $I_3^-$) is much larger than $n_c$ and can be treated as a constant, that recombination is first order with respect to acceptor species as well as electrons in the semiconductor, and that it does not occur directly from surface trap states, the rate of recombination $U_n$ can be formulated as:

$$U_n = k_r \cdot n_c(x) = \frac{n_c(x)}{\tau_0} \tag{6}$$

Here, $k_r$ is the rate constant of recombination (containing the concentration of acceptor species)[94] and $\tau_0$ is the lifetime of conduction band electrons.[90]

By inserting equations (4), (5), and (6) into the continuity equation, one obtains:[87]

$$\frac{\partial n_c(x,t)}{\partial t} = \eta_{inj}\alpha(\lambda) I_0 e^{-\alpha(\lambda)x} + D_0 \frac{\partial^2 n_c(x)}{\partial x^2} - \frac{n_c(x)}{\tau_0} \tag{7}$$

Eq. (7) or similar expressions (in particular, with modified terms for $U_n$) are used as a basis to derive solutions for the electron density profile $n(x,t)$ for various different situations with respect to illumination and bias voltage in the DSC. This way, theoretical models are developed to describe and evaluate experimental data from different measurement methods. Two basic cases can be distinguished: the time-independent case (steady state), in which $\frac{\partial n_c(x,t)}{\partial t} = 0$, and the time-dependent case $\frac{\partial n_c(x,t)}{\partial t} \neq 0$. The steady-state continuity equation is relevant for current-voltage characteristics and quantum efficiency measurements (chapters 1.4.2 and 1.4.3), while the time-dependent form must be used for descriptions of time- and frequency-dependent measurements such as transient photocurrent and photovoltage measurements, impedance spectroscopy, and intensity-modulated photocurrent and photovoltage spectroscopy (sections 1.4.4 to 1.4.7).

At this point, it is useful to consider two specific solutions of the time-independent form of eq. (7) to illustrate the basic difference between the situation in which no current flows through the cell (open circuit) and the situation in which the maximum current flows (short circuit). The $n_c(x)$ obtained for these cases for illumination from the substrate side are presented graphically in ***Figure 4*** together with the corresponding quasi-Fermi level profiles $E_{fn}(x)$ obtained via eq. (1).[87, 111, 112]

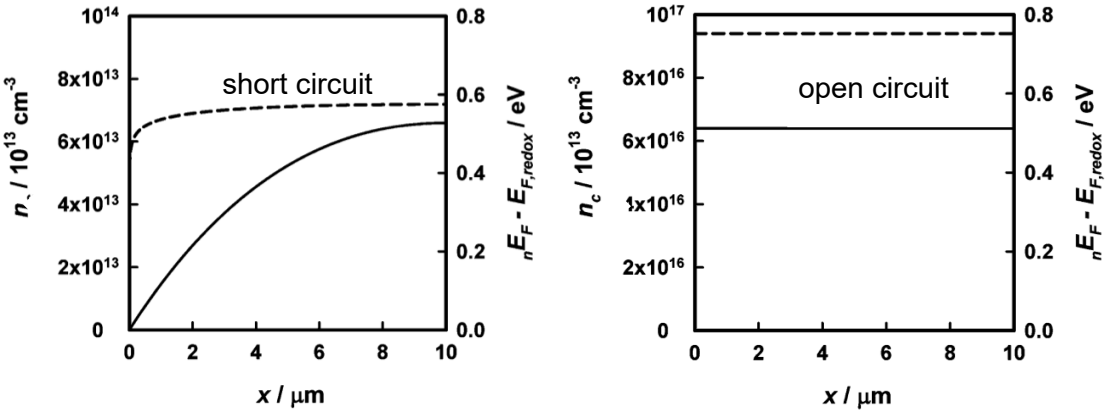


***Figure 4:*** *Calculated profiles of the electron concentration n (solid lines) and the quasi-Fermi level with respect to the redox level of the electrolyte $_nE_F$-$E_{F,redox}$ (dashed lines) in a porous dye-sensitized semiconductor under illumination. Adapted from ref. [111]. x is the location along the axis perpendicular to the substrate, with x = 0 corresponding to the substrate/semiconductor interface. Parameters used for the calculations were: $I_0 = 10^{17}$ cm$^{-2}$s$^{-1}$, $N_c = 10^{21}$ cm$^{-3}$, $D_0 = 0.4$ cm$^2$s$^{-1}$, and $\tau_0 = 0.001$ s.*

$n_c(x)$ and $E_{fn}(x)$ under open-circuit conditions are constant over the whole thickness of the porous semiconductor film. Under short-circuit conditions, on the other hand, the electron density and the quasi-Fermi level show a gradient with a steep decrease towards the substrate/semiconductor interface ($x$ = 0 µm), which constitutes the driving force for the diffusion of electrons to the back contact. Note that the quantities $E_{fn}$ and the corresponding voltage $V_f = E_{fn}/q$ (see chapter 1.4.2) in the present work generally refer to the value at $x$ = 0 µm and that whenever a current flows the quasi-Fermi level at the semiconductor/electrolyte interface ($x = d$) will be higher than that given value at x = 0 µm.

Eq. (7) is a useful approximation, but it does not account for the presence of a large density of trap states in the band gap, a characteristic property of dye-sensitized

nanostructured electrodes.[87, 113, 114] In fact, charge extraction measurements have confirmed that under most experimental conditions the density of electrons in traps greatly exceeds the density of conduction band electrons.[87, 113, 115] The effect of trapping on charge transport and recombination is most commonly described by the multiple trapping (MT) model.[85, 116, 117] According to this model, electrons moving through the semiconductor via conduction band states will be captured by trap states and subsequently detrapped again by thermal activation many times on their way to the back contact. The probability of trapping and detrapping and, hence, the diffusion coefficient of the electrons, depend on the position of the quasi-Fermi level. Recombination will be affected as well, which can be explained by the fact that the balance between the density of trapped electrons and the density of conduction band electrons will shift towards the latter if the Fermi level is raised, thus increasing the density of charge carriers available for recombination.[85, 87, 111] The MT model is supported by a vast amount of experimental data on transport and recombination in DSCs (see following two chapters).[86, 114, 116, 118, 119] With respect to the theoretical description using a continuity equation, a common approach to treat trapping and detrapping is to set up a continuity equation for conduction band electrons and add a term describing the effect of traps on the conduction band electron density:[120]

$$\frac{\partial n_c(x,t)}{\partial t} = D_0 \frac{\partial^2 n_c(x,t)}{\partial x^2} + \eta_{inj}\alpha(\lambda) I_0 e^{-\alpha(\lambda)x} - \frac{n_c(x,t)}{\tau_0} - \frac{\partial n_t(x,t)}{\partial t} \tag{8}$$

From eq. (8) it is apparent that, in the case of linear recombination with respect to the electron density, trapping will not affect the steady-state response of the solar cell, because the trapping term is dropped in this time-independent case. This implies that steady-state characteristics such as current-voltage curves and quantum efficiency spectra should not be influenced by trapping.[85, 94, 97, 109, 112] However, certain solar cell properties that help understand variations in the global device parameters, such as the electron lifetime, are only accessible experimentally via time- or frequency-dependent characterization,[85, 87, 90, 121] so that an understanding of the trap-influenced non-steady-state case is, nevertheless, crucial. Furthermore, DSCs commonly show non-linear recombination kinetics, which has been discussed as being caused by the presence of trap states at the surface of the porous semiconductor.[90, 94, 111] For non-linear recombination, the formal treatment (see chapter 1.2.3) results in a variation of the electron diffusion length

with the quasi-Fermi level,[94] which leads to a (surface trap-induced) non-ideality of the *steady-state* device characteristics and of their dependence on the light intensity.[94, 111]

### 1.2.2 Electron Transport in the Nanostructured Semiconductor

Electron transport in the mesoporous semiconductor of a DSC is strongly affected by the intimate intermixing of semiconductor, electrolyte, and dye on the nanometer scale. The positive ionic charges in the electrolyte as well as the dye cations screen the electron charge. In combination with the small size of the $TiO_2$ particles (or wires) and their typically low intrinsic doping density, the effect of this is that no significant band bending and hence no built-in electric field forms.[97, 122] Therefore, transport in standard DSC anodes based on nanoparticulate $TiO_2$ is primarily driven by the electron concentration gradient, i.e., it occurs by diffusion (eq. (5)). It has to be kept in mind, though, that this might not always be the case for certain electrode materials and/or geometries, because band bending according to the Poisson equation is influenced by the above-mentioned particle size and doping density, as well as by the dielectric constant.[63] For example, Oekermann et al. investigated electron transport in electrodeposited, porous ZnO films sensitized with the dye eosin Y and their results indicated that field-driven electron transport indeed played a role in a less porous part of the film closest to the substrate.[123] As a result of the electrostatic interaction between electrons in the semiconductor and positive ions in the electrolyte, electron transport is influenced by the type of cation used.[124] In several works, transport has therefore been described in the framework of ambipolar diffusion, in which electrons and electrolyte cations move jointly at the same velocity, the slower species being accelerated and the faster one being slowed down.[110, 125] However, this model is merely a first-order approximation of the real situation at the semiconductor/dye/electrolyte interface in a DSC, as it neglects the presence of various other charged species that contribute to local charge neutrality, such as the oxidized dye.[126]

Since charge transport through the nanostructured semiconductor is also affected by the presence of trap states in the band gap, many groups have investigated the energetic distributions of these traps, not only by photoelectron spectroscopy,[70] but also by charge extraction measurements,[113, 127] impedance spectroscopy,[114, 128] cyclic voltammetry and spectroelectrochemistry.[129] In most cases, an exponential density of states distribution

$g^t(E)$ with increasing density towards the conduction band edge $E_c$ was found:[87, 113, 114, 127, 128]

$$g^t(E) = \alpha \cdot \frac{N_t}{kT} \cdot \exp\left[\frac{\alpha(E - E_c)}{kT}\right] \tag{9}$$

where $\alpha$ is the so-called trap distribution parameter, and $N_t$ is the total trap density. Using the zero-Kelvin approximation of the Fermi-Dirac distribution,[63] the following expression for the density of trapped electrons $n_t$ as function of the quasi-Fermi level is obtained:

$$n_t(E_{fn}) = N_t \cdot \exp\left[\frac{\alpha(E_{fn} - E_c)}{kT}\right] \tag{10}$$

Nevertheless, deep-level traps with a narrow energy distribution (sometimes called "mono-energetic traps") or a combination of exponential and "mono-energetic" traps have also been observed.[90, 129-131] There is still some uncertainty as to the nature and exact location of the traps. It is not clear, for example, what share of traps is located at the surface of the semiconductor and what share is located in the bulk. As for the possible origins of band gap states in $TiO_2$, it has been suggested that undercoordinated titanium surface atoms play a major role.[69] On the other hand, some authors have proposed that trapping may be of Coulombic nature, i.e., due to local field effects between electrons and cations in the electrolyte.[132] The traps that are being discussed for the alternative photoelectrode material ZnO will be addressed in chapters 1.3.1 and 1.3.2.

An important consequence of multiple trapping observed in numerous experimental studies is that the diffusion coefficient measured by small-perturbation characterization methods depends on the electron density, i.e., on the position of the quasi-Fermi level $E_{fn}$ (also see chapters 1.4.5 and 1.4.6).[87, 118] An expression for this trapping-influenced diffusion coefficient is obtained by applying the quasi-static approximation[85] to the continuity equation with trapping term, eq. (8). In the quasi-static approximation, trapping and detrapping are assumed to be fast relative to other processes in the cell, so that the concentration of trapped electrons is in a quasi-equilibrium with the concentration of conduction band electrons or, in other words, changes in $n_t$ can be described being directly linked to changes in $n_c$:[85]

$$\frac{\partial n_t}{\partial t} = \frac{\partial n_t}{\partial n_c}\frac{\partial n_c}{\partial t} \tag{11}$$

With the help of this approximation, eq. (8) can be simplified to a treatment of free carriers including a modified diffusion coefficient (and electron lifetime, see 1.2.3) resulting from trapping (cf. Supporting Information of ref. [109]):[87]

$$\frac{\partial n_c(x,t)}{\partial t} = D_n \frac{\partial^2 n_c(x,t)}{\partial x^2} + \eta_{inj}\alpha(\lambda) I_0 e^{-\alpha(\lambda)x} - \frac{n_c(x,t)}{\tau_n} \tag{12}$$

Here, $D_n$ is the effective electron diffusion coefficient, which is related to the diffusion coefficient of conduction band electrons (without influence of trapping) via a trapping factor[85]

$$D_n = D_0\left(1+\frac{\partial n_t}{\partial n_c}\right)^{-1} \approx D_0\left(\frac{\partial n_t}{\partial n_c}\right)^{-1} \tag{13}$$

To determine the dependence of $D_n$ on the quasi-Fermi level in this model, the trapping factor can be rewritten as[111, 128]

$$\frac{\partial n_t}{\partial n_c} = \frac{\partial n_t}{\partial E_{fn}}\frac{\partial E_{fn}}{\partial n_c} = \alpha\frac{n_t}{n_c} = \alpha\frac{N_t}{N_c}\cdot\exp\left[\frac{(\alpha-1)\cdot(E_{fn}-E_c)}{kT}\right] \tag{14}$$

and inserted into eq. (13) to result in

$$D_n = D_0\frac{N_c}{\alpha\cdot N_t}\exp\left[\frac{(1-\alpha)\cdot(E_{fn}-E_c)}{kT}\right] \tag{15}$$

For an exponential distribution of traps, $D_n$ is thus expected to vary exponentially with the quasi-Fermi level.

### 1.2.3 Recombination

Recombination reactions have a crucial effect on the performance of solar cells. The net output current density of a cell is determined by the sum of photogenerated current density and recombination current density, which flow in opposite directions. Recombination reduces the output current over the whole range of bias voltages, and at zero net current the balance between photogeneration of electrons and recombination determines the open-circuit voltage $V_{oc}$ (cf. chapters 1.1.2 and 1.4.2). A central goal in DSC research is to investigate the origins and mechanisms of recombination characteristic of specific cell structures and to develop customized methods to suppress undesired losses. As briefly introduced in section 1.1.2, recombination in dye-sensitized solar cells can

occur between semiconductor and oxidized dye or electrolyte, or at contact points between substrate and electrolyte. Recombination via the substrate, albeit critical for device performance, is omitted in most quantitative models because it is effectively prevented by coating the substrate by a compact layer blocking electron transfer to the electrolyte but allowing for extraction of electrons at the back contact.[91, 92] Such layers are routinely prepared for instance by spray pyrolysis,[92] sputter deposition,[133] or electrodeposition.[134-138] Furthermore, in many cases recombination with the dye is also negligible and, thus, omitted in model descriptions.[86, 87, 97] In this section, recombination will be treated as a process occurring solely between semiconductor and electrolyte first, before the effects of dyes on recombination will be addressed.

According to general chemical kinetics, the rate of recombination can be written as the product of a rate constant and the concentrations of reactants, each accompanied by an exponent expressing the order of the reaction with respect to the particular reactant. In DSCs with iodide/triiodide electrolytes, both $I_3^-$ as well as $I_2$ have been discussed as electron-accepting species involved in recombination with the electrolyte.[95, 139] It has been found that the recombination reaction is approximately first order with respect to either $I_3^-$ or $I_2$.[139, 140] Concerning the reaction order with respect to the conduction band electron density $n_c$ in the porous semiconductor, a first-order model was introduced as a first approach in eq. (6). However, real DSCs usually show sub-linear recombination kinetics (reaction order < 1) with respect to $n_c$.[86, 109, 141] Under the same assumptions (except for first-order kinetics with respect to $n_c$) made in connection with eq. (6), a useful way to express the rate of recombination is then[90, 94, 142]

$$U_n = k_{el}[I_3^-]{n_c}^{\beta} = k_r {n_c}^{\beta} \tag{16}$$

where $k_r$ is the rate constant containing the concentration of acceptor species in the electrolyte and $0 < \beta \leq 1$ is the reaction order with respect to $n_c$, also known as the recombination parameter. The experimental observation of $\beta < 1$ has been suggested to be the result of recombination mediated via surface traps (capture of conduction band electrons by surface trap states, followed by transfer to the electrolyte) in addition to directly from the conduction band.[90, 111]

At a given energy $E$, the rate constant of recombination between donor states in the semiconductor and acceptor states in the electrolyte can be described following non-

adiabatic electron transfer theory, which is based on the work of Marcus and of Gerischer:[71, 96, 143]

$$k_{\mathrm{el}} = \frac{2\pi}{\hbar}\overline{|H_{AB}|}^2 \frac{1}{\sqrt{4\pi\lambda kT}} \exp\left[-\frac{\left(\lambda + \Delta G^0\right)^2}{4\lambda kT}\right] \tag{17}$$

Here, $\overline{|H_{AB}|}^2$ is the value of the absolute square of the perturbation matrix element averaged over the final states (with $H_{\mathrm{AB}}$ as the perturbation or coupling),[71] $\lambda$ is the reorganization energy (cf. section 1.1.2), and $\Delta G^0 = E_{fn} - E_{\mathrm{redox}}$ is the free energy change, which depends on the quasi-Fermi level in the semiconductor and influences the activation energy $\Delta G^* = \frac{\left(\lambda + \Delta G^0\right)^2}{4\lambda}$ of the electron transfer reaction. $\overline{|H_{AB}|}^2$, often simply referred to as the electronic coupling, exponentially depends on the distance between semiconductor and acceptor.[96, 144] Because recombination can take place from a range of energy levels in the semiconductor (conduction band or surface trap states) to a range of energy levels in the electrolyte, the overall recombination rate depends on the integral of eq. (17) over all possible energy levels, i.e., on the overlap of occupied states in the semiconductor with unoccupied states in the electrolyte.[96]

The presence of dye molecules in the interface between semiconductor and electrolyte can have a number of effects on recombination. First of all, as indicated above, electrons in the semiconductor may recombine with oxidized dye molecules if regeneration by the electrolyte is too slow. In this case, the rate constant $k_{\mathrm{r}}$ and other recombination parameters such as the effective electron lifetime $\tau_{\mathrm{n}}$ may be interpreted as reflecting a combined effect of recombination with dye and electrolyte. Dye molecules as well as other non-sensitizing adsorbates (e.g., coadsorbates used to prevent aggregation) can also influence the rate of charge transfer between semiconductor and electrolyte.[145-149] In many cases, increasing the amount of dye was found to block recombination, most likely by forming a physical barrier between semiconductor and electrolyte and thereby decreasing the electronic coupling in eq. (17).[148, 150] Some types of dyes, however, promote recombination rather than to block it, probably by offering a binding site for $I_2$ or $I_3^-$ close to the semiconductor surface.[145, 148, 151] Besides influencing the distance between semiconductor and electrolyte acceptor species, adsorption of dyes and coadsorbates can affect recombination by shifting the position of the semiconductor energy levels through a change of the surface charge or as a result of their dipolar field, thus

affecting the overlap of donor and acceptor states participating in recombination.[67, 128, 152]

Like electron transport in the DSC, recombination is affected by the presence of band gap states and the measured electron lifetime corresponds to the $E_{fn}$-dependent effective lifetime $\tau_n$ rather than to the constant lifetime of electrons in the conduction band, $\tau_0$. In the quasi-static approximation of the multiple trapping model (cf. previous section),[85]

$$\tau_n = \tau_0 \left( 1 + \frac{\partial n_t}{\partial n_c} \right) \approx \tau_0 \frac{\partial n_t}{\partial n_c} \tag{18}$$

As described further above, this result is derived from a continuity equation assuming that recombination is first order with respect to $n$, with $k_r = \tau_0^{-1}$. For the more realistic case of sub-linear recombination, the influence of trapping can still be described by eq. (18) as long as the lifetime characteristic for direct recombination of conduction band electrons, $\tau_0$, is replaced by a lifetime reflecting both direct recombination as well as surface state-mediated electron transfer, often termed $\tau_f$.[90] Substituting the trapping factor in eq. (18) by eq. (14) delivers the relationship between the effective electron lifetime and the quasi-Fermi level:

$$\tau_n = \tau_0 \cdot \alpha \frac{N_t}{N_c} \cdot \exp\left[ \frac{(\alpha - 1) \cdot (E_{fn} - E_c)}{kT} \right] \tag{19}$$

This shows that the Fermi level-dependence of $\tau_n$ should be determined by the trap distribution parameter $\alpha$, assuming an exponential distribution of trap states and neglecting recombination via surface states. If surface state-mediated recombination is considered (replacement of $\tau_0$ by $\tau_f$), the slope of the lifetime vs. $E_{fn}$ in a semilogarithmic plot is expected to be $(\alpha\text{-}\beta)/kT$ instead of $(\alpha\text{-}1)/kT$ due to the dependence of $\tau_f$ on the energetic distribution of surface states.[90, 109, 141] This prediction was confirmed in several experimental studies.[90, 141]

In section 1.1.2, the diffusion length $L_n = \sqrt{D_n \tau_n}$ (eq. (2)) was introduced as an important measure for the charge collection efficiency in a DSC. Having deduced expressions linking $D_n$ and $\tau_n$ to the corresponding "free" (not trap-influenced) parameters in the quasi-static approximation, eq. (13) and eq. (18), said equations can now be combined to yield:[115]

$$L_n = \sqrt{D_n \tau_n} = \sqrt{D_0 \tau_0} = L_0 \tag{20}$$

$L_0$ is often referred to as the steady-state diffusion length. This result shows that in the quasi-static approximation of the MT model and under the assumption of first-order recombination, the trapping factors in $D_n$ and $\tau_n$ are predicted to cancel and the diffusion length $L_n$ is expected to be a constant, i.e., independent of the quasi-Fermi level. However, in real DSCs the diffusion length calculated from the measured $D_n$ and $\tau_n$ usually shows a slight dependence on $E_{fn}$.[86, 141] This is likely caused by recombination via surface states, which, as explained above, is expected to lead to different energy-dependences for $D_n$ and $\tau_n$. Recombination in dye-sensitized solar cells will be further discussed in conjunction with the recombination resistance determined by electrochemical impedance spectroscopy (chapter 1.4.4).

## 1.3 Selected Materials

### 1.3.1 ZnO as Photoelectrode Material in DSCs

ZnO is a semiconducting material with intrinsic n-type conductivity and is used for a wide range of technological applications, such as transparent conductive films, piezoelectric devices, and varistors.[153, 154] Its most stable form under ambient conditions is wurtzite, which shows a hexagonal crystal structure.[63, 154] The rich defect chemistry of bulk ZnO has been investigated in much detail over the past decades.[154] The most frequently discussed shallow donors in intrinsic bulk ZnO are oxygen vacancies and zinc interstitials.[155] More recently, it has been suggested that the n-type conductivity of native ZnO is related to unintentional incorporation of impurities, most likely hydrogen, acting as donors.[156] Intrinsic ZnO has a direct band gap of 3.37 eV at room temperature,[154] similar to the band gap of anatase-type $TiO_2$ (3.28 eV),[157] the standard anode material in DSCs.[19] Compared to the latter, however, ZnO shows a higher bulk electron mobility (around 200 $cm^2\ V^{-1}\ s^{-1}$ vs. about 10 $cm^2\ V^{-1}\ s^{-1}$ in $TiO_2$).[157, 158] Furthermore, ZnO can be deposited in a variety of different nanostructures suitable for dye-sensitized solar cells even at low temperatures.[21] Preparation methods include doctor blading, screen printing or dip-coating using dispersions of ZnO nanoparticles (typically synthesized by sol-gel processing),[159-161] chemical bath deposition,[162] anodic etching,[163] and electrochemical deposition.[26] As a result of the above-mentioned advantages, ZnO has been widely investigated as alternative anode material in DSCs.[25, 43, 141, 160, 164, 165] Rela-

tively efficient cells could be obtained when ZnO was combined with selected Ru sensitizers or indoline dyes and liquid $I^-/I_3^-$ electrolytes.[25, 160, 165, 166] However, to date the best conversion efficiency attained with ZnO-based DSCs of $\eta$ = 7.5%[165] is significantly lower than the top efficiencies achieved with $TiO_2$ (cf. chapter 1.1.1). Multiple aspects have been discussed as possible factors limiting the efficiency. First, it was found that the use of standard Ru(II) dyes that are efficient in combination with $TiO_2$ is complicated by the fact that their high acidity and the presence of their complex-forming ligands lead to undesired reactions with ZnO,[167, 168] which is less stable in acidic environments than $TiO_2$.[169] The adsorption conditions and sensitization time have to be carefully optimized to avoid the formation of $Zn^{2+}$-dye complexes and deterioration of the ZnO surface.[160, 167] Dyes that do not show undesired chemical interaction with ZnO include the indoline dyes used in the present work (cf. following chapter).[170] The weaker interaction between ZnO and such dyes, however, can lead to insufficient stability of the ZnO-dye bond in certain electrolytes, including solutions containing efficiency-enhancing additives like 4-*tert*-butylpyridine.[170, 171] Another factor believed to contribute to the yet limited efficiency of ZnO-based DSCs is hindered electron injection as a result of interfacial intermediate states in the excitation/injection process, which has been reported for several different dyes on the basis of ultrafast spectroscopy.[172-174] This phenomenon may enhance recombination between oxidized dye molecules and electrons in ZnO, thus hindering diffusion of the latter through the nanostructure to the back contact.[174] In order to make use of the advantageous properties of ZnO as electrode material while minimizing losses due to undesired dye-$Zn^{2+}$ interactions or hindered electron injection, new dyes and/or dye combinations must be investigated as sensitizers, and the understanding of different microscopic processes in ZnO-based DSCs must be deepened. The present work contributes to both of these challenges while focusing on electrodeposited ZnO as electrode material, which offers the benefits of a simple, low-cost and low-temperature preparation and will be addressed in detail in the following chapter.

### 1.3.2 Electrodeposited Compact and Porous ZnO

Electrochemical deposition from aqueous solutions represents an attractive way to prepare ZnO films at low temperatures. This method allows both the preparation of compact as well as porous structures for dye-sensitized solar cells. The compact ZnO films serve as blocking layers preventing recombination between the conductive glass sub-

strate and the electrolyte (cf. 1.1.2),[136, 138] while the porous films are used to prepare photosensitized electrodes.[25, 26] Electrodeposition of crystalline ZnO films at temperatures between 25°C and 80°C was first described by Peulon et al.[135] and Izaki et al.,[175] who used aqueous electrolytes containing $Zn^{2+}$ together with dissolved oxygen[135] or nitrate[175] as oxidant. In a later study, deposition based on an electrolyte with hydrogen peroxide ($H_2O_2$) instead of nitrate or oxygen was reported.[176] Film formation is achieved by applying a cathodic potential to the working electrode (i.e., the substrate), which leads to reduction of the oxidant $NO_3^-$, $O_2$ or $H_2O_2$. The concomitant local increase in pH causes precipitation of ZnO (via zinc hydrate as intermediate) on the surface of the substrate. In the case of oxygen-based deposition, the reaction steps are:[25, 177]

$$O_2 + 2H_2O + 4e^- \rightarrow 4OH^- \quad (21)$$

$$Zn^{2+} + 2OH^- \rightarrow \text{“}Zn(OH)_2\text{“} \rightarrow ZnO + H_2O \quad (22)$$

The complete reaction can thus be written as:[25, 135, 177]

$$Zn^{2+} + ½O_2 + 2e^- \rightarrow ZnO \quad (23)$$

***Figure 5*** shows the morphology of ZnO films deposited by this method on FTO/glass at 80°C, using a working electrode potential of -0.85 V vs. the Ag/AgCl reference electrode. The left structure is the result of film deposition without substrate pretreatment, while the one on the right was attained following cathodic pre-electrolysis in the absence of the zinc precursor.[135] The electrochemical pretreatment activates the FTO substrate and promotes nucleation during the subsequent film deposition, leading to dense ZnO films as opposed to the otherwise obtained open-structured layers. When performed in combination with electrochemical activation of the substrate, electrodeposition of ZnO from $O_2$-based deposition baths thus yields films that fully cover the substrate, as desired for blocking layers.

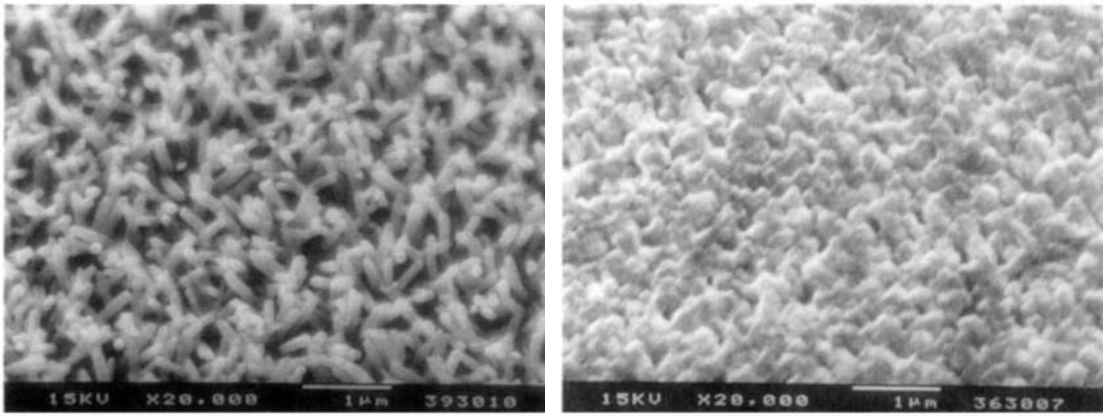


***Figure 5:*** *Scanning electron microscope (SEM) images of surfaces of ZnO films electrodeposited from aqueous oxygen-saturated solutions of 5 mM $ZnCl_2$ and 0.1 M KCl at 80°C using a deposition potential of -0.85 V vs. Ag/AgCl, without (left) or with (right) electrochemical activation of the FTO substrate prior to deposition. From ref.* [135].

In terms of crystallographic texture, a strong preferential orientation with the [002] direction (c-axis) perpendicular to the substrate was detected.[135] Depending on the deposition parameters, the optical band gap of as-deposited films was found to be 3.45 – 3.6 eV,[135] which is slightly higher than the band gap of intrinsic ZnO (3.37 eV, see previous section). It has been suggested that this is due to high ($\geq 10^{20}$ $cm^{-3}$) doping levels leading to a shift of the Fermi level into the conduction band (Burstein-Moss effect).[135, 178] Oxygen vacancies, interstitial Zn, and chloride ions on oxygen sites have been discussed as possible bulk defects in the electrodeposited material.[135, 179, 180] On the surface, -OH and -Cl groups were detected.[180, 181] This deposition technique can be easily modified to yield nanostructured films with highly attractive properties as photoelectrodes in DSCs (***Figure 6***). When certain structure-directing agents (SDA) such as coumarin 343,[182, 183] tetrasulfonated metallophthalocyanines,[184] or eosin Y[26] are added to the deposition bath, they bind to the ZnO surface and are incorporated into the growing film, thereby controlling its structure. Following deposition, these template molecules can be removed to yield the pure ZnO matrix. Depending on the type of SDA, various film textures and morphologies can be obtained, as reviewed in ref. [25]. ZnO deposition from oxygen-based deposition baths in the presence of eosin Y results in the most interesting structures with respect to application in DSCs.[25]

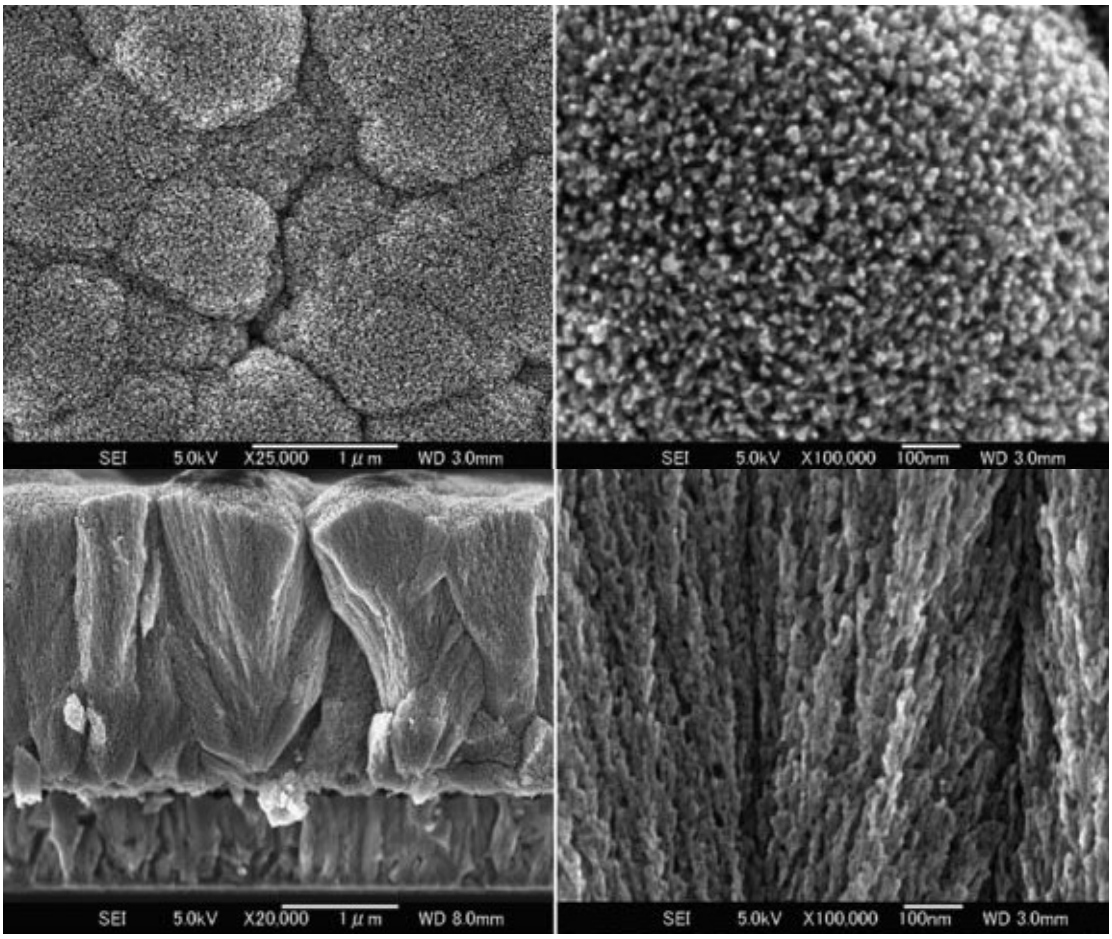


***Figure 6:*** *SEM images of a nanoporous ZnO film on FTO/glass, electrodeposited from an aqueous solution containing 5 mM $ZnCl_2$, 0.1 M KCl and 45 µM of the structure-directing agent eosin Y. The temperature of the deposition bath was 70°C and the deposition potential was -0.96 V vs. Ag/AgCl. Images were taken after removal of eosin Y. From ref.* [25].

If the deposition is carried out at potentials more cathodic than -0.85 V vs. Ag/AgCl, eosin Y is reduced and forms complexes with $Zn^{2+}$, which are precipitated in parallel to pure ZnO.[25, 26] Further deposition is blocked in places where ZnO/eosin Y complexes are located, guiding the film growth into other directions and eventually resulting in a hybrid ZnO/eosin Y layer consisting of a porous ZnO matrix with the SDA molecules occupying the pores.[25, 26, 185] Eosin Y can be easily and completely removed from such films by treatment in soft alkaline solution.[26, 183] An example of a ZnO layer obtained this way is shown in ***Figure 6***. The films consist of micrometer-sized crystals showing a columnar internal nanostructure reminiscent of a sponge, with a pore size in the range of 10 – 20 nm.[27, 186] The total porosity is about 50-60%[26, 136, 185, 187] and the roughness fac-

tor (internal surface area per projected film area) was determined to be up to 400.[25, 186] The band gap energy after removing eosin Y and drying the films at 150°C was estimated to be ~ 3.4 eV.[186] The µm-sized crystals were found to be highly crystalline and show a high level of preferential orientation with the c-axis widely parallel to the surface normal,[26] which is beneficial for charge transport through the film.[28] In fact, intensity-modulated photocurrent spectroscopy[28] and electrochemical impedance spectroscopy[136] indicated that diffusion was faster in porous electrodeposited ZnO compared to nanoparticulate ZnO films even though the latter had been post-treated at 450°C to ensure sufficient particle necking, while the electrodeposited films were either used as-deposited or dried at a moderate temperature of 150°C. Effective diffusion coefficients were found to be in the same range ($\sim 10^{-5}$ $cm^2 s^{-1}$)[28] as for sintered nanoparticulate $TiO_2$ electrodes.[87, 88] In spite of these promising results on transport, the top power conversion efficiency achieved with porous electrodeposited ZnO has so far remained at a comparatively low level of 5.6%,[25] which was attained by sensitization with the indoline dye D149. This suggests that other aspects of the cell operation, such as recombination and charge injection from the dye to the semiconductor have to be examined more closely to gain a better understanding of the cells and reveal possible strategies for improvement. Regarding recombination, electrochemical impedance spectroscopy measurements by Pauporté et al.[136, 186] yielded smaller effective electron lifetimes in electrodeposited indoline dye-sensitized ZnO films compared to sintered nanoparticulate ZnO films, which was explained by an increased density of surface trap states as indicated by photoluminescence measurements.[136] In order to clarify the origins of the still limited efficiency of these ZnO films with highly attractive nanostructure, further work in this area was necessary and is pursued in the present work.

### 1.3.3 Screen Printing of Porous Metal Oxide Films

Screen printing is a simple and versatile method to prepare two-dimensionally patterned films for many different areas of application. It is widely used on an industrial scale, for instance in textile and paper printing[188] and, more recently, in the production of printed electronics such as sensors and antennas.[189] On the laboratory scale, different types of solar cells, including polymer solar cells[190] and dye-sensitized solar cells,[161, 191-194] have been fabricated by screen printing.

For a successful preparation of nanostructured $TiO_2$ or ZnO films for DSCs by screen printing, suitable nanoparticle pastes with low volatility and rather high viscosity have to be prepared.[190, 191, 194, 195] One approach is to mix commercially available nanoparticle powders with solvents, often water and alcohols.[191, 195] The paste is distributed on a screen consisting of a mesh stretched upon a frame, which is positioned closely above the substrate to be printed without touching it.[190, 196] The mesh itself is impermeable for the paste but is patterned, i.e., it contains openings of desired shape and size, thus allowing to coat defined areas of the substrate with the paste. A squeegee is forced into the screen to bring it into line contact with the substrate and is moved linearly across the screen.[190, 196] Thereby, the nanoparticle paste is pushed through the open areas of the mesh onto the substrate, where it remains as the mesh moves back away from the substrate.[190, 196] The obtained film is dried at elevated temperatures to remove the solvents and, if necessary, the printing procedure is repeated until the desired film thickness is achieved.[191] To improve necking of the metal oxide nanoparticles in the film, the film deposition is finalized by post-treatments such as high-temperature (up to 500°C) sintering[191, 193, 195] or hydrothermal treatment.[197]

### 1.3.4 Organic Dyes, Coadsorbates, and Co-Sensitizers

Organic dyes have gained increasing interest as alternatives to Ru(II) photosensitizers for DSCs based on ZnO or $TiO_2$. Metal-free molecules studied as DSC sensitizers include coumarins,[50, 173, 198, 199] tetrahydroquinolines,[200, 201] indolines,[52, 202, 203] triarylamines,[204-206] merocyanines,[207, 208] and squaraines.[32, 209] The main advantages of such organic sensitizers are their high molar absorptivities (often $\varepsilon > 40000\ M^{-1}cm^{-1}$ in the absorption maximum),[32, 51, 199, 202, 204] often simple and cost-efficient synthesis routes,[52] and the possibility of easily modifying their molecular structure.[32, 52, 200, 202, 210] Although organic dyes show relatively narrow absorption bands compared to Ru(II) sensitizers, this disadvantage can be approached by co-sensitization strategies (see below).[211] Most organic dyes exhibit a donor-acceptor or donor-π-bridge-acceptor structure: when electrons in the dye are excited by absorption of light, an intramolecular shift of electron density from the donor unit (through the π-bridge) into the acceptor occurs (push-pull character).[15, 34, 80] The molecules are ideally designed so that the anchoring group with which they bind to the semiconductor is part of the acceptor.[80] Hence, electron density is shifted towards the semiconductor upon excitation, enabling efficient electron injec-

tion as a result of the shortened distance between electron-donating orbitals of the sensitizer and electron-accepting states in the semiconductor. Among the organic dyes that have received the most scientific attention are indoline dyes (cf. ***Figure 7***), which were first introduced as photosensitizers for DSCs in 2003 by Horiuchi et al.[52] In combination with $TiO_2$, promising efficiencies of up to 9.52% have been reported.[203]

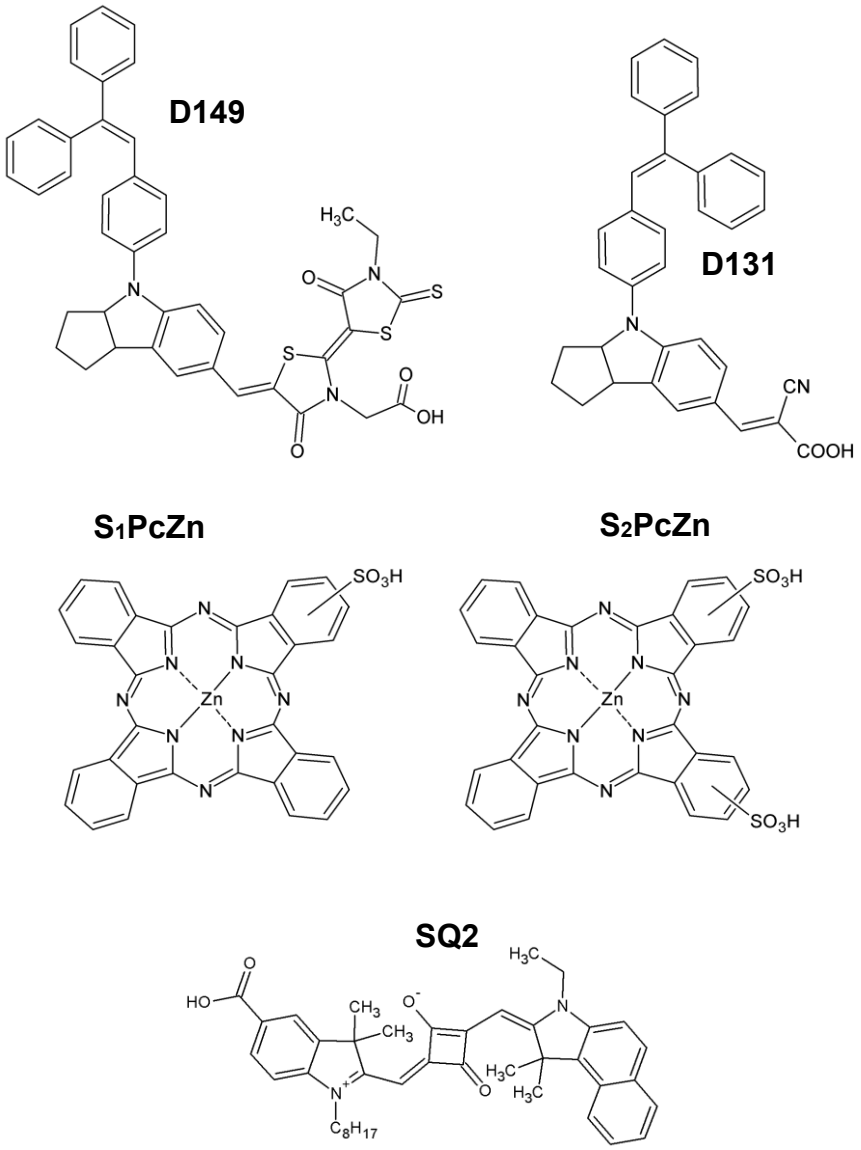


***Figure 7**: Molecular structures of the indoline dyes D149 (M = 741.94 g/mol) and D131 (M = 508.61 g/mol), of Zn(II) phthalocyanine mono- and di-sulfonic acid, and of the squaraine dye SQ2 (M = 630.81 g/mol). The Zn(II) phthalocyanine sample used for the experiments in this work was a mixture of the monosulfonic acid ($S_1$PcZn, 85%) and the disulfonic acid ($S_2$PcZn, 15%), referred to as $S_{1.15}$PcZn, with an average molecular weight of M = 670.01 g/mol.*

On ZnO, the indoline dye D149 (***Figure 7***, top left) has been successful as well, yielding $\eta$ of up to 6.1%[212] (compared to a top efficiency of ZnO DSCs of 7.5%).[165] As mentioned above, D149 is the best sensitizer found so far for porous electrodeposited ZnO ($\eta$ of up to 5.6%),[25] the main photoanode material used in the present work (cf. previous chapter). The donor part of D149 is made up of its substituted indoline unit, while the double-rhodanine unit constitutes the acceptor.[213] Theoretical investigations[213] found that the HOMO is relatively delocalized over the donor unit, and the LUMO is located on the acceptor unit, i.e., D149 exhibits the favorable push-pull character. However, the calculations also indicated that the carboxylic acid anchoring group is decoupled from the rest of the molecule and shows no significant contributions to the LUMO, which can potentially hinder electron injection to a semiconductor.[213] It is interesting to compare the characteristics of D149 to those of the indoline dye D131 (***Figure 7***, top right), which has been investigated as DSC dye in several previous studies[31, 214-216] and has been used in the experiments of the present work as well (see below). D131 has the same substituted indoline donor unit, but features a cyanoacrylic acid acceptor unit (instead of the two rhodanine rings in D149). For this molecule, sizeable contributions of the carboxylic acid anchoring group to the LUMO were calculated,[213] indicating a close proximity of electron density in the excited molecule to conduction band states in the semiconductor. Moreover, the LUMO energy of D131 was found to be 0.3 eV higher than that of D149,[213] which should increase the energetic overlap of the occupied states in the excited dye with empty conduction band states in the semiconductor (cf. ***Figure 3*** and corresponding text). Both of the above factors should contribute to an increased probability of electron injection to the semiconductor for D131 with respect to D149. However, the extent to which these calculated properties of the individual dye molecules can be transferred to the situation in a real device strongly depends on the specific properties of the employed semiconductor electrode. On electrodeposited mesoporous ZnO, for instance, D149 delivered higher photocurrents compared to D131,[216] while on $TiO_2$ nanorods, the opposite result was obtained.[217]

Many studies, in particular those focusing on DSCs with organic dyes, have reported the formation of dye aggregates on the surface of the porous semiconductor and have observed limitations in the photovoltaic performance due to aggregate-related injection limitations and enhanced recombination.[51, 80, 137, 202, 218, 219] An effective way to suppress aggregation and to thus significantly enhance the photovoltaic characteristics is to add

coadsorbates such as cholic acid (CA) or fatty acids like octanoic acid (OA) (***Figure 8***) to the dye adsorption solution.[51, 80, 137, 202, 218, 219]

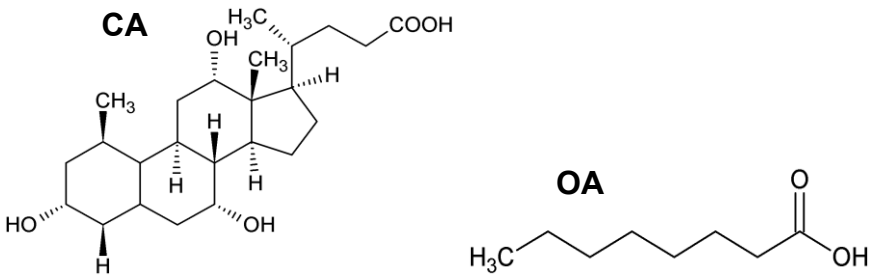


***Figure 8:*** *Structures of the coadsorbates cholic acid (left) and octanoic acid (right).*

By acting as spacers in between the sensitizer molecules, coadsorbates reduce the probability of radiationless decay and consequently increase the probability of electron injection into the semiconductor.[220] Besides affecting injection and, hence, the short-circuit current, aggregation was also reported to deteriorate open-circuit voltage and fill factor by increasing recombination.[137, 221] One of the aims of this work is to investigate the effects of dye aggregation on various microscopic DSC processes in more detail in order to add to the understanding of this aspect that often limits the efficiency.

In order to achieve panchromatic absorption of DSCs based on organic main sensitizers, dyes with complementary absorption spectra can be added to the semiconductor surface as co-sensitizers.[34, 222-227] As the typical organic DSC dyes mostly have their main absorption band located in the short- to mid-wavelength region of the visible spectrum (~450-600 nm),[202, 228] many studies have focused on finding appropriate sensitizers absorbing at longer wavelengths to be used as co-sensitizers in combination with established shorter-wavelength absorbers.[34, 222, 225-227, 229, 230] For example, the Zn(II) phthalocyanine TT1, which shows high absorptivity in the spectral range around 700 nm, was combined with the organic dye JK2 on $TiO_2$ to yield efficiencies of about 7.7%, which was clearly above the efficiencies of 3.5% and 7.1% observed for the two individual sensitizers.[222] While metalated phthalocyanines such as TT1 do not represent fully organic molecules, the choice of earth-abundant central metals such as Zn still renders them compatible with the requirement for cheap and environmentally sustainable production methods of DSCs. Like TT1, the asymmetrical squaraine sensitizer SQ1 has been used as an effective co-sensitizer with JK2 in ionic liquid electrolyte-based DSCs, resulting in $\eta$ = 6.4%.[226] A slightly modified version of the molecule,

SQ2 (***Figure 7***, bottom), which as an individual sensitizer delivered higher efficiencies compared to SQ1, was found to be well suited for combination with other dyes as well.[33, 223, 225] Some studies have focused on extending the photoelectrode absorption in the shorter-wavelength range.[31, 215] On porous electrodeposited ZnO, the indoline dye D131 (***Figure 7***, top right), which has its absorption maximum at around 420 nm, was combined with the indoline dye D149 to yield a broadened incident photon-to-electron conversion efficiency spectrum (section 1.4.3) and enhanced power conversion efficiency.[31] However, to date the absorption of dye-sensitized electrodeposited ZnO has not yet been successfully extended into the red part of the spectrum. The main absorption peak of D149 when adsorbed to $TiO_2$ or ZnO is centered around 550 nm and extends no further than to wavelengths of around 620-650 nm,[25, 137, 202] leaving out a significant portion of the spectral solar irradiance. Part of the goal of this work was therefore to extend the absorption in dye-sensitized electrodeposited ZnO into the red by using an appropriate co-sensitizer for D149. Inspired by the approaches of the above-mentioned previous studies,[33, 222, 223, 225, 230] either a mixture of Zn(II) phthalocyanine monosulfonic acid and disulfonic acid (***Figure 7***, middle) or the squaraine dye SQ2 were utilized for this purpose.

## 1.4 Characterization of Dye-Sensitized Solar Cells: Experimental Techniques and Their Theoretical Background

### 1.4.1 Optical Analysis by UV/Vis Absorption Spectroscopy

When a light-absorbing medium such as a dye solution or a dye-sensitized semiconductor film is illuminated by visible light, the light is partially reflected, partially absorbed, and partially transmitted.[63] Moreover, light can be forward scattered, i.e., transmitted through the material at a deflected angle with respect to the straight path.[231, 232] In this work, forward scattered photons will be treated as part of transmission, which is generally useful in optical analysis of photovoltaic materials as these photons leave the material without having generated free charge carriers. Provided that the dye is homogeneously distributed and its concentration is not too high, the photon flux density $\phi$ (or light

intensity) after passing through a sample of thickness $d$ is described by the Beer-Lambert law:[232]

$$\phi = \phi_0 \cdot 10^{-\varepsilon \cdot c \cdot d} \tag{24}$$

where $\phi_0$ is the photon flux density (or light intensity) before passing the sample, $\varepsilon$ is the wavelength-dependent molar absorptivity (formerly called molar extinction coefficient) of the absorbing species, and $c$ is the concentration of the latter in the sample. $\varepsilon$ depends on the dielectric environment of the light-absorbing species[233, 234] and, hence, can differ between a dye in solution and the same dye when adsorbed to a semiconductor surface.[235] The product $\varepsilon cd$ is called optical density or absorbance $abs$.[232] An alternative way to write the Beer-Lambert law, using the absorption coefficient $\alpha_{abs}$ of the absorbing medium, is:[232]

$$\phi = \phi_0 \cdot e^{-\alpha_{abs} \cdot d} \tag{25}$$

In a traditional UV/Vis absorption spectrometer, the sample is positioned between a combination of white light source and monochromator and a detector. The wavelength of light incident on the sample is varied and the photon flux density transmitted through the sample, $\phi$, is detected for each wavelength.[232] In some alternative spectrometer set-ups, on the other hand, the sample is illuminated by white light, the transmitted white light is dispersed into a spectrum of wavelengths by a fixed grating, and the different wavelengths are detected by a photodiode array.[236] The measured transmitted photon flux is related to the photon flux detected in a reference measurement performed in the same geometry but without the sample in the light path.[237] The transmittance $T_{trans}$ of the sample (fraction of transmitted light) is given by the ratio of $\phi$ and the initial light intensity $\phi_0$, the latter being equivalent to the intensity determined in the reference measurement:[237]

$$T_{trans}(\lambda) = \frac{\phi(\lambda)}{\phi_0(\lambda)} \tag{26}$$

$T_{trans}$ is then used to calculate the **absorbance** ***abs*** = $\varepsilon cd$ by means of eq. (24), or to determine the **light harvesting efficiency** $\eta_{lh}$, which is equivalent to the absorptance (fraction of absorbed light),[231] based on the simple energy conservation relationship:

$$\eta_{lh} = 1 - R_{refl} - T_{trans} \tag{27}$$

where $R_{refl}$ is the reflectance (fraction of reflected light). Reflection losses can be either directly estimated by measuring the transmittance of a sample that shows similar reflectance as the specimen but does not absorb visible light, or they can be accounted for by placing such a sample into the light path in the reference measurement.[237] In the case of dye-sensitized porous semiconductor electrodes, a porous semiconductor film of the same thickness and on the same type of substrate without dye is an appropriate choice for this purpose. For dye solutions, a cuvette filled with the solvent without dye constitutes a suitable reference sample.[237]

In basic transmission measurement arrangements consisting of light source, monochromator (if required), sample, detector, as well as lenses and mirrors,[237] forward scattered light may remain undetected depending on the angle at which it leaves the sample. For strongly scattering materials, this results in a significant underestimation of the transmittance and corresponding overestimation of the light harvesting efficiency and absorbance.[231] Using an integrating sphere to collect all transmitted and forward scattered light (***Figure 9***) allows a more exact analysis of the absorption properties of such samples.[238]

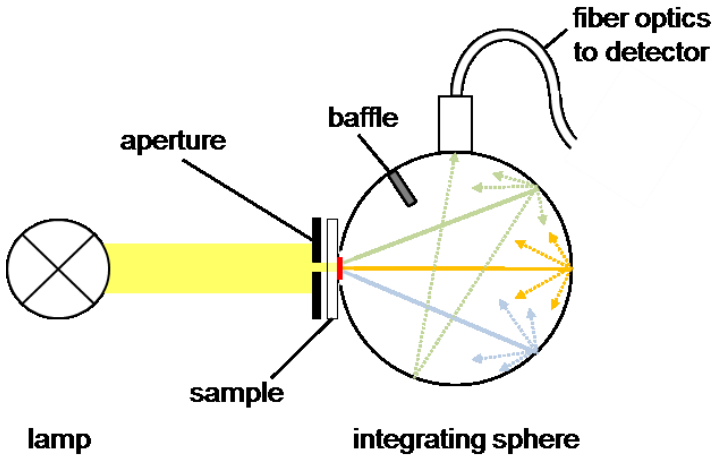


***Figure 9:*** *Scheme of a basic optical transmission measurement using an integrating sphere to collect transmitted and diffusely transmitted (forward scattered) light.*

As described above, the absorbance is proportional to the concentration of light-absorbing species in the sample. This allows determination of the dye concentration $c$ in solutions or dye-sensitized films from the absorbance in the peak of their absorption spectrum, $abs(\lambda_{max})$, provided that the molar absorptivity $\varepsilon(\lambda_{max})$ of the dye at the corre-

sponding wavelength as well as the thickness of the absorbing film (or the cuvette size, in the case of solutions) are known. For dye-sensitized films, the absorption peak is often broadened and/or shifted with respect to the solution spectrum due to dye-semiconductor interaction[71, 234] and, in some cases, dye aggregation.[52, 208, 239, 240] In this case, the **integrated absorbance**

$$abs_{\text{int}} = \int_{\lambda_1}^{\lambda_2} abs \, d\lambda \tag{28}$$

(with $\lambda_1$ and $\lambda_2$ as the wavelengths at which the absorption begins and vanishes) may be used to estimate the dye concentration rather than $abs(\lambda_{\max})$. The rationale behind this will be discussed in more detail in chapter 5.1. An alternative way to estimate the amount of dye in a dye-sensitized film is to dissolve the dye molecules out of the sample using a defined volume of a solvent, and to measure the UV/Vis absorption spectrum of the resulting solution. In the (usually highly diluted) solution, the dye molecules are mostly present in their monomeric form and the dye concentration can be accurately determined using $abs(\lambda_{\max})$ and $\varepsilon(\lambda_{max})$.

### 1.4.2 Current-Voltage Characterization

To obtain the current-voltage characteristics (often referred to as i-V or J-V curve) of a solar cell, a linear forward bias voltage sweep is applied between the working electrode (in DSCs, the dye-sensitized semiconductor electrode) and counter electrode, and the resulting current $i$ or current density $J$ is measured. This analysis is commonly done in the dark as well as under illumination. To investigate the cell properties under realistic operating conditions, the light intensity (spectrally integrated power density) is set to 100 $mWcm^{-2}$ and the spectrum of the illumination source is adjusted to AM1.5G conditions.[108, 112, 131] ***Figure 10*** shows an example of current-voltage characteristics (dark and illuminated) of a solar cell, together with the voltage-dependent power density under illumination.

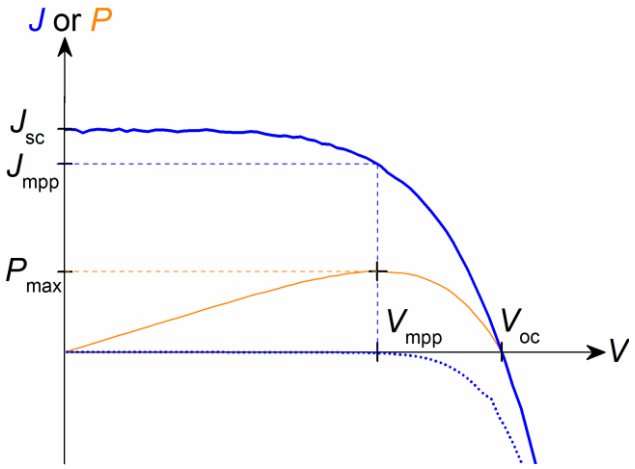


***Figure 10:*** *Current density-voltage curve of a solar cell in the dark (dotted blue line) and under illumination (solid blue line), as well as corresponding power density (solid orange line). The current density at $V = 0$ is the short-circuit current density $J_{sc}$, the voltage at $J = 0$ is the open-circuit photovoltage $V_{oc}$. The maximum power density $P_{max}$ of the cell corresponds to the product of the photocurrent density and photovoltage at the maximum power point (mpp), $J_{mpp}$ and $V_{mpp}$.*

The chart also contains several important photovoltaic parameters:[108, 131] the **short-circuit photocurrent density $J_{sc} = J(V = 0)$**, the **open-circuit photovoltage $V_{oc} = V(J = 0)$**, and the photocurrent density and photovoltage at the maximum power point, $J_{mpp}$ and $V_{mpp}$. The product of $J_{mpp}$ and $V_{mpp}$ yields the maximum power density $P_{max}$ of the cell. The ratio of $P_{max}$ to the product of $J_{sc}$ and $V_{oc}$ is defined as the **fill factor *FF***:[108, 131]

$$FF = \frac{J_{mpp}V_{mpp}}{J_{sc}V_{oc}} = \frac{P_{max}}{J_{sc}V_{oc}} \tag{29}$$

Finally, the overall cell performance is described by the **power conversion efficiency $\eta$**:[108, 131]

$$\eta = \frac{P_{max}}{P_{in}} \tag{30}$$

where $P_{in}$ is the power density of the incident light (e.g. 100 mWcm$^{-2}$).

A formal expression of the *J-V* characteristics can be obtained by solving the continuity equation for the steady-state case accounting for non-linear recombination with respect to conduction band electrons by using the semi-empirical $\beta$-recombination model to describe the recombination rate (eq. (16), $U_n = k_r n_c^{\beta}$).[109, 112, 128] This yields the following

diode-type equation, with the total current $J$ described as the sum of positive photocurrent and negative recombination current $J_{rec}$:[128]

$$J = J_{sc} - J_{rec} = J_{sc} - J_0\left[\exp\left(\frac{\beta \cdot qV_f}{kT}\right) - 1\right] \tag{31}$$

where $\beta$ is the previously introduced recombination parameter and $V_f$=($E_{fn}$-$E_{redox}$)/$q$ is the Fermi-level voltage, i.e., the voltage corresponding to the energy difference between the electron quasi-Fermi level $E_{fn}$ in the semiconductor and the redox energy of the electrolyte $E_{redox}$.[128] The factor $J_0$ can be considered an exchange current density and contains the dependence of the current on the position of the conduction band edge in the semiconductor, $E_c$, and on the rate constant $k_r$:[128]

$$J_0 = J_{0k} \cdot \exp\left(-\frac{\beta \cdot E_c}{kT}\right) = qk_r d \cdot {N_c}^{\beta} \cdot \exp\left(\frac{\beta \cdot E_{redox}}{kT}\right) \cdot \exp\left(-\frac{\beta \cdot E_c}{kT}\right) \tag{32}$$

where $J_{0k}$ describes the dependence of the current on the recombination rate constant $k_r$ independent of the conduction band edge, $q$ is the electron charge, $d$ is the porous semiconductor film thickness, and $N_c$ is the effective density of states at the conduction band edge. Combining equations (31) and (32), an expression for $J$ as a function of the four basic parameters $J_{sc}$, $J_{0k}$, $\beta$ and $E_c$ is attained:

$$J = J_{sc} - J_{0k} \cdot \exp\left(-\frac{\beta \cdot E_c}{kT}\right) \cdot \left[\exp\left(\frac{\beta \cdot qV_f}{kT}\right) - 1\right] \tag{33}$$

For the open-circuit case ($J$ = 0), rearranging eq. (33) under the assumption that $\exp\left(\frac{\beta \cdot qV_f}{kT}\right) >> 1$ yields the dependency of $V_{oc}$ on these four parameters:[128]

$$V_{oc} \cong \frac{E_c}{q} + \frac{kT}{q \cdot \beta} \cdot \ln\left(\frac{J_{sc}}{J_{0k}}\right) \tag{34}$$

Eq. (34) shows that changes in the position of the conduction band edge directly correspond to changes in $V_{oc}$, while changes in $J_{sc}$ and $J_{0k}$ affect the open-circuit voltage logarithmically. Equations (29) and (31) can be used to derive a formula for $FF$ as a function of $V_{mpp}$, $V_{oc}$ and $\beta$.[128] As the dependence of $V_{mpp}$ on $V_{oc}$ and $\beta$ can only be expressed as an implicit function,[128] an explicit function $FF(V_{oc},\beta)$ is not readily obtained. However, the fill factor is well described by the approximation[241]

$$FF = \frac{\beta \cdot \frac{qV_{oc}}{kT} - \ln\left(\beta \cdot \frac{qV_{oc}}{kT} + 0.72\right)}{\beta \cdot \frac{qV_{oc}}{kT} + 1} \tag{35}$$

Current-voltage characteristics are not only measured under standard operating conditions (white light, AM 1.5G conditions, 100 mWcm$^{-2}$), but often additionally recorded for different light sources (e.g., LEDs) and/or a series of different light intensities.[141, 160, 242, 243] From an applications point of view, such measurements are relevant for solar cell operation under conditions such as solar irradiation through cloud-covered skies, or indoor illumination. Hence, it is useful to examine the expected light-intensity dependence of the parameters $J_{sc}$ and $V_{oc}$. The short-circuit photocurrent depends on the spectral photon flux density $\phi(\lambda)$ of the source as well as the wavelength-dependent external short-circuit quantum efficiency of the solar cell (IPCE; see following section):[109, 244]

$$J_{sc} = q \cdot \int_{\lambda_{min}}^{\lambda_{max}} IPCE(\lambda) \cdot \phi(\lambda) \mathrm{d}\lambda \tag{36}$$

where $\lambda_{min}$ and $\lambda_{max}$ are the wavelengths at which the photocurrent sets in and vanishes, respectively. For illumination with monochromatic light of a single wavelength $\lambda$ the equation simplifies to:

$$J_{sc}(\phi(\lambda)) = q \cdot IPCE(\lambda) \cdot \phi(\lambda) \tag{37}$$

According to eq. (37), $J_{sc}$ varies linearly with the photon flux density as long as the IPCE is independent of it. As far as the open-circuit voltage is concerned, a logarithmic dependence on the monochromatic photon flux density is found by combining eq. (34) and eq. (32) with eq. (37):[97, 128]

$$V_{oc}(\phi(\lambda)) \cong \frac{kT}{q \cdot \beta} \cdot \ln\left(\frac{IPCE(\lambda) \cdot \phi(\lambda)}{J_0}\right) \tag{38}$$

### 1.4.3 Measurement of the External Quantum Efficiency

The external quantum efficiency or **incident photon-to-electron conversion efficiency (IPCE)** spectrum of a solar cell is obtained by measuring the short-circuit photocurrent density under illumination with monochromatic light as a function of the wavelength

$\lambda$.[128, 131] The IPCE corresponds to the ratio of wavelength-dependent electron flux density $J_{sc}/q$ to photon flux density $\phi$ (cf. eq. (37)):[131]

$$IPCE(\lambda) = \frac{J_{sc}(\lambda)}{q \cdot \phi(\lambda)} \tag{39}$$

The IPCE of a DSC can be expressed as the product of the partial quantum efficiencies of light harvesting, electron injection, charge collection and dye regeneration introduced in chapter 1.1.2:[107]

$$IPCE(\lambda) = \eta_{lh}(\lambda) \cdot \eta_{inj}(\lambda) \cdot \eta_{reg}(\lambda) \cdot \eta_{cc}(\lambda) \tag{40}$$

Another useful quantity to characterize the operation of the cell under short-circuit conditions is the internal quantum efficiency or **APCE (absorbed-photon-to-electron conversion efficiency)**, which corresponds to the ratio of photogenerated electron flux to *absorbed* photon flux and is determined by dividing the IPCE by the light harvesting efficiency:[131]

$$APCE(\lambda) = \eta_{inj}(\lambda) \cdot \eta_{reg}(\lambda) \cdot \eta_{cc}(\lambda) \tag{41}$$

Once the IPCE spectrum of a sample has been measured, it can be used in combination with the photon flux density spectrum used for the *J-V* characterization (typically, the AM1.5G spectrum) to calculate the expected short-circuit photocurrent density based on eq. (36) of the previous chapter. This procedure serves to double check the $J_{sc}$ obtained from the current-voltage curves.[128]

### 1.4.4 Electrochemical Impedance Spectroscopy (EIS)

In impedance spectroscopy,[128, 131, 245] a small-amplitude voltage perturbation superimposed onto a constant bias voltage is applied to the sample. The voltage perturbation is typically sinusoidal and causes a corresponding alternating current. Amplitude and phase shift (with respect to the input signal) of the current are measured as a function of the frequency.

The impedance $Z$ is defined as the ratio of the a.c. part of the voltage, $V_{ac}(t)$, and the a.c. part of the current, $i_{ac}(t)$:[246]

$$Z = \frac{V_{ac}(t)}{i_{ac}(t)} = \frac{\hat{V}}{\hat{i}} \cdot e^{i(\omega t - \theta)} \tag{42}$$

where $\hat{V}$ and $\hat{I}$ are the amplitudes of voltage and current signal, $\omega$ is the angular frequency, and $\theta$ is the phase shift. The measurement is typically repeated at a series of different bias voltages,[128] so that the frequency-dependent impedance is obtained for a number of different steady states of the sample. In the characterization of dye-sensitized solar cells, this series of EIS measurements is typically performed under illumination with a constant light intensity, for example at AM1.5G type conditions, and is often repeated in the dark for comparison.[128, 136, 247] An alternative to the approach of using constant illumination intensity and varied bias voltage is to perform measurements under a series of different illumination intensities while the cell is kept at open-circuit conditions.[141] To extract information about various processes in the solar cell from experimental EIS data, the data is fitted using an appropriate equivalent circuit and the corresponding impedance function.[128, 131]

The simplest equivalent circuit describing charge accumulation and recombination in a solar cell under a.c. electrical perturbation corresponds to the diode model outlined in section 1.4.2, and is illustrated in ***Figure 11***. The circuit consists of a parallel combination of the d.c. voltage-dependent chemical capacitance $C_\mu(V_f)$ and recombination resistance $R_{rec}(V_f)$.[128, 131]

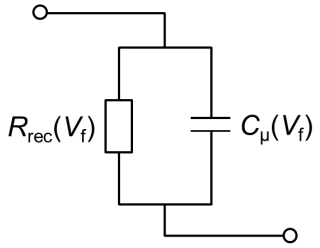


***Figure 11****: Parallel combination of recombination resistance $R_{rec}$ and chemical capacitance $C_\mu$ as simplest a.c. equivalent circuit describing a dye-sensitized solar cell.*

When a time-dependent small-amplitude voltage perturbation is applied to the electrodes of the solar cell in an EIS measurement, the electron quasi-Fermi level $E_{fn}$ will follow this perturbation and will be shifted upwards and downwards accordingly. The macroscopic **chemical capacitance $C_\mu$** describes how the total electron density $n$ in the porous semiconductor film changes with this variation in the quasi-Fermi level:[114, 128, 131]

$$C_\mu = dA(1-p)\cdot c_\mu = dA(1-p)\cdot q^2 \frac{\partial n}{\partial E_{\mathrm{fn}}} \tag{43}$$

where $d$ is the semiconductor film thickness, $A$ is the projected film area, $p$ is the porosity, $c_\mu$ is the chemical capacitance per unit volume ($F\cdot cm^{-3}$), and $q$ is the electron charge. Use of the relationship $\frac{\partial n}{\partial E_{\mathrm{fn}}} = g(E_{fn})$, as obtained in the zero-Kelvin limit of the Fermi-Dirac distribution,[63] leads to an approximation for eq. (43):[131]

$$C_\mu = dA(1-p)\cdot q^2 \cdot g(E_{\mathrm{fn}}) \tag{44}$$

where $g(E_{\mathrm{fn}})$ is the density of states at the quasi-Fermi level in the porous semiconductor. As already mentioned further above, the majority of electrons in a DSC photoanode are located in traps for $E_{\mathrm{fn}} < E_c$, so that the chemical capacitance will be dominated by these trapped electrons and their density of states at the quasi-Fermi level, $g^t(E_{\mathrm{fn}})$:

$$C_\mu \approx C_\mu{}^{\mathrm{t}} = dA(1-p)\cdot q^2 \cdot g^{\mathrm{t}}(E_{\mathrm{fn}}) \tag{45}$$

The macroscopic **recombination resistance $R_{\mathrm{rec}}$** is related to the change in the rate of recombination $U_n$ (cf. section 1.4.1) with the quasi-Fermi energy:[131]

$$R_{\mathrm{rec}} == \frac{r_{\mathrm{rec}}}{dA(1-p)} = \frac{1}{dA(1-p)}\cdot\frac{1}{q^2}\left(\frac{\partial U_{\mathrm{n}}}{\partial E_{\mathrm{fn}}}\right)^{-1} \tag{46}$$

where $r_{\mathrm{rec}}$ is the recombination resistance per unit volume ($\Omega\cdot cm^3$).

The product of $C_\mu$ and $R_{\mathrm{rec}}$ (eq. (43) and eq. (46)) corresponds to the **effective electron lifetime $\tau_n$** introduced in chapter 1.1.2:[90, 128, 131]

$$R_{\mathrm{rec}}C_\mu = \left(\frac{\partial U_{\mathrm{n}}}{\partial n}\right)^{-1} = \tau_{\mathrm{n}} \tag{47}$$

The simple diode model with its corresponding equivalent circuit in ***Figure 11*** is based on the assumptions of homogeneous photogeneration along the thickness of the porous semiconductor/dye film as well as fast transport of photogenerated charge carriers to the outer contacts of the solar cell.[128] A more comprehensive model that is widely used to describe the processes in dye-sensitized solar cells is the diffusion-recombination model, described by eq. (7) or similar forms of the continuity equation.[94, 97, 112, 248] This model considers generation, diffusion and recombination of electrons in the porous semiconductor as a function of space. In terms of an a.c. equivalent circuit, it leads to a transmission line (TL) model[128, 131, 247] (***Figure 12***, part highlighted in green) containing

$r_{rec}$ (in the graphics referred to as $r_r$) and $c_\mu$ in combination with the transport resistance per unit length per area $r_{tr}$ ($\Omega \cdot cm$), which describes electron diffusion through the semiconductor. Note that the macroscopic **transport resistance $R_{tr}$** is obtained via[131]

$$R_{tr} = r_{tr} \cdot \frac{d}{A(1-p)} \tag{48}$$

The transport resistance and the total film capacitance $C$ determine the **transport time $\tau_{tr}$** (also termed transit time, sometimes represented by the symbol $\tau_d$), i.e., the time electrons require to be transported through the thickness of the porous layer:[128, 131]

$$\tau_{tr} = R_{tr} \cdot C \tag{49}$$

In principle, the total capacitance of a semiconductor in contact with an electrolyte may contain contributions by the chemical capacitance $C_\mu$, depletion capacitance ($\propto V^{-1/2}$), and a Helmholtz capacitance related to the electrochemical double layer at the semiconductor surface (independent of $V$), which are connected in series.[126, 128, 131] Nanostructured semiconductors in contact with electrolytes are expected not to show a depletion layer (cf. chapter 1.2.2).

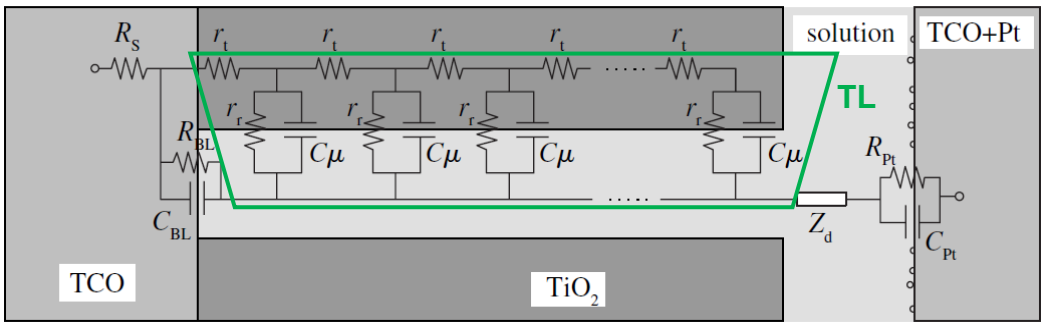


***Figure 12**: Equivalent circuit for a complete dye-sensitized solar cell including a transmission line (TL, highlighted in green) to describe charge transfer and accumulation across the interface between dye-sensitized semiconductor (here: $TiO_2$) and electrolyte and charge transport through the semiconductor. Figure taken from chapter 12 of ref. [131] and modified to highlight the TL.*

Therefore, the total measured capacitance is typically a chemical capacitance as long as the contribution by the Helmholtz capacitance is negligible, which is usually the case over a large range of bias voltages relevant for solar cell operation.[128]

The transmission line can be understood as a result of the geometry of the porous semiconductor electrode. As obvious from the simplified wire structure in ***Figure 12***, at any given point along the conductive path electrons may either move on by diffusing parallel to the path, or they may be transferred in the direction perpendicular to it, for example to recombine with the electrolyte. This is accounted for by the fact that the line of $r_{tr}$ elements is continuously interrupted by parallel $r_{rec}c_{\mu}$ elements. The total impedance $Z_{TL}$ of the TL depicted in ***Figure 12*** is:[128, 247]

$$Z_{TL}(\omega) = \left( \frac{R_{tr} R_{rec}}{1 + i\omega / \omega_{rec}} \right)^{1/2} \coth\left[ (R_{tr} / R_{rec})^{1/2} (1 + i\omega / \omega_{rec})^{1/2} \right] \tag{50}$$

where $\omega_{rec} = \tau_n^{-1} = (R_{rec} C_{\mu})^{-1}$. In addition to $r_{tr}$, $r_{rec}$ and $c_{\mu}$, the equivalent circuit for a complete device in ***Figure 12*** contains two parallel $RC$ elements, $R_{BL}||C_{BL}$ and $R_{Pt}||C_{Pt}$, representing charge accumulation and transfer at the interfaces between substrate (or blocking layer, BL) and electrolyte and between electrolyte and Pt-counter electrode, respectively. Further circuit elements are the resistance $R_s$ of the conductively coated glass substrate, and the impedance element $Z_d$ representing diffusion of the redox species in the electrolyte. The latter comprises ionic transport both in the porous matrix as well as in the bulk of the electrolyte and is described by:[36, 249]

$$Z_d = R_d \cdot \frac{\tanh\left[ \left( i\omega / \omega_d^p \right)^{1/2} \right]}{\left( i\omega / \omega_d^p \right)^{1/2}} \tag{51}$$

where $R_d$ is the diffusion resistance of ions in the electrolyte, and $\omega_d^p$ is the characteristic frequency of diffusion. The fact that, in the commonly used equivalent circuit in ***Figure 12***, the impedance of electrolyte diffusion in the pores is not part of the transmission line is equivalent to a decoupling of this impedance from the impedance response of the porous semiconductor. This decoupling relies on the assumption that $\omega_d^p << \omega_{rec}$, i.e., the characteristic frequencies (and time constants) of diffusion in the electrolyte and of recombination are well separated, which is appropriate for typical liquid electrolytes.[128, 131, 247, 250] In situations where the characteristic frequencies $\omega$ are similar, a more complex transmission line including two transport channels is required.[62, 128, 250] Typical impedance spectra (Nyquist plots) of a dye-sensitized solar

cell at lower and intermediate bias voltages (here, -0.25 V and -0.55 V) are shown in ***Figure 13***.[128, 247]

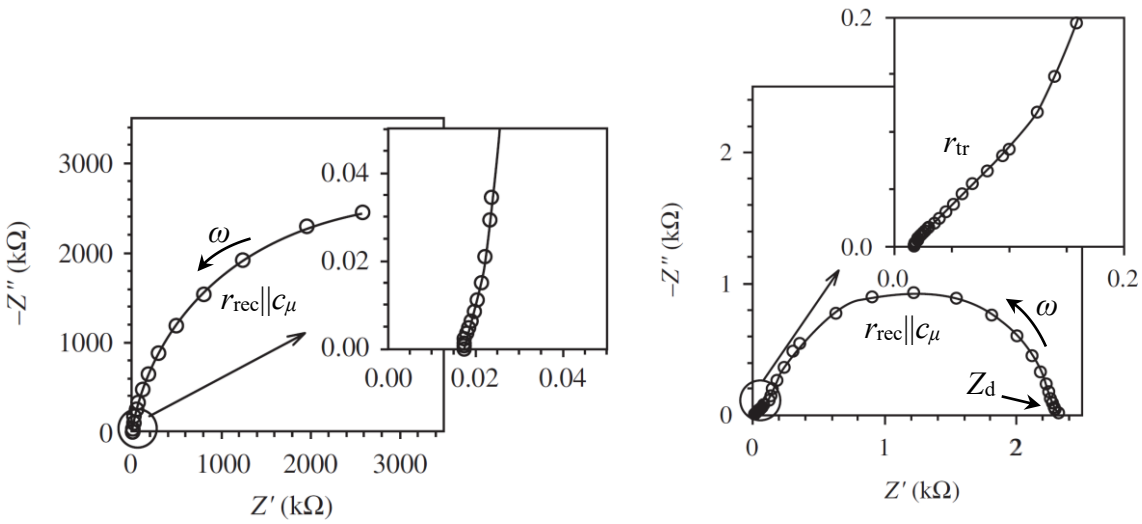


***Figure 13****: Typical Nyquist plots of the impedance of a dye-sensitized solar cell (Z': real part, Z'': imaginary part), obtained at low (left) and intermediate (right) bias voltages. Adapted from ref.* [247] *and extended by explanatory labels indicating which equivalent circuit element dominates the impedance in different frequency ranges.*

The main arc in both cases is caused by charge transfer across the semiconductor/dye/electrolyte interface and charge accumulation in the porous semiconductor ($r_{rec}||c_\mu$). At intermediate bias voltages, an additional, Warburg-type feature (line with a slope of about 1) reflecting the diffusion of electrons in the porous semiconductor (with transport resistance $r_{tr}$) can be observed towards higher frequencies. Furthermore, a feature related to the impedance of diffusion in the electrolyte, $Z_d$, may be seen in the low-frequency limit (see below), although at intermediate voltages it is often concealed by the recombination arc. When the bias voltage is further increased (here, to -0.7 V, ***Figure 14***) the Fermi level in the porous semiconductor is raised and the concentration of electrons becomes so high that the transport resistance becomes negligible and the Warburg feature disappears from the spectrum.[247]

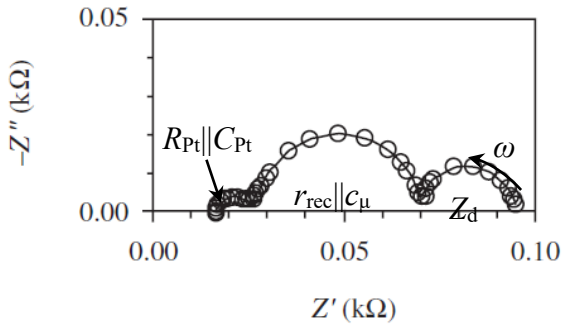


***Figure 14**: Typical impedance plot of a dye-sensitized solar cell obtained at higher bias voltages. Labels correspond to the equivalent circuit elements that dominate the response in different frequency ranges. Adapted with modifications from ref. [247].*

In this higher-voltage range the Nyquist plot of the impedance typically shows three distinct semicircles:[128, 247] a high-frequency arc related to $R_{Pt}$ and $C_{Pt}$, a mid-frequency arc resulting from $R_{rec}$ and $C_{\mu}$, and a low-frequency feature associated with diffusion in the electrolyte. As the transport resistance is negligible, the equivalent circuit of the active layer (i.e., the transmission line) can be simplified and the simple diode model of ***Figure 11*** is recovered.[128, 247] The complete device equivalent circuit for this case is depicted in ***Figure 15***. It should be noted that a high bias voltage is not the only circumstance under which no linear region can be observed in the Nyquist plot of the impedance. In fact, in dye-sensitized solar cells using ZnO instead of $TiO_2$ the transport-related feature is often not observed at all, independent of the bias voltage, so that a transport resistance cannot be reliably extracted from the spectra.[141, 251] It has been suggested that this might be a result of the higher electron mobility in ZnO compared to $TiO_2$.[141]

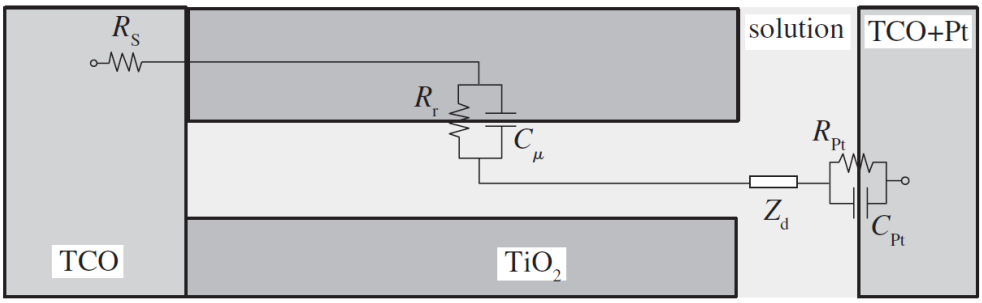


***Figure 15**: Simplified equivalent circuit of a complete DSC for the case of high conductivity in the porous semiconductor, as for example observed at high bias voltages. The symbol $R_r$ corresponds to $R_{rec}$ in the text. Taken from chapter 12 of ref. [131].*

As discussed above, measuring EIS spectra at a range of applied bias voltages and fitting the obtained spectra with an appropriate equivalent circuit delivers $R_{rec}$, $C_\mu$, and (if distinguishable) $R_{tr}$ as important parameters related to the dye-sensitized nanostructured film, as well as $R_s$, $R_{Pt}$, and $R_d$ as additional parameters related to the complete device. Valuable information can be found[86, 128, 141] by analyzing the voltage-dependence of $R_{rec}$, $C_\mu$, and (if applicable) $R_{tr}$ and comparing it with the behavior predicted by models, some of which will be discussed in the following.

As indicated further above, the chemical capacitance in DSCs is typically governed by the density of states in the band gap, which in most cases shows an exponential distribution as given in eq. (9) in chapter 1.2.2. In consequence, eq. (45) yields[128]

$$c_\mu = q^2 \cdot \alpha \cdot \frac{N_t}{kT} \cdot \exp\left[\frac{\alpha \cdot q(V_f - E_c/q)}{kT}\right] \cdot \exp\left[\frac{\alpha \cdot E_{redox}}{kT}\right] \tag{52}$$

with the **trap-distribution parameter** $\boldsymbol{\alpha}$, the total trap density $N_t$, and the Fermi-level voltage $V_f$ (see further below for a description of how $V_f$ is determined). If $c_\mu$ is plotted semilogarithmically vs. $V_f$ for a set of different samples with the same total trap density $N_t$ and trap distribution parameter $\alpha$, the shifts of the curves along the voltage axis will therefore correspond exactly to **relative conduction band edge shifts** $\boldsymbol{\Delta E_c}$ between the samples (***Figure 16***). In other words, for a set of samples with comparable trap distributions, the chemical capacitance curves allow for a determination of conduction band edge shifts with respect to a reference sample.

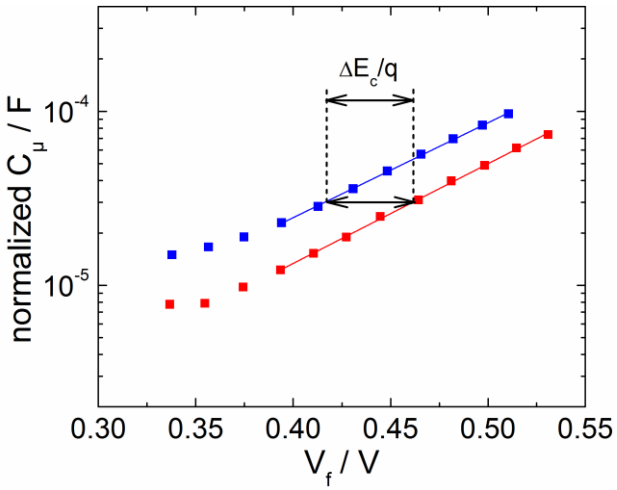


***Figure 16****: Plot of the voltage-dependent, EIS-derived chemical capacitance of two DSCs with equal trap distribution parameter α, highlighting the relative conduction band edge shift $\Delta E_c$ between the two cells.*

While the assumption of same $N_t$ is commonly made without experimental evidence, some recent works[121, 252, 253] have emphasized that this parameter should be monitored and quantitatively taken into account in the determination of conduction band edge shifts, especially when it comes to sets of samples in which different bulk or surface treatments (including adsorption of dyes and coadsorbates) have been applied to the porous semiconductor. Total trap densities with respect to a reference sample are experimentally accessible via time-resolved short-circuit photocurrent decay measurements,[252] as explained in section 1.4.7. In the case of samples with identical $\alpha$ but different $N_t$, accurate results for $\Delta E_c$ are then attained by normalizing the chemical capacitance by the relative total trap density before measuring the shifts of the curves along the voltage axis.[252]

A simple model that is commonly used for $R_{rec}$ and often delivers a good description of the experimental data is based on the empirical $\beta$-recombination model introduced in section 1.2.3.[86, 128, 141] Using equations (46), (16), (2) and (32), one obtains

$$r_{rec} = \frac{kT}{q \cdot \beta \cdot J_0} \cdot \exp\left(\frac{-\beta \cdot qV_f}{kT}\right) \tag{53}$$

As shown in chapter 1.4.2, the factor $J_0$ depends on the position of the conduction band edge in the porous semiconductor $E_c$, on the **recombination parameter $\beta$**, and on the rate constant for interfacial charge transfer $k_r$. Thus, a semilogarithmic plot of $r_{rec}$ or $R_{rec}$ vs. $V_f$ for a set of different samples will show how the recombination resistances of the samples differ at each voltage, but will fail to reveal the origins of these differences, i.e. whether they are caused by shifts in $E_c$, differences in $\beta$, or differences in the kinetics of the charge transfer reaction. In many cases the latter are of great interest,[121, 128, 141, 252] so that it is desirable to detangle the different influencing factors. This can be approached by inserting eq. (32) into eq. (53) to yield a modified expression for $r_{rec}$:

$$r_{rec} = \frac{kT}{q \cdot \beta \cdot J_{0k}} \cdot \exp\left[\frac{-q\beta \cdot (V_f - E_c/q)}{kT}\right] \tag{54}$$

Describing the conduction band edge position with respect to a reference sample, $E_c = E_{c,ref} + \Delta E_c$, further leads to

$$r_{rec} = \frac{kT}{q \cdot \beta \cdot J_{0k}} \cdot \exp\left[\frac{-q\beta \cdot (V_f - \Delta E_c/q - E_{c,ref}/q)}{kT}\right] \tag{55}$$

On the basis of the dependence apparent from eq. (55) it is a common practice in EIS of dye-sensitized solar cells to semi-logarithmically plot the recombination resistance vs. the corrected voltage $V_f$-$\Delta E_c/q$.[128, 141, 254] For a set of samples with same $\beta$, such a plot will directly reveal changes in $J_{0k}$ and thus in the rate constant $k_r$ (cf. eq. (32)). Some studies have developed more sophisticated expressions for the recombination resistance, which are based on the Marcus-Gerischer model for electron transfer between semiconductor and electrolyte (eq. (17)) and take into account a distribution of surface states via which recombination can occur.[90, 255] Nevertheless, in most cases – including the majority of samples studied in this work – the simple model of eq. (55) delivers an adequate description of measurement data, so that the use of more complex models containing a larger number of unknown variables can be avoided.

As apparent from equations (52) and (53), recombination resistance and chemical capacitance are functions of the (constant part of the) **Fermi-level voltage $V_f$** rather than of the applied d.c. voltage $V$. If a current flows through the solar cell, there is a voltage drop at the **total series resistance $R_{series}$**=$R_s$+$R_{Pt}$+$R_d$ of the cell,[128] and as a consequence $V_f$ will be different from $V$. For a correct analysis it is therefore necessary to determine $V_f$, which can be done via the relationship[128]

$$V_f(J) = V(J) - V_{series}(J) \tag{56}$$

where $J$ here is the d.c. current density flowing through the cell as a result of the applied d.c. voltage $V$, and $V_{series}$ is the voltage drop at the series resistance. The latter can be obtained by integration of $R_{series}$ over the current density:[128, 248]

$$V_{series}(J') = A \cdot \int_0^{J'} R_{series}(J)dJ \tag{57}$$

where $A$ is the projected sample area. Alternatively, $V_f$ can be determined more directly by integrating the resistance of the nanostructured semiconductor film ($R_{film}$=1/3 $R_{tr}$+$R_{rec}$ for $R_{rec} > R_{tr}$)[128] over the d.c. cell current density $J$ and adding the result to the open-circuit voltage $V_{oc}$ measured in the EIS measurements:[128, 248]

$$V_f(J') = V_{oc} + A \cdot \int_0^{J'} \tfrac{1}{3} R_{tr} + R_{rec}(J)dJ \tag{58}$$

If the transport resistance $R_{tr}$ is small, the integral in eq. (58) can be approximated by the integral over $R_{rec}$.

### 1.4.5 Intensity-Modulated Photocurrent and Photovoltage Spectroscopy (IMPS and IMVS)

Similar to electrochemical impedance spectroscopy, intensity-modulated photovoltage and photocurrent spectroscopy (IMVS and IMPS) involve applying a modulated, small-amplitude signal to the solar cell and measuring the time-dependent response as a function of the frequency.[88, 118, 256-259] In IMVS and IMPS, the modulated input signal is the photon flux: the cell is illuminated with a constant background illumination $\phi_0$, onto which a small (typically, 10% or less of the background signal)[28, 84, 88] sinusoidal perturbation with amplitude $\hat{\phi}$ is superimposed (see orange line in ***Figure 17***). Commonly, IMPS is performed under short-circuit conditions and IMVS at open circuit.[28, 84, 87, 88] The sinusoidal modulation of the light intensity causes a corresponding modulation of the rate of electron injection and thereby generates a sinusoidal photocurrent (IMPS) or photovoltage (IMVS) output of the solar cell, superimposed on the background steady-state short-circuit photocurrent $J_{sc}$ or open-circuit photovoltage $V_{oc}$, cf. ***Figure 17***. The amplitude and phase shift of the modulated part of the photocurrent/photovoltage are recorded over a range of frequencies.

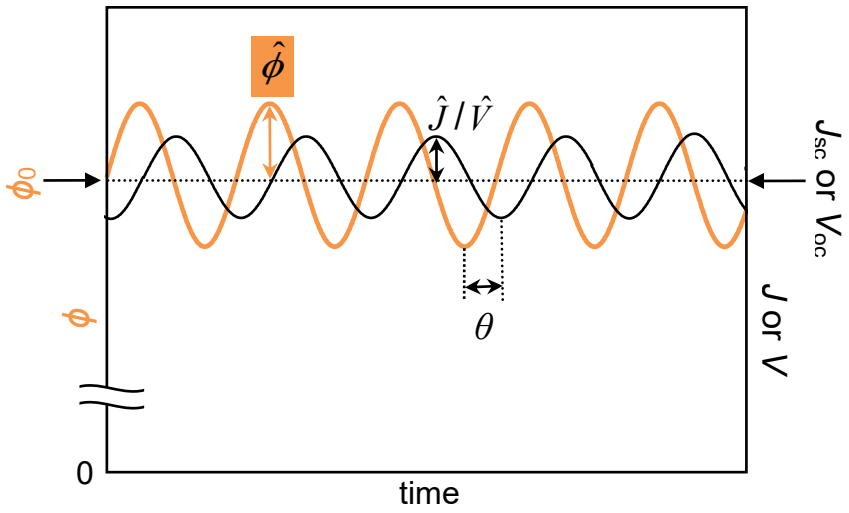


***Figure 17:*** *Schematic representation of input and output signals in IMPS/IMVS measurements of DSCs. The sinusoidal illumination signal $\phi$ (orange line) causes a corresponding voltage or current response (black line) with phase shift $\theta$.*

The frequency-dependent transfer functions $\Phi$ are determined according to[88, 257, 258]

$$\Phi_{IMPS}(\omega) = \frac{\hat{J}(\omega)}{q \cdot \hat{\phi}} \tag{59}$$

$$\Phi_{IMVS}(\omega) = \frac{\hat{V}(\omega)}{\hat{\phi}} \tag{60}$$

where $\hat{J}(\omega)/q$ is the amplitude of the electron flux density, $\hat{V}$ is the amplitude of the photovoltage and $\omega$ is the angular frequency. $\Phi_{IMPS}(\omega)$ can be considered the frequency-dependent form of the steady-state IPCE (cf. eq. (39)) and for small frequencies approaches the latter.[88] Both intensity-modulated photocurrent and photovoltage spectroscopy are usually measured for a broad range of background light intensities to obtain the corresponding transfer function for a series of different steady states.[84, 88, 118]

A complex plane plot of $\Phi_{IMVS}(\omega)$ of a dye-sensitized solar cell typically shows a single semicircle in the fourth quadrant, see ***Figure 18*** (a), with positive real parts and negative imaginary parts indicating that the photovoltage lags behind the illumination signal.[245]

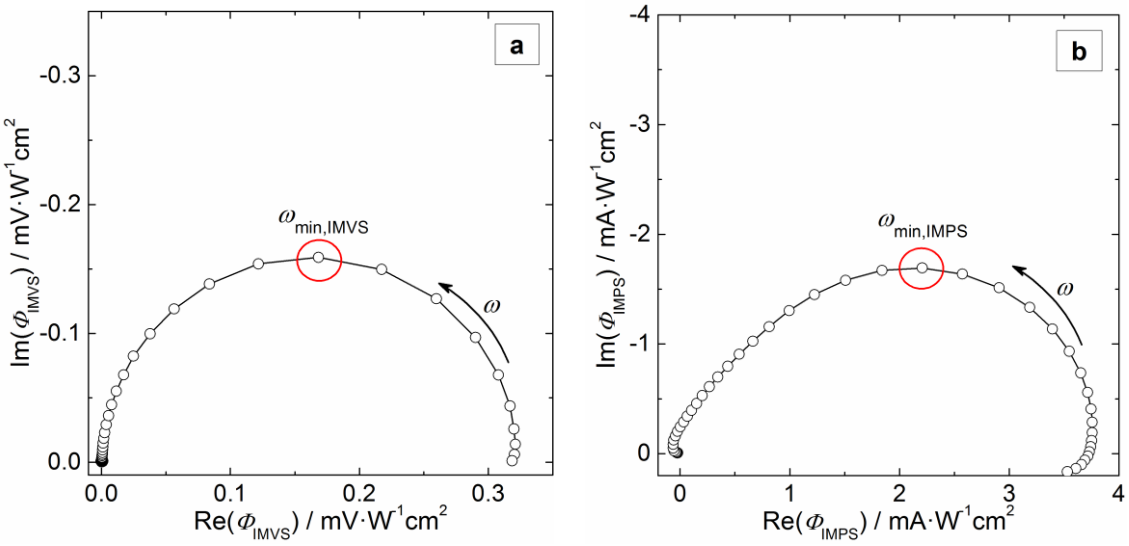


***Figure 18:*** *Typical IMVS (a) and IMPS (b) transfer functions in the complex plane.*

To extract information about recombination reactions in the DSC under open-circuit conditions from the IMVS plot, the transfer function is fitted to an appropriate analytical function. The modulated voltage output $\hat{V}$ in IMVS depends on the rate at which the

electron density relaxes (cf. eq. (1)) in response to the change in the rate of electron injection induced by the modulated light intensity. The theoretical description of this time-dependent variation of the electron density is obtained by solving the time-dependent continuity equation for a sinusoidal perturbation, cf. eq. (7), as for example demonstrated in ref. [256]. For the real part and imaginary part of the IMVS transfer function, one thus obtains:

$$\mathrm{Re}(\Phi) = \frac{-M}{1+(\omega^2/\omega_{\mathrm{min}}^2)} \tag{61}$$

$$\mathrm{Im}(\Phi) = \frac{-(\omega/\omega_{\mathrm{min}})\cdot M}{1+(\omega^2/\omega_{\mathrm{min}}^2)} \tag{62}$$

where $M$ is a scaling factor that depends on the electron injection efficiency and the amplitude of the light intensity.[256] Eq. (61) and eq. (62) describe the typically observed semicircle in the complex plane, cf. ***Figure 18*** (a), with $\omega_{\mathrm{min}}$ denoting the frequency at which the imaginary part of the transfer function shows its minimum. It was shown[90, 142] that the time constant corresponding to $\omega_{\mathrm{min}}$ is equivalent to the **effective electron lifetime $\tau_n$** introduced in chapters 1.1.2 and 1.2.3:[84, 131, 256]

$$\omega_{\mathrm{min,IMVS}} = \tau_n^{-1} \tag{63}$$

Repeating this analysis of the IMVS response obtained at a series of constant background illumination intensities yields $\tau_n$ as a function of $\phi_0$ or $V_{oc}$, which can be compared to analogous plots obtained by impedance spectroscopy or time-dependent characterization methods (see following section).

The typical complex plane plot of the IMPS transfer function $\Phi_{\mathrm{IMPS}}(\omega)$ of dye-sensitized nanocrystalline semiconductors is not a simple semicircle as in IMVS, but instead shows a semicircular region at lower frequencies and a more linear region at higher frequencies, see ***Figure 18*** (b).[88, 131] In analogy to IMVS, the position of the plot in the fourth quadrant indicates that the photocurrent lags behind the illumination signal. Fitting of the IMPS response allows to determine electron transport-related quantities of the dye-sensitized nanocrystalline semiconductor and can be realized by using analytical expressions derived from the continuity equation (eq. (7) or eq. (8) including trapping), as for example reported by Dloczik et al..[88] Their model is based on the assumptions that electron transport occurs only by diffusion, dye molecules are homogeneously dis-

tributed within the dye-sensitized film (Beer-Lambert-type absorption, eq. (24)), and the recombination rate is first order in electron concentration (eq. (6)) and determined by charge transfer to the oxidized species in the electrolyte (fast regeneration of the dye). The influence of trapping and detrapping was accounted for in the framework of the quasi-static approximation (cf. chapter 1.2.2) by replacing electron diffusion coefficient and lifetime by the intensity-dependent effective quantities $D_n$ and $\tau_n$, cf. eq. (13) and eq. (18). For substrate side illumination under short-circuit conditions, the following solution for the complex IMPS transfer function was obtained:[88]

$$\Phi_{IMPS}(\omega) = \frac{\alpha_{abs}}{\alpha_{abs}+\gamma} \cdot \frac{e^{\gamma d} - e^{-\gamma d} + 2\alpha_{abs}\dfrac{e^{-\alpha_{abs}d} - e^{-\gamma d}}{\gamma - \alpha_{abs}}}{e^{\gamma d} + e^{-\gamma d}} \tag{64}$$

where $\alpha_{abs}$ is the absorption coefficient of the dye-sensitized photoelectrode, $d$ is the film thickness, and

$$\gamma = \sqrt{\left(\frac{1}{D_n \tau_n} + \frac{i\omega}{D_n}\right)} \tag{65}$$

with $i$ as the imaginary unit. Simulations of $\Phi_{IMPS}(\omega)$ based on eq. (64)[88] showed that the linear high-frequency region typically observed in the complex plane plot, cf. ***Figure 18*** (b), is determined by the diffusion of charge carriers to the back contact (cf. diffusion-limited case in ref. [88]). Further, the calculations demonstrated the influence of a varying effective electron lifetime $\tau_n$ on the IMPS response, see ***Figure 19***. As the lifetime was decreased, the IMPS plot gradually became more dominated by recombination and the transport-related feature became harder to distinguish.

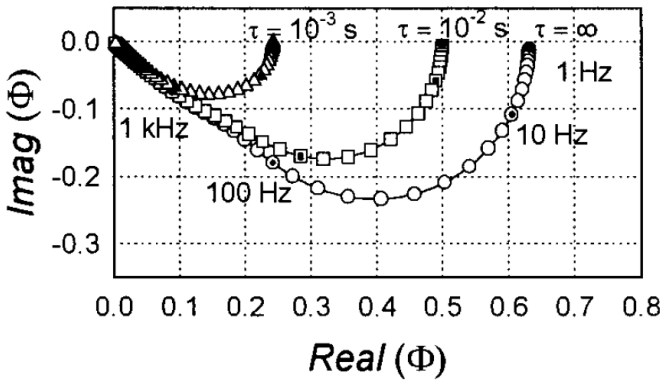


***Figure 19****: Complex-plane representation of calculated IMPS responses for a series of different electron lifetimes τ, corresponding to $\tau_n$ in the text. Taken from ref. [88].*

Another effect that influences the IMPS transfer function in the high-frequency range is the attenuation of the current by the parallel combination of the series resistance and capacitance of the whole cell (RC attenuation), which can be described by an attenuation factor[88, 257]

$$\widetilde{A}(\omega) = \frac{1}{1 + i\omega RC} \tag{66}$$

At short circuit, the series resistance is typically dominated by the sheet resistance of the conductive glass substrate (e.g., FTO/glass) and the capacitance is governed by charge accumulation at the substrate/electrolyte or substrate/semiconductor interface.[28, 88, 260] RC attenuation appears in the form of an additional time constant in the complex plane plot of $\Phi_{\mathrm{IMPS}}(\omega)$ and thus leads to an increased phase shift between illumination signal and current.[88] The measured IMPS data should therefore be fitted using the modified function[88, 257]

$$\Phi_{\mathrm{meas}}(\omega) = \Phi_{IMPS}(\omega) \cdot \widetilde{A}(\omega) \tag{67}$$

Analysis of the IMPS response of DSCs by full fits of the frequency-dependent data to eq. (67) with eq. (64) is complicated by the fact that the effective electron lifetime at short circuit (cf. eq. (65)) is hard to access experimentally: IMVS measurements cannot be performed at short-circuit, because the smallest modulations in the electron injection rate at that point of the *J-V* curve (cf. ***Figure 10***) would lead to huge, non-linear oscillations of the voltage. EIS data (cf. previous section) can normally not be evaluated down to short-circuit conditions either, because the current changes occurring in response to the modulated applied voltage tend to approach the detection limit and the obtained data are highly scattered. Open-circuit photovoltage decay measurements (see following section) get very noisy towards low voltages as well because of the small change of $V_{\mathrm{oc}}$ per time compared to the resolution of the voltage detection. Due to the lack of reliable short-circuit lifetime values, IMPS data are frequently analyzed by a simplified routine on the basis of the frequency in the minimum of the main semicircle, $\omega_{\mathrm{min,IMPS}}$ (cf. ***Figure 18*** (b)), and the related time constant, $\tau_{\mathrm{IMPS}} = 1/(\omega_{\mathrm{min,IMPS}})$,[98, 118, 242] which can be determined by fits of the real and imaginary parts of the response (limited to the semicircular region) to equations analogous to eq. (61) and eq. (62). $\tau_{\mathrm{IMPS}}$ reflects the combined effect of electron recombination and diffusion to the back contact (cf. ***Figure 19***):[98]

$$\tau_{\mathrm{IMPS}} = \frac{1}{\tau_{\mathrm{n}}^{-1} + \tau_{\mathrm{tr}}^{-1}} \tag{68}$$

where $\boldsymbol{\tau_{tr}}$ is the **electron transport time** (cf. section 1.4.4). Under short-circuit conditions, $\tau_{\mathrm{n}}$ is normally much larger than $\tau_{\mathrm{tr}}$,[136, 261] so that $\tau_{\mathrm{IMPS}} \approx \tau_{\mathrm{tr}}$ and the **effective diffusion coefficient of electrons in the semiconductor, $\boldsymbol{D_{\mathrm{n}}}$,** can be determined via a relationship attained in previous studies based on the continuity equation:[88, 141, 262, 263]

$$\tau_{\mathrm{IMPS}} \approx \tau_{\mathrm{tr}} = \frac{d^2}{\zeta \cdot D_{\mathrm{n}}} \tag{69}$$

$\zeta$ is a numerical factor[263] that weakly depends on the direction of illumination and on the product $\alpha_{\mathrm{abs}}d$.[88, 141, 242] As shown in the Supporting Information of ref. [141] and ref. [242], for illumination from the substrate side $\zeta$ approaches 2.54 for small values of $\alpha_{\mathrm{abs}}d$ and takes on a value of 2.8 for $\alpha_{\mathrm{abs}}d$ = 3. As in the case of IMVS, the IMPS response is evaluated at a series of constant background illumination intensities to yield $\tau_{\mathrm{tr}}$ or $D_{\mathrm{n}}$ as a function of $\phi_0$ or $J_{\mathrm{sc}}$.

### 1.4.6 Transient Photovoltage and Photocurrent Measurements

An alternative approach to frequency-resolved characterization of photoelectrochemical dynamics is to employ *time*-dependent (i.e., transient) measurements of the decay of the short-circuit photocurrent or open-circuit photovoltage in response to a decrease in illumination intensity. While the analysis of such transient measurements can in some cases be limited by noise in the decay curves, the measurements allow for a quick and easy determination of electron transport times and lifetimes equivalent to the corresponding values obtained by EIS and IMPS/IMVS,[120, 142, 264] which is particularly useful if a fast screening of a large number of solar cells is required. Analysis of recombination by time-dependent photovoltage decay measurements can be realized in two different ways: either the illumination is completely turned off and the full decay down to open-circuit voltages approaching 0 V is measured (referred to as open-circuit voltage decay or OCVD)[120, 142] or the illumination intensity is only changed by a small amount and the corresponding small change in open-circuit voltage is monitored. Together with the corresponding transient photocurrent measurements, the latter is sometimes referred to as SLIM-PCV (stepped light-induced transient measurements of photocurrent and photovoltage).[121, 264, 265]

In OCVD measurements, the cell is illuminated by a rectangular light pulse (AM1.5G-type illumination[142] or monochromatic light[120, 266]) at open circuit and the time-dependent decay of $V_{oc}$ after the light is switched off is recorded, see ***Figure 20***.[119, 120, 142, 266] To gain information about recombination reactions, the slope of the decay curves are evaluated by means of appropriate analytical models. A frequently used[141, 242, 251, 266, 267] expression for the voltage decay after switching off the light source was derived by Bisquert et al.[142] on the basis of the continuity equation for the dark situation at open circuit, i.e., eq. (7) with generation and transport terms set to 0. They started their derivation with the assumption of a linear rate of recombination (eq. (6), $U_n = k_r n_c = n_c/\tau_0$), which, together with eq. (1) yielded the simple solution $dV_{oc}/dt = kT/q\tau_0$ for the decay of $V_{oc}$ with time. This corresponded to a linear decay, which is in contrast to the non-linear behavior typically observed for dye-sensitized nanocrystalline solar cells, as indicated in ***Figure 20***.

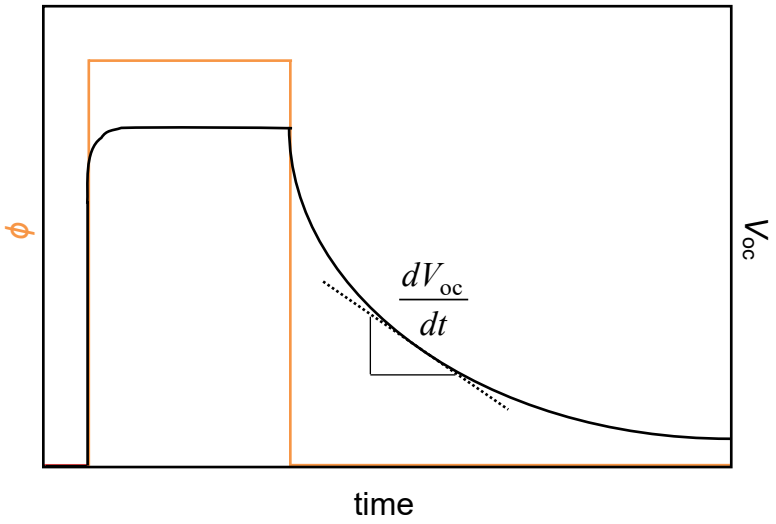


***Figure 20****: Schematic representation of time-dependent light intensity $\phi$ and the resulting open-circuit voltage $V_{oc}$ response in an OCVD measurement.*

When nonlinear recombination was considered via the $\beta$-recombination model (cf. section 1.2.3), i.e., $U_n = k_r n_c^{\beta}$, the obtained solution for $dV_{oc}/dt$ was more complex and hardly practicable for data analysis.[142] However, it was suggested that for $\beta$ values close to 1 the simple model still constitutes a very good approximation.[142] Further including trapping and detrapping terms by use of the quasi-static assumption in their treatment, the following approximation for the voltage decay was obtained:

$$\tau_n = -\frac{kT}{q}\left(\frac{dV_{oc}}{dt}\right)^{-1} \tag{70}$$

where the **effective electron lifetime $\tau_n$** (effective indicating the influence of traps, see chapters 1.1.2 and 1.2.3) is a function of $V_{oc}$ and, in practice, is determined by calculating the voltage-dependent derivative of the decay curve. In spite of the simplifying assumptions made to obtain eq. (70), it is commonly found[141, 266] to deliver effective electron lifetimes equivalent to the $\tau_n$ values obtained by EIS or IMVS, as expected based on formal considerations.[90, 142] Calculations by Peter et al.[120] have demonstrated that a plot of the voltage decay vs log(time) should be linear for long times (> 0.1 s after the light is switched off) if the nanostructured semiconductor shows an exponential distribution of trap states and the quasi-static approximation holds. Moreover, Cameron et al. have shown that such linear behavior is indicative of negligible recombination between the substrate and the electrolyte.[266] Thus, the shape of the semilogarithmic plot of the voltage decay can be used as an indicator for the presence or absence of recombination via the substrate in a given cell.

An alternative way to analyze recombination by time-dependent voltage measurements is to measure the change in voltage following a *small* change in the illumination intensity.[121, 264, 265] In the present work, this approach has been realized as part of the SLIM-PCV technique,[264] which was available at Gifu University in lieu of an IMPS/IMVS setup. The cell is illuminated by laser light of a certain intensity and the open-circuit voltage transient induced by a stepwise change in laser intensity is measured as a function of the time *t*, see ***Figure 21***.

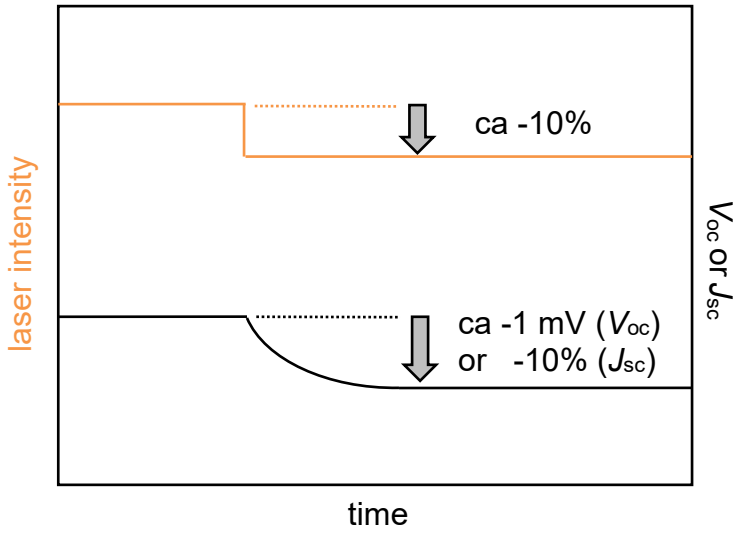


***Figure 21**: Time-dependence of laser intensity and resulting open-circuit voltage $V_{oc}$ or short-circuit current $J_{sc}$ in SLIM-PCV measurements.*

The $V_{oc}$ transients are fitted with a mono-exponential function of the type $\exp(-t/\tau_n)$ (see detailed function in chapter 2.9.4) to extract the time constant of the decay, which is equivalent to the effective electron lifetime $\tau_n$, as shown by a formal treatment similar to that described above for the OCVD method.[121, 264] The fact that the small-amplitude voltage transient can be fitted by a monoexponential decay function relies on the changes in laser intensity and electron density being small with respect to the corresponding initial steady-state values. The measurement is repeated for a series of different initial laser intensities and resulting initial open-circuit voltages to yield the lifetime $\tau_n$ as a function of $V_{oc}$.[264]

The measurement of short-circuit photocurrent transients by SLIM-PCV presents the time-resolved analogue of IMPS and thus delivers information on the transport of electrons through the porous semiconductor.[264] A small decrease in the laser intensity here leads to a decay in the short-circuit photocurrent that is monitored over time, cf. ***Figure 21***. In analogy to the voltage transients measured by SLIM-PCV, the small perturbation of the light intensity compared to the initial intensity allows the current transient to be adequately fitted with a mono-exponential equation that under the assumption of negligible recombination at short circuit was shown to have the form $\exp(-t/\tau_{tr})$ (see chapter 2.9.4 for detailed function),[121, 264] where the time constant of the decay corresponds to the **electron transport time $\tau_{tr}$** introduced in section 1.4.5.[121, 264] The SLIM-PCV measurement setup at Gifu University automatically used $\tau_{tr}$ to determine the **effective**

**diffusion coefficient $D_n$** of electrons in the nanostructured semiconductor based on the relationship reported by Nakade et al.:[264]

$$D_n = \frac{d^2}{2.77 \cdot \tau_{tr}} \tag{71}$$

Comparison of eq. (71) with eq. (69) and comments (section 1.4.5) reveals that using the (empirical) factor of 2.77 in the denominator corresponds to the case of $\alpha_{abs}d \approx 3$ (relatively strong absorption). For each cell, the measurement of the small current decay is repeated for a series of different initial laser intensities to obtain $D_n$ as a function of the steady-state $J_{sc}$.

### 1.4.7 Charge Extraction

In addition to delivering information on electron transport and recombination, photocurrent and photovoltage measurements in the time domain offer the possibility to determine the charge density in the nanostructured semiconductor under different electrical and illumination conditions. Such methods, collectively referred to as charge extraction, involve illumination of the solar cell until a steady state is established, followed by switching off the source of illumination and extracting the electrons accumulated in the photoelectrode by allowing a current to flow.[113, 121, 242, 252]

Determination of the charge stored at short circuit consists of a simple measurement of the full current transient in response to turning off the light source.[242, 252] The cell is kept under short-circuit conditions throughout the whole measurement. The current decay is then integrated over time to yield the amount of charge stored in the semiconductor under short-circuit conditions, $Q_{sc}$, which can be converted into the short-circuit electron density $n_{sc}$ using the geometric area $A$, film thickness $d$, and porosity $p$ of the porous semiconductor film:

$$n = \frac{Q}{qAd(1-p)} \tag{72}$$

with $Q$ denoting the charge and $n$ the electron density. The measurement is repeated for a series of different illumination intensities to yield $n_{sc}$ as a function of the steady-state short-circuit photocurrent density $J_{sc}$, see example in ***Figure 22***.[252]

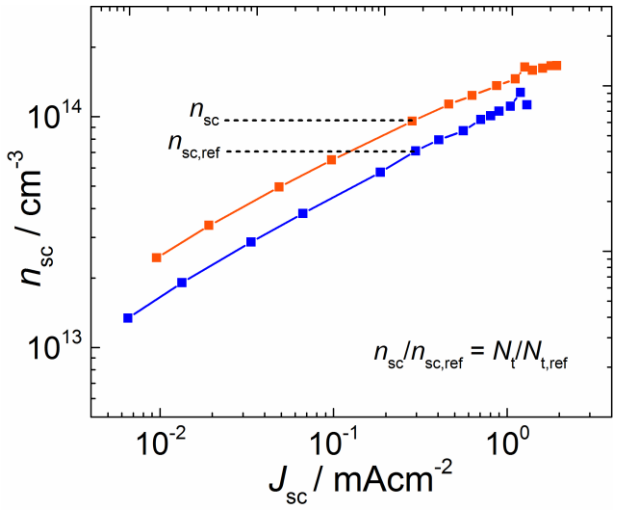


***Figure 22**: Example of a plot of the short-circuit charge density vs. the short-circuit photocurrent density, illustrating how relative total trap densities are determined.*

Plots as the one above are used to assess the total trap density $N_t$ in dye-sensitized nanocrystalline semiconductors with respect to a reference sample (blue curve in the example), as first suggested by O'Regan et al..[252] Provided that current flow through the DSC occurs only by diffusion of electrons in the conduction band (no hopping between traps) and that the electron diffusion coefficient in the cells under comparison is constant, an equal $J_{sc}$ of two different cells corresponds (eq. (5)) to an equal electron density gradient and hence (eq. (1)) to an equal gradient of the quasi-Fermi level $E_{fn}$ across the cells. Since all trap states below $E_{fn}$ are occupied, relative differences in the total trap density $N_t$ between the two cells will lead to proportionally changed densities of trapped electrons (cf. eq. (10)) and, hence, extracted charge densities at a given short-circuit current density. In other words, the ratio of the extracted short-circuit electron density of a cell to the extracted short-circuit electron density of a reference cell, $n_{sc}/n_{sc,ref}$, is equal to the **relative total trap density $N_t/N_{t,ref}$** of the cell. Knowledge of the relative total trap density is crucial for an accurate analysis of the results of other characterization methods such as EIS and IMPS, because the quantities attained by these methods (e.g., the chemical capacitance $C_\mu$ and the transport time $\tau_{tr}$) depend on $N_t$.

An experimental technique used to obtain the **charge $Q_{oc}$** stored in the porous semiconductor **under open-circuit conditions** was described by Peter et al. in 2000.[113] The charge extraction method they described consists of three sequential parts, see ***Figure 23***. In the first part, the solar cell is illuminated under open-circuit conditions so that a

steady-state open-circuit voltage is established. The light source is then switched off and the voltage is allowed to decay to a certain value before the cell is short-circuited to extract the electrons remaining in the porous semiconductor. As in the case of short-circuit charge extraction, the measured extraction current is then integrated over time to yield $Q_{oc}$[113] and the corresponding electron density $n_{oc}$ is determined using eq. (72). Repeating the experiment with different waiting times between turning off the light source and initiating the extraction delivers $n_{oc}$ as a function of $V_{oc}$ (the voltage at which the extraction was initiated).[113] Analogous to the analysis of voltage-dependent capacitance curves (cf. ***Figure 16***), $V_{oc}$-dependent plots of $n_{oc}$ normalized by the total trap density, see examples in ***Figure 24***, can be used to determine relative shifts of the conduction band edge $\Delta E_c/q$ between different DSCs with similar trap distribution,[149, 252] as apparent from eq. (10) if the exponential part is rewritten analogous to eq. (52).

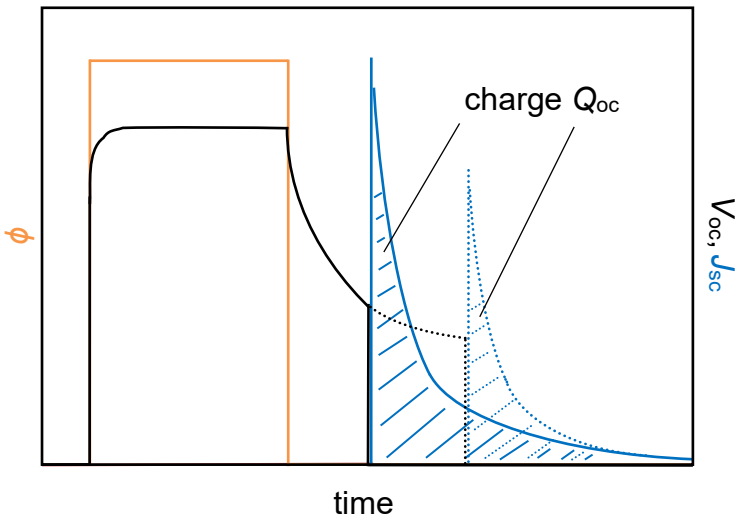


***Figure 23****: Scheme of the principle of open-circuit charge extraction measurements, with the time dependence of light intensity signal (orange), open-circuit voltage (black) and short-circuit current (blue). Voltage and current transients, together with the corresponding extracted charges, are indicated for two sequential measurements in which the DSC is short-circuited after different delay times.*

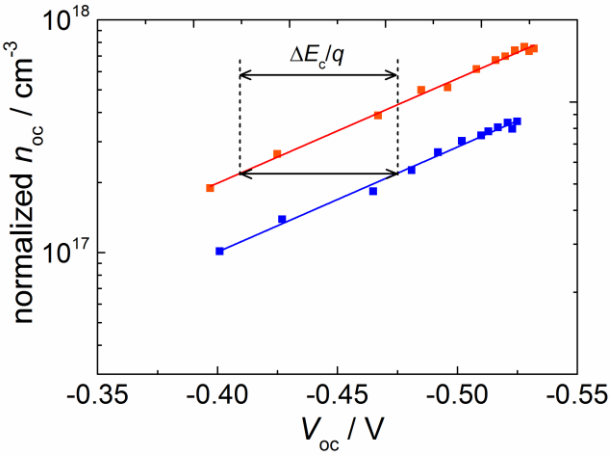


***Figure 24**: Example of a plot of the open-circuit electron density (normalized by the relative total trap density) as a function of the open-circuit photovoltage for two DSCs, with illustration of the determination of the relative conduction band edge shift between the cells.*

# 2 Experimental Procedures

## 2.1 Sample Groups

This work presents results of five main experimental series that all used ZnO films to build dye-sensitized solar cells, “D149 with CA” and “D149 without CA” (chapter 5), “D149+D131+SQ2” (chapter 6), “np-ZnO+D149+D131+SQ2” (chapter 7), and “D149+$S_{1.15}$PcZn” (chapter 8). All series used electrodeposited ZnO films except for np-ZnO+D149+D131+SQ2, in which screenprinted nanoparticulate ZnO films were utilized. ***Table 30*** (Appendix A) contains a full list of all samples with date of film preparation, date of sensitization, photosensitizers used, as well as additional information.

## 2.2 Preparation of Electrodeposited ZnO Films

The electrodeposition of the porous ZnO films used in this work (including pre- and post-treatment) was performed in the laboratory of T. Yoshida at Gifu University, Japan. ***Table 1*** lists the materials utilized in these experiments. The films used to build the cells of the series D149 without CA, D149+D131+SQ2, and D149+$S_{1.15}$PcZn were deposited by Shigeo Hori.

A 7 cm x 8 cm piece of FTO-coated glass was pre-cut to allow breaking it into eight equal-sized pieces later (***Figure 25*** (a)). The glass was cleaned by consecutively sonicating for 15 minutes each in water, detergent solution, acetone, and distilled 2-propanol. Following each of the cleaning steps the glass was rinsed with water. After the cleaning procedure it was transferred into 2-propanol for storage. On the day of film preparation, the FTO/glass was taken out of the 2-propanol, rinsed with water, dried in an air flow and cleaned in a UV/ozone cleaner (Filgen UV253H with UV253-OZ Ozone Killer unit) for 30 minutes. The conductive side was then coated with positive-type photoresist by spin-coating for 35 seconds at 1500 rpm using 2 ml of a photoresist solution.

***Table 1:*** *Materials for electrodeposition of porous ZnO with pre- and post-treatment.*

| material | supplier | purity | further specifications |
|---|---|---|---|
| FTO (fluorine-doped tin oxide)-coated glass, type "U" | Asahi | n.a. | thickness 1.1 mm, sheet resistance < 12 Ω/□, effective transmittance > 80 % |
| water ($H_2O$) | Gifu University | Milli-Q | resistivity 18.2 MΩ cm |
| detergent "vista#50" | Inui-Syoji | n.a. | -- |
| acetone ($C_3H_6O$) | Wako | ≥ 99.5% | -- |
| 2-propanol ($C_3H_8O$) | Wako | 99.7% | -- |
| positive-type photoresist "PMER P-LA 300 PM" | Tokyo Ohka Kogyo | n.a. | -- |
| developer "PMER P-7G" | Tokyo Ohka Kogyo | n.a. | -- |
| copper (Cu) tape | Teraoka | n.a. | -- |
| indium (In) | Wako | 99.98% | -- |
| gallium (Ga) | Nacalai tesque | 99.9999% | -- |
| masking tape "ELEP" | Nitto Denko | n.a. | -- |
| potassium chloride (KCl) | Merck | ≥ 99.5% | -- |
| zinc chloride ($ZnCl_2$) | Merck | ≥ 98% | -- |
| eosin Y ($C_{20}H_6Br_4Na_2O_5$) | Wako | ≥ 85% | -- |
| potassium hydroxide (KOH) | Nacalai tesque | ≥ 85% | -- |

The glass was placed onto a hot plate (140°C) for 7 minutes and then left to cool down for 10 minutes. Photostructurization was realized by illumination with a UV lamp (Ushio) through a custom-built mask using an exposure machine with a conveyor belt (Orix). Subsequent dipping into a developing solution for 6 minutes led to removal of the insulating photoresist in the non-illuminated areas as shown in ***Figure 25*** (b). This way, conductive circular areas of 6 mm diameter for electrodeposition of the films and conductive stripes with a width of about 0.5 cm for contacting the electrodes were defined. The glass sheet was rinsed with water and dashed along the pre-cut lines into eight rectangular pieces measuring 2 cm x 3.5 cm (***Figure 25*** (c)). The samples were placed on electrode holders designed to allow rotation of the substrates during deposition, and

contacted on two sides using Cu tape and an equimolar mixture of In and Ga heated to 130°C (***Figure 25*** (d) and (e)). The resistance of the contacts was below 12 Ω. The samples were then fixed on the electrode holders by ready-punched pieces of insulating masking tape with circular holes of 7 mm diameter in the center, ***Figure 25*** (f).

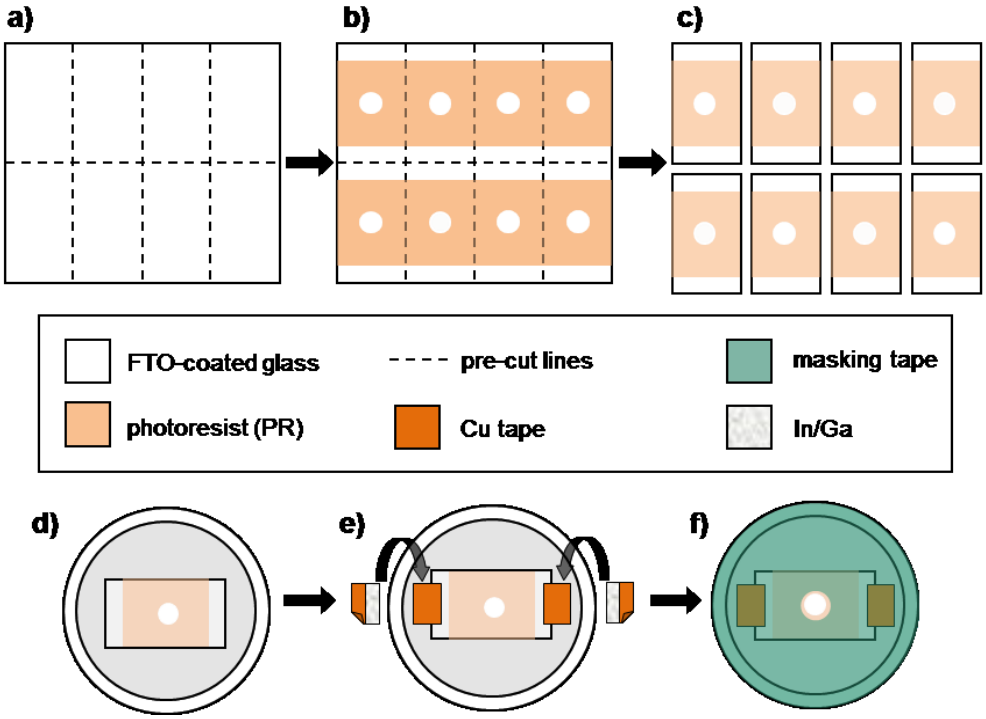


***Figure 25:*** *(a) – (c): Preparation of eight photostructured FTO-coated glass substrates (each 3.5 cm x 2 cm) from a larger piece of FTO-coated glass. (d) – (f): Contacting and fixing of an individual photostructured substrate on an electrode holder.*

For parallel electrodeposition of ZnO on eight substrates, a custom-built setup[268] (Dainippon Screen) with a circular arrangement of eight rotating electrode holders was used in combination with a 16-channel potentiostat system (Bio-Logic, VMP3) and the software EC-Lab V10.10. Throughout the deposition procedure, the current density was monitored at each of the eight electrodes. 2.1 L of a freshly prepared 0.1 M aqueous KCl solution were filled into the container of the deposition setup and heated to 80 °C. The eight electrode holders with the substrates were installed together with a Pt wire counter electrode, a RedRod (Radiometer) reference electrode (0 mV vs. Ag/AgCl) and a glass tube with a Pyrex® glass frit tip used to introduce oxygen gas into the deposition bath. The oxygen flow was adjusted to 2.0 L/min. The rotation of the eight electrode holders was set to 500 rpm and the setup was left in this condition for 30 minutes to

achieve oxygen saturation of the electrolyte. After this, a 30-minute pre-electrolysis of the working electrodes in the $O_2$-saturated KCl solution at -1.05 V vs. the RedRod reference electrode was performed in order to achieve electrochemical activation of the FTO-coated substrates.[269] Successful activation was confirmed by observation of the diffusion-limited current density in the chronoamperograms (see chapter 3). While the applied potential was being kept at -1.05 V vs. RedRod, an appropriate amount of a high-concentration stock solution of $ZnCl_2$ to yield a $Zn^{2+}$ concentration of 5 mM (depending on the concentration of the stock solution) was added to the electrodeposition bath. This triggered the growth of compact ZnO layers (blocking layers). After 10 minutes, the Pt wire counter electrode was exchanged by a Zn wire counter electrode, the applied potential was lowered to -0.75 V vs. RedRod, and an appropriate amount of a high concentration stock solution of eosin Y necessary to achieve a concentration of 300 μM of the structure-directing agent in the electrolyte was added (depending on the concentration of the stock solution). This started the deposition of porous ZnO/eosin Y hybrid films on top of the blocking layers, which was carried out for 30 minutes.

Following electrodeposition, the electrode holders with the coated samples were transferred from the deposition bath into a bowl containing warm water (ca. 70°C) to allow for slow cooling of the deposited films. After about 15 minutes, the masking tape and Cu tape were removed, the samples were transferred into a Petri dish with water (room temperature), and the residual In/Ga was removed with the help of cotton buds. Finally, the samples were rinsed with water, immersed into aqueous KOH solution with a pH of 10.5 (+/- 0.1), controlled by a pH meter, and placed in front of a window for 1 day in order to remove the eosin Y out of the porous ZnO films. After removing them from the KOH solution the electrodes were rinsed with water and subsequently immersed into acetone for about 3 minutes to remove the photoresist from the FTO-coated glass with the help of cotton buds. The samples were rinsed with acetone and water, dried in a drying closet at 100°C for 60 minutes, and cleaned in the UV/ozone cleaner for 30 minutes.

## 2.3 Preparation of Nanoparticulate ZnO Films

The screen printing of the nanoparticulate ZnO films used in this work (series np-ZnO+D149+D131+SQ2) was performed by Hayato Kurotaki at Yamagata University (Japan), the new location of the laboratory of T. Yoshida. 7 cm x 8 cm pieces of FTO-

coated glass (Asahi Glass, type “DU”, thickness 1.8 mm, sheet resistance 10 Ω/□) were pre-cut to allow breaking them into eight equal-sized pieces each later on. Using a SERIA SSA-TF150E screen printer fitted with a patterned 250 mesh screen, ZnO nanoparticle (Nippon Paint) paste was screen printed onto the FTO/glass plates so that eight circular ZnO films with a diameter of 6 mm were deposited on each substrate. In order to remove the solvent and clean the samples, the coated substrates were placed, consecutively, into vacuum (0.1 mbar), a drying closet at 80°C for 30 minutes, and a UV/ozone cleaner (Filgen UV253H) for 60 minutes. The samples were soaked in warm (60°C) water (Milli-Q, resistivity 18.2 MΩ cm) for 10 minutes (hydrothermal treatment) to promote necking of the ZnO particles via dissolution/recrystallization reactions and subsequently rinsed with fresh water. The thickness of the films was approximately 10 µm.[161, 270] Prior to further processing, the large substrates were broken into eight pieces with a size of 2 cm x 3.5 cm along the pre-cut lines, resulting in eight samples with circular ZnO films in their center (geometry equivalent to that of electrodeposited ZnO samples, cf. previous chapter).

## 2.4 UV/Vis Absorption Spectroscopy of Dye Solutions

Dye solutions were characterized by UV/Vis absorption spectroscopy in (1x1x4) $cm^3$ quartz cuvettes by means of a Hitachi U-4100 spectrophotometer (Gifu University) or a tec5 spectrometer system with LS-CH lamp unit, LOE-USB CCD detector unit (spectral range 310 – 1100 nm, spectral resolution < 10 nm), fiber optics and custom-made dark box (University of Gießen). For the reference measurements, the pure solvent in quartz cuvettes was used.

## 2.5 Adsorption of Dyes

### 2.5.1 D149 with CA (Gifu)

The dye D149 (5-[[4-[4-(2,2-Diphenylethenyl)phenyl]-1,2,3-3a,4,8b-hexahydrocyclopent[b]-indol-7-yl]methylene]-2-(3-ethyl-4-oxo-2-thioxo-5-thiazolidinylidene)-4-oxo-3-thiazo-lidineacetic acid) and the coadsorbate cholic acid (CA) were adsorbed to the surface of porous electrodeposited ZnO films from a solution of 0.5 mM D149 and 1 mM CA in a 1:1 (by volume) mixture of acetonitrile and *tert*-butanol (materials as listed in

***Table 2***). To fully dissolve the dye and obtain a clear solution, the solution was sonicated for 60 minutes and afterwards filtered. The dried and UV/ozone-cleaned films (cf. section 2.2) were immersed into 50 mL of the dye solution, and adsorption was carried out in the dark (covered with Al foil) for 1, 2, 10 or 120 minutes. After that, the films were removed from the solution, rinsed with ethanol, dried at air and stored in the dark in tightly closing plastic cases until further use.

***Table 2:*** *Materials for adsorption of D149 with cholic acid in Gifu.*

| material | supplier | purity | further specifications |
|---|---|---|---|
| D149 ($C_{42}H_{35}N_3O_4S_3$) | Chemicrea | n.a. | batch A |
| cholic acid ($C_{24}H_{40}O_5$) | Wako | ≥ 98% | -- |
| acetonitrile ($CH_3CN$) | Wako | 99.5% | -- |
| *tert*-butanol ($C_4H_{10}O$) | Wako | 99.0% | -- |
| filter paper, type 5C | Toyo Roshi Kaisha | n.a. | -- |
| ethanol ($C_2H_6O$) | Wako | 99.5% | -- |

### 2.5.2 D149 without CA (Gießen)

Using the materials in ***Table 3***, a solution of 0.5 mM D149 (batch A) in a 1:1 (by volume) mixture of acetonitrile and *tert*-butanol was prepared under inert gas atmosphere in a glove box (M. BRAUN LABmaster) in order to minimize contamination by water. For comparison experiments, 1 mM cholic acid (Wako, ≥ 98%) was added to a part of the solution. After removal from the glove box, the solutions were sonicated for 30 minutes at 40 – 60°C, so that they were clear to the eye. The porous ZnO films electrodeposited at an earlier date (cf. ***Table 30*** in Appendix A) were dried in an oven at 100°C for 1 – 2 hours, left to cool for 5 minutes, and then immersed into the dye solution. Adsorption was carried out in the dark (covered with Al foil) for 1, 2, 10 or 120 minutes, after which the samples were removed from the adsorption solution and rinsed with ethanol, dried at air and stored in the dark in $N_2$-filled and Parafilm®-sealed plastic cases until further use.

***Table 3:*** *Materials for adsorption of D149 at University of Gießen.*

| material | supplier | purity | further specifications |
|---|---|---|---|
| D149 ($C_{42}H_{35}N_3O_4S_3$) | Chemicrea | n.a. | batch A |
| acetonitrile ($CH_3CN$) | Sigma-Aldrich | 99.8% | anhydrous |
| *tert*-butanol ($C_4H_{10}O$) | Sigma-Aldrich | ≥ 99.5% | anhydrous |
| ethanol ($C_2H_6O$) | Roth | ≥ 99.8% | denatured |

### 2.5.3 D149+D131+SQ2 and np-ZnO+D149+D131+SQ2 (Gießen)

On the basis of previously established adsorption procedures,[31, 32, 226, 271] the photosensitizers D149, D131 (2-Cyano-3-[4-[4-(2,2-diphenylethenyl)phenyl]-1,2,3,3a,4,8b-hexahydrocyclo-pent[b]indol-7-yl]-2-propenoic acid) and SQ2 (5-carboxy-2-[[3-[(2,3-dihydro-1,1-dimethyl-3-ethyl-1H-benzo[e]indol-2-ylidene)methyl]-2-hydroxy-4-oxo-2-cyclobuten-1-ylidene]methyl]-3,3-dimethyl-1-octyl-3H-indolium) were adsorbed to the inner surface of electrodeposited or screen printed porous ZnO films either individually or in various combinations using eight different types of dye solutions prepared by use of the materials in ***Table 4***.

***Table 4:*** *Materials for adsorption of D149, D131, SQ2 or mixtures thereof.*

| material | supplier | purity | further specifications |
|---|---|---|---|
| D149 ($C_{42}H_{35}N_3O_4S_3$) | Chemicrea | n.a. | batch B |
| D131 ($C_{35}H_{28}N_2O_2$) | Chemicrea | n.a. | -- |
| SQ2 ($C_{41}H_{46}N_2O_4$) | Solaronix | n.a. | -- |
| cholic acid ($C_{24}H_{40}O_5$) | Wako | ≥ 98% | -- |
| octanoic acid ($C_8H_{16}O_2$) | Roth | ≥ 99.5% | melting point 16.7°C |
| ethanol ($C_2H_6O$) | Roth | ≥ 99.8% | denatured |
| acetonitrile ($CH_3CN$) | Roth | ≥ 99.9% | anhydrous (ROTIDRY®) |
| *tert*-butanol ($C_4H_{10}O$) | Roth | ≥ 99.5% | -- |

For D149, D131 and D149/D131, a 1:1 (by volume) mixture of acetonitrile and *tert*-butanol was utilized as solvent, while SQ2 was dissolved in ethanol. To some of the dye

solutions, cholic acid or octanoic acid (OA, measured using a Socorex micropipette) were added. ***Table 5*** and ***Table 6*** show the concentrations of dyes and coadsorbates in the various solutions as well as the adsorption times used for the electrodeposited or screen printed samples.

***Table 5:*** *Composition of solutions and adsorption times used to sensitize porous electrodeposited ZnO films with D149, D131 and/or SQ2.*

| **sample** | **0.5 mM D149 ○ = +1 mM CA** | **0.5 mM D131** | **0.25 mM D149 + 0.25 mM D131 ○ = +1 mM OA** | **0.1 mM SQ2 ○ = +10 mM CA** |
|---|---|---|---|---|
| 7-01 D149 | 2 h | - | - | - |
| 7-02 D131 | - | 2 h | - | - |
| 7-03 D149/D131 | - | - | 2 h | - |
| 7-04 SQ2 | - | - | - | 4 h |
| 7-07 SQ2+D149 | 2 h[b] | - | - | 4 h[a] |
| 7-06 SQ2+D149/D131 | - | - | 2 h[b] | 4 h[a] |
| 3-04 D149/CA | 2 h ○ | - | - | - |
| 4-01 D149/D131/OA | - | - | 2 h ○ | - |
| 4-03 SQ2/CA+D149/CA | 2 h ○[b] | - | - | 4 h ○[a] |
| 4-08 SQ2/CA | - | - | - | 4 h ○ |
| 4-07 SQ2/CA +D149/D131/OA | - | - | 2 h ○[b] | 4 h ○[a] |

[a] first step of sequential co-sensitization. [b] second step of sequential co-sensitization.

For each experimental series (D149+D131+SQ2 and np-ZnO+D149+D131+SQ2), fresh dye solutions were used, i.e., a total of 15 dye solutions were prepared. The solutions containing both D149 and D131 were prepared by mixing equal volumes of D149 and D131 solutions or by combining appropriate amounts of both dyes with the solvent mixture. All dye solutions were sonicated for 10 minutes.

***Table 6:*** *Dye solutions and adsorption times used to sensitize screenprinted nanoparticulate ZnO films with D149, D131, SQ2 or mixtures thereof.*

| sample | 0.5 mM D149 ○ = +1 mM CA | 0.5 mM D131 ○ = +1 mM OA | 0.25 mM D149 + 0.25 mM D131 ○ = +1 mM OA | 0.1 mM SQ2 ○ = +10 mM CA |
|---|---|---|---|---|
| NP-01 SQ2 | - | - | - | 4 h |
| NP-08 D149 | 2 h | - | - | - |
| NP-10 D131 | - | 2 h | - | - |
| NP-11 D149/D131 | - | - | 2 h | - |
| NP-02 SQ2+D149 | 2 h[b] | - | - | 4 h[a] |
| NP-13 SQ2+D149/D131 | - | - | 2 h[b] | 4 h[a] |
| NP-04 SQ2/CA | - | - | - | 4 h ○ |
| NP-09 D149/CA | 2 h ○ | - | - | - |
| NP-15 D131/OA | - | 2 h ○ | - | - |
| NP-12 D149/D131/OA | - | - | 2 h ○ | - |
| NP-05 SQ2/CA+D149/CA | 2 h ○[b] | - | - | 4 h ○[a] |
| NP-06 SQ2/CA+ D149/D131/OA | - | - | 2 h ○[b] | 4 h ○[a] |
| NP-07 SQ2/CA+D131/OA+ D149/D131/OA | - | 5 min ○[b] | 2 h ○[c] | 4 h ○[a] |

[a] first step of sequential co-sensitization. [b] second step of sequential co-sensitization. [c] third step of sequential co-sensitization

The porous ZnO films were cleaned in a UV/ozone cleaner (custom-built by A. Dragässer[272]) for 5 – 10 minutes and dried in an oven at 100 – 140°C for at least 1 hour. They were left to cool for 5 minutes before being immersed into the dye solutions. All adsorptions were carried out in the dark (covered by Al foil). Co-sensitization with D149 and D131 was achieved by adsorbing both dyes at a time from the mixed solutions, while combination of SQ2 with one or both of the indoline dyes was reached by

sequential adsorption: the samples were immersed in the first solution, rinsed with ethanol and dried at air, and subsequently immersed into the second solution (***Table 5***). In one case (sample NP-07), a third step followed after rinsing with ethanol and drying at air. As a final step of the adsorption procedures, each film was rinsed (once again) with ethanol, dried at air and stored in the dark in an $N_2$-filled and Parafilm®-sealed plastic case until further use.

### 2.5.4 D149+$S_{1.15}$PcZn (Gießen)

Ethanolic (Roth, ≥ 99.8%, denatured) solutions of D149 (Chemicrea, batch B), $S_{1.15}$PcZn (BASF Switzerland, product code C-1663: mixture of 85% Zn(II) phthalocyanine monosulfonic acid and 15% Zn(II) phthalocyanine disulfonic acid), or both dyes, all containing cholic acid (Wako, ≥ 98%), were prepared with the concentrations specified in ***Table 7***.

***Table 7:*** *Composition of solutions and adsorption times used to sensitize porous electrodeposited ZnO films with D149 and/or $S_{1.15}$PcZn.*

| **sample** | **0.5 mM D149 + 1 mM CA in ethanol** | **0.75 mM $S_{1.15}$PcZn + 1 mM CA in ethanol** | **0.5 mM D149 + 0.75 mM $S_{1.15}$PcZn + 1 mM CA in ethanol** |
|---|---|---|---|
| 5-02 D149/$S_{1.15}$PcZn/CA-2h | - | - | 2 h |
| 5-05 D149/$S_{1.15}$PcZn/CA-17.5h | - | - | 17.5 h |
| 5-06 $S_{1.15}$PcZn/CA | - | 17.5 h | - |
| 5-07 D149/CA | 17.5 h | - | - |

The solutions were sonicated at 40 – 60°C for 30 minutes. Porous electrodeposited ZnO samples were treated in a UV/ozone cleaner (custom-built by A. Dragässer[272]) for 5 minutes, dried in an oven at 140°C for approximately 1 hour and left to cool for 5 minutes before they were immersed into the dye solutions. After 2 hours or 17.5 hours

(cf. ***Table 7***), the films were removed from the solutions and rinsed with ethanol, dried at air and stored in $N_2$-filled and Parafilm®-sealed plastic cases in the dark until further use.

## 2.6 Characterization of (Dye-Sensitized) ZnO Films

### 2.6.1 Analysis of Film Structure and Thickness by Scanning Electron Microscopy (SEM)

Scanning electron microscopy (SEM) images of cross sections of bare ZnO films not used for cell assembly were taken using a Hitachi S-4800 field emission scanning electron microscope. For this purpose, small pieces of the samples were cut and fixed on electrode holders using conductive carbon tape as shown in ***Figure 26***. To prevent charging of the films during the measurement, carbon tape was used to form a contact between the film and FTO/glass and the metallic sample holder.

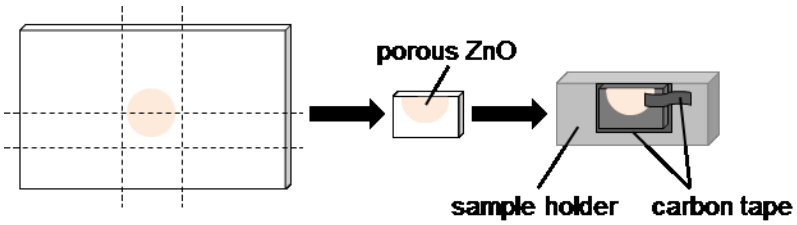


***Figure 26:*** *Preparation of ZnO samples for cross sectional SEM analysis.*

Acceleration voltage and emission current were set to 5 kV and 10 µA. The porous film thickness of 10 samples was determined from the SEM cross section images and compared with the charge transferred during their electrodeposition to obtain a factor allowing conversion of transferred charge to film thickness (see details in chapter 3).

### 2.6.2 UV/Vis Absorption Spectroscopy of Films

UV/Vis absorption spectra of the dye-sensitized ZnO films were measured in transmission mode by means of a Hitachi U-4000 spectrophotometer equipped with integrating sphere (used for films sensitized with D149/CA at Gifu University) or using the tec5 spectrometer system described in chapter 2.4 in combination with a tec5 SPH-REFL-50 integrating sphere (employed for all remaining films). The samples were illuminated

from the substrate side (back side) through a black aperture (diameter of 3 – 4 mm), positioned directly adjacent to the substrate. For the reference measurement, only the aperture was placed in the light path. For comparison, UV/Vis absorption spectra of uncoated FTO glass plates and bare porous ZnO films (without dye) were recorded. All solid-state UV/Vis spectra shown in this work were corrected for constant offsets due to light reflection and absorption by the substrate, determined at a wavelength where none of the dyes absorbed light (typically, 800 nm).

### 2.6.3 Determination of D149 Loading via Desorption

For the determination of the dye loading of ZnO films sensitized with D149 in the presence or absence of cholic acid (not used for cell assembly), D149 was dissolved out of the porous ZnO by immersing either whole films or film quarters into dimethylacetamide (DMAA) (Wako, ≥ 98%) or dimethylformamide (DMF) (Roth, ≥ 99%) in Parafilm®-sealed lidded glass bottles or quartz cuvettes for 1 day. UV/Vis absorption spectra of the resulting D149 solutions were measured as described in 2.4. From the absorbance spectra, the heights of the absorption maxima (located at 530 – 532 nm) were determined. The dye concentration in the solution was then calculated using abs = $\varepsilon cd$ (chapter 1.4.1), with *abs* as the absorbance value in the maximum, $d$ = 1 cm, and $\varepsilon$ = 72350 L mol$^{-1}$ cm$^{-1}$ (reported for a wavelength of 530 nm for D149 dissolved in DMF, see Supporting Information of ref. [31], and used as an approximation for both DMF and DMAA solutions in this work). The result was multiplied by the volume of the solution (5 mL or 10 mL) and divided by the sample area to yield the dye loading in nmolcm$^{-2}$. If sample pieces rather than whole ZnO films (area = 0.28 cm$^2$) were used, the pieces were scanned in front of millimeter paper on a Sharp office printer/scanner and the area was determined by pixel counting using the image analysis software GIMP2.0.

## 2.7 Preparation of Counter Electrodes

For all solar cells with photoelectrodes made of electrodeposited ZnO, counter electrodes based on ATO (antimony-doped $SnO_2$)-coated glass (Geomatec, thickness 1.1 mm, sheet resistance 5 Ω/□) were used. These were prepared in the Yoshida laboratory at Gifu University as described below. Some of the counter electrodes (used for the series D149 without CA, D149+S1.15PcZn, and D149+D131+SQ2) were prepared by

Shigeo Hori. For the cells with screenprinted nanoparticulate ZnO films as photoelectrodes, counter electrodes based on FTO-coated glass (Asahi, type "DU", thickness 1.8 mm, sheet resistance 10 ohm/□) prepared by Hayato Kurotaki at Yamagata University were used, because the Yoshida group had discontinued the use of ATO-coated glass in their laboratory. For the preparation of Pt-coated counter electrodes, the conductively coated glass was cut into 3.5 cm x 2 cm pieces. The glass sheets were immersed into water (Milli-Q) with their conductive side facing down, and holes were drilled in their center using a Minimo drilling system with a KM11H 35 motor, a HO11 head, and a diamond-coated drill bit. The samples were rinsed with water (Milli-Q), dried in an air flow and cleaned in a UV/ozone box (Filgen UV253H with Ozone Killer unit UV253-OZ) for 5 – 10 minutes. For d.c. sputter deposition of platinum (Sanyu Electron Co. Ltd., 99.99%) on the ATO-coated side of the counter electrodes, a Quick Coater SC-708 (Sanyu Electron Co. Ltd.) was employed. Ar gas (GC Tokai, 99.999%) was used to create the plasma, and the sputtering current was adjusted to 24 mA. The sputtering time was 5 minutes, yielding semi-transparent films.

## 2.8 Assembly of Solar Cells

To assemble sandwich-type solar cells, hot-melt foil (Surlyn®, thickness 30 µm) was cut into 2 cm x 2 cm pieces, and holes with a diameter of 6 mm were punched into the center of each piece. The pieces were cleaned with ethanol (Wako, 99.5% or Roth, ≥ 99.8) and dried in an air or nitrogen flow. Pt-coated counter electrodes (cf. section 2.7) were cleaned in a UV/ozone cleaner (Filgen UV253H or custom-built model[272]) for 5 minutes prior to their use, if not used shortly after preparation. A part of the cut and punched pieces of Surlyn® foil were kindly supplied by S. Hori of Gifu University, and some of the Pt-sputtered counter electrodes were kindly provided by S. Hori of Gifu University or H. Kurotaki of Yamagata University (cf. section 2.7). Dye-sensitized ZnO working electrodes (typically sensitized 0 – 2 days, but never more than 5 days, prior to cell assembly) and counter electrodes were assembled at a 90° angle to each other in the bottom part of a custom-built 2-piece steel mounting device (***Figure 27***), with their conductive sides facing each other and with the cut and punched hot-melt foil in between (***Figure 28***).

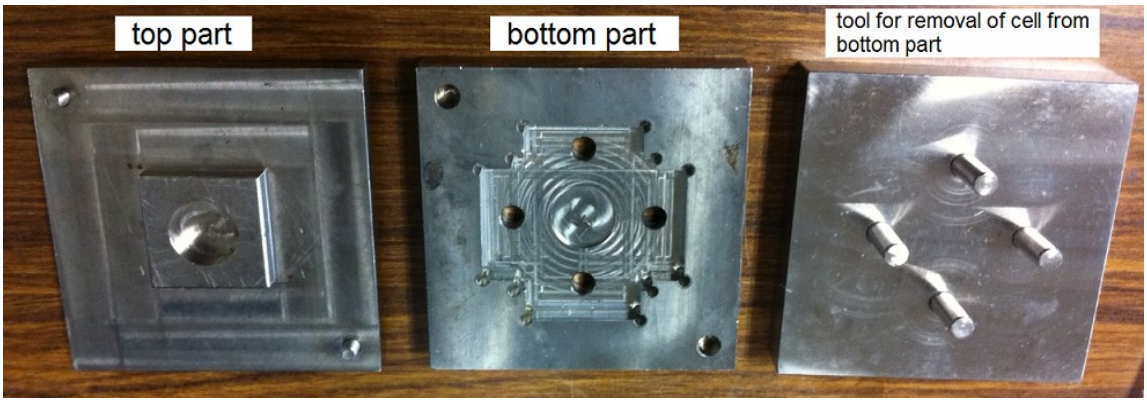


***Figure 27:*** *Custom-built mounting device for assembly of dye-sensitized solar cells. Replica of a device custom-built by Gifu University, prepared by the workshop of the Department of Physics at University of Gießen.*

In order to pre-seal the electrodes together, the top part of the mounting device was heated to 140 – 190°C on a ceramic top hot plate or in an oven and manually pressed down on the stacked electrodes in the bottom part of the mounting device. The pre-sealed cell was then taken out of the mounting device, both top and bottom parts of the latter were heated to 140 – 190°C, and the sealing was finalized by placing the cell into the heated mounting device on the hot plate or on a laboratory countertop and firmly pressing the top part down by hand for about 30 seconds.

The thus-obtained "dry" (before insertion of the electrolyte) cells were stored in the dark in $N_2$-filled and Parafilm®-sealed plastic cases for typically ≤ 1 week (but never more than 3 weeks), before the electrolyte was inserted on the day of their first photovoltaic and photoelectrochemical characterization as described below. As an exception from this, the cells of the series D149 with CA (chapter 5) were fully assembled, filled with electrolyte, and then stored in tightly closing plastic sample cases in a desiccator (in the dark) for up to 2 days before being characterized (cf. ***Table 30*** in Appendix A). As an electrolyte, a freshly prepared or stock solution (up to 4 weeks old) of 0.1 M $I_2$ (Wako, 99.8% or Scharlau, ≥ 99.8%) and 1 M tetrapropylammonium iodide (TPAI) (Alfa Aesar, ≥ 98% or Aldrich, ≥ 98%) in a 4:1 (by volume) mixture of ethylene carbonate (Wako, ≥ 98% or Merck, ≥ 99%) and acetonitrile (Wako, ≥ 99.5% or Roth, ≥ 99.9%, anhydrous (ROTIDRY®)) was used.

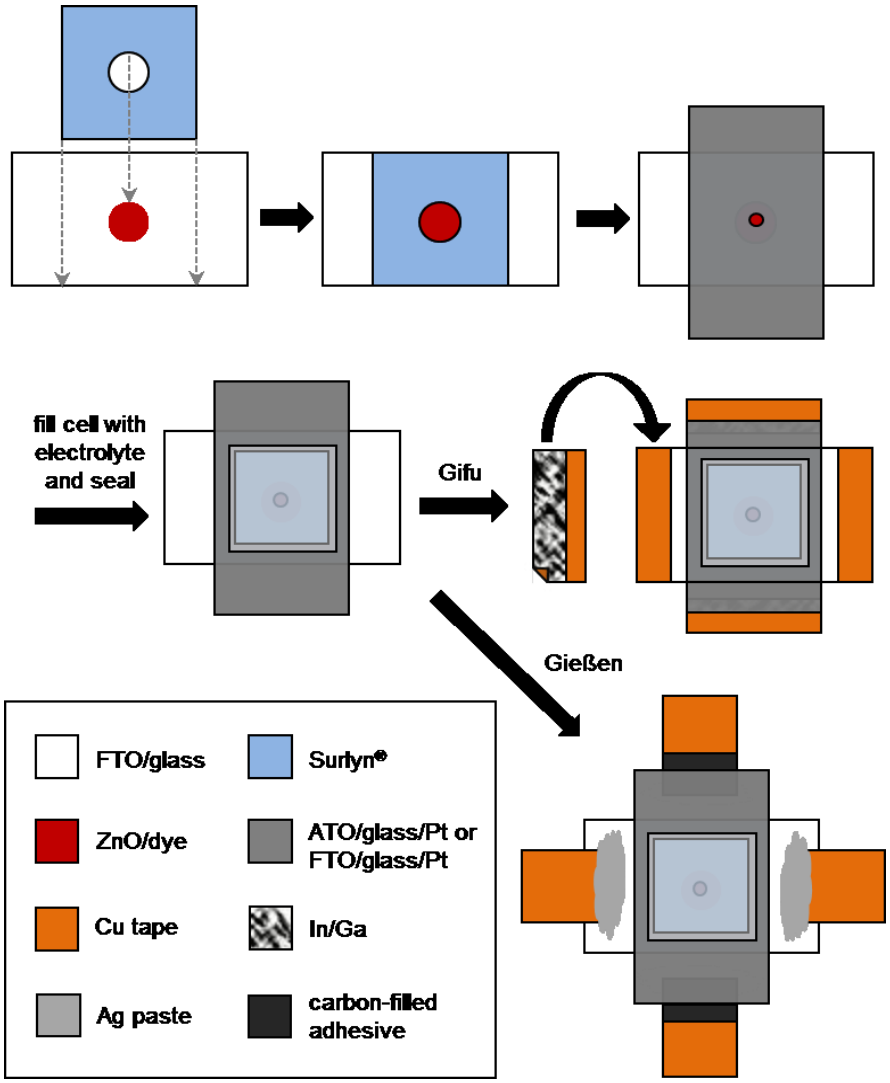


***Figure 28:*** *Scheme showing the steps of solar cell assembly and contacting.*

A small drop of the electrolyte was placed onto the hole in the counter electrode and the cell was placed into a vacuum drying oven (Yamato DP3) or into the small transfer chamber of a glove box (M. BRAUN LABmaster). The box or transfer chamber was evacuated and the cell was left in that condition for about 30 seconds to remove air from the space between counter electrode and ZnO/dye film and to fill the space with electrolyte solution. The pressure was increased back to atmospheric pressure, the sample was taken out, and the excess electrolyte was removed thoroughly from the back side of the counter electrode using laboratory wipes and a small amount of ethanol, if necessary. The hole was sealed by placing a piece of Surlyn® (1.5 cm x 1.5 cm) and a 1.8 cm x 1.8 cm cover slip (Matsunami, thickness 0.12 – 0.17 mm or Roth, thickness 0.13 – 0.16 mm) onto the back side of the counter electrode and lightly pressing down on the cover

slip either with the hot (140 °C) top part of the mounting device (cf. ***Figure 28***) or with a soldering iron heated to 240°C. On the day of cell characterization, the working and counter electrodes were contacted as illustrated in ***Figure 28*** using either In/Ga alloy and Cu tape (Gifu University) or Cu tape (Plano, product no. G3940) and conductive silver paint (ACHESON 1415 via Plano, product no. G3692) (University of Gießen). The active area of the solar cells was 0.28 $cm^2$.

## 2.9 Characterization of Solar Cells

The main characterization of the cells of series D149 with CA was performed at Gifu University, while the remaining cells were fully characterized at University of Gießen. The characterization in Gießen was largely realized using a customized Zahner CIMPS (controlled intensity-modulated photocurrent and photovoltage spectroscopy) system for photoelectrochemical measurements. This system was established as part of this work and is described in detail in Appendix B. For the cells of series D149+$S_{1.15}$PcZn, D149+D131+SQ2 as well as np-ZnO+D149+D131+SQ2, *J-V* characterization under illumination with LED light, EIS at open-circuit under illumination of varied intensity, OCVD, charge extraction from open-circuit conditions, short-circuit photocurrent decay, IMPS, IMVS as well as intensity-dependent short-circuit current and open-circuit voltage were measured in an automated sequence using an AutoHotkey script programmed by André Dragässer.[272] In all other measurements, the input of the parameter settings and starting of the measurements was performed manually.

### 2.9.1 Current-Voltage Characterization

The current-voltage curves were recorded using a Hokuto Denko HSV-100 potentiostat or a Zahner IM6 electrochemical workstation. The IM6 workstation was controlled via the "CIMPS" add-on of the software Thales, which was modified by M. Beu and A. Dragässer to allow use of external light sources (cf. Appendix B) when employing the "Start Max. P & FF" feature intended for *J-V* characterization. To measure the *J-V* characteristics under AM1.5G conditions, the cell was illuminated by a Yamashita Denso YSS-50 solar simulator or an LOT Oriel solar simulator LS0106 with AM1.5G filter LSZ189. The light intensity of 100 $mWcm^{-2}$ was set by means of a Si reference solar cell or an EKO LS-100 spectroradiometer. The Yamashita Denso YSS-50 solar simula-

tor and the Si reference solar cell belong to the Solid-state Electronics Engineering Laboratory at Gifu University (Prof. Nonomura), who kindly permitted use of their equipment. At Gifu University, the sample was positioned on a flat surface illuminated from the top for the measurement of the *J-V* curves under AM1.5G conditions, while dark characteristics were measured with the light source turned off and the sample covered by a thick black piece of felt. At University of Gießen, the sample was fixed on a sample holder in a custom-built dark box to exclude the influence of ambient light and allow only the light of the solar simulator to enter through a hole (cf. Appendix B). For the measurement of the dark *J-V* characteristics, the hole in the dark box was closed by a shutter. If not indicated otherwise, the illuminated cell area was generally limited to 0.196 $cm^2$ using a black shadow mask with a circular hole with a diameter of 5 mm (compared to a diameter of 6 mm of the dye-sensitized films, yielding a total active area of 0.28 $cm^2$). Current densities were calculated using the illuminated cell area. This approach relies on the assumption that the limitation of the illuminated area did not significantly change the recombination current compared to a fully illuminated cell. Comparative *J-V* measurements with and without mask confirmed the validity of this assumption (chapter 9.2). The internal current-voltage characteristics (illuminated) were obtained by plotting the measured cell current against the Fermi-level voltage $V_f$ determined using the results of impedance spectroscopy measurements under AM1.5G-type illumination (see details in 2.9.3). For plots of the series resistance-corrected current-voltage curves in the dark, the $V_f$ values from EIS under AM1.5G type illumination were used as well, because dark EIS data had typically not been obtained. This procedure is based on the assumption that the total series resistance (cf. chapter 1.4.4) is independent of illumination. The influence of elevated temperatures on the current-voltage characteristics in the dark and under illumination was tested on a few of the cells with D149 and cholic acid by using a hairdryer (Clatronic) to heat the air around the cell to about 70°C (as determined by a Greisinger GTH 1200 digital thermometer) and measuring *J-V* curves under these conditions by means of the Zahner/LOT Oriel setup.

### 2.9.2 Measurement of the Incident Photon-to-Electron Conversion Efficiency (IPCE)

Measurements of the incident photon-to-electron conversion efficiency were performed at short-circuit, i.e. with a bias voltage of 0 V applied to the solar cell. The illuminated

cell area was restricted to 0.196 $cm^2$ using a black shadow mask and current densities and IPCE values were calculated based on this area. At Gifu University, the measurements were realized using a Bunko-Keiki CEP-2000 system. The photon flux density was kept constant at $5 \cdot 10^{15}$ $s^{-1}cm^{-2}$, both over time and over the wavelength range investigated. The cell was contacted to the cables of the setup and placed on a sample stage so that the active area was positioned in the light beam. By making slight manual adjustments to the sample position the location of highest light intensity (i.e. in which the cell showed the highest photocurrent) was found, and the sample was fixed there for the subsequent measurement. The wavelength range of the IPCE measurement was 300 – 800 nm and the step width was 5 nm. For IPCE measurements at University of Gießen, two different systems were used comparatively, referred to as Zahner system and Acton/Ivium system (cf. Appendix C). The Zahner system consisted of a customized Zahner CIMPS setup (cf. Appendix B) with CIMPS-pcs add-on containing a TLS02 light source (including a monochromator), as well as the Thales software add-on CIMPS-pcs for control. The light source was operated galvanostatically with a sinusoidally modulated current of 300 mA (d.c. bias current) +/- 100 mA (a.c. amplitude). The frequency of the modulation was generally set to 1 Hz, and the number of cycles recorded and averaged for each wavelength ("count") was 20. In some earlier measurements (series D149 without CA), a modulation frequency of 10 Hz was used with a count of 100. The Acton/Ivium system was developed as part of this work in cooperation with J. Birkenstock[273] and combined a 1000 W Xe arc lamp (Oriel) with an Acton SpectraPro 2300i monochromator and a LabVIEW-based software created by J. Birkenstock.[273] The light beam leaving the monochromator entered a dark box, in which the sample was fixed on a sample holder, through a hole. The photon flux density was constant over time (i.e., not modulated) and its value at the location of the sample was determined as a function of the wavelength prior to the measurement of the spectral solar cell current using a Thorlabs FDS100 Si photodiode fixed on the sample holder. The maximum photon flux density was observed at 470 nm, and typically showed a value around $7 \cdot 10^{15} – 8 \cdot 10^{15}$ $s^{-1}cm^{-2}$ (spectrum in Appendix C). The IPCE values at each wavelength were calculated from the wavelength-dependent photon flux at the location of the sample and the wavelength-dependent solar cell current density under the assumption that the IPCE did not change due to the variation of the photon flux over the range of different wavelengths. This was confirmed (see Appendix C) by their experimentally ob-

served linear dependence of the cells' current density on the light intensity of a red LED (Zahner RTR01, $\lambda_{max}$ = 632 nm). The wavelength range and step width were 430 – 730 nm (maximum range) and 5 nm for the Zahner system, and 350 – 700 nm (350 – 800 nm for cells with red-absorbing photosensitizers) and 10 nm for the Acton/Ivium system.

### 2.9.3 Electrochemical Impedance Spectroscopy (EIS)

For electrochemical impedance spectroscopy (EIS) measurements, a Solartron Impedance/Gain-Phase Analyzer 1260 combined with a Solartron potentiostat/galvanostat 1287, or a customized Zahner CIMPS system with IM6 electrochemical workstation (cf. Appendix B) was employed. Measurements at varied bias voltage under white light were performed using ~60 mWcm$^{-2}$ illumination by a 200 W Xe arc lamp (Ushio) or using AM1.5G-type illumination (100 mWcm$^{-2}$) by an LOT Oriel solar simulator LS0106. Additionally, many of the samples were studied by EIS at open circuit at a series of light intensities by a red LED (Zahner RTR01, $\lambda_{max}$ = 632 nm), and a small selection of cells was analyzed by EIS at varied bias voltage in the dark. ***Table 33*** (Appendix D) contains a detailed list of the types of EIS measurements performed for the different groups of cells, and specifies the corresponding bias voltage range, amplitude of the voltage modulation, and frequency range. In the measurements under illumination, generally the full cell area of 0.28 cm$^2$ was illuminated, except in the measurements performed at Gifu University, where the illuminated area was limited to 0.196 cm$^2$ with a black mask with circular hole. All impedance spectra were fitted to the equivalent circuit shown in ***Figure 106*** (Appendix D) using the software ZView2 to obtain the recombination resistance $R_{rec}$, chemical capacitance $C_\mu$, substrate resistance $R_s$, and ohmic parts of the electrolyte and counter electrode resistances, $R_d$ and $R_{Pt}$. The Fermi-level voltage $V_f$ was determined using eq. (56) and eq. (57) or, alternatively, using eq. (58) with the approximation $R_{tr}$ = 0 ($R_{tr}$ could not be determined as it was not distinguishable in the EIS spectra). The density of states $g(E_{fn})$ in the nanostructured ZnO films was calculated from the chemical capacitance $C_\mu$ obtained by EIS using eq. (45), assuming a porosity of 0.6 for the electrodeposited ZnO films and 0.7 for the nanoparticulate screenprinted ZnO films.[136] To obtain the normalized chemical capacitance (normalized $C_\mu$), $C_\mu$ was divided by the relative total trap density $N_t/N_{t,ref}$ (cf. section 2.9.7).

### 2.9.4 Stepped Light-Induced Transient Measurements of Photocurrent and Voltage (SLIM-PCV)

Time-resolved measurements of the decay of photovoltage or photocurrent after a small stepped change in light intensity (SLIM-PCV)[264] were realized at Gifu University with the help of an EKO PSL-100 system with red diode laser (660 nm).

For the transient measurement of the photovoltage, the cell was kept at open circuit throughout the experiment. Measurements with six different initial laser voltages were performed: 0.9 V, 1.2 V, 1.5 V, 1.9 V, 2.3 V, 3.5 V. The light intensities corresponding to these laser voltages were measured using an EKO LS-100 spectroradiometer. Following a 10-60 s settling time, in which the cell was illuminated with the initial laser intensity and allowed to equilibrate, the system began to record voltage-time data. The sampling interval was set to 200 µs and the total number of recorded data points was 1000, resulting in a total recording time of 0.2 s. After 10% of the specified total time, the laser voltage was automatically stepped down to a previously defined final laser voltage. The latter was chosen to be 0.01 – 0.03 V smaller than the initial laser voltage, leading to a small reduction of the light intensity and a decrease of the open-circuit photovoltage by typically 1 mV. With the help of the PSL-100 software, the electron lifetime $\tau_n$ was determined by fitting the obtained voltage decays to a monoexponential decay function of the type $V_{oc} = V_{oc,0} - const \cdot \left[1 - \exp\left(\frac{-(t-t_0)}{\tau_n}\right)\right]$, where $V_{oc}$ is the open-circuit photovoltage, $V_{oc,0}$ is its equilibrium value before the onset of the decay, *const* is a constant, $t$ is the time and $t_0$ is the time of the onset of the decay.

The transient photocurrent measurements using the EKO PSL-100 system were performed under short-circuit conditions. The same set of initial laser voltages as in the voltage measurements was used, and the final laser voltages were again 0.01 – 0.03 V smaller than the corresponding initial voltages. While the settling time was again chosen to be between 10 s and 60 s, the sampling interval and total number of data points were set to 30 µs and 1300, amounting to a total measurement time of 39 ms. As in the voltage measurements, the laser voltage was set to be stepped down after 10% of this total recording time, i.e. 3.9 ms. The resulting current decays were fitted to a monoexponential function of the type $J_{sc} = J_{sc,0} - const \cdot \left[1 - \exp\left(\frac{-(t-t_0)}{\tau}\right)\right]$ using the PSL-100 soft-

ware, where $J_{sc}$ is the short-circuit current, $J_{sc,0}$ is its equilibrium value before the onset of the decay, *const* is a constant, $t$ is the time, $t_0$ is the time of the onset of the decay, and $\tau$ is the time constant of the decay. Based on the fit result, the software automatically calculated the diffusion coefficient $D_n$ via eq. (71).

### 2.9.5 Open-Circuit Voltage Decay (OCVD) Measurements

To measure the decay of the photovoltage under open-circuit conditions, the customized Zahner CIMPS system (Appendix B) with CIMPS-fit add-on was used with a red LED (Zahner RTR01). The cell was illuminated with a light intensity of 25 $mWcm^{-2}$. After a settling time of 5 s, the voltage measurement was automatically started. The resolution and total measurement time (parameter "record time") were set to 0.1 ms and 60 s. After 10% (value of the parameter "pretrigger share") of the total measurement time, i.e. 6 s, the LED was turned off by the system and the voltage started to decay. Using OriginPro 9.1 software, the voltage decay curves were smoothed (Savitzky-Golay smooth, 2$^{nd}$ order, 500-points windows) and differentiated, and the results were used to determine the voltage-dependent electron lifetime $\tau_n$ according to eq. (70).

### 2.9.6 Charge Extraction Measurements from Open-Circuit Conditions

Charge extraction from open-circuit conditions was realized by means of the EKO PSL-100 measurement setup with 660 nm laser or using the "Q-extraction" function of the Zahner CIMPS system with red LED (RTR01, $\lambda_{max}$ = 632 nm) or cyan LED (Zahner CYR01, $\lambda_{max}$ = 513 nm). In the measurements with the PSL-100 system, the laser voltages corresponded to the ones used in the time-dependent current and voltage measurements (see section 2.9.4). For each laser intensity, the exact open-circuit voltage was determined prior to the charge extraction measurements by applying the $V_{oc}$ observed in the first part of the time-resolved photovoltage measurements (section 2.9.4) and then making small changes to this applied voltage until the current measured by the PSL-100 system was as close to zero as possible. The thus-determined open-circuit photovoltage was then applied to the cell while it was being illuminated with the corresponding laser intensity. After an equilibration time of 10 s, the data measurement was started by the system. The sampling interval and total number of data points were 200 µs and 6000, resulting in a total measurement time of 1.2 s. After 10% of this total time (i.e. 0.12 s),

the laser was turned off and the bias voltage was switched to 0 V (short-circuit condition), causing the charge stored in the ZnO to be extracted. By means of the PSL-100 software, the current recorded during the extraction part was integrated over time to yield the charge $Q_{oc}$ stored in the porous ZnO films under open-circuit conditions at different light intensities. In the measurements with the Zahner CIMPS system, the target voltage was set to 0 V and the discharge current (Zahner-specific parameter)[274] was typically set to 400 µA. The sample time (resolution) was 10 ms. The cell was illuminated under open-circuit conditions for 10 s, after which the LED was automatically turned off and the cell was simultaneously short-circuited. The resulting current was measured for 20 s, and the system delivered the extracted charge $Q_{oc}$ (current integrated over time) as an output. The measurement was performed at 12 different LED intensities between 0.5 and 25 $mWcm^{-2}$. The $Q_{oc}$ obtained by both measurement systems were converted into the electron density $n_{oc}$ using eq. (72), with the porosity $p$ assumed to be 0.6 for the electrodeposited ZnO films and 0.7 for the nanoparticulate screenprinted ZnO films.[136]

### 2.9.7 Short-Circuit Photocurrent Decay Measurements (Charge Extraction from Short-Circuit Conditions)

Time-resolved measurements of full short-circuit photocurrent decays to determine the charge stored in the porous ZnO under short-circuit conditions, $Q_{sc}$, were performed using the EKO PSL-100 system (cf. sections 2.9.4 and 2.9.6) or the Zahner CIMPS system with red Zahner LED (RTR01, $\lambda_{max}$ = 632 nm) and CIMPS-FIT add-on. For the measurements with the PSL-100 setup, the same procedure and parameters as in the charge extraction measurements from open-circuit conditions were applied, but the cell bias voltage was set to 0 V (short-circuit) for all laser intensities. For each cell, the background current due to small amounts of background light was measured by repeating the short-circuit charge extraction measurement with a laser voltage of 0 V. All charges were automatically determined from the current decay curves by the PSL-100 system. The background charge was subtracted from the charges measured at different laser intensities to yield the intensity-dependent $Q_{sc}$. In the measurements with the Zahner CIMPS system, the cell was allowed to equilibrate during a settling time of 5 s before the recording of measurement data was started by the system. Resolution and total measurement time (parameter “record time”) were set to 0.1 ms and 5 s. The LED was

switched off to start the current decay after 1 s, corresponding to a value of 20% of the parameter "pretrigger share" (i.e. the share of total measurement time after which the LED is switched off). The experiment was performed at 14 different LED intensities between 0.1 and 25 mWcm$^{-2}$. Integration of the current over time, which was performed in OriginPro 9.1 in an automated process using an Origin-based script programmed by André Dragässer,[272] yielded $Q_{sc}$ for each of the light intensities investigated. $Q_{sc}$ values from the measurements with both setups were converted into the electron density $n_{sc}$ using eq. (72), assuming $p = 0.6$ for the electrodeposited ZnO films and $p = 0.7$ for the nanoparticulate screenprinted ZnO films.[136] The short circuit electron density was plotted logarithmically against the short-circuit current density $J_{sc}$, and the factors necessary to align the $n_{sc}$ vs. $J_{sc}$ curves with a reference curve were determined. These factors correspond to relative values of the total density of trap states $N_t$ with respect to the reference cell,[252] which will be referred to as $N_t/N_{t,ref}$ in this work.

### 2.9.8 Intensity-Modulated Photocurrent/Photovoltage Spectroscopy (IMPS/IMVS)

All IMPS and IMVS measurements were performed using the customized Zahner CIMPS setup with red LED (Zahner RTR01). The constant background light intensity was varied between 0.1 and 25 mWcm$^{-2}$, with up to 12 light intensities in between. The amplitude of the light modulation was set to be about 5 – 10% of the constant background light intensity, except for the smallest light intensities of 0.1 and 0.2 mWcm$^{-2}$, for which the amplitude was about 25 – 45% of the background intensity when using the smallest value the system allows. The lower frequency limit was chosen between 100 mHz and 1 Hz, while the upper limit was 100 kHz or 1 MHz. IMPS was measured under short-circuit conditions, while IMVS was done under open-circuit conditions. The real part (Re) and imaginary part (Im) of the IMPS and IMVS spectra were fitted using eq. (61) and eq. (62),[256] with $\omega_{min} = 1/\tau_n$ in the case of IMVS and $\omega_{min} = 1/\tau_{tr}$ in IMPS, to obtain the effective electron lifetime $\tau_n$ and the electron transit time $\tau_{tr}$. For each cell, the fitting for the complete series of measurements at different light intensities was performed in OriginPro 9.1 in an automated way using an Origin-based script programmed by André Dragässer.[272] The script allowed either a separate fitting of the imaginary part or a combined fitting of real part and imaginary part yielding values for the parameters

$M$ and $\tau$ that are optimized for both functions. If not otherwise mentioned, the results obtained by the combined fitting are presented.

### 2.9.9 Intensity-Dependent Measurements of Short-Circuit Photocurrent and Open-Circuit Photovoltage

The short-circuit photocurrent and open-circuit photovoltage of the solar cells were measured as a function of the light intensity using the "static transfer function" feature of the customized Zahner CIMPS system with red LED (RTR01). The intensity was varied between 0 and 25 $mWcm^{-2}$ in 0.5 $mWcm^{-2}$ steps. After each change in light intensity, a settling time of 2 s allowed the cell to adjust to a new equilibrium.

# 3 Nanostructure and Film Thickness of the Electrodeposited Porous ZnO Films

The preparation of porous ZnO by electrodeposition in the presence of the structure-direction agent eosin Y is most commonly realized using an eosin Y concentration of 40 to 50 µM and a cathodic deposition potential of -0.85 V vs. Ag/AgCl or more negative.[25, 136, 137, 186, 219] Under these conditions, a fast deposition of ZnO/eosin Y hybrid films is observed and the structure-directing agent can be completely removed from the pores of the ZnO matrix by soft alkaline treatment.[26, 183] The resulting porous ZnO structure exhibits typical pore sizes of around 10 – 20 nm.[27, 186] At less negative deposition potentials (and using 40-50 µM of eosin Y), smaller amounts of eosin Y are incorporated into the film and it is difficult to extract the SDA.[275]

In the electrodeposition of the porous ZnO layers used in this work, a slightly different approach was utilized, which has first been studied in a PhD project in the group of T. Yoshida.[276] In this approach, an increase of the concentration of eosin Y in the deposition bath to several hundreds of µM opens up the possibility of applying a less cathodic deposition potential but nonetheless obtaining hybrid films with high loadings of eosin Y that are fully removable by the standard alkaline treatment.[136, 276] Besides the advantage of requiring a smaller polarization potential, it was found that it leads to films with a more homogeneous film thickness and improved mechanical stability compared to porous ZnO prepared under the above-described standard conditions.[276] The specific deposition parameters used here – 300 µM of eosin Y and a potential of -0.75 V vs. Ag/AgCl – yielded ZnO layers with a nanostructure as seen in the scanning electron microscopy image in ***Figure 29***. The columnar structure closely resembles that of films deposited at more negative potentials using lower concentrations of eosin Y,[26, 27, 136, 277] with a similar[27] average pore diameter estimated from this image to be in the range of 20 – 30 nm.

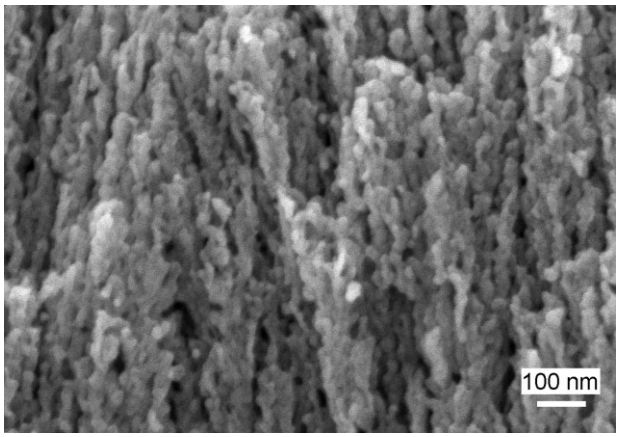


***Figure 29**: High resolution cross-sectional SEM image of an electrodeposited porous ZnO film typical of the films used in this work. The sample was prepared by electrodeposition from an aqueous, oxygen-saturated bath containing 0.1 M KCl, 5 mM $ZnCl_2$ and 300 µM eosin Y. The deposition potential was -0.75 V vs. Ag/AgCl. Reprinted from ref. [278], Copyright 2013, with permission from Elsevier.*

The fabrication of the samples used for the studies in this thesis was realized by means of a custom-built setup permitting electrodeposition of ZnO on eight substrates at a time under exactly the same conditions with respect to temperature and concentrations of reagents in the bath. Besides being time-efficient, this approach was expected to offer the advantage of fabricating sets of films of highest reproducibility, which is a crucial precondition for the systematic study of modifications in the photosensitizer layer intended in this work. To verify the comparability of simultaneously deposited ZnO layers and examine the batch-to-batch reproducibility, the current-time curves attained during deposition were analyzed for each sample utilized to build test solar cells (cf. full list of samples in **Table 30**). A number of films that were not used for cell assembly were further analyzed by cross-sectional scanning electron microscopy (SEM) to relate the observed current-time curves to the film thickness.

A representative example of a set of chronoamperograms obtained in the deposition of eight ZnO films can be seen in ***Figure 30***. On the left, the current-time curves during electrochemical activation of the substrates and deposition of the compact ZnO blocking layers are shown, and on the right, the curves recorded during deposition of the porous ZnO films are presented. The observed behavior is typical for this pretreatment and deposition routine[26, 269, 279] The achieved current density during activation was similar to

that reported previously for the same procedure,[269] confirming successful activation of the substrate and, as a result, observation of a diffusion-limited oxygen reduction current. Note that the chronoamperograms all exhibit very similar shapes and the current densities show little sample-to-sample scattering. This suggests that the reduction of $O_2$ and the film growth proceeded identically, which gives a first indication that the internal morphologies and film thicknesses of these layers should be comparable as well. Samples with a notably different behavior of the activation or deposition current (such as "2" in ***Figure 30***, left) were generally sorted out and not used to build DSCs.

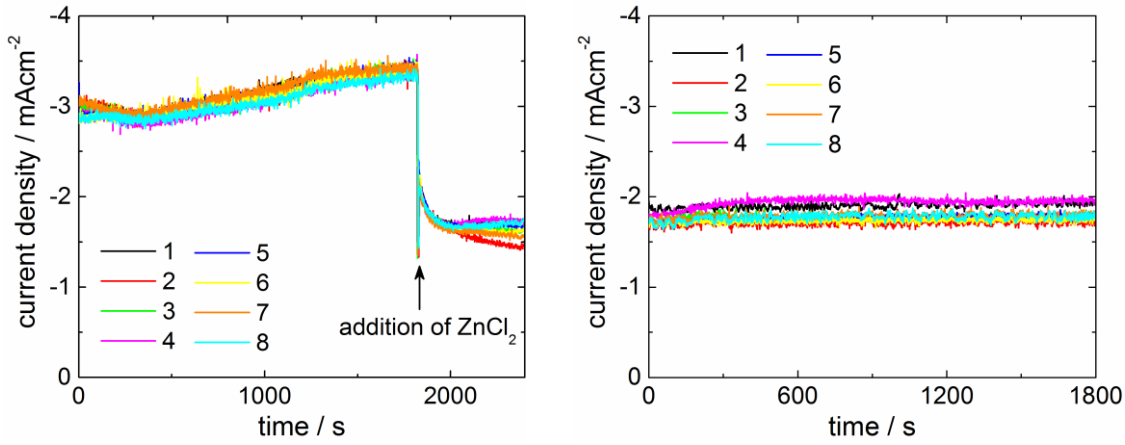


***Figure 30**: Chronoamperograms recorded during the simultaneous electrochemical preparation of 8 ZnO films. Left: current density during electrochemical activation (electrolysis in the absence of $ZnCl_2$ and eosin Y) for 30 minutes and subsequent blocking layer deposition for 10 minutes. Right: Current density during deposition of the porous layer in the presence of eosin Y for 30 minutes (directly following activation and blocking layer deposition).*

***Figure 31*** presents cross-sectional SEM images of five of the samples corresponding to the chronoamperograms shown above. Porous film, compact film and FTO layer could be easily distinguished based on differences in contrast (see areas highlighted in green, red, and blue). The thickness of the porous layer was measured from images taken at three different places along the diameter of each film using image analysis software. The averaged values ranged from 4.4 to 4.7 µm, with lateral variations of ≤ 0.1 µm (***Figure 31***). This SEM-based thickness measurement was repeated for five more films taken from two other batches.

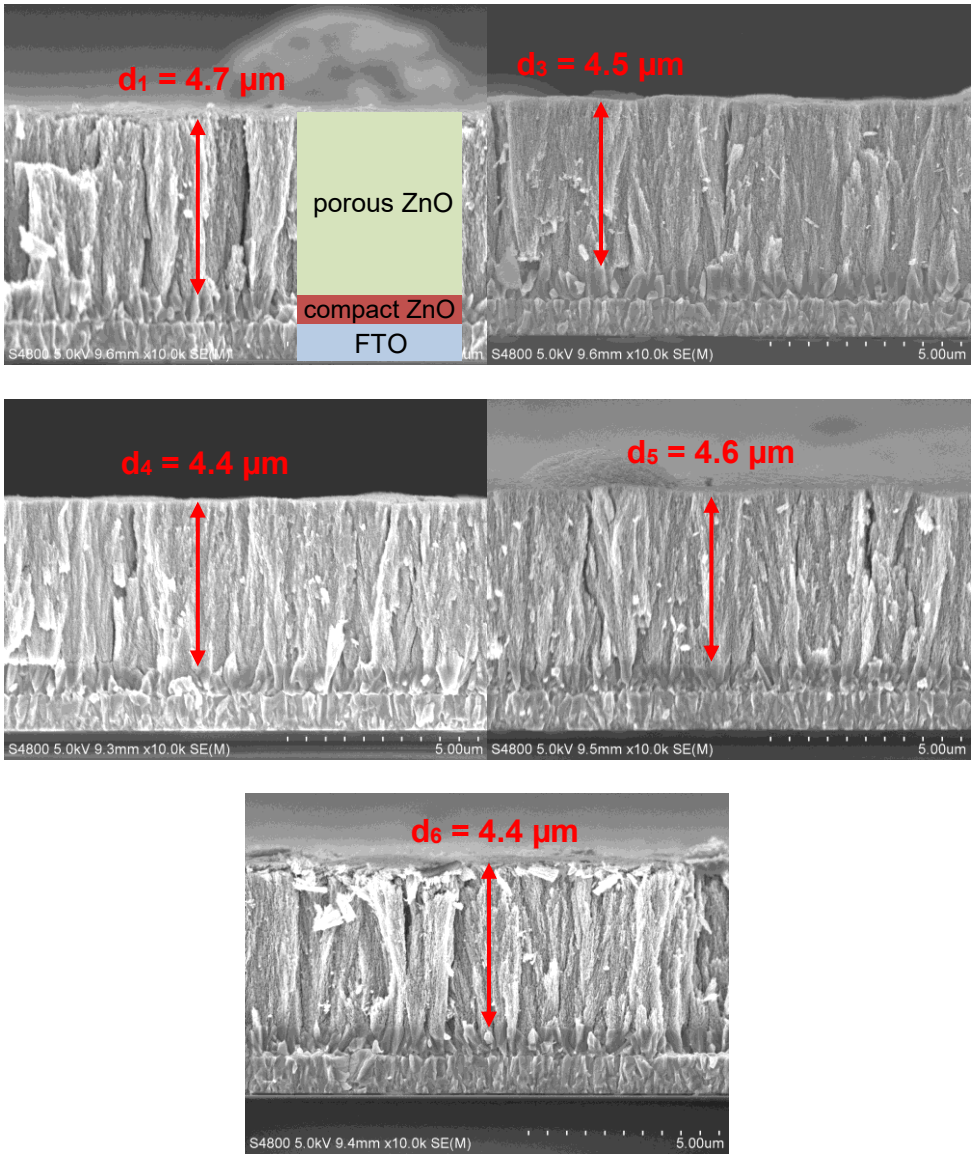


***Figure 31**: Scanning electron microscopy of cross sections of ZnO films electrodeposited in parallel using a custom-built 8-electrode deposition setup. Deposition conditions as specified in **Figure 29**. The film thicknesses d (subscript indicates sample no.) are averages of values determined from three different images taken along the diameter of each film: close to the left edge, in the film center, and close to the right edge.*

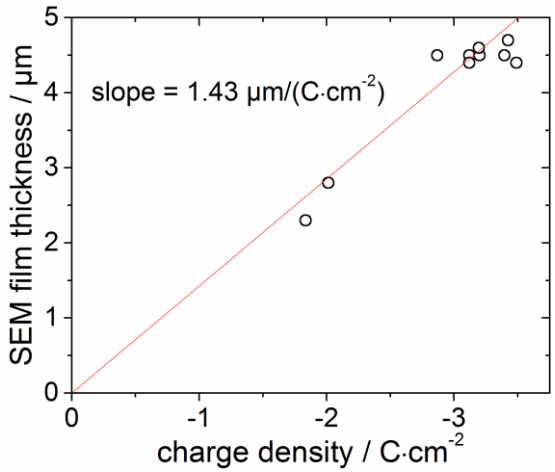


***Figure 32**: Film thickness of porous electrodeposited ZnO films determined from SEM cross sections as a function of the charge transferred during their deposition. The red line is a linear fit to the data (intercept fixed at SEM film thickness = 0 µm).*

Based on these results, the thickness of each of the electrodeposited ZnO films used for DSC assembly in this work (see ***Table 30***, Appendix) was determined using the deposited charge and the conversion factor of 1.43 µm·(C·cm$^2$)$^{-1}$, cf. ***Figure 32***. The narrow distribution of thicknesses for this large number of samples, ***Figure 33***, further confirms the high sample-to-sample and batch-to-batch reproducibility of the electrodeposition of porous ZnO using the 8-electrode setup.

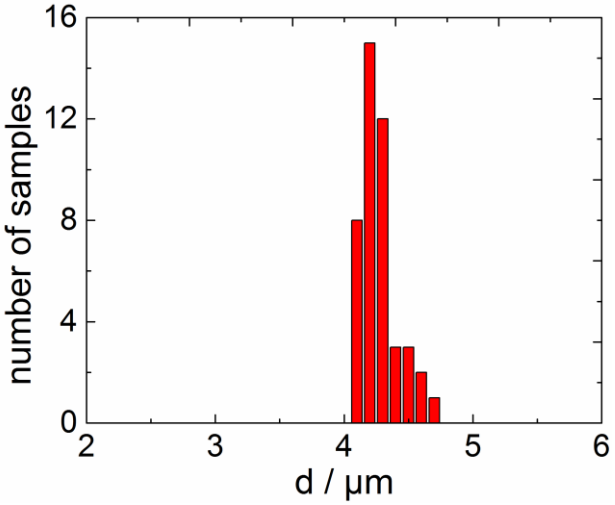


***Figure 33**: Thickness distribution of the electrodeposited ZnO films used in the present work.*

# 4 Reproducibility of the Properties of Standard Cells

Each of the experimental series discussed in the present work included one or more standard[25] ZnO-based DSCs sensitized with D149 or D149/CA for 2 hours (cf. ***Table 30***). The properties of these cells mostly served as a reference point to discuss the influence of adsorbing different sensitizers and/or coadsorbates. The present chapter will mainly focus on the reproducibility among the two groups of standard samples (D149 and D149/CA), while the significant difference between samples with and without CA will be discussed in detail in chapter 5.

The absorption spectra of the D149- or D149/CA-sensitized electrodeposited ZnO films of chapter 5 (***Figure 34*** (a)), which were fabricated at Gifu University or University of Gießen, showed negligible variations within each set of 3 identically prepared films stored for the same time prior to sensitization (see labels in ***Figure 34***).

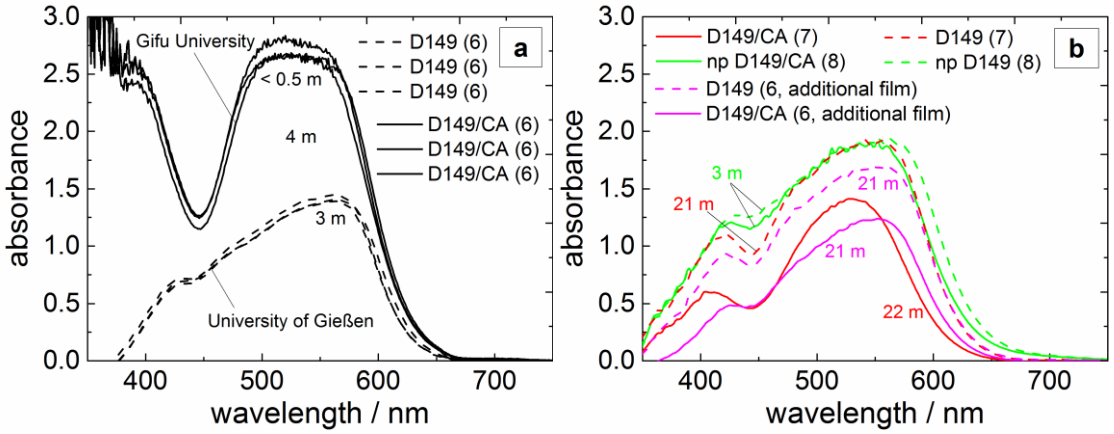


***Figure 34****: UV/Vis absorption spectra of various porous ZnO films sensitized with D149 or D149/CA for 2 hours using D149 of synthesis batch A (a) or synthesis batch B (b). Curve labels correspond to the age of the ZnO films (in months) at the time of dye sensitization. In the legends, the numbers in parentheses indicate the chapter numbers in which the samples will be discussed in detail.*

This demonstrates excellent reproducibility of the dye loading (cf. eq. (24)) for electrodeposited films of the same age sensitized at a given laboratory, which allowed to forgo the preparation of multiple samples with identical preparation conditions in chapters 6 through 8 in favor of exploring a large number of different dye/dye and dye/coadsorbate combinations. The optical absorption of ZnO films sensitized with a different batch of

D149 at University of Gießen at a later time (dashed lines in ***Figure 34*** (b)) was largely comparable to that of the three films with D149 of chapter 5 (dashed black lines in ***Figure 34*** (a)) except for slightly increased peak heights. Thus, neither the increased age of the electrodeposited films at the time of sensitization (21 – 22 months compared to 3 months, cf. ***Figure 34***), resulting from separated experimental periods, nor the use of a different D149 synthesis batch had a significant effect on the amount of D149 loaded into the ZnO films in the absence of CA. The D149/CA samples prepared at University of Gießen (solid lines in ***Figure 34*** (b)), on the other hand, presented clearly smaller absorption peaks than the D149/CA samples prepared in Gifu. This may, at least in part, be related to the fact that the sensitization and optical characterization were performed in two different laboratories, i.e., under slightly different experimental conditions (cf. chapter 2.5). Moreover, the increased age of the samples might have led to a change of the ZnO surface (see below) that, in the competitive adsorption of D149 and CA, favored adsorption of CA over adsorption of D149. For electrodeposited ZnO films of similar age sensitized with D149 or D149/CA in Gießen (red and pink curves), quite comparable absorbance curves were found, again confirming reproducibility at a given laboratory.

The trend of the short-circuit photocurrent densities $J_{sc}$ and open-circuit photovoltages $V_{oc}$ in the current-voltage characteristics (***Figure 35***) of the solar cells built from the D149-sensitized ZnO films was approximately in line with the trend of their dye loading: the cells with D149/CA of chapter 5 showed reproducible $J_{sc}$ and $V_{oc}$, which were larger than those of the cell with D149/CA based on nanoparticulate ZnO (chapter 7). The smallest $J_{sc}$ and $V_{oc}$ were found for the sample with D149/CA of chapter 6. For the cells with D149 (without CA) based on electrodeposited ZnO, $J_{sc}$ and $V_{oc}$ also decreased between the cells of chapter 5 (again all showing similar curves) and those of chapter 6, even though the dye loading was slightly larger in the latter. This indicates a reduced efficiency of electron injection from D149 to ZnO (cf. chapter 6.5), which was probably the result of chemical changes of the ZnO surface under the influence of atmospheric oxygen and water during the longer storage times of the ZnO films prior to dye adsorption (which, however, did not negatively affect the dye's ability to adsorb to the surface in the absence of CA).

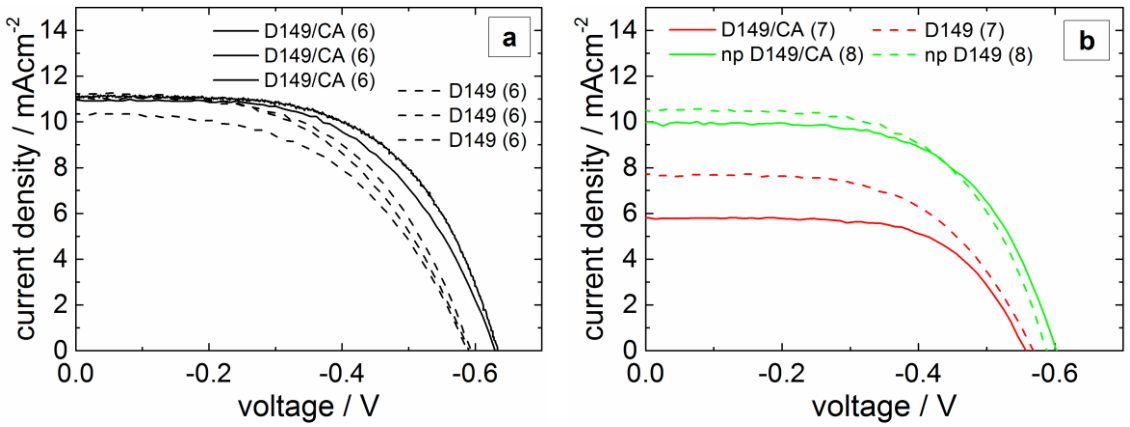


***Figure 35**: Current-voltage characteristics of the DSCs based on D149- or D149/CA-sensitized ZnO of different chapters, as indicated by the numbers in parentheses. No cells were built from the two additional films produced for comparison in chapter 5 (pink curves in the previous figure).*

In a Master's project performed within the group in 2013, a 90% decay of power conversion efficiency was found for DSCs based on D149/CA-sensitized ZnO in cases in which the ZnO films had been stored in water for 100 – 120 days prior to their use.[280] Storage under air of the present films may have caused a similar type of degradation, albeit less pronounced given the smaller changes in the cell performance. The time-dependent development of the properties of fully assembled DSCs will be addressed in depth in chapter 9.

Since the D149 or D149/CA cells all contained the same sensitizer or sensitizer/coadsorbate combination, variations in the recombination behavior among these samples should primarily be determined by differences in their trap distributions (cf. section 1.2.3, eq. (19)), see ***Figure 36***. The D149 and D149/CA cells based on electrodeposited ZnO of chapter 6 and a D149/CA cell prepared from a 19 months old electrodeposited ZnO film with longer adsorption time (chapter 8) all showed comparable trap distributions. A slightly reduced density of states at a given Fermi level was observed for the D149 cells of chapter 5 and a clearly steeper trap distribution featuring a significantly reduced density of states at higher energies was found for the D149/CA cells of chapter 5. The good reproducibility within the groups of D149 or D149/CA of chapter 5 was again confirmed.

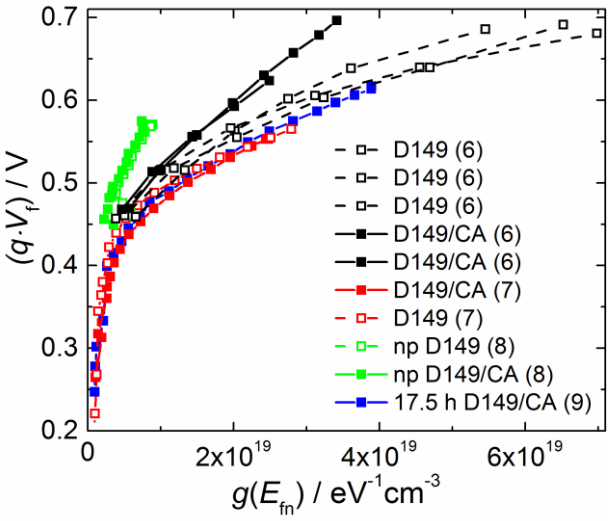


***Figure 36**: Density of states $g(E_{fn})$ within the ZnO band gap as a function of the quasi-Fermi energy ($E_{fn} = qV_f$) for cells with D149 or D149/CA of different chapters, as indicated in parentheses. $g(E_{fn})$ was calculated from the chemical capacitance measured by impedance spectroscopy (eq. (45)).*

The difference between the trap distributions of the electrodeposited cells with D149 or D149/CA of chapter 5 could have been an effect of the coadsorbate cholic acid (cf. chapter 5) that was not reproduced in later experiments as a result of the different batch of D149 used. It is conceivable that batch B of the indoline dye contained impurities that coadsorbed to ZnO and had a similar effect on the trap distribution as CA, thus masking the effect of the additional presence of CA on the trap distribution in D149/CA cells with respect to D149 cells. On the other hand, the trap distribution in the electrodeposited ZnO films may also be influenced by the age of the film, so that the increase of $g(E_{fn})$ from the D149/CA cells of chapter 5 to the D149 cells of chapter 5 to the samples of chapters 6 and 8 may reflect an increase of the density of traps with increasing film age from less than 2 weeks to 3 months to > 19 months. The D149 and D149/CA cells fabricated from nanoparticulate ZnO show clearly different trap distributions compared to the electrodeposited cells, suggesting that the properties of these cells should be discussed separately from those of the electrodeposited cells, see chapter 7.

# 5 Influence of D149 and Cholic Acid Molecules on Photovoltaic Performance and Recombination in Dye-Sensitized Solar Cells Based on Electrodeposited ZnO[III]

## 5.1 Optical Properties of the ZnO/D149 Photoelectrodes

The indoline dye D149 was adsorbed to electrodeposited porous ZnO films for 1, 2, 10 or 120 min with or without the coadsorbate cholic acid in the dye solution. The UV/Vis absorption spectra of the resulting ZnO/dye and ZnO/dye/coadsorbate films, all exhibit a main absorption band in the same wavelength range as the solution spectrum, i.e., around 500 – 550 nm (***Figure 37***).

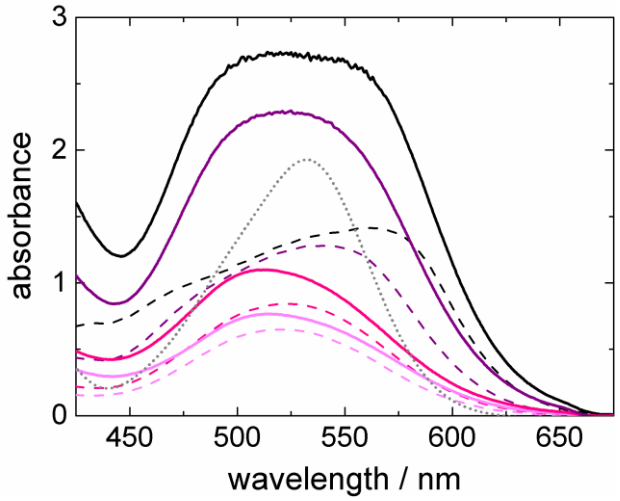


***Figure 37****: UV/Vis absorption spectra of D149-sensitized ZnO films with (Gifu, ——) or without (Gießen, ----) coadsorbate, and of D149 in DMF solution (····). The dye adsorption time for the films was 1 (light magenta), 2 (pink), 10 (purple) or 120 (black) min. Each film spectrum is the average of spectra of 3 identically prepared samples. Reprinted from ref.* [278]*, Copyright 2013, with permission from Elsevier.*

[III] Most of the original work presented in this chapter has been published in *J. Electroanal. Chem.* 709 (**2013**), 10-18.

However, the film spectra are significantly broader and in some cases show a different shape. These observations are the result of dye-dye interaction (aggregation) and/or differences in the dielectric environment of the dye caused by adsorption to ZnO. The strongest deviations from the solution spectrum are found for long adsorption times (10 min, 120 min) in the absence of cholic acid (purple and black, dashed lines). The corresponding spectra show strongly asymmetric absorption bands with a red-shifted maximum with respect to the solution spectrum. This kind of peak shape has previously been observed in UV/Vis absorption spectra of the indoline dye D102 adsorbed on $TiO_2$ and has been suggested to indicate the presence of J-aggregates.[52, 240, 281] In this type of aggregates, the molecules, which are generally expected to lie almost flat with respect to the semiconductor surface,[281] are arranged head-to-tail, with the head roughly corresponding to the carboxylic acid anchoring group and the tail corresponding to the 4-(2,2-diphenylethenyl)phenyl group.[281] However, it should be noted that in the present spectra, there is not only an increase in electronic transitions with lower energies (higher wavelengths), but a part of the oscillator strength is also transferred to a blue-shifted transition. This is even more apparent in the spectra of the films with cholic acid (all adsorption times) or without cholic acid and shorter adsorption times (1 min, 2 min). Here, the maximum of the absorption band is shifted to slightly shorter wavelengths compared to the peak of the solution spectrum, as observed before for D149-sensitized ZnO.[282] Blue-shifted absorption bands of dyes can indicate the presence of H-aggregates, in which the molecules are arranged face-to-face, i.e., with their molecular planes on top of each other.[240, 281, 283] On the other hand, the observed blue shift may also be the consequence of the difference in dielectric environment between the dyes in solution and adsorbed to ZnO.[284] Hence, the optical measurements of the present films only tentatively suggest the presence of H-aggregates under all conditions, but deliver stronger evidence of (additional) formation of J-aggregates at high adsorption times in the absence of CA. When comparing the spectra of films prepared with adsorption times of 10 min or 120 min with or without cholic acid, it can be clearly seen that the use of the coadsorbate removes the asymmetry and red-shift of the main absorption band. Thus, the presence of cholic acid at least partially suppressed aggregation of D149, even though in the present group of samples the dye loading in films with cholic acid was higher than in films without CA (see discussion further below). While the aggregation-

preventing influence of cholic acid or cholic acid derivatives has already been suggested in previous studies on the basis of efficiency improvements,[137, 202, 219] the present results deliver the first clear confirmation of this effect by optical absorption measurements.

Assuming that the absorption of light by the D149 -sensitized films can be described by the Beer-Lambert law (eq. (24)), the spectra can be used to assess the concentration of dye molecules in the films. The presence of dye aggregates with excitation energies different from that of monomeric D149, particularly in films with long adsorption times, indicates that the integrated absorbance (eq. (28)) rather than the peak value of the absorbance should be used as a measure for the total dye concentration in the samples investigated here:

$$\begin{aligned} abs_{\mathrm{int}} &= \int_{425nm}^{700nm} \mathrm{abs}\, d\lambda = \int_{425nm}^{700nm} \left(\mathrm{abs}_{\mathrm{M}} + \mathrm{abs}_{\mathrm{A1}} + \mathrm{abs}_{\mathrm{A1}} + \ldots\right) d\lambda = d \cdot \int_{425nm}^{700nm} \left(\varepsilon_{\mathrm{M}} c_{\mathrm{M}} + \varepsilon_{\mathrm{A1}} c_{\mathrm{A1}} + \varepsilon_{\mathrm{A2}} c_{\mathrm{A2}} + \ldots\right) d\lambda \\ &= d \cdot \left( c_{\mathrm{M}} \cdot \int_{425nm}^{700nm} \varepsilon_{\mathrm{M}} d\lambda + c_{\mathrm{A1}} \cdot \int_{425nm}^{700nm} \varepsilon_{\mathrm{A1}} d\lambda + c_{\mathrm{A2}} \cdot \int_{425nm}^{700nm} \varepsilon_{\mathrm{A2}} d\lambda + \ldots \right) \end{aligned} \tag{73}$$

where the integral was chosen to extend over the width of the main absorption band (425 – 700 nm). In eq. (73), the overall measured absorbance is described as a superposition of contributions arising from dye monomers (M) and different types of dye aggregates (A1, A2, and possible further types), with every species exhibiting a different wavelength-dependence of the molar absorptivity ($\varepsilon_{\mathrm{M}}$, $\varepsilon_{\mathrm{A1}}$, $\varepsilon_{\mathrm{A2}}$, etc.). $c_{\mathrm{M}}$ is the concentration of dye molecules in monomeric form and $c_{\mathrm{A1}}$, $c_{\mathrm{A2}}$, etc. are the concentrations of molecules in aggregates. The integral of the molar absorptivity $\varepsilon$ over the wavelength is proportional to the oscillator strength of the transition and depends on the average transition wavelength.[285] Since aggregation in the present case only shifts the average transition wavelength by small amounts and since the total oscillator strength of the transition can be expected to be constant for a monomeric dye and a dye in an aggregate,[240] the three integrals in the last part of eq. (73) should be approximately equal. As a consequence, $abs_{\mathrm{int}}$ should be a suitable measure for the sum of the monomer concentration and the aggregate concentrations. To test the validity of this approach, two separate sets (not used for cell assembly) of D149-sensitized ZnO films with and without CA were prepared and characterized by solid-state UV/Vis absorption spectroscopy before the D149 was desorbed from the films using dimethylformamide and the optical absorption

of the obtained solutions was measured. The $abs_{int}$ determined from the solid-state spectra is plotted in ***Figure 38*** (left) against the dye loading in the films per projected surface area ($\Gamma_{dye}$) as determined from the maximum absorbance of the desorption solution spectra assuming a corresponding molar absorptivity of 72350 $M^{-1}cm^{-1}$.[31] For comparison, ***Figure 38*** (right) shows the relationship between the maximum absorbance of the solid-state spectra and $\Gamma_{dye}$. Both $abs_{int}$ and $abs_{max}$ (films) show approximately linear dependence on $\Gamma_{dye}$. As expected, however, the correlation between $abs_{int}$ and $\Gamma_{dye}$ is more significant than the one between the maximum absorbance of the solid-state spectra and $\Gamma_{dye}$ (adjusted $R^2$ of 0.952 compared to 0.900). This confirms that $abs_{int}$ is a better measure for the amount of D149 in the films than $abs_{max}$, for all adsorption times and in the presence or absence of cholic acid.

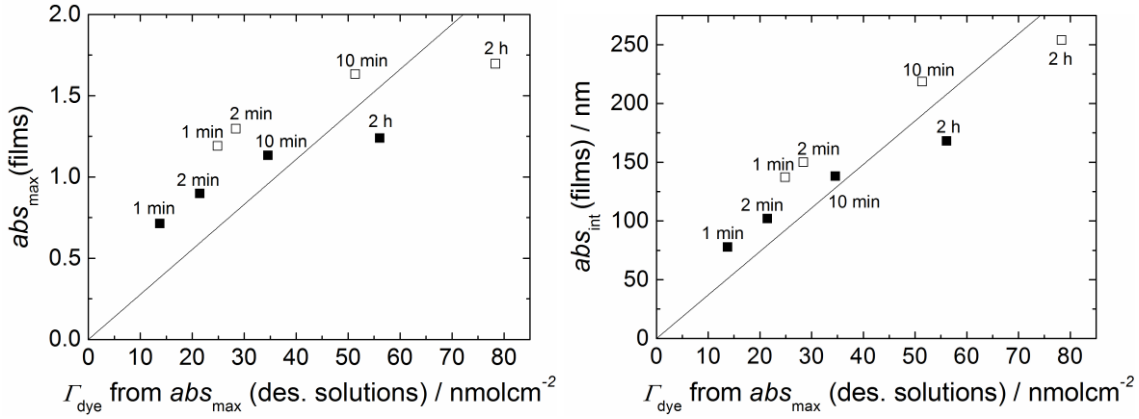


***Figure 38****: Maximum absorbance $abs_{max}$ (left) and integrated absorbance $abs_{int}$ (right) from solid-state UV/Vis absorption spectra of ZnO films sensitized with D149 for different adsorption times (see labels) in the presence (filled symbols) or absence (empty symbols) of cholic acid. The values are plotted against the dye loading in the films. The lines are linear fits to the data with fixed intercept at (0|0).*

The integrated absorbance values determined from the spectra in ***Figure 37*** are given in ***Table 8***. Upon increasing the adsorption time from 1 min to 120 min, $abs_{int}$ and hence the amount of D149 in the ZnO films increased by a factor of approximately 4.5 (with cholic acid) or by a factor of about 3 (without cholic acid), respectively. More D149 was adsorbed to ZnO in experiments with coadsorbate than in those without coadsorbate at equal adsorption times. This is clearly an unexpected result, as cholic acid reduces the

number of adsorption sites available for D149 and, accordingly, was found to decrease the amount of adsorbed dye in previous studies.[31, 137, 149, 219] What must be kept in mind, though, is that the two series of adsorptions were performed in two different laboratories, at Gifu University (Japan) and at Justus Liebig University Gießen (Germany). Although greatest care was taken to perform the experiments identically, it cannot be entirely ruled out that subtle, unmonitored details affected the procedure in a way that higher dye loadings were obtained in Gießen (samples without cholic acid) compared to the films prepared in Gifu. Regarding the two sets of comparison samples fabricated entirely at Justus Liebig University Gießen, the amount of D149 in films sensitized in the presence of CA was smaller than in films sensitized without coadsorbate for any given adsorption time (***Figure 38***), as expected and reported earlier.

| | $t_{ads}$ / min | $abs_{int}$ (+/- 16) / nm |
|---|---|---|
| **with CA (Gifu)** | 1 | 92 |
| | 2 | 124 |
| | 10 | 303 |
| | 120 | 396 |
| **without CA (Gießen)** | 1 | 97 |
| | 2 | 108 |
| | 10 | 197 |
| | 120 | 258 |

***Table 8**: Integrated absorbance $abs_{int}$ - serving as a measure for the amount of D149 in samples - determined from the absorption spectra of dye-sensitized ZnO films prepared with various adsorption times $t_{ads}$ (cf. **Figure 37**). Each value presents an average over the integrated absorbance of the spectra of three identically prepared films and the largest observed deviation of individual values from the average is given as an estimated error.*

## 5.2 Photovoltaic Performance of ZnO/D149 Solar Cells

The measured external and calculated (eq. (56) and eq. (57)) internal current-voltage curves of the DSCs built from the different D149-sensitized ZnO films (***Figure 39***)

show a systematic increase of $J_{sc}$ and $V_{oc}$ with the adsorption time as a result of the increase in dye loading (***Figure 37***) and the concomitant increase in the rate of electron injection according to eq. (4).

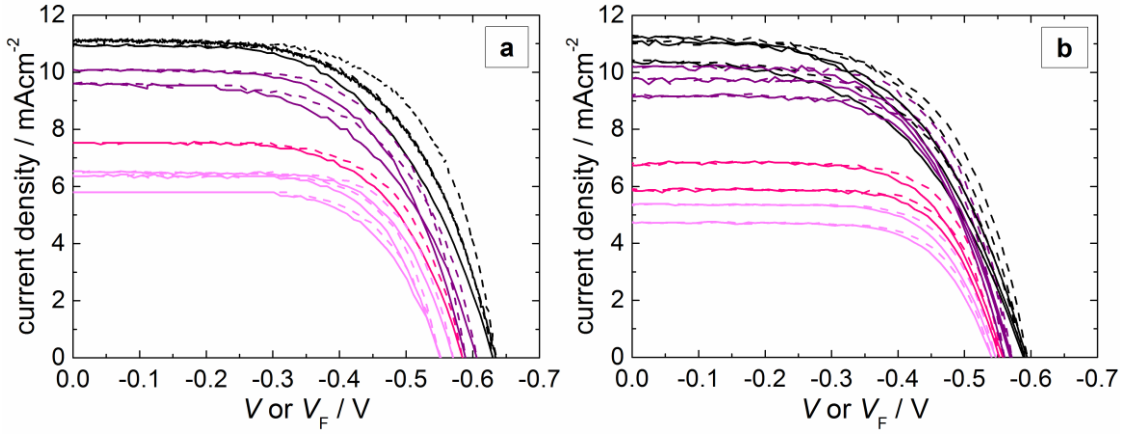


***Figure 39***: *Measured external (——; current density vs. applied voltage V) and internal (- - - -; current density vs. series resistance-corrected Fermi-level voltage $V_f$) current-voltage characteristics for ZnO/D149 solar cells with (a) or without (b) coadsorbate. D149 was adsorbed for 1 (light magenta), 2 (pink), 10 (purple) or 120 min. Adapted from ref.* [278]*, Copyright 2013, with permission from Elsevier.*

For the sets of samples analyzed here, the maximum $J_{sc}$ attained for an adsorption time of 120 minutes shows a value of around 11 mA cm$^{-2}$ independent of the presence or absence of cholic acid. For the open-circuit photovoltage, on the other hand, higher maximum values of -0.63 V were achieved for the cells with cholic acid, as compared to -0.59 V without CA. Knowing that the dependence of the dye loading on the adsorption time differs for the cells with and without CA, a further discussion of the photovoltaic parameters should focus on their dependence on the integrated absorbance rather than on the adsorption time. A representation of $V_{oc}$, $J_{sc}$, fill factor $FF$ and power conversion efficiency $\eta$ as a function of $abs_{int}$ (as a measure of the dye loading), ***Figure 40***, reveals that the use of cholic acid in the presently discussed cells led to a weaker increase of $J_{sc}$ with the dye loading for cells with CA compared to those without coadsorbate. This may indicate (cf. eq. (36) and eq. (40)) a decrease in the electron injection efficiency.

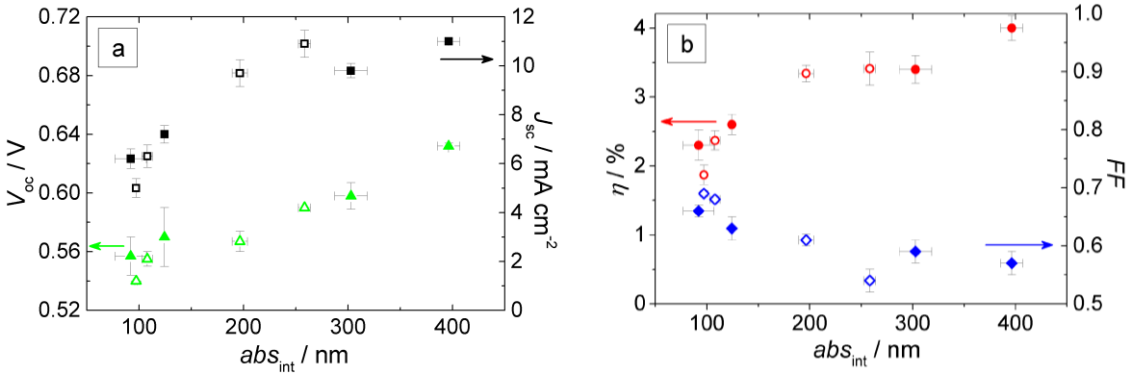


***Figure 40**: Dependence of open-circuit voltage (a; ▲,Δ), short-circuit current density (a; ■,□), power conversion efficiency (b; ●,○) and fill factor (b; ♦,◊) of the ZnO/D149 solar cells on the integrated absorbance. Filled and open symbols represent cells with and without cholic acid, respectively. The data points shown were obtained by averaging results of one to three cells per condition and error bars are largest deviations of individual values from the average. Reprinted from ref. [278], Copyright 2013, with permission from Elsevier.*

In spite of causing a lower rate of charge injection towards higher dye loadings, the coadsorbate did not affect the $V_{oc}$ at a given $abs_{int}$. This may be explained by an adsorption time-dependent upward shift of the conduction band or reduction of the exchange current density $J_{0k}$ for recombination in cells with CA (eq. (34)). As reported before,[137] the fill factor decreases with increasing dye loading, indicating that larger amounts of D149 molecules on the ZnO surface promote recombination in the intermediate voltage range (at $V \approx V_{mpp}$). The decay of *FF* with $abs_{int}$ appears steeper for cells without cholic acid compared to cells without CA, leading to a significantly smaller value already at relatively low dye loadings. The presence of the coadsorbate, on the other hand, keeps the *FF* at a comparatively large value even for higher dye loadings. A closer examination of the origins of the observed trends of $J_{sc}$, $V_{oc}$, and *FF* will follow in the discussion of the electrochemical impedance spectroscopy measurements below. The increase of the overall efficiency with the dye loading shows that the decay of *FF* is overcompensated by the observed increase in $J_{sc}$ and $V_{oc}$. However, in cells without cholic acid $\eta$ shows a saturation at intermediate dye loadings, while there is a monotonous increase up to the highest dye loadings for cells with CA, underlining the overall benefit of using cholic

acid as a coadsorbate. The maximum values achieved are ~3.5% without CA and ~4% with CA.

## 5.3 Impedance Spectroscopic Analysis

### 5.3.1 Distribution of Trap States

The capacitances derived from impedance spectroscopy measurements (cf. sample spectra in ***Figure 104***) increased exponentially towards more negative Fermi-level voltages (***Figure 41***). This shows that the measured capacitance was dominated by the chemical capacitance $C_\mu$ rather than by a depletion capacitance (cf. section 1.4.4) and is in line with the typical observation for dye-sensitized nanostructured semiconductors.

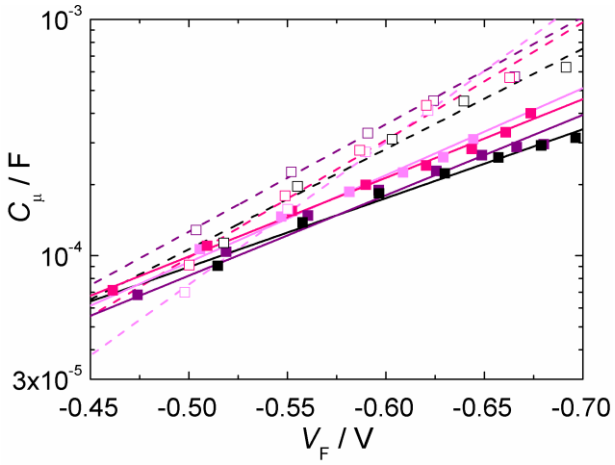


***Figure 41****: Chemical capacitance of ZnO/D149 solar cells with (filled symbols, solid lines) and without (open symbols, dashed lines) the coadsorbate cholic acid, fabricated with D149 adsorption times of 1 (light magenta), 2 (pink), 10 (purple) or 120 (black) minutes as a function of the Fermi-level voltage (data representative of results observed for one to three samples per condition). The lines are linear fits in the semilogarithmic representation. Reprinted from ref.* [278]*, Copyright 2013, with permission from Elsevier.*

Linear fits of the data to eq. (52) yielded values of the trap-distribution parameter $\alpha$ between 0.17 and 0.38 (***Table 9***), which is higher than the trap distribution parameters commonly observed for DSCs based on nanoparticulate ZnO films (0.10 – 0.13).[136, 141, 251] Thus, the trap distribution in electrodeposited nanostructured ZnO films was less

steep, which has also been suggested in a previous report[136] and will be confirmed for a separate set of samples in chapter 7. Comparing the solar cells with (prepared at Gifu University) and without (prepared at University of Gießen) cholic acid, the former exhibited a smaller $\alpha$ value than the latter.

***Table 9:*** *Trap distribution parameters α and relative conduction band edge shifts $\Delta E_c/q$ for the different ZnO/D149 solar cells (positive $\Delta E_c/q$ correspond to downward shifts, negative values correspond to upward shifts). Values represent averages obtained from one to three identically prepared samples, with the maximum difference between individual values and average given as an error estimate.*

| | $t_{ads}$ / min | $\alpha$ (+/- 0.06) | $\Delta E_c/q$ (+/- 15) / mV |
|---|---|---|---|
| **with CA (Gifu)** | 1 | 0.24 | - 11 |
| | 2 | 0.18 | 0 (ref.) |
| | 10 | 0.17 | - 24 |
| | 120 | 0.18 | - 17 |
| **without CA (Gießen)** | 1 | 0.37 | + 33 |
| | 2 | 0.36 | + 37 |
| | 10 | 0.33 | + 40 |
| | 120 | 0.27 | + 34 |

As directly apparent from the plot of the density of states $g(qV_f) = g(E_{fn})$ (calculated from $C_\mu$ according to eq. (44)) in ***Figure 42***, this means that the trap distribution in the cells with D149/CA (Gifu) was higher than in the D149 samples prepared in Gießen. As a result, in the energy range $qV_f > 0.55$ eV the density of states in the former was generally reduced by about 50% compared to the latter. The steeper trap distribution in the cells prepared in Gifu was either related to the presence of cholic acid molecules, which could have reduced the density of certain surface traps by binding to coordinatively unsaturated surface sites, or it was the result of the fact that the ZnO films were aged for a shorter time than the ones used in Gießen (cf. chapter 4, ***Figure 36***). Increasing the adsorption time in samples with CA from 1 minute to 120 minutes caused a small additional decrease of $g(E_{fn})$, indicating that the effect was at least in part caused by coad-

sorption of CA (and thus became stronger when the amount of CA was increased by increase of the adsorption time).

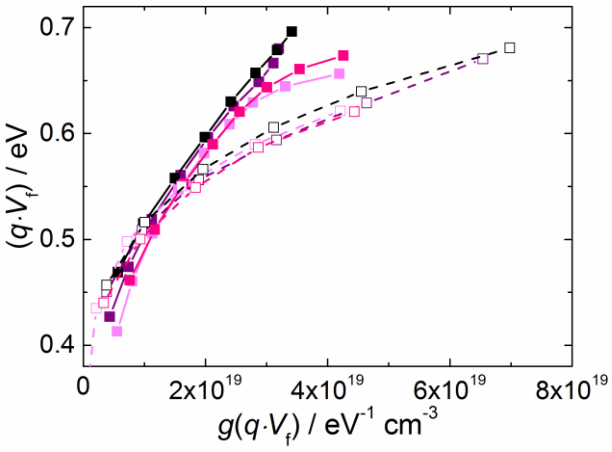


***Figure 42**: Density of states of ZnO/D149 cells (color and symbol code as in previous figures). Reprinted from ref. [278], Copyright 2013, with permission from Elsevier.*

In cells without cholic acid, on the other hand, no significant influence of the soaking time can be noticed, suggesting that the density of states is largely independent of the amount of D149. While the nature of surface states in dye-sensitized solar cells is still subject of investigations, it is known that anchoring molecules to semiconductor surfaces can entail a reduction of the density of surface traps or a change of their energetic distribution compared to bare surfaces (cf. chapter 1.1.2).[68-70, 90] For instance, a dipole-induced shift has been observed upon adsorption of dyes with carboxylic acid functions to $TiO_2$.[70] Cholic acid does have a carboxylic acid group that acts as anchoring group for adsorption to the semiconductor surface. Thus, its possible influence on the density of states could have been caused by a dipole effect. On the other hand, D149 possesses a carboxylic acid function as well, but did not show any notable effect on $g(E_{fn})$. This may indicate that the dipole moment associated with the carboxylic acid group of D149 did not have a strong effect on the ZnO energy levels, which likely resulted from a relatively weak interaction between D149 and ZnO, as reported in earlier studies on indoline dye-sensitized ZnO.[286]

The fact that in the presently discussed experimental series the trap distribution parameter $\alpha$ varied between cells fabricated with different parameters precludes a reliable and exact determination of relative shifts of the conduction band edge $\Delta E_c/q$ according to

the procedure illustrated in ***Figure 16*** (chapter 1.4.4). Nevertheless, approximate values were obtained to enable a discussion of a range of possible conduction band edge shifts (***Table 9***). ***Figure 43*** demonstrates the approximate alignment across a limited voltage range resulting from shifts of the curves by these estimated $\Delta E_c/q$ values.

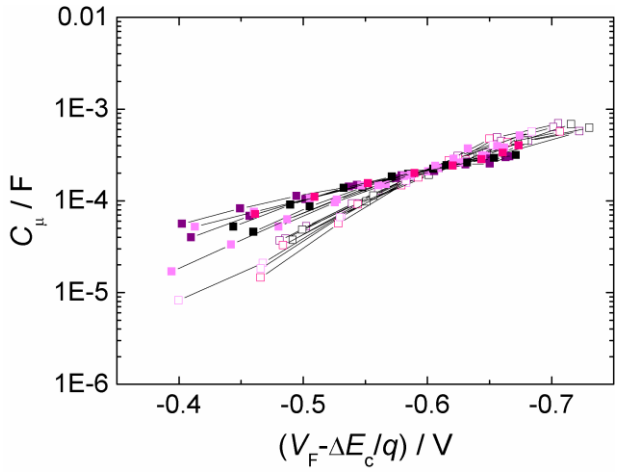


***Figure 43****: Chemical capacitance curves of the D149-sensitized ZnO solar cells shifted along the voltage axis by* $\Delta E_c/q$ *(**Table 9**), resulting in approximate alignment in the voltage range -0.55 V to -0.7 V. Due to the different slopes of the curves, no complete alignment could be achieved and the shifts* $\Delta E_c/q$ *merely represent rough estimations of the relative conduction band edge shifts. Reprinted from ref.* [278]*, Copyright 2013, with permission from Elsevier.*

A possible upward shift of the conduction band edge by about 40 – 60 mV is indicated in the cells containing CA with respect to the cells without coadsorbate (***Table 9***), with a tendency of higher shifts for the cells prepared with longer adsorption times (10 min, 120 min). A similar trend is suggested by the $V_f$ *vs.* $g(E_{fn})$ plots in ***Figure 42***, which approach different saturation voltages. Accounting for the estimated error of +/- 15 mV, the approximation obtained here would be roughly comparable to the upward shift of the conduction band edge by 80 mV previously observed for $TiO_2$-based DSCs with Ru(II) sensitizers upon coadsorption of chenodeoxycholic acid, a derivative of CA.[149] An upward shift of the conduction band edge in the cells with CA, in particular at high dye loadings, thus may have contributed (via eq. (34)) to the fact that the $V_{oc}$ at a given dye loading was constant in the presence or absence of CA in spite of the lower rates of charge injection in the cells with coadsorbate (chapter 5.2). Since an upward shift of the

conduction band edge can cause a reduction in the electron injection efficiency (cf. section 1.1.2), these results may also deliver an explanation for the decreased slope of the short-circuit current density in cells with CA (cf. ***Figure 40***).

### 5.3.2 Recombination

The EIS-based recombination resistance $R_{rec}$ of the ZnO/D149 solar cells shows an exponential decrease as $V_f$ becomes more negative, ***Figure 44*** (a), as expected for nanostructured semiconductors based on eq. (53).

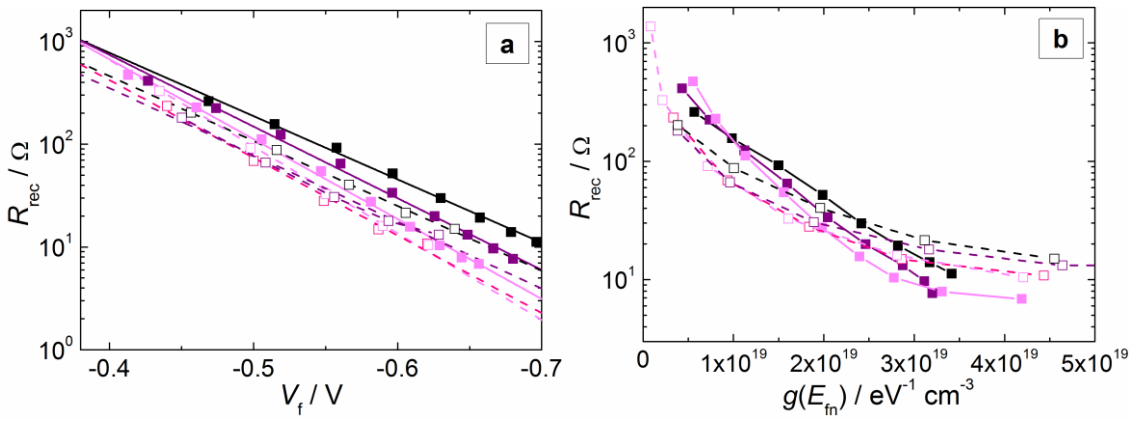


***Figure 44****: Recombination resistance of D149-sensitized solar cells with (solid symbols) or without (open symbols) cholic acid. (a) $R_{rec}$ as a function of the Fermi-level voltage $V_f$, together with linear fits; (b) $R_{rec}$ vs. the density of states $g(E_{fn})$ (lines are a guide to the eye only). Increasing color depth represents increasing adsorption time as in the figures above. Reprinted from ref. [278], Copyright 2013, with permission from Elsevier.*

As explained in detail in section 1.4.4, the recombination resistance at a given voltage of a set of samples under comparison can only be used as a measure of the probability of interfacial recombination events if the samples exhibit the same conduction band edge position $E_c$ and the same recombination parameter $\beta$ (see below), or if they show the same $\beta$ and are plotted against $V_f$-$\Delta E_c/q$, cf. eq. (54). The physical origin behind this approach is that, at a given Fermi-level voltage, samples with different $E_c$ and $\beta$ would show different relative occupancies of trap and conduction band states, which has an effect on the total rate of recombination and would mask possible differences of $R_{rec}$ caused solely by differences in the interfacial rate constant of recombination. In the pre-

sent case, the analysis of $R_{rec}$ is complicated by two factors: (1) a reliable determination of $\Delta E_c/q$ was precluded due to the variations in the trap distribution between differently fabricated cells; (2) the slope of the $R_{rec}$ vs. $V_f$ curves (and, hence, $\beta$) is not constant either (***Figure 44*** (a)). Some previous studies have intended to avoid such complications by plotting the effective electron lifetime $\tau_n$ of cells with different trap distributions as a function of the total density of states $g(E_{fn})$ or the total electron density $n$ instead of analyzing $R_{rec}$ as a function of $V_f$-$\Delta E_c/q$.[57, 136] To formally confirm the validity of this approach, the dependence of $\tau_n$ on density of states and electron density according to the multiple-trapping model (cf. eq. (47), (18), (9) and (10) as well as ref. [90]) is considered:

$$\tau_n = R_{rec} C_\mu \approx \left( \frac{\partial n_t}{\partial n_c} \right) \cdot \tau_f = \frac{g^t(E_{fn})}{g^{cb}(E_{fn})} \cdot \left( k_r^{cb} + k_r^{ss} \right)^{-1} = \frac{\alpha n_t}{n_c} \cdot \left( k_r^{cb} + k_r^{ss} \right)^{-1} \quad (74)$$

where $n_t$ and $n_c$ are the density of trapped and conduction band electrons, $\tau_f$ is the free-electron lifetime describing recombination without the influence of bulk trapping but including the influence of surface state-mediated recombination, $g^t(E_{fn})$ and $g^{cb}(E_{fn})$ are the densities of states of trapped and conduction band electrons (assumed to be exponential to obtain the last part of the equation), and $k_r^{cb}$ and $k_r^{ss}$ are the rate constants for recombination from the conduction band or from surface states. In combination with eq. (1), eq. (74) shows that a plot of $\tau_n$ *vs*. $g(E_{fn}) \approx g^t(E_{fn})$ or $R_{rec}$ *vs*. $g(E_{fn}) \approx g^t(E_{fn})$ (cf. eq. (45)) will only adequately reveal sample-to-sample differences in the interfacial rate constants for recombination if $g^{cb}(E_{fn})$, determined by the effective density of states at the conduction band edge $N_c$, is constant in the samples under comparison. $N_c$ depends on the effective electron mass in the conduction band and is a (temperature-dependent) material constant.[63] As the present experiments all used the same ZnO structures with the only difference being different surface modifications, it is expected that $g^{cb}(E_{fn})$ was equal for the series of cells studied here and, hence, $R_{rec}$ is plotted as a function of the measured density of states in ***Figure 44*** (b).[IV] In the range of $g(E_{fn}) \geq 1.5 \cdot 10^{-19}$ $eV^{-1}cm^{-3}$, the recombination resistance increases with increasing adsorption time (i.e., dye loading) for both groups of cells, with and without coadsorbate. Comparison with ***Figure 40*** and ***Figure 42*** shows that this range of the density of states includes the $g(E_{fn})$ observed

under open-circuit conditions. Based on the above considerations, the increase in $R_{rec}$ reflects a decrease of either or both of the rate constants for recombination from conduction band states or surface states, which should be related to the increased average spacing between semiconductor and electrolyte in the presence of the adsorbed dye entailing a reduced electronic coupling between the two phases (cf. eq. (17)). With the conduction band edge position being largely independent of the adsorption time (***Table 9***), the slower recombination kinetics at higher $g(E_{fn})$ by increase of the dye loading delivers a partial explanation of the increase of $V_{oc}$ with the dye loading (cf. ***Figure 40***), while the remaining increase resulted from the increase in $J_{sc}$ (eq. (34)). Moving towards smaller densities of states in the range $g(E_{fn}) < 1.5 \cdot 10^{-19}$ $eV^{-1}cm^{-3}$ (corresponding to voltages less negative than $V_{oc}$), the improvement of the recombination resistance with the dye loading at a given $g(E_{fn})$ becomes notably weaker until the trend is even reversed for $g(E_{fn}) \approx 0.5 \cdot 10^{-19}$ $eV^{-1}cm^{-3}$. At these lowest levels of the quasi-Fermi level, $R_{rec}$ tends to be smaller in samples prepared with longer adsorption times than in those with shorter adsorption times. The observed inversion is connected to a variation of the slope of the recombination resistance curves with the dye loading (***Figure 44*** (a)), which will be discussed in the following section. By comparing the $R_{rec}$ of cells prepared with a given adsorption time with and without coadsorbate, it can be seen that for $g(E_{fn}) \geq 2.5 \cdot 10^{-19}$ $eV^{-1}cm^{-3}$ recombination is stronger in samples with CA than in those without CA. Taking into account that, in the present set of samples, the dye loading in cells with coadsorbate was higher than in those without CA (***Table 8***) and that a blocking effect of D149 on recombination in the range of high $g(E_{fn})$ was detected as discussed above, the difference between samples with and without coadsorbate is probably not related to the difference in the dye loadings. Rather, it indicates that CA may have a catalytic effect on recombination at high levels of $E_{fn}$. A comparable effect was seen upon coadsorption of chenodeoxycholic acid in DSCs based on Ru(II) dye-sensitized TiO.[149] Nevertheless, the present cells containing the coadsorbate showed comparable open-circuit voltages at a given dye loading as cells without CA (cf. ***Figure 40***). Thus, the higher open-circuit rate constant of recombination as well as the lower rate of charge injection for cells with

[IV] Note that the common procedure of plotting $\tau_n$ *vs.* $n \approx n_t$ is only valid for an evaluation of rate constants of recombination if samples with the same trap distribution parameter $\alpha$ are compared and therefore is not an option for the present samples.

larger dye loadings (***Figure 40***) in the samples with CA must both have been compensated by a gain in $V_{oc}$ resulting from the presumed upward shift of the conduction band edge of up to ~60 mV (***Table 8***). With decreasing density of states below $2.5 \cdot 10^{-19}$ $eV^{-1}cm^{-3}$, the $R_{rec}$ curves of the cells with CA intersect with the ones of samples without CA and, hence, the recombination resistance becomes higher in the cells with coadsorbate. This means that under conditions of low electron densities in the semiconductor the effect of cholic acid is to reduce recombination with respect to DSCs without CA, which is likely the consequence of the anti-aggregation effect of the coadsorbate, as will be discussed in more depth below.

### 5.3.3 Voltage-Dependence of the Recombination Resistance

The recombination parameters $\beta$ of the ZnO/D149-based DSCs, obtained from fits of the voltage-dependent recombination resistance (***Figure 44*** (a)) to eq. (53), showed values between 0.35 and 0.53 (***Figure 45***), which is slightly lower than the values of 0.45 to 0.64 previously reported for D149-sensitized ZnO.[136, 141].

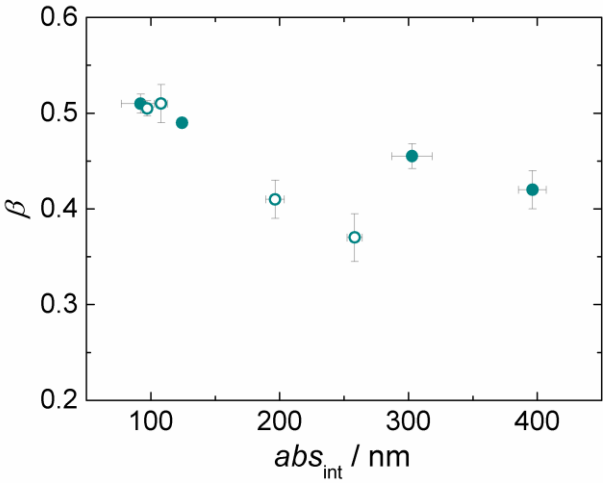


***Figure 45:*** *Dependence of the recombination parameter β on the integrated absorbance (representing the dye loading) of ZnO/D149 DSCs with (filled symbols) and without (open symbols) cholic acid (data points represent averages of one to three individual values per preparation condition). Reprinted from ref. [278], Copyright 2013, with permission from Elsevier.*

$\beta$ clearly decreased with increasing dye loading, with a significant difference in slope depending on the presence of the coadsorbate: Cells that did not contain CA exhibited a strong decrease of the recombination parameter by approximately 30% over the range of dye loadings studied, while in DSCs with cholic acid $\beta$ was only reduced by 10%, even though the maximum dye loading achieved in those cells was higher than in the series without CA. The fact that the flattening of the voltage-dependent $R_{rec}$ curves with increasing amount of D149 was less pronounced in the cells with cholic acid may indicate that the coadsorbate counteracted the dye-related increase of recombination at lower voltages (cf. ***Figure 44***).

The voltage dependence of the recombination resistance is generally determined by charge transfer from a distribution of surface states in the semiconductor. It has been derived that $\beta$ can be expressed as $\beta = 0.5+\alpha_{ss}$, where $\alpha_{ss}$ is the trap distribution parameter of surface states.[90] Based on this, a correlation between $\beta$ and the measured trap distribution parameter $\alpha$, which reflects an average of the trap distributions in the bulk and at the surface, was expected. However, the samples containing cholic acid showed generally *lower* values of $\alpha$ than their coadsorbate-free counterparts (***Table 9***), while $\beta$ at high dye loadings was *higher* with respect to cells without CA. Moreover, the amount of dye was not found to influence $\alpha$, whereas it had a considerable effect on $\beta$. Thus, in the cells investigated in this study, the voltage dependence of the recombination resistance did not seem to correlate with the energy distribution of electronic states in the dye-sensitized porous ZnO film. This suggests that it was rather the distribution of electrolyte acceptor states that controlled how the recombination rate changed with $E_{fn}$. The fact that the drop in $\beta$ and *FF* is less pronounced in the cells with cholic acid, in which D149 was less aggregated (***Figure 37***), suggests that the dye-related increase of the recombination rate at lower voltages is mainly caused by D149 *in aggregates*.

### 5.3.4 Origins of the Variations of the Fill Factor

The experimental external fill factor *FF* is generally influenced by the series resistance as well as by $V_{oc}$ and $\beta$ (cf. eq. (35)). Comparison of the internal fill factors $FF_{int,exp}$ (determined from the internal *J-V* curves in ***Figure 39***) with *FF* (***Table 10***) reveals that in the present set of samples the series resistance lowered the fill factor by up to 10%, as discussed in more detail below. Theoretical fill factors $FF_{int,calc}$ expected based on the

experimental $V_{oc}$ and $\beta$ values were calculated using the corresponding full expression of the $\beta$-recombination model (eq. (26) of ref. [128]), see ***Table 10***.

***Table 10****: Experimental internal and external fill factors, FF and $FF_{int,exp}$, as well as theoretical internal fill factors $FF_{int,calc}$ for ZnO/D149 solar cells with different dye loadings, represented by the integrated absorbance $abs_{int}$.*

| | $abs_{int}$ (+/- 16) / nm | *FF* | $FF_{int,exp}$ | $FF_{int,calc}$ |
|---|---|---|---|---|
| **with CA (Gifu)** | 92 | 0.66 | 0.69 | 0.71 |
| | 124 | 0.63 | 0.66 | 0.71 |
| | 303 | 0.59 | 0.63 | 0.70 |
| | 396 | 0.57 | 0.62 | 0.69 |
| **without CA (Gießen)** | 97 | 0.69 | 0.71 | 0.71 |
| | 108 | 0.68 | 0.71 | 0.71 |
| | 197 | 0.61 | 0.66 | 0.67 |
| | 258 | 0.54 | 0.59 | 0.65 |

For small D149 loadings, the calculated values $FF_{int,calc}$ are well in line with $FF_{int,exp}$. Furthermore, the experimentally observed weaker decay of the fill factor with the dye loading in cells containing CA is confirmed: a decay from 0.71 to 0.69 is calculated for the cells with CA, compared to a decrease from 0.71 to 0.65 for the samples without coadsorbate. Because the change of $V_{oc}$ with the dye loading was identical for cells with or without CA, this result shows that the decay of the fill factor with $abs_{int}$ was caused by the decay of $\beta$. For larger amounts of dye, the cells show smaller internal fill factors than expected according to the model. A possible reason for this may be that the rate of recombination in the model is approximated by an empirical expression including a constant (i.e., voltage-independent) recombination rate constant $k_r$ (cf. eq. (32)). However, in the present cells $k_r$ may have depended on the voltage, since there was evidence for additional recombination at lower voltages in the cells with high dye loadings. A more precise description should include an energy-dependent average rate constant of recombination rather than a constant one, as for example suggested by Wang et al..[86]

### 5.3.5 Series Resistance

The comparison of the internal and external fill factors given in ***Table 10*** revealed that the efficiency of the DSCs analyzed in this chapter was significantly limited by the series resistance $R_{series}$. In ***Figure 46***, the various contributions to $R_{series}$ are illustrated for a sample cell (adsorption time of 120 minutes, without CA) as a function of the d.c. cell current density flowing through the cell at different d.c. bias voltages.

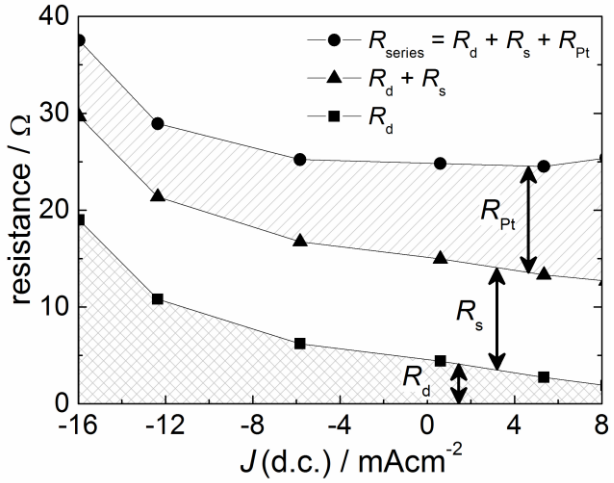


***Figure 46****: Graphs illustrating the different EIS-derived contributions to the series resistance of a sample ZnO/D149 solar cell. $R_d$: diffusion resistance of the electrolyte, $R_s$: resistance of the FTO-coated glass substrate, $R_{Pt}$: resistance of the Pt-coated counter electrode.*

In the current range relevant for solar cell operation (positive *J*), the resistances of the substrate and of the counter electrode ($R_s$ and $R_{Pt}$) presented the main contributions to the total series resistance. For negative *J*, on the other hand, the diffusion resistance $R_d$ of ions in the electrolyte became increasingly dominant. The constant distance between the curves showing $R_d$ and $R_d$+$R_s$ in ***Figure 46*** demonstrates that the resistance of the FTO-coated glass substrate was constant in the current range investigated. The diffusion resistance of the electrolyte, however, clearly increased towards negative *J*, while the counter electrode resistance tended to grow with increasing positive *J*.

Comparing the counter electrode resistance for all different preparation conditions studied in this chapter (***Figure 47***), there was a tendency of an increase of $R_{Pt}$ with the ad-

sorption time, which was particularly pronounced for cells without cholic acid. $R_{Pt}$ was clearly smaller in samples with coadsorbate compared to those without CA.

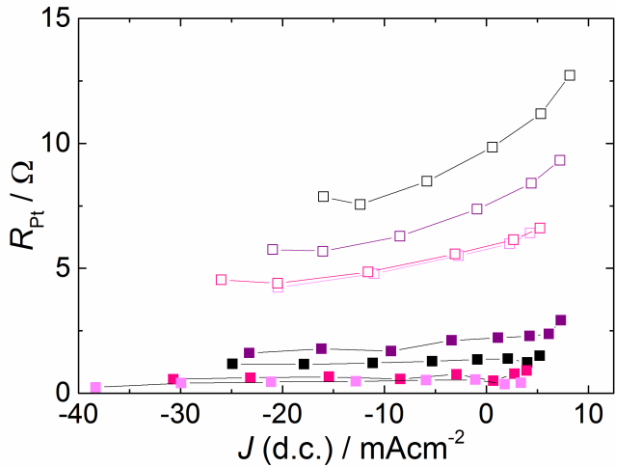


***Figure 47**: Charge-transfer resistance at the electrolyte/counter electrode interface vs. the d.c. cell current density for ZnO/D149 solar cells with (filled symbols) or without (open symbols) coadsorbate cholic acid. Curves belong to one solar cell each and are representative of the behavior of samples with identical adsorption conditions. Assignment of colors as in previous figures.*

The diffusion resistance of the electrolyte (***Figure 48***) exhibited a similar dependence on adsorption time and coadsorbate as $R_{Pt}$: increasing $t_{ads}$ tended to increase $R_d$ and samples with CA showed a somewhat lower diffusion resistance than those without coadsorbate. Since $R_{Pt}$ and $R_d$ reflect properties of the electrolyte and the electrolyte/counter electrode interface, their dependence on the adsorption time indicates that the D149 molecules partially desorbed from the ZnO surface and dissolved in the redox electrolyte when the DSCs were filled with the solution. This may have affected the transport of charges between counter electrode and dye-sensitized ZnO. Once dissolved in the electrolyte, it is likely that some of the dye molecules adsorbed onto the surface of the Pt/FTO counter electrode, hindering charge transfer between electrolyte and counter electrode.

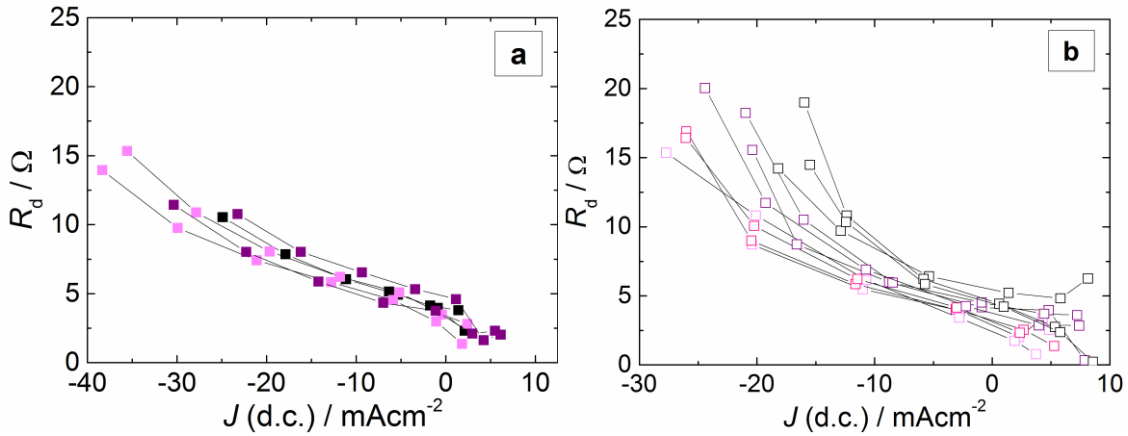


***Figure 48**: Diffusion resistance of the electrolyte (0.1 M $I_2$ and 1 M TPAI in 4:1 ethylene carbonate:acetonitrile) of ZnO/D149 solar cells with (a) or without (b) cholic acid, determined by fitting the impedance spectra.*

In a laboratory project performed by J. Schmidt under the supervision of the author,[287] the influence of D149 molecules intentionally added to an $I^-/I_3^-$ electrolyte (identical composition as used in this thesis) on charge transport through the electrolyte and charge transfer at the interface to Pt-coated FTO/glass were investigated. Current-voltage characterization and electrochemical impedance spectroscopy of symmetrical Pt/electrolyte/Pt cells showed that with increasing concentration of D149 (between 0 M and 5 mM) the diffusion coefficient of $I_3^-$ decreased by a factor of about 1.5, while the charge-transfer resistance of the Pt/electrolyte interface increased by a factor of almost 20. These results strongly support the hypothesis that the variations of $R_{Pt}$ and $R_d$ observed for cells with different dye loadings in the present work were caused by different amounts of dye that desorbed from the ZnO film and dissolved in the electrolyte. In the cells containing CA, D149 may have been more stably bound to the ZnO surface, so that less dye molecules were present in solution and at the counter electrode surface and $R_{Pt}$ was smaller than in cells without coadsorbate. Repeated *J-V* measurements of the present samples four weeks after preparation (see chapter 9.2) showed a significant decrease of the short-circuit photocurrent in the cells without CA, while those with coadsorbate in fact exhibited an increase of $J_{sc}$, supporting the suggestion that the stability of the D149 attachment may have been lower in the cells without coadsorbate. As larger amounts of dye aggregates were present in the samples without CA, a weaker attach-

ment to ZnO of D149 molecules in aggregates compared to monomeric D149 molecules could be the reason for the observed differences.

## 5.4 Summary and Conclusions for This Chapter

In this chapter, an in-depth analysis of the influence of dye loading and coadsorption of cholic acid in dye-sensitized solar cells based on D149-sensitized electrodeposited ZnO was presented. By varying the dipping time of ZnO films in D149 solution with or without cholic acid (CA) between 1 minute and 120 minutes, ZnO/D149 films with varied amounts of D149 were attained, as demonstrated by UV/Vis absorption spectroscopy. The optical measurements further indicated aggregation of D149 molecules on the surface of the ZnO, which was particularly pronounced for samples prepared with longer adsorption times of 10 – 120 minutes in the absence of CA.

In DSCs fabricated from ZnO/D149 electrodes without cholic acid, the increase of the dye loading caused an improvement of the short-circuit photocurrent, open-circuit photovoltage and overall conversion efficiency. However, a concomitant deterioration of the fill factor notably limited the increase of the efficiency. Analysis by electrochemical impedance spectroscopy showed that the decay of the fill factor upon increasing the adsorption time was caused by two separate effects: an increase in the series resistance and a decrease of the recombination resistance at lower quasi-Fermi levels. The growth of the series resistance with the adsorption time was found to originate in an increase in the diffusion resistance of the electrolyte as well as the charge-transfer resistance at the electrolyte/counter electrode interface, indicating that D149 molecules detached from the ZnO surface and were present in electrolyte and at the Pt counter electrode surface, hindering charge transport and transfer in these parts of the cells. The decrease of the recombination resistance $R_{rec}$ at lower voltages was reflected in a decay in the recombination parameter $\beta$ with the dye loading. For open-circuit conditions, on the other hand, increasing the amount of D149 had a blocking effect on recombination, as seen in an increase of $R_{rec}$. This, together with the enhanced rate of electron injection (increase in the short-circuit photocurrent density), caused the open-circuit voltage to rise with the D149 loading.

In ZnO/D149 solar cells containing the coadsorbate cholic acid, aggregation of D149 at high dye loadings was clearly reduced. Short-circuit photocurrent, open-circuit photovoltage and power conversion efficiency again increased with increasing adsorption time. The fill factor still decreased, but the decay was significantly less pronounced than in the absence of CA, which in turn allowed the conversion efficiency to reach higher values than in cells without coadsorbate, emphasizing the benefit of coadsorbing cholic acid in DSCs based on D149-sensitized electrodeposited ZnO. Two reasons were found to lead to the improvement of the fill factor at a given dye loading: the series resistance remained at a low level up to the highest adsorption times – possibly indicating a more stable bond between D149 and ZnO – and the decrease of the recombination resistance at lower quasi-Fermi levels was clearly reduced. On the basis of the observed effects of adsorption time and the presence of cholic acid, it was proposed that aggregated D149 molecules in the cells without CA caused the additional recombination in the energy range that is crucial for the fill factor, which entailed systematic changes in the voltage-dependence of the recombination resistance as a function of the dye loading. Coadsorption of cholic acid prevented strong aggregation of D149 on the ZnO surface and, hence, had a positive influence on the fill factor. In contrast to this, the rate of recombination at a given D149 loading under cell conditions close to open-circuit (higher quasi-Fermi levels) was increased in the cells with CA. However, the open-circuit photovoltage was not affected negatively by this, since the samples with coadsorbate also exhibited a negative shift of the conduction band edge by about 60 mV.

# 6 Panchromatic Dye-Sensitized Solar Cells Obtained by Co-Sensitization of Electrodeposited ZnO with Indoline and Squaraine Dyes[v]

## 6.1 UV/Vis Absorption of Dye Solutions and Sensitized ZnO Films

The optical properties of the dye solutions used for sensitization of electrodeposited ZnO with the indoline dye D149, the indoline dye D131, the squaraine dye SQ2, and/or combinations of these sensitizers were studied by UV/Vis absorption spectroscopy both as-prepared and after dilution, ***Figure 49***.

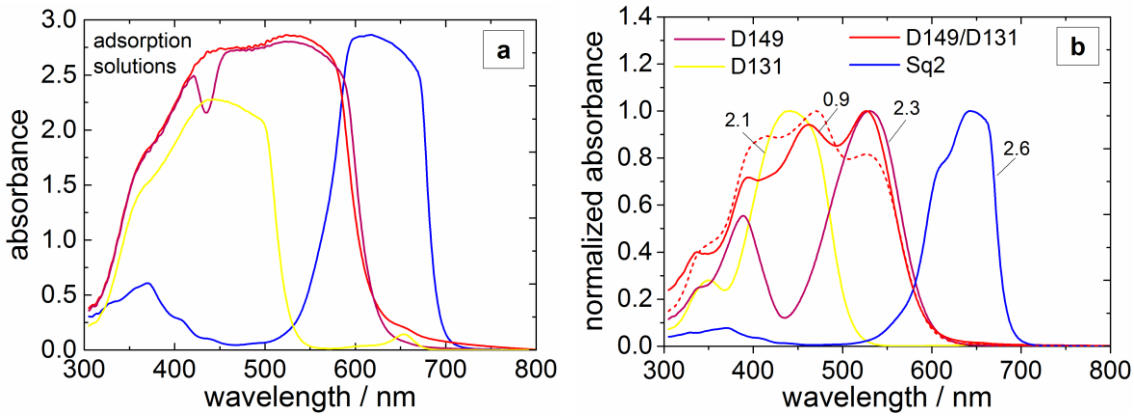


***Figure 49:*** *UV/Vis absorption spectra of solutions of 0.5 mM D149, 0.5 mM D131, and 0.25 mM/0.25 mM D149/D131 in acetonitrile:tert-butanol (1:1) and of 0.1 mM SQ2 in ethanol, before (a) and after (b, normalized) dilution, together with a superposition of the D131 and D149 (diluted) spectra (-----). Labels in (b) indicate peak heights of the corresponding unnormalized spectra. Adapted with permission from ref.[288]. Copyright 2015 American Chemical Society.*

The undiluted adsorption solutions (***Figure 49*** (a)) show very broad and high peaks in the range 350 – 500 nm (D131), 350 – 600 nm (D149, D149/D131), and 500 – 700 nm

[v] Most of the original work presented in this chapter has been published in *J. Phys. Chem. C* 119 (**2015**), 1298-1311.

(SQ2), indicating pronounced aggregation of the dye molecules. The spectra of the diluted solutions (***Figure 49*** (b), dilution factor ca 1:0.2 for D149, D131, and SQ2, and ca 1:2.5 for D149/D131), on the other hand, exhibit considerably narrower absorption bands, indicating that the dyes were largely present in their monomeric form. The absorption maxima of D149 and D131 are found at 390 nm and 530 nm, and at 350 nm and 440 nm, respectively, which is in accordance with previously reported results.[48, 213, 282, 289, 290] The two absorption bands seen in each spectrum are associated with the HOMO → LUMO (peak at higher wavelength) and HOMO → LUMO+1 (peak at lower wavelength) transitions, where LUMO+1 represents the second excited state of the dye.[213, 282] The equimolar mixed solution of D149 and D131 shows a wider absorption feature with three maxima at 395 nm, 462 nm, and 527 nm. This is in line with a calculated spectrum obtained by simple addition of the individual spectra of D149 and D131 (***Figure 49*** (b)), indicating that the D149 and D131 molecules do not interact with each other in the diluted solution. SQ2 exhibits its absorption maximum in the wavelength range of ~ 550 – 700 nm, complementary to the spectra of D149 and D131. Based on its optical absorption, the squaraine dye therefore constitutes a suitable choice of a red-absorbing co-sensitizer to be used together with the indoline dyes to create panchromatic solar cells. From earlier investigations, it is known that the absorption spectrum of SQ2 in DMF solution shows a narrow band centered at 662 nm and a shoulder located at about 610 nm.[32] These features can been assigned to the HOMO → LUMO transition[32] and (by analogy to a structurally similar squaraine sensitizer)[291] to excitation from the ground state to higher vibrational states, respectively. The spectrum in ethanol measured in the present study exhibits a broader peak centered at 643 nm, with prominent shoulders at 610 nm and 660 nm. The differences in peak position and shape compared to the literature spectra are probably the result of aggregation of SQ2 molecules even in the diluted ethanolic solution.

Comparing the UV/Vis absorption spectra of the diluted dye solutions with the corresponding spectra of electrodeposited porous ZnO films sensitized with D149, D131, SQ2, or D149/D131 (***Figure 50*** (a), dashed lines), similar peak positions are found.

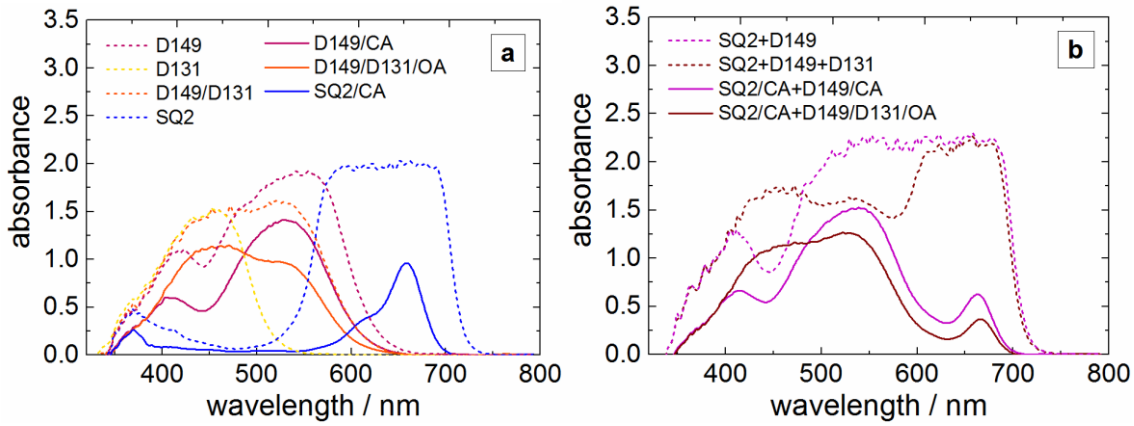


***Figure 50:*** *UV/Vis absorption spectra of electrodeposited porous ZnO films photosensitized with different dyes or dye combinations in the presence (solid lines) or absence (dashed lines) of the coadsorbates cholic acid and/or octanoic acid. Reprinted with permission from ref.*[288]*. Copyright 2015 American Chemical Society.*

However, for D149 and especially SQ2, the absorption bands of the films are much broader and more closely resemble the spectra of the concentrated adsorption solutions, suggesting that these dyes had formed aggregates on the ZnO surface.[271, 282] The peak broadening and slight asymmetry observed for the spectrum of the film sensitized with D149 is comparable to the findings of chapter 5, where aggregation of D149 was discussed in detail. The broadening of the absorption peak of SQ2 is consistent with a previous study reporting the appearance of an additional absorption band at about 600 nm due to formation of H-aggregates,[271] as also observed in the spectrum of the undiluted adsorption solution. In the case of D131 and D149/D131, the absorption bands for the sensitized films are hardly broader than the corresponding peaks in the diluted solution spectra, indicating that D131 shows little aggregation when adsorbed to ZnO and that the tendency of D149 to form aggregates is reduced when adsorbed together with D131. When the porous electrodeposited ZnO was first sensitized with SQ2 and subsequently immersed into a D149 or a D149/D131 solution, the indoline dyes were successfully adsorbed to the ZnO without removing significant amounts of previously adsorbed SQ2. As a result, the ZnO films co-sensitized with SQ2 and D149 or with SQ2, D149, and D131 showed panchromatic optical absorption (***Figure 50*** (b), dashed lines). As in the case of the films with SQ2 or D149 as individual sensitizers, the absorption bands of the co-sensitized film SQ2+D149 are strongly broadened, so that the individual absorption

features of D149 and SQ2 are largely merged. For SQ2+D149/D131, the individual peaks of D131 and D149 can still be distinguished, indicating smaller amounts of the indoline dyes and/or less pronounced aggregation compared to the sample SQ2+D149. As a result of using cholic acid and/or octanoic acid as coadsorbates, narrower absorption bands with decreased height are observed when compared with films sensitized without coadsorbates (***Figure 50***, solid lines). This points to a reduced dye loading and to a smaller extent of dye aggregation. The coadsorbate molecules occupy a part of the surface adsorption sites and, hence, both limit the number of dye molecules on the surface and prevent undesired dye-dye interaction. While the two films sensitized with SQ2 or with D149 in the absence of CA show comparable maximum absorbance, the peak height of the corresponding samples prepared in the presence of the coadsorbate is different, with SQ2 showing a notably smaller maximum absorbance. Given that the molar absorptivity of SQ2 in its absorption maximum is more than four times as high as the molar absorptivity of D149 ($\varepsilon_{SQ2}$ = 319,000 $M^{-1}cm^{-1}$ at 662 nm[32] and $\varepsilon_{D149}$ = 72,350 $M^{-1}cm^{-1}$ at 530 nm,[31] both for solutions in DMF), it can be concluded that the amount of SQ2 molecules adsorbed to the porous ZnO from ethanolic solution over an adsorption time of 4 hours is considerably smaller than the amount of D149 adsorbed to ZnO from acetonitrile:*tert*-butanol solution within 2 hours.

## 6.2 Steady-State Characterization: Photovoltaic Performance and Quantum Efficiency

The photovoltaic characteristics under AM1.5G-type illumination of DSCs built from the ZnO films with different sensitizers or sensitizer combinations (see ***Figure 51*** and ***Table 11***) will be discussed together with the incident photon-to-electron conversion efficiency (IPCE) spectra (***Figure 52***) and with the theoretical short-circuit current densities $J_{sc}^{theo}$ (***Table 11***) calculated from the latter via eq. (36). The highest $J_{sc}$ among the cells without coadsorbates was 7.8 $mAcm^{-2}$ and was observed for the cell with D149 as a result of its comparatively high and wide IPCE peak. The lowest short-circuit current of 2.6 $mAcm^{-2}$ was obtained with SQ2 as individual sensitizer, in line with the fact that the IPCE spectrum of this cell shows a very small (albeit broad) peak with a maximum of IPCE = 25%.

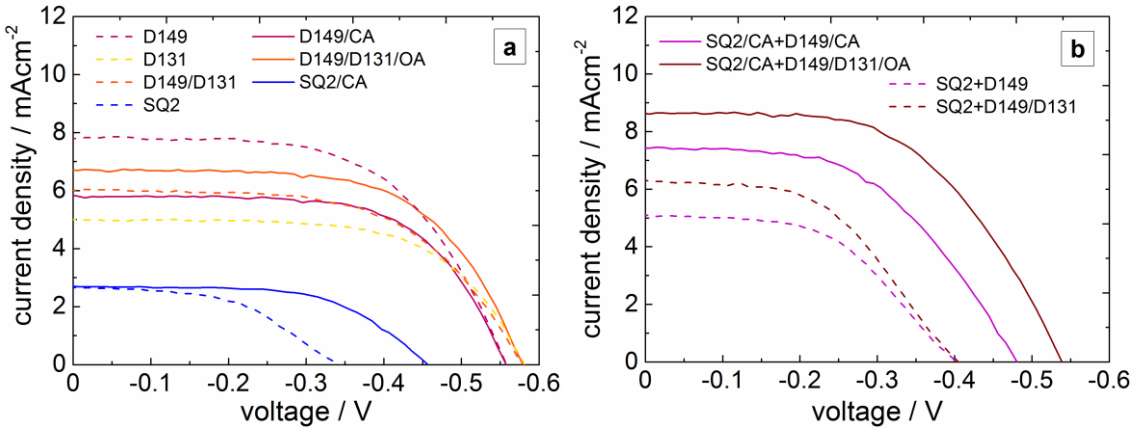


***Figure 51:*** *Current-voltage curves of dye-sensitized solar cells based on electrodeposited porous ZnO films and different dyes or dye combinations with (solid lines) or without (dashed lines) coadsorbates. Reprinted with permission from ref.*[288]*. Copyright 2015 American Chemical Society.*

Given the high and broad absorbance peak of the sample SQ2 (cf. ***Figure 49***), corresponding to a maximum light harvesting efficiency of 99% (cf. section 6.5), the poor IPCE should not be due to insufficient light harvesting but must rather be ascribed to a poor electron injection efficiency between SQ2 and electrodeposited ZnO and/or to slow regeneration of oxidized SQ2 by the electrolyte.

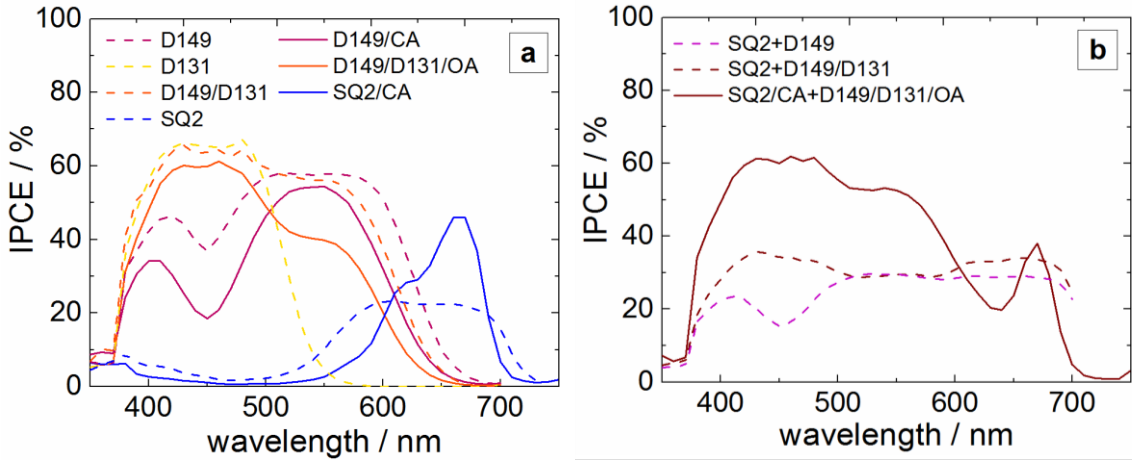


***Figure 52:*** *Incident photon-to-electron conversion efficiency (IPCE) spectra of ZnO-based solar cells with D149, D131, D149/D131, SQ2 (a), or combinations thereof (b). Reprinted with permission from ref.*[288]*. Copyright 2015 American Chemical Society.*

***Table 11:*** *Photovoltaic parameters derived from the J-V curves and theoretical short-circuit current density $J_{sc}^{theo}$ of ZnO-based DSCs with different dyes or dye mixtures. Adapted with permission from ref.[288]. Copyright 2015 American Chemical Society.*

| **sample code** | $J_{sc}$ **/ mAcm$^{-2}$** | $J_{sc}^{theo}$ **/ mAcm$^{-2}$** | $V_{oc}$ **/ mV (+/- 5 mV)** | ***FF*** | $\eta$ **/ %** |
|---|---|---|---|---|---|
| D149 | 7.8 | 7.6 | - 558 | 0.59 | 2.57 |
| D131 | 5.0 | 4.4 | - 581 | 0.64 | 1.84 |
| D149/D131 | 6.0 | 7.8 | - 578 | 0.59 | 2.04 |
| SQ2 | 2.6 | 2.7 | - 344 | 0.51 | 0.45 |
| SQ2+D149 | 5.1 | 5.2 | - 403 | 0.52 | 1.04 |
| SQ2+ D149/D131 | 6.0 | 6.2 | - 405 | 0.49 | 1.2 |
| D149/CA | 5.8 | 5.6 | - 557 | 0.64 | 2.06 |
| D149/D131/OA | 6.7 | 6.0 | - 579 | 0.63 | 2.42 |
| SQ2/CA | 2.7 | 2.9 | - 457 | 0.61 | 0.74 |
| SQ2/CA+ D149/D131/OA | 8.6 | 8.7 | - 539 | 0.55 | 2.55 |

Electrochemical measurements of the energy levels of the dye SQ2 have shown that the Fermi level $E^0(S^+/S^*)$ (cf. ***Figure 3***) of excited SQ2 is located at about -3.7 eV,[32] which is well above the conduction band edge of ZnO at ca -4.5 eV to -3.9 eV.[42, 292] The Fermi level $E^0(S^+/S)$ of ground-state SQ2 is situated at -5.3 eV,[32] which is clearly below the redox level of the acetonitrile-based $I^-/I_3^-$ electrolyte ($E_{redox}$ = -4.85 eV).[35] Consequently, the energetic alignment between the squaraine sensitizer and the semiconductor or the electrolyte, respectively, should allow for efficient electron injection and regeneration of SQ2. Most probably, the small injection efficiency or regeneration efficiency in the cell with SQ2 can therefore be attributed to the pronounced aggregation observed for this squaraine sensitizer on ZnO, as aggregation can effect a high rate of self-quenching of

the dye excited state without electron injection into the semiconductor and may also block access of the electrolyte to a part of the oxidized dye molecules.

The combination of D149 and D131 in the present series of experiments yielded a short-circuit current density of 6.0 $mAcm^{-2}$, which is smaller than the 7.8 $mAcm^{-2}$ obtained with D149 only. This finding contrasts with the IPCE curves and corresponding $J_{sc}^{theo}$ attained for the same cell (***Figure 52*** and ***Table 11***), with the results of previous investigations,[31] as well as with the results obtained for DSCs based on nanoparticulate ZnO in chapter 7 of this work, all of which showed a higher $J_{sc}$ for the combination D149/D131 than for D149 only. Thus, the relatively low $J_{sc}$ measured for D149/D131 in the current-voltage characterization was most likely an exception caused by an involuntary deviation from the standard measurement conditions. As for the IPCE spectrum, the use of D131 as a co-sensitizer with D149 leads to a considerable gain in the shorter-wavelength range, while the value in the longer-wavelength region is only slightly reduced because of a decrease in the D149 loading (cf. ***Figure 50***). The relatively large IPCE of the DSC with D131 as individual sensitizer and of the sample D149/D131 in the absorption range of D131 point towards a higher electron injection efficiency for D131 compared to D149. This finding is in accordance with previous experimental work[31, 214, 217] and with theoretical studies[213, 217] demonstrating that unlike in D149, the HOMO-LUMO excitation in D131 shows a notable shift of charge density to the carboxylic acid anchoring group. Furthermore, D131 – unlike D149 – did not show signs of aggregation on the ZnO surface (***Figure 50***), which may have additionally contributed to a higher electron injection efficiency. Co-sensitization of D149 or D149/D131 with SQ2 resulted in a decay of the short-circuit photocurrent density, which can be understood with reference to the corresponding IPCE spectra. While the D149 or D149/D131 loading in the co-sensitized films is comparable to that of the films with D149 and D149/D131 only (cf. ***Figure 50***), the IPCE of the corresponding cells in the range of absorption of the indoline dyes is decreased by half. A possible explanation for this could be undesired energy transfer from excited D131 and D149 to SQ2, which would deactivate the excited states of the indoline dyes without electron injection to ZnO, leaving only SQ2 as a (poor) electron injector.

As for the open-circuit photovoltage $V_{oc}$, the highest value in the absence of coadsorbates is ~ -580 mV and was achieved by the two cells with D131 or D149/D131. This is

closely followed by $V_{oc}$ = -558 mV for the sample with D149. With $V_{oc}$'s of -344 mV, -403 mV and -405 mV, the squaraine sensitizer SQ2 and the dye combinations SQ2+D149 and SQ2+D149/D131 produced drastically lower open-circuit voltages than the cells with indoline sensitizers. In contrast, $TiO_2$ films sensitized with SQ2 have yielded very good $V_{oc}$'s of up to -667 mV.[32] Impedance spectroscopy served to detangle the effects that governed the open-circuit voltage and to determine what microscopic processes limited the voltage in the present cells, as discussed in the following sections. The best fill factor among cells without coadsorbates was attained with D131 (64%). D149 and D149/D131 yielded a *FF* of 59%, and SQ2 and the dye mixtures SQ2+D149 and SQ2+D149/D131 resulted in the lowest *FF* of only ~50%. Since the fill factor is influenced by the same factors as the open-circuit photovoltage,[128] the impedance spectroscopic analysis further below will also address possible reasons for the trends observed for this parameter.

Coadsorption of cholic acid or octanoic acid resulted in a reduction of the dye loading and, thus, in the light harvesting efficiency for all dyes and dye mixtures (cf. ***Figure 50***). For the samples D149/CA and D149/D131/OA, this lower light harvesting efficiency caused a decrease of the overall external quantum efficiency (***Figure 52***) and, as a result, of the theoretical short-circuit current density (***Table 11***). For the sample with D149/CA, the measured $J_{sc}$ follows this theoretical prediction, but for D149/D131/OA the short-circuit current density is unexpectedly higher than for D149/D131. This can be assumed to be another result of the presumed experimental deviation in the current-voltage characterization of D149/D131, as discussed above. Comparing the IPCE spectra of the two cells with SQ2 and with SQ2/CA, the latter shows a narrower but significantly higher peak in the range of 600 – 700 nm. The combined result of these two effects is a slightly higher theoretical and experimental short-circuit current density for the cell SQ2/CA in spite of its reduced dye loading. This indicates that the reduced level of aggregation in the presence of cholic acid resulted in an improved efficiency of electron injection and/or dye regeneration for the squaraine sensitizer. For the dye combination SQ2+D149/D131, the coadsorption of CA and OA enhanced the external quantum efficiency both in the molecular absorption band of SQ2 and in the absorption range of the indoline dyes. The improvement in the shorter wavelength range was significant enough (increase by a factor of ~2) that the IPCE in this range became comparable to

that of the sample D149/D131. As a result, the cell SQ2/CA+D149/D131/OA achieved the highest $J_{sc}$ of the samples studied in this series of 8.6 mAcm$^{-2}$, which corresponds to a 43% increase compared to the $J_{sc}$ of the corresponding cell without coadsorbates (6.0 mAcm$^{-2}$). Thus, it appears that the coadsorbate blocks undesired energy transfer from D149 and D131 to the squaraine sensitizer, allowing each of the three dyes to inject electrons into the ZnO film and thereby contribute to the photocurrent generation.

The open-circuit voltage reached with D149 and D149/D131 was not noticeably affected by coadsorption of cholic acid or octanoic acid. For SQ2 and SQ2+D149/D131, however, $V_{oc}$ was enhanced from -344 mV and -405 mV to -457 mV and -539 mV. The fill factor was improved by the presence of CA and/or OA for all cells, with the most significant increase from 0.51 to 0.61 observed for the coadsorption of CA with SQ2.

## 6.3 Impedance Spectroscopy Analysis

### 6.3.1 Trap Distribution and Total Trap Density

***Figure 53*** shows the voltage-dependent capacitance of the DSCs with different dyes or dye combinations as determined by electrochemical impedance spectroscopy.

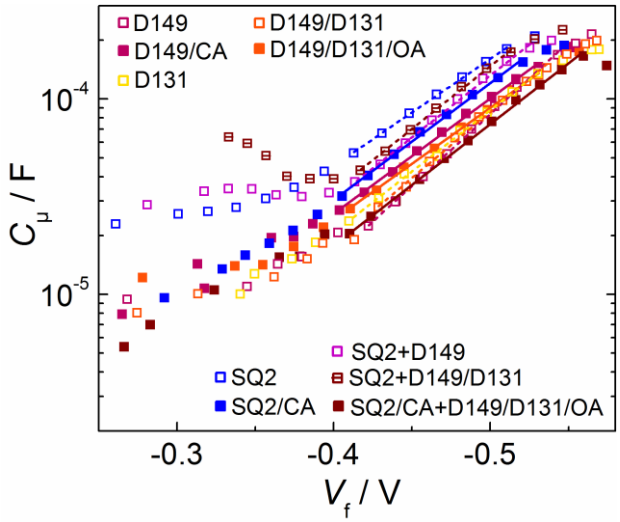


***Figure 53:*** *Chemical capacitance of the DSCs based on sensitized or co-sensitized ZnO as a function of the Fermi-level voltage $V_f$. The lines represent linear fits to the higher-voltage parts of the data and were used to determine the trap distribution parameters α. Adapted with permission from ref.*[288]*. Copyright 2015 American Chemical Society.*

The linear behavior in the semilogarithmic plot for voltages of -0.4 V or more negative confirms the expected presence of exponentially distributed trap states also in the present set of samples. The generally reduced slope of the curves at voltages less negative than -0.4 V is a common observation and typically points to a transition from a range in which the measured capacitance reflects $C_\mu$ to a range where it is dominated by charge accumulation at internal interfaces such as the blocking layer/electrolyte interface.[128] However, in case of the cells containing the squaraine sensitizer without coadsorbate, i.e., SQ2, SQ2+D149, and SQ2+D149/D131, the change in the slope of the capacitance is much more significant than for the remaining samples, with a plateau or even a local maximum visible at about $V_f$ = -0.3 V. This finding suggests the presence of deep trap states in ZnO that are narrowly distributed around a single energy level (so-called monoenergetic traps), in addition to the exponentially distributed band gap states.[90, 128, 293] Alternatively, the additional density of states could correspond to electronic states in the dye molecules themselves.[294] When CA or OA were coadsorbed with SQ2 or with the SQ2/indoline dye combinations, the pronounced change in slope of the capacitance was removed, indicating that the additional density of states was associated with the presence of *aggregated* SQ2 molecules. Regarding the exponentially distributed traps, the majority of samples exhibit equal trap distribution parameters $\alpha$ of 0.37 +/- 0.03 (***Table 12***), as determined from fits of the higher-voltage section of the capacitance curves to eq. (52), cf. ***Figure 53***. With $\alpha$ = 0.44 and $\alpha$ = 0.32, the $\alpha$ values of the samples with D149 or SQ2 as individual sensitizers are slightly outside that range. As for the effect of coadsorbates, combining D149 with cholic acid causes a decrease of $\alpha$ from 0.44 to 0.35. Similarly, coadsorbing OA with D149/D131 slightly decreases the trap distribution parameter from 0.39 to 0.34. Hence, the trap distribution in electrodeposited ZnO films sensitized with D149 or D149/D131 is somewhat steeper in the presence of OA or CA, roughly in accordance with observations discussed in chapter 5. For the squaraine sensitizer SQ2, on the other hand, the presence of cholic acid causes an increase in the value of $\alpha$ from 0.32 to 0.36, i.e., the distribution of trap states is slightly flattened.

***Table 12**: Trap distribution parameters α and relative values of the total trap density $N_t$ of the ZnO solar cells with different dyes or dye combinations.*

| sample code | $\alpha$ | $N_t/N_{t,ref}$ |
|---|---|---|
| D149 | 0.44 | 1 (ref.) |
| D131 | 0.37 | 1 |
| D149/D131 | 0.39 | 0.9 |
| SQ2 | 0.32 | 0.5 |
| SQ2+D149 | 0.39 | 0.7 |
| SQ2+D149/D131 | 0.38 | 0.7 |
| D149/CA | 0.35 | 0.5 |
| D149/D131/OA | 0.34 | 0.4 |
| SQ2/CA | 0.36 | 0.4 |
| SQ2/CA+D149/D131/OA | 0.37 | 0.5 |

The largely similar slopes of the capacitance curves enable the determination of relative conduction band edge shifts $\Delta E_c/q$ (see following section). As apparent from eq. (52), $\Delta E_c/q$ can only be accurately determined from the shifts of the $C_\mu$ curves along the voltage axis if both the trap distribution parameters and the total trap densities $N_t$ within the set of cells to be compared are equal. While total trap densities are commonly assumed to be equal for cells based on a given semiconductor material, it has been argued in a previous report[252] that $N_t$ is influenced by surface treatments such as adsorption of dyes or coadsorbates and should therefore be monitored experimentally and taken into account in the determination of conduction band edge shifts from voltage-dependent charge density plots (an alternative to obtaining $\Delta E_c$ from $C_\mu$). The method suggested by O'Regan et al. involved determination of relative values of $N_t$ by means of short-circuit charge extraction measurements (cf. section 1.4.7), followed by normalization of the open-circuit charge density by the relative trap densities before determining $\Delta E_c$.[252] The present chapter introduces a protocol similar to that proposed by O'Regan to allow for a

normalization of $C_\mu$ curves in order to more reliably determine conduction band edge shifts from these curves. Values of $N_t$ relative to that of the cell with D149 were obtained by determining the factors necessary to align the short-circuit charge density vs. $J_{sc}$ data measured using illumination by a red LED (***Figure 54***), see ***Table 12***.

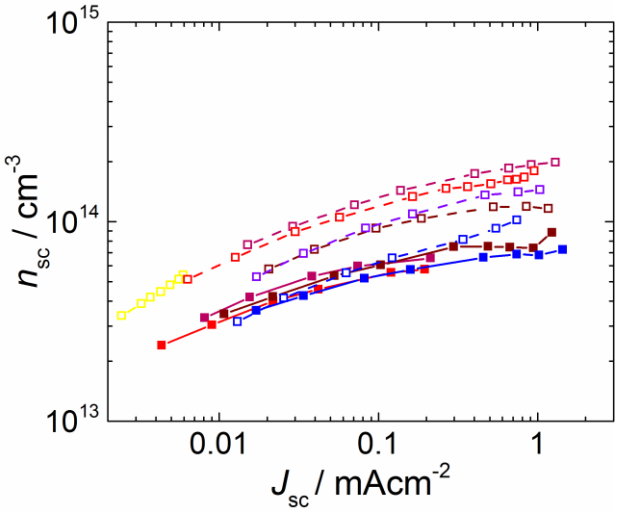


***Figure 54****: Electron density in the ZnO at short circuit under different levels of illumination by a red LED ($\lambda_{max}$ = 632 nm), corresponding to different steady-state short-circuit current densities $J_{sc}$ (lines are a guide to the eye only). Color and symbol assignment as in previous figures.*

It is assumed that the use of red light instead of simulated solar light did not have an effect on the charge at a given short-circuit current density, as the intensity and spectral distribution of the light source will only affect the achieved $J_{sc}$ but is not expected to influence the Fermi-level gradient and, hence, the occupation of trap states corresponding to a given $J_{sc}$ value. $N_t$ is nearly constant in the cells with D149 (reference), D131, and D149/D131. For the sample sensitized with SQ2, however, it is reduced to about half compared to $N_t$ of the indoline dye-sensitized samples. When the squaraine sensitizer is combined with D149 or with D149/D131, the relative total trap density becomes 0.7, which is roughly the average of the values of the cell with SQ2 and the cells with indoline dyes, as expected based on the shared coverage of the internal surface area of the ZnO by SQ2 and indoline dye molecules. Coadsorption of CA or OA with D149 or D149/D131, respectively, decreases $N_t/N_{t,ref}$ to about one half of that in the correspond-

ing samples without coadsorbates. In the case of SQ2, the coadsorbate CA only effected a minimal reduction of the total trap density, indicating that $N_t$ (by adsorption of SQ2) had already reached a lower limit, which may be determined by the constant density of bulk traps. As the relative $N_t$ in the cells with SQ2/CA and D149/D131/OA are comparable, the combination SQ2/CA+D149/D131/OA, in which the surface is covered partially by "SQ2/CA" and partially by "D149/D131/OA", showed the same $N_t/N_{t,ref}$ well. The systematic change of the total trap density in response to variations in the surface dye/coadsorbate layer demonstrates that the majority of trap states must be surface states as opposed to bulk traps. Coadsorption of CA or OA with indoline dyes decreases the relative total trap density by ca 50%, indicating that the two coadsorbates passivate surface trap states, for instance by attaching to coordinatively unsaturated surface atoms that would otherwise form electronic states in the band gap.[90] These observations are in accordance with the conclusions drawn in chapter 5 on the basis of changes in the trap distribution by coadsorption of cholic acid with D149. In view of the reduced values of $N_t$ measured for the cells containing SQ2 without coadsorbate (samples SQ2, SQ2+D149, and SQ2+D149/D131), it is important to re-evaluate the finding that their capacitance curves suggested the presence of additional "trap" states (in ZnO or the dye itself) in these cells, which were not observed in the samples with indoline dyes only. Provided the trap distributions remain otherwise constant, the additional presence of these monoenergetic traps should, in principle, increase the total trap density. The overall *reduction* of $N_t$ in the three cells with SQ2 (without coadsorbate) compared to indoline dye cells (without coadsorbate) must therefore have resulted from a reduction of the density of exponentially distributed traps that overcompensated the expected increase of $N_t$ due to the additional deep traps.

### 6.3.2 Conduction Band Edge Shifts

Normalization of the voltage-dependent capacitance of ***Figure 53*** by the relative total trap densities (***Table 12***) notably influenced the horizontal shifts of the $C_\mu$ curves relative to each other (***Figure 55***), which highlights the importance of accounting for variations in $N_t$. ***Table 13*** (middle column) shows the conduction band edge shifts $\Delta E_c/q$ obtained for the different DSCs from the normalized capacitance. The shifted capacitance curves, ***Figure 56***, show excellent overlap across the entire exponential part, confirming

that the variations of the trap distribution parameter in the present cells are sufficiently small and, hence, the determined conduction band edge shifts are meaningful.

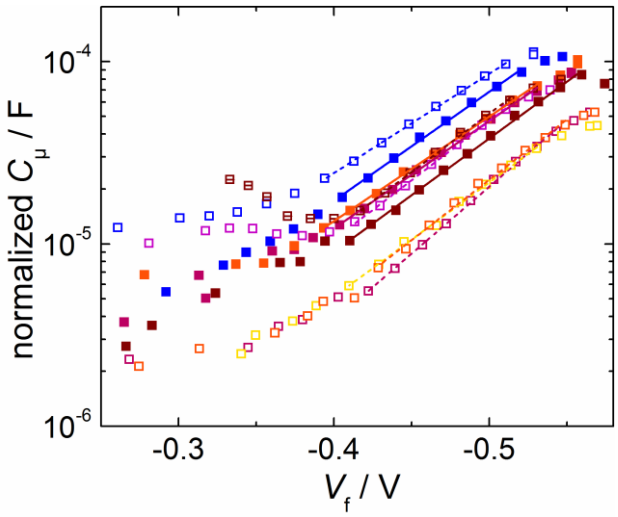


***Figure 55:*** *Chemical capacitance of the ZnO-based DSCs (assignment of colors and symbols as in Figure 53) following normalization by the relative total trap density. Lines are linear fits to selected ranges of the data. Adapted with permission from ref.*[288]*. Copyright 2015 American Chemical Society.*

The three samples with indoline dyes without coadsorbates (D149, D131, and D149/D131) show almost identical positions of the ZnO conduction band edge. Compared to these cells, the sample with SQ2 shows a pronounced positive (towards $E_{redox}$) shift of the conduction band edge by about 110 mV. This large $\Delta E_c$ explains half of the difference in open-circuit photovoltage between the DSCs with D149 or SQ2 (see further discussion in chapter 6.4). A relative positive shift of $E_c$ can indicate the presence of a stronger dipole pointing towards the surface of the semiconductor (or a weaker dipole pointing away from the surface).[67, 146, 295, 296] De Angelis et al. have reported computations for $TiO_2$ showing that all dyes they investigated introduced upward shifts of the conduction band edge with respect to bare $TiO_2$, but the upward shift was much more pronounced if the dye was adsorbed in a bridged bidentate mode (i.e., as a charged molecule) as opposed to monodentate mode (i.e., as a neutral molecule).[67, 296] Thus, the present relative downward shift of $E_c$ observed for SQ2 may reflect differences in the attachment of SQ2 compared to D149, possibly related to the strong aggregation of SQ2 having suppressed the formation of stable bidentate bonds to the ZnO surface.

***Table 13**: Relative shifts $\Delta E_c/q$ of the conduction band edge between the DSCs discussed in this chapter. Positive values indicate downward shifts (towards $E_{redox}$), negative values indicate upward shifts.*

| sample code | $\Delta E_c/q$ from $C_\mu$/ mV | $\Delta E_c/q$ from $n_{oc}$/ mV |
|---|---|---|
| D149 | +/- 0 (ref.) | +/- 0 (ref.) |
| D131 | - 1 | + 38 |
| D149/D131 | + 6 | + 27 |
| SQ2 | + 108 | + 186 |
| SQ2+D149 | + 56 | + 80 |
| SQ2+D149/D131 | + 64 | + 93 |
| D149/CA | + 59 | + 87 |
| D149/D131/OA | + 65 | + 82 |
| SQ2/CA | + 88 | + 105 |
| SQ2/CA+D149/D131/OA | + 42 | + 64 |

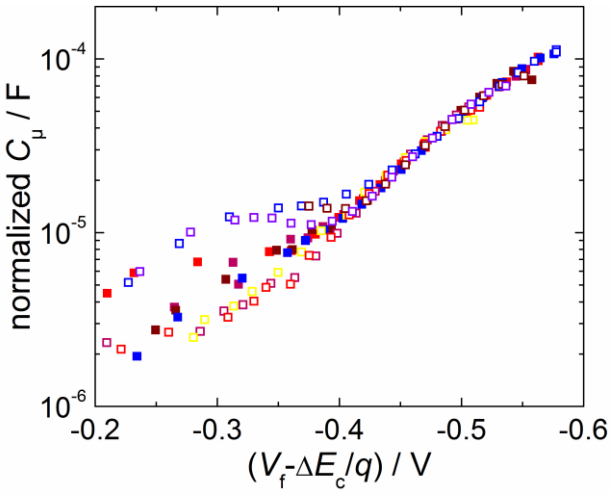


***Figure 56**: Normalized capacitance vs. the band edge shift-corrected voltage. Reprinted with permission from ref.[288]. Copyright 2015 American Chemical Society.*

Moreover, in a previous study investigating D149-sensitized electrodeposited ZnO it was proposed that D149 does not form a covalent bond to the ZnO but rather adsorbs

via ionic interaction.[137] Negatively charged adsorbed D149 ions could have created a stronger dipolar field relative to adsorbed SQ2 molecules, resulting in a stronger upward shift of $E_c$. Using the conduction band edge position of D149 as a reference point, this is detected as a relative downward shift of the conduction band edge in the cell with SQ2. For a deeper analysis of the origins of the relative conduction band edge shifts between DSCs with SQ2 and with D149, theoretical calculations[67, 296] or experimental methods like vibrational spectroscopy[297] must be employed to clarify the binding mode of the different dyes and coadsorbates, which was beyond the scope of this work. The relative $E_c$ shifts of the co-sensitized cells with SQ2+D149 or SQ2+D149/D131 are both about half way in between the $\Delta E_c$ of the cells with indoline dyes and that of the sample with SQ2. Thus, the effects of SQ2 and D149 and/or D131 on the energetics of the porous ZnO are averaged when the dyes are combined. Coadsorption of cholic acid or octanoic acid with D149 or D149/D131 in the present study led to a downward shift of $E_c$ with respect to the cells without CA or OA by about 60 mV. Based on the results of chapter 5, which suggested an upward shift of the conduction band edge by CA in D149-sensitized ZnO, this finding at first appears unexpected. In fact, studies by other groups that have addressed the influence of cholic acid or cholic acid derivatives (e.g. deoxycholic acid and chenodeoxycholic acid) on the conduction band edge position of ZnO or $TiO_2$ have not been unambiguous either: both upward and downward shifts of $E_c$ have been reported.[146, 219, 298] This apparent inconsistency may be explained by variations in the total trap density of the semiconductor that were not accounted for, leading to faulty results for $\Delta E_c$. In the study presented in chapter 5, for instance, $N_t$ was not yet monitored experimentally and was assumed to be identical in cells with D149 and with D149/CA when estimating conduction band edge shifts. Based on the assumption that D149 and D149/CA exhibited similar differences with respect to the total trap density as observed in this chapter ($N_{t,D149/CA} \approx 0.5\ N_{t,D149}$), the apparent upward shift of $E_c$ by CA by ~50 mV (cf. ***Table 9***, values for cells with adsorption time of 120 mins) would change into a downward shift by approximately 30 mV, roughly confirming the trend found after normalization of $C_\mu$ in the present set of cells. The relative downward shifts of $E_c$ induced in cells with indoline dyes by the presence of CA and OA is most reasonably explained by a different mode of adsorption of the coadsorbates via their carboxylic acid groups compared to D149 and D131.[298] Adding cholic acid or octanoic acid to

the squaraine sensitizer or to the mixture of SQ2, D149 and D131 causes a small upward shift (away from $E_{redox}$) of the conduction band edge of ZnO by about 20 mV compared to SQ2 or SQ2+D149/D131 without coadsorbates. The above results suggest a situation in which the indoline dyes induce the strongest upward shift of $E_c$, the coadsorbates cause a smaller upward shift, and adsorption of SQ2 creates an even smaller negative shift of $E_c$.[67, 296] Adsorbing combinations of several dyes and/or coadsorbates effects an averaging of their various individual impacts on the position of the conduction band edge. As a result, the three cells with D149, D131 or D149/D131 showed the highest position of $E_c$ and all other samples exhibited conduction band edges positive of that.

For comparison, the relative band edge shifts were determined from shifts of the voltage-dependent open-circuit electron density (normalized by $N_t/N_{t,ref}$, see ***Figure 57***) along the voltage axis (cf. chapter 1.4.7).

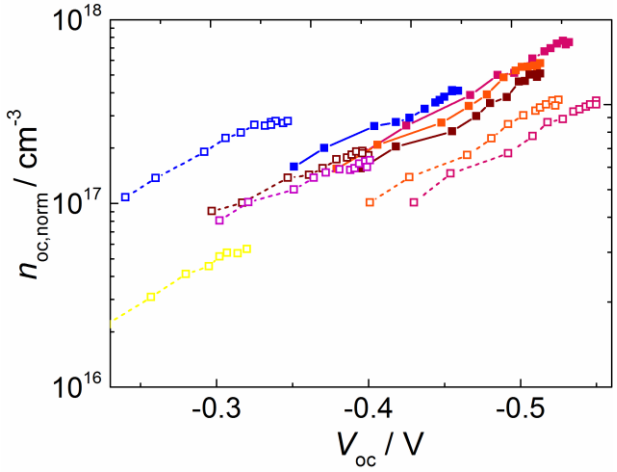


***Figure 57****: Open-circuit electron density $n_{oc}$ normalized by relative differences in the total trap density ($N_t/N_{t,ref}$), plotted against the open-circuit photovoltage (lines are a guide to the eye only). The data was obtained by charge extraction measurements from various illumination intensities of a red LED ($\lambda_{max}$ = 632 nm). Color and symbol assignment as in previous figures.*

The $\Delta E_c$ values attained by this method (***Table 13***, right column) are altogether larger, but qualitatively show largely the same trends with respect to the influence of different dyes and coadsorbates, thus providing an independent confirmation of the results de-

rived from the capacitance curves. In particular, the strong downward shift of the conduction band edge in the cells with SQ2 without coadsorbates and the downward shift of $E_c$ by CA or OA in indoline dye cells were confirmed.

### 6.3.3 Recombination

***Figure 58*** shows semilogarithmic plots of the recombination resistance $R_{rec}$ from EIS as a function of the Fermi-level voltage $V_f$ (a) and the corrected Fermi-level voltage $V_f$-$\Delta E_c/q$ (b), respectively. While the plot against the uncorrected voltage gives an insight into the sample-to-sample differences in the rate of recombination as a combined effect of various factors, the focus here will be on the plots against the band edge shift-corrected voltage, which, according to the $\beta$-recombination model, allow to interpret $R_{rec}$ as a measure of the rate constant of interfacial charge transfer (cf. eq. (55) and eq. (32)).[128, 252] Note that the expression for $R_{rec}$ in the $\beta$-recombination model is obtained by use of an empirical formulation for the rate of recombination $U_n$ (eq. (16)) that accounts for the influence of surface trap states only by introducing the exponent $\beta$. More sophisticated models include a specific distribution and density of surface trap states and of acceptor states, which leads to an expression for $R_{rec}$ that reveals its dependence on the reciprocal value of the total surface trap density, see for example eq. (15) and (16) in ref.[86]. Thus, in the interpretation of the $R_{rec}$ vs. $V_f$-$\Delta E_c/q$ plots of the present cells with varied densities of surface traps (cf. section 6.3.1), both changes in $k_r$ or the surface trap density may be responsible for (inverse) changes in $R_{rec}$. In the corrected voltage range more negative than about -0.35 V, most semilogarithmic $R_{rec}$ curves show the linear decrease typical for cells with an exponential distribution of surface states (eq. (54)).[128] This range is characterized by similar recombination parameters $\beta$ of ca. 0.4 – 0.5 for most samples, as obtained from linear fits to eq. (54), see ***Figure 58*** (b) and ***Table 14***. With $\beta$ = 0.21, the cell with SQ2/CA+D149/D131/OA shows the only larger deviation from this range, representative of a steeper exponential distribution of surface states than in the remaining samples.

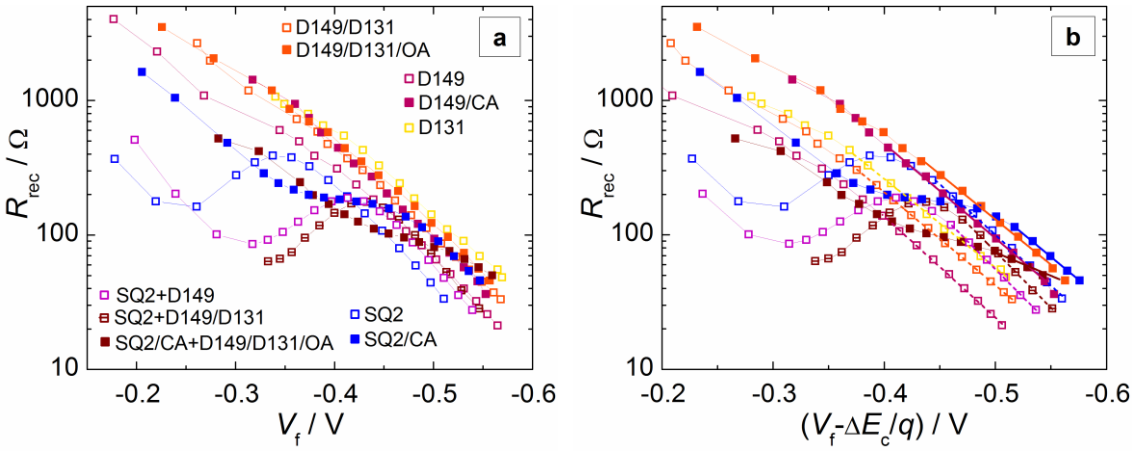


***Figure 58:*** *Plot of the recombination resistance of the ZnO-based DSCs against the Fermi-level voltage before (a) and after (b) correction by relative conduction band edge shifts. Thin lines are a guide to the eye only, thick lines in the higher-voltage range of (b) represent linear fit curves (dashed: without coadsorbate, solid: with coadsorbate). Plot in (b) adapted with permission from ref.*[288]*. Copyright 2015 American Chemical Society.*

When comparing the $\beta$ values of the samples with D149 or D149/CA with those of the corresponding samples of chapter 5, differing effects of the coadsorbate cholic acid are observed. In chapter 5, the recombination parameter was higher for the cells with cholic acid at a given dye loading (cf. ***Figure 45***), which was explained by the breaking-up of D149 aggregates by CA and related decrease of recombination at energies further away from the conduction band edge. In the present set of cells, the $\beta$ value for the D149-sensitized cells with and without cholic acid is virtually identical. The dye loading in the sample with coadsorbate was clearly smaller, with an integrated (integration range 425 nm to 700 nm) absorbance of 170 nm compared to 280 nm in the film without CA. According to the trend presented in ***Figure 45*** of chapter 5, the present cell without CA should thus exhibit a smaller $\beta$ than the value found here and the sample with CA should show a larger recombination parameter. Thus, the effect of CA on the voltage-dependence of recombination in the cells discussed here deviates from the influence that was found for the samples studied in chapter 5. A possible explanation (cf. chapter 4) for this could be the fact that different batches of D149 were utilized in the two experimental series and that, for the dye batch used in the present chapter, the coadsorbate had a less significant effect on the voltage-dependence of $R_{rec}$ than in the previous chapter.

***Table 14**: Recombination parameter for DSCs based on electrodeposited ZnO and various dyes or dye combinations with or without coadsorbates. Values were extracted from the linear part of the $R_{rec}$ curves observed for higher voltages and do not describe the full voltage-dependence of the recombination resistance.*

| sample code | $\beta$ |
|---|---|
| D149 | 0.44 |
| D131 | 0.39 |
| D149/D131 | 0.41 |
| SQ2 | 0.45 |
| SQ2+D149 | 0.50 |
| SQ2+D149/D131 | 0.50 |
| D149/CA | 0.43 |
| D149/D131/OA | 0.40 |
| SQ2/CA | 0.41 |
| SQ2/CA+D149/D131/OA | 0.21 |

The slightly reduced slope of $R_{rec}$ seen for many cells at smaller voltages is typical and reflects a transition to a regime in which the measured resistance is dominated by the charge transfer resistance of the electrolyte/blocking layer interface instead of the recombination resistance.[128] The samples with SQ2 without coadsorbate, however, exhibit a very different behavior with a pronounced local minimum of $R_{rec}$ centered at a corrected voltage of about -0.3 V. By comparison with the chemical capacitance of the corresponding samples (***Figure 56***), this strong increase in recombination around $V_f$-$\Delta E_c/q$ = -0.3 V is due to the presence of the additional electronic states that led to an increase in $C_\mu$ in the same voltage range.[90, 128, 293] In the presence of coadsorbates (cells SQ2/CA and SQ2/CA+D149/D131/OA), the pronounced decrease of $R_{rec}$ towards lower voltages

is considerably reduced, in line with the absence of signs for additional states in the chemical capacitance. (A certain smaller increase in $C_\mu$ expected from lower densities of such additional states is probably concealed by the exponential background). Note that in the range of $V_f$-$\Delta E_c/q$ of -0.5 V or more negative, cells with SQ2 with or without coadsorbate show high recombination resistances compared to the indoline dye cells with or without coadsorbate, respectively. This particularly low rate of recombination outside the energetic range of the additional density of states is probably related to the overall significantly reduced density of ZnO surface trap states in the samples with SQ2 (cf. ***Table 12*** and discussion), corresponding to a reduced density of electron donor states able to participate in recombination reactions to the electrolyte or oxidized dye molecules. Among the samples with indoline dyes, D131 and D131/D149 (without OA) show higher recombination resistances vs. $V_f$-$\Delta E_c/q$ than D149 (without CA). As the total trap density in the ZnO films was similar for these three cells, the differences point to a lower rate constant of recombination in cells containing D131, which could reflect a more efficient physical blocking of the ZnO surface from the electrolyte by D131 molecules (reduced electronic coupling in eq. (17)). The addition of CA or OA entailed a very pronounced decrease of $R_{rec}$ vs. $V_f$-$\Delta E_c/q$ both for D149 and for D149/D131, which was at least in part the result of the reduction in the total trap density (***Table 12***).

Taking the influence of the different positions of the conduction band edge into account (***Figure 58*** (a)), the cells with SQ2 without coadsorbate show the highest rate of recombination at a given Fermi-level voltage due to the strong downward shifts of the conduction band edge (see previous section). D149 (without CA) shows similarly poor properties, while D131 altogether exhibits the most favorable recombination behavior. The addition of CA and OA overall leads to an improvement of the recombination resistance in the higher voltage range. A further discussion of the different factors influencing recombination and, eventually, the open-circuit photovoltage, will be presented in the following section.

In the ZnO/D149 cells studied in chapter 5, cholic acid increased $R_{rec}$ over a large range of voltages, but was found to have the opposite effect at voltages beyond -0.55 V ($g(E_{fn}) > 2 \cdot 10^{19}$ $eV^{-1}cm^{-3}$, cf. ***Figure 44***). The data of the present cells with indoline dyes show no indications of a decrease of $R_{rec}$ at high voltages by the presence of CA or OA. It must be kept in mind, however, that the voltage or $g(E_{fn})$ axes in the plots of the recom-

bination resistance in chapter 5 were not corrected for possible variations in the total trap density between the samples and thus might not have accurately reflected the rate constant of recombination. If the ratio of total trap densities between cells with D149 and cells with D149/CA in chapter 5 was similar to the one found in this chapter ($N_{t,D149/CA} \approx 0.5\ N_{t,D149}$), the recombination resistance in a plot vs. the normalized (by relative total trap densities) density of states would have been higher for the cell with CA over the whole measurement range. This would have suggested a generally lower rate constant of recombination in the presence of CA, as found in the present cells with indoline dyes.

Since the recombination resistance is related to the slope of the voltage-dependent recombination current $J_{rec}$ (eq. (46)), local minima in $R_{rec}$, as observed due to additional recombination for the cells containing aggregated SQ2, should appear as inflection points (S-shape) in plots of the recombination current against the voltage.[90] The dark recombination currents $J_{rec}^{dark}$ (equivalent to the total dark current) as a function of the corrected Fermi-level voltage $V_f$-$\Delta E_c/q$ exhibit the typical exponential increase, without any indications of inflection points (***Figure 59*** (a)).

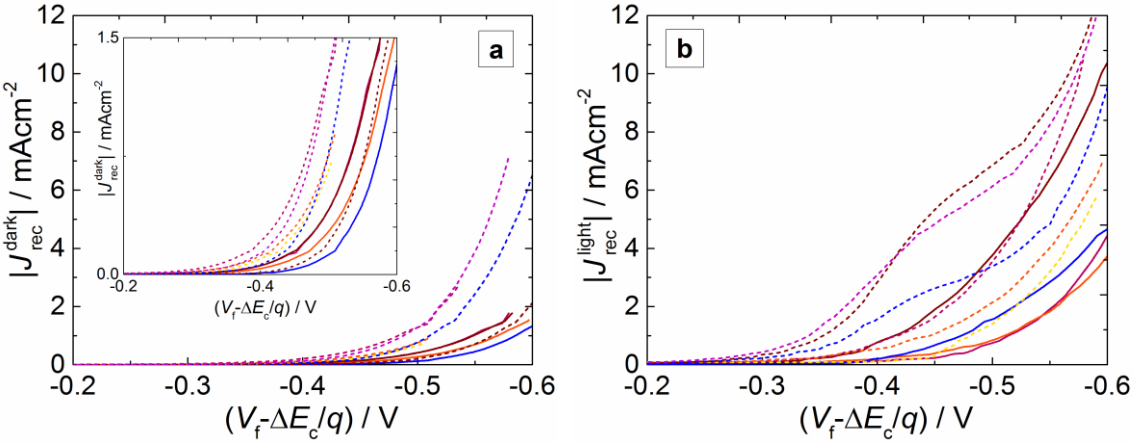


***Figure 59:*** *Recombination current vs. corrected voltage in the dark (a, inset shows blow-up) and under AM1.5G illumination (b) of DSCs with different dyes (assignment of colors as in previous figures), with (solid lines) or without (dashed lines) CA/OA. Adapted with permission from ref.*[288]*. Copyright 2015 American Chemical Society.*

However, the lower estimates for the voltage-dependent recombination current under illumination ($J_{rec}^{light}$, ***Figure 59*** (b))[VI] for the cells with SQ2, SQ2+D149, or SQ2+D149/D131 exhibit the S-shape indicative of additional recombination in a limited voltage range, thus independently verifying the results of the EIS analysis. Based on the exclusive appearance of the inflection points in the illuminated recombination current, it can be concluded that only *oxidized* SQ2 in aggregates caused the voltage-dependent increase in recombination. The fact that the $J_{rec}^{light}$ generally showed a voltage-independent increase compared to the dark recombination currents probably resulted from an increased concentration of oxidized redox species formed in the pores of the ZnO film during solar cell operation.[95]

Assuming that the observed trap states related to oxidized SQ2 in aggregates correspond to unoccupied electronic states in the ground-state dye, the energy level around which the states were centered should coincide with the maximum of the distribution of unoccupied states in SQ2 ($E^0_{ox}$ in ***Figure 3***). The traps were detected around ca 0.3 eV above $E_{redox}$, i.e., at -4.55 eV, [32] cf. ***Figure 53*** and ***Figure 58***. Previous studies have determined the Fermi level $E^0(S/S^+)$ of the oxidation potential of SQ2 to be situated at -5.33 eV, i.e., approximately 0.5 eV below $E_{redox}$ of the $I^-/I_3^-$ electrolyte.[32] Thus, if the position of the monoenergetic trap states detected in $C_\mu$ and $R_{rec}$ does correspond to $E^0_{ox}$, the reorganization energy of the adsorbed SQ2 molecules would be 0.8 eV. This is in the range of typical reorganization energies of 0.4 – 1 eV reported for DSC dyes,[205, 299] which makes it reasonable to assume that the observed traps did, in fact, correspond to unoccupied states in oxidized SQ2 molecules. For the sake of convenience, the following discussion will continue to refer to these traps as (additional) monoenergetic trap states.

[VI] Calculated by subtracting $J_{sc}$ from the total current density measured under AM1.5G illumination. This approach relies on the simplifying assumption of negligible recombination under short-circuit conditions (not always the case, cf. ref. 92), thus delivering lower estimates rather than exact values.

## 6.4 Detangling the Different Effects Influencing the Open-Circuit Voltage and Fill Factor

Having analyzed photovoltaic characteristics, trap distributions and recombination properties of the ZnO-based DSCs with different sensitizers and coadsorbates in the previous sections, the following discussion will now use these results to quantitatively determine the origins of the experimentally observed variations $\Delta V_{oc}$ in the open-circuit photovoltage (as well as the fill factor) of the cells. According to the $\beta$-recombination model (eq. (34)), differences in the open-circuit photovoltage are due to changes in the conduction band edge $E_c$, the recombination parameter $\beta$, the rate of electron injection reflected by the short-circuit photocurrent density $J_{sc}$, and/or the rate constant $k_r$ of recombination under illumination (or the total trap density $N_t$, cf. discussion in 6.3.3), which is contained in the factor $J_{0k}$, cf. eq. (32). For cells with similar recombination parameters $\beta$, such as the samples studied in this chapter (cf. ***Table 14***), expressions for the change of photovoltage with respect to a reference cell "ref" solely caused by differences in $J_{0k}$ or $J_{sc}$ can be readily derived from eq. (34):

$$\Delta V_{oc}(\Delta J_{sc}) = \frac{kT}{q \cdot \beta} \cdot \ln\left(\frac{J_{sc}}{J_{sc,ref}}\right) \tag{75}$$

$$V_{oc}(\Delta J_{rec}^{light}) = \frac{kT}{q \cdot \beta} \cdot \ln\left(\frac{J_{rec}^{light}}{J_{rec,ref}^{light}}\right) \tag{76}$$

In eq. (76), the parameter $J_{0k}$ has been replaced by the recombination current under illumination, $\Delta J_{rec}^{light}$ (cf. section 6.3.3), exploiting the fact that in the case of same $\beta$ and $E_c$ the ratio $J_{0k}/J_{0k,ref}$ is equivalent to $\Delta J_{rec}^{light} / \Delta J_{rec,ref}^{light}$ (cf. eq. (31) and eq. (32)).[128] The $\Delta J_{rec}^{light}$ values were taken from plots against $V_f$-$\Delta E_c/q$ (***Figure 59*** (b)), thus removing the influence of differences in $E_c$, and were determined outside the range influenced by the additional monoenergetic trap states (at -0.55 V) to ensure applicability of the $\beta$-recombination model. The enhancement of recombination due to the presence of monoenergetic deep traps in cells with SQ2 without coadsorbates cannot be described by the $\beta$-recombination model, so that the calculations made in this section do not account for the effects of this additional recombination on the open-circuit voltage. As discussed further above, the recombination parameters determined from the high-voltage range of

the $R_{rec}$ curves are between 0.4 and 0.5 for most samples. To enable the calculations based on eq. (75) and eq. (76), the average $\beta$ value of 0.44 (not including the single outlier of $\beta$ = 0.21) was used. Based on the simplifying assumptions made above, the results attained by eq. (75) and (76) must be considered rough approximations rather than precise values. Regarding $\Delta V_{oc}(\Delta J_{sc})$, it should also be kept in mind that any increase (or decrease) in the short-circuit current density may entail an increased (or decreased) rate of recombination to oxidized dye molecules. Since indications for recombination with oxidized dye molecules were indeed observed in several of the cells of this chapter, it is likely that the change in open-circuit voltage due to the change in $J_{sc}$ is slightly underestimated for these samples.

The three calculated contributions to the changes in $V_{oc}$, ***Table 15***, were summed up for each cell to yield the theoretical total change in the open-circuit voltage, $\Delta V_{oc,calc}=\Delta E_c/q+\Delta V_{oc}(\Delta J_{sc})+\Delta V_{oc}(\Delta J_{rec}^{light})$. In spite of the simplifications made in the calculations, the majority of the values of $\Delta V_{oc,calc}$ are very close (+/- 10 mV) to the experimentally observed values of $\Delta V_{oc}=V_{oc}-V_{oc}$(D149) (***Table 15***), proving the applicability of the model. The cells with SQ2 or combinations of SQ2 and indoline dyes (without coadsorbates) show larger deviations of about 60 mV between theoretical and experimental change in $V_{oc}$, which shows that the presence of the additional monoenergetic trap states in these samples induced an additional loss in photovoltage by 60 mV. The results in ***Table 15*** clearly show that the two DSCs containing D131 and D149/D131 exhibited the best (most negative) open-circuit photovoltages among the cells of this chapter owing to the small rate constant of recombination (cf. section 6.3.3). The favorable influence of the sluggish recombination on $V_{oc}$ was slightly counteracted by a loss due to the smaller $J_{sc}$ of these cells compared to the reference cell with D149. If the short-circuit photocurrent density would have been as high as that of the reference, the open-circuit voltage would have been even more negative by 15 – 25 mV. The cell containing the squaraine dye SQ2 without cholic acid yielded the lowest $V_{oc}$ as a consequence of the strong downward shift of $E_c$ (cf. 6.3.2) coupled with its very low $J_{sc}$. Although the calculations suggest that the photovoltage losses due to the small injection rate and the conduction band edge downward shift are counteracted by reduced recombination due to the decreased surface trap density (cf. ***Table 12*** and section 6.3.3), this finding does not accurately describe the situation in the real cell, since the $\Delta V_{oc,calc}$ for

the containing SQ2 without coadsorbates did not include the voltage loss due to recombination via monoenergetic trap states.

***Table 15**: Partial changes $\Delta V_{oc}$ (...) of the open-circuit voltages of ZnO-based DSCs with different sensitizers and coadsorbates with respect to a reference cell. $\Delta V_{oc,calc}$ is the calculated total change of $V_{oc}$ (sum of $\Delta V_{oc}$ (...)'s) and $\Delta V_{oc}$ is the experimental total change of $V_{oc}$. Adapted with permission from ref.[288]. Copyright 2015 American Chemical Society.*

| sample code | $\Delta V_{oc}$ ($\Delta E_c/q$) /mV | $\Delta V_{oc}$ ($\Delta J_{sc}$) /mV | $\Delta V_{oc}$ ($\Delta J_{rec}^{light}$) /mV | $\Delta V_{oc,calc}$ /mV | $\Delta V_{oc}$ /mV |
|---|---|---|---|---|---|
| D149 | +/- 0 (ref.) | +/- 0 (ref.) | +/- 0 (ref.) | +/- 0 (ref.) | +/- 0 (ref.) |
| D131 | - 1 | + 26 | - 46 | - 21 | - 23 |
| D149/D131 | + 6 | + 16 | - 33 | - 11 | - 20 |
| SQ2 | + 108 | + 65 | - 21 | + 152 | + 214 |
| SQ2+D149 | + 56 | + 25 | + 9 | + 90 | + 155 |
| SQ2+D149/D131 | + 64 | + 16 | + 15 | + 95 | + 153 |
| D149/CA | + 59 | + 18 | - 77 | 0 | + 1 |
| D149/D131/OA | + 65 | + 9 | - 77 | - 3 | - 21 |
| SQ2/CA | + 88 | + 63 | - 54 | + 97 | + 101 |
| SQ2/CA+ D149/D131/OA | + 42 | - 6 | - 5 | + 31 | + 19 |

For the two co-sensitized cells with SQ2+D149 or SQ2+D149/D131, the open-circuit photovoltage reached higher values than for the sample with SQ2 as an individual sensitizer because of the smaller downward shift of the conduction band edge and the higher $J_{sc}$. When D149 or D149/D131 were combined with coadsorbates, the open-circuit photovoltage remained the same, because the beneficial effect of decreased recombination (reduced total trap density, cf. ***Table 12***) was fully compensated by losses resulting from

the lowered $J_{sc}$ and the downward shift of $E_c$. Coadsorbing cholic acid with the squaraine sensitizer, however, led to a great improvement in $V_{oc}$ on account of the reduction of both the downward shift of the conduction band edge and recombination losses. For the co-sensitized cell with SQ2/CA+D149/D131/CA, an improvement of the open-circuit photovoltage compared to the corresponding sample without coadsorbates was achieved through the less pronounced downward shift of $E_c$, the higher short-circuit photocurrent density, and reduced recombination losses. This cell yielded a higher short-circuit current density than the reference cell with D149, but exhibited a lower $V_{oc}$ due to the ~40 mV downward shift of the conduction band edge, thus resulting in a marginally smaller power conversion efficiency. For the different cells containing SQ2 as individual sensitizer or in combinations, the results of the $\Delta V_{oc}$ analysis are summarized in the illustration in ***Figure 60***.

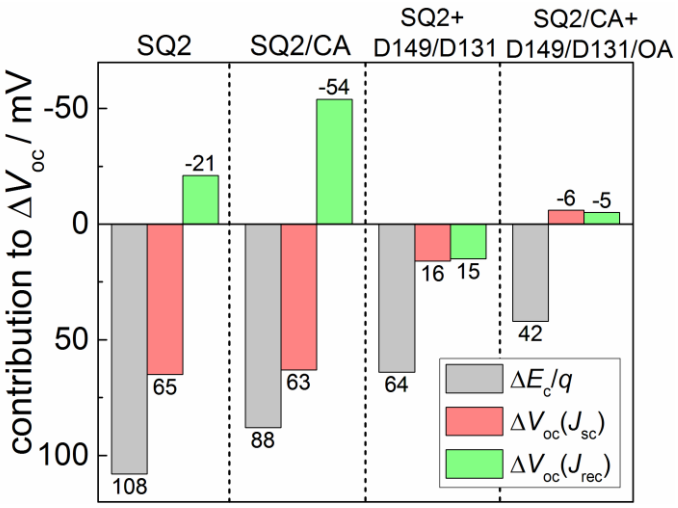


***Figure 60****: Graphic representation of the three calculated contributions to the total open-circuit photovoltage change of four of the DSCs with respect to the reference sample D149: conduction band edge shifts (grey), differences in the short-circuit photocurrent density (coral), and differences in the rate of recombination (green). Negative values indicate gains of the (negative) open-circuit photovoltage, positive values indicate losses.*

For an analysis of the microscopic origins of the different fill factors of the cells in this chapter, it should be noted that the (internal) fill factor *FF* depends on the same basic

factors as the open-circuit photovoltage, i.e., $\beta$, $E_c$, $J_{rec}^{light}$ and $J_{sc}$, cf. eq. (35). To study *FF* independent of influences of the series resistance, its internal value was determined and was plotted vs. the experimental $V_{oc}$ in ***Figure 61***. An exact analysis to examine which microscopic parameters determined *FF* would involve a plot of the internal fill factor against the calculated $V_{oc}$ based on the parameters $E_c$, $J_{0k}$, $\beta$ and $J_{sc}$ (eq. (34)), rather than against the experimental $V_{oc}$. However, calculated absolute voltage values could not be determined for the present samples, as $E_c$ and $J_{0k}$ were only accessible as relative quantities. The data was compared to a simulated curve based on the above equation under the assumption of a constant $\beta$ value of 0.44 (see discussion above).

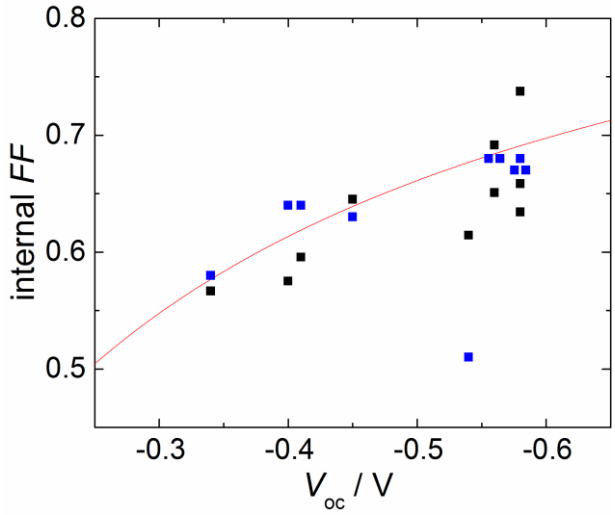


***Figure 61****: Internal fill factor of the ZnO-based dye-sensitized solar cells with various photosensitizers plotted vs. the experimental open-circuit photovoltage. Black symbols are experimental values, blue symbols are calculated values obtained by inserting the measured $V_{oc}$ and β values of each sample into eq. (35). The red line is a simulation based on eq. (35) with a fixed β value of 0.44.*

A fair agreement of the experimental data with the simulated behavior can be seen, indicating that the variations of the fill factor between different samples are mostly the result of the above-discussed changes in the open-circuit photovoltage. In other words, the differences in the fill factors of the various cells are largely due to the variations in $E_c$, $J_{rec}^{light}$ and $J_{sc}$ that were responsible for the variations in $V_{oc}$, cf. ***Table 15***. Calculating the internal fill factor of each sample based on the measured $V_{oc}$ of each individual sam-

ples and considering their individual experimental $\beta$ values (blue symbols in ***Figure 61***) does not lead to a significantly improved congruence between experimental internal fill factor and theoretical value. Thus, the small variation of the $\beta$ values does not seem to have a crucial influence on *FF*.

## 6.5 Analysis of the Factors Determining the External Quantum Efficiency

This section will first focus on a quantitative estimation of the factors limiting the IPCE (cf. eq. (40)). Explicit investigations of the electron injection efficiency $\eta_{inj}$ and the dye regeneration efficiency $\eta_{reg}$ generally require specific experimental methods such as ultrafast transient absorption spectroscopy and scanning electrochemical microscopy,[82, 105, 282, 300] which were beyond the experimental scope of this work. The present discussion of those quantities will therefore be limited to the combined effect of $\eta_{inj}$ and $\eta_{reg}$ at short circuit as concluded based on the determined charge collection efficiency $\eta_{cc}$ and light harvesting efficiency $\eta_{lh}$, which is a typical approach in photoelectrochemical and impedance studies of complete DSCs.[28, 141] $\eta_{cc}$ is commonly assessed by comparing the electron diffusion length $L_n = \sqrt{\tau_n D_n}$ (eq. (2)) with the film thickness *d*. Since effective electron lifetime $\tau_n$ and effective diffusion coefficient $D_n$ depend on the bias voltage/illumination, a correct determination of $L_n$ must use $\tau_n$ and $D_n$ values at the same electrical condition,[111] which is the short-circuit condition in the present analysis of the IPCE and $J_{sc}$. For $\tau_n$, the value at an applied voltage $V$ = -0.3 V (obtained from $C_\mu$ and $R_{rec}$ via eq. (47)) was used as an approximation for the short-circuit value because the impedance spectra could not be reliably fitted anymore at less negative voltages. Approximate values of $D_n$ were obtained by means of eq. (69) using the electron transport time $\tau_{tr}$ measured by IMPS under 25 mWcm$^{-2}$ illumination by a red LED at short circuit (cf. ***Figure 75***) and a factor $\zeta$ of 3.1, as roughly estimated based on an extrapolation of the chart in the Supplementary Information of ref. [141] to $\alpha_{abs}d \approx 5$, the value corresponding to the highest peak absorbance of 2.2 among the samples of this chapter.[VII]. Consid-

[VII] $\zeta$ = 3.1 constitutes a higher value than used in most other studies (cf. ref. 141, 242, 263, and 264) chosen here to ensure that $D_n$ is underestimated rather than overestimated.

ering that $\tau_n$ increases towards smaller voltages and $\tau_{tr}$ decreases with increasing light intensity,[87, 90] the $L_n$ values determined using $\tau_n$ at $V$ = -0.3 V and $\tau_{tr}$ under 25 mWcm$^{-2}$ illumination represent conservative lower estimates for the short-circuit diffusion length under standard AM1.5G operating conditions. Nearly all of the estimated short-circuit electron diffusion lengths for the different cells are at least 3 times as large as their film thickness $d$ (***Table 16***), demonstrating that the charge collection efficiency approached 100%[87] and the IPCE was not limited by this part of the photon-to-current conversion (cf. ***Table 17***). The cell D149/D131 exhibits an $L_n/d$ ratio of 2.6 (as a result of a relatively low electron diffusion coefficient), which according to a graphical estimation based on Figure (17) of ref. [87] should still correspond to a charge collection efficiency $\eta_{cc}$ of about 97%.

***Table 16****: Effective electron lifetime (at an applied voltage of -0.3 V) and diffusion length (at short circuit) $\tau_n$ and $D_n$, film thickness d, estimated short-circuit electron diffusion length $L_{n,sc}$, and ratio of $L_{n,sc}$ and d for ZnO solar cells with different dyes with and without coadsorbates.*

| **sample code** | **$\tau_n$ ($V$=-0.3 V) / ms** | **$D_n$ (s.c.) / $10^{-5}$ cm$^2$s$^{-1}$** | **$d$ / µm** | **$L_{n,sc}$ / µm** | **$L_{n,sc}/d$** |
|---|---|---|---|---|---|
| D149 | 6.6 | 3.2 | 4.2 | 14.6 | 3.5 |
| D131 | 10.7 | n.a. | 4.3 | n.a. | n.a. |
| D149/D131 | 8.9 | 1.3 | 4.2 | 10.8 | 2.6 |
| SQ2 | 7.2 | 14.5 | 4.2 | 32.2 | 7.6 |
| SQ2+D149 | 2.9 | 11.6 | 4.2 | 18.3 | 4.3 |
| SQ2+D149/D131 | 4.1 | 10.5 | 4.3 | 20.6 | 4.8 |
| D149/CA | 18.3 | 2.7 | 4.1 | 22.1 | 5.3 |
| D149/D131/OA | 16.5 | 2.1 | 4.6 | 18.6 | 4.0 |
| SQ2/CA | 3.9 | 5.6 | 4.4 | 14.7 | 3.3 |
| SQ2/CA +D149/D131/OA | 3.8 | 5.2 | 4.5 | 14.1 | 3.1 |

The spectral light harvesting efficiency, determined from the optical loss-corrected absorbance curves in ***Figure 50***,[VIII] exhibits very high peak values of 97 – 99% for cells without coadsorbates, while the samples with CA and/or OA show slightly smaller maximum $\eta_{lh}$ of 89 – 96%, ***Figure 62***.

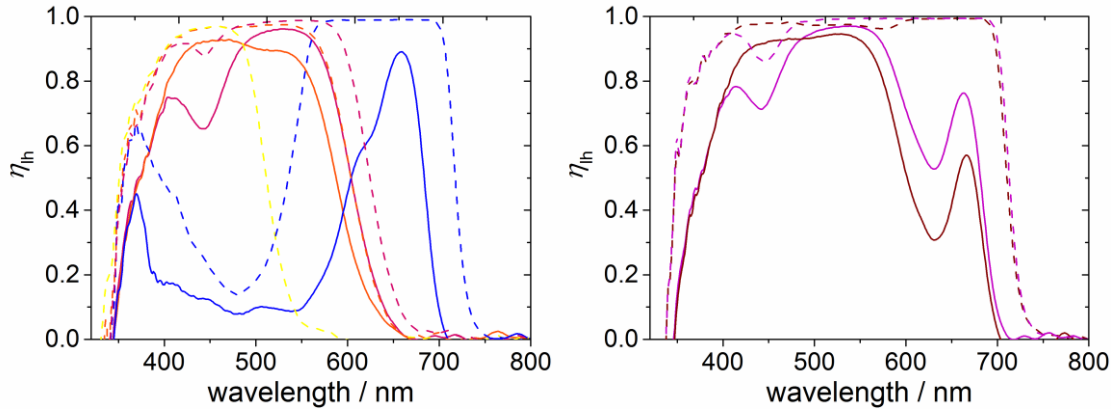


***Figure 62***: *Light harvesting efficiencies of the DSCs with SQ2, D149, and/or D131, calculated from the absorbance.*

For the solar cell performance, the spectrally integrated light harvesting efficiency $\eta_{lh,int}$ is the relevant quantity. The $\eta_{lh,int}$ values of the various DSCs were determined using an integration range of 350 – 750 nm and were referred to the integrated light harvesting efficiency of a hypothetical ideal absorber showing $\eta_{lh} = 1$ over the range 350 – 750 nm (the corresponding $\eta_{lh,int}$ is 400 nm) to attain relative integrated light harvesting efficiencies with values between 0 and 100%, ***Table 17***.

Having quantified $\eta_{cc}$ and $\eta_{lh,int}$, it is now possible to assess the combined effect of electron injection and dye regeneration on the quantum efficiency. For this purpose, the IPCE curves of ***Figure 52*** were first corrected for optical losses of 20%[IX] (i.e., divided by 0.8) to yield an internal IPCE that refers to the light intensity actually arriving at the

[VIII] These "internal" values of the light harvesting efficiencies represent are smaller than those determined from the uncorrected absorbance, acknowledging that a part of the non-transmitted light intensity cannot contribute to the photocurrent generation but is rather reflected or absorbed by the FTO/glass substrate, see further below.

[IX] Estimated based on an offset of 0.09 of the absorbance curves at 800 nm, where none of the dyes absorb, i.e., any measured absorbance must be due to the substrate.

active layer. The corrected IPCE spectra were then spectrally integrated (350 – 750 nm) and the results were divided by the integrated IPCE of a hypothetical cell with IPCE = 1 over the whole range (i.e., by 400 nm) to yield relative values between 0 and 100%, ***Table 17***.

***Table 17****: Relative integrated internal IPCE (corrected for 20% optical losses), short-circuit charge collection efficiency, relative integrated light harvesting efficiency (corrected for optical losses), and product of electron injection efficiency and dye regeneration efficiency of DSCs based on electrodeposited porous ZnO with various dyes and coadsorbates.*

| **sample code** | **rel. IPCE$_{int}$ corr. /%** | **$\eta_{cc}$ /%** | **rel. $\eta_{lh,int}$ /%** | **$\eta_{inj} \cdot \eta_{reg}$ /%** |
|---|---|---|---|---|
| D149 | 40 | 100 | 63 | 64 |
| D131 | 28 | 100 | 37 | 77 |
| D149/D131 | 44 | 97 | 59 | 77 |
| SQ2 | 13 | 100 | 60 | 22 |
| SQ2+D149 | 26 | 100 | 87 | 30 |
| SQ2+D149/D131 | 32 | 100 | 87 | 37 |
| D149/CA | 30 | 100 | 51 | 59 |
| D149/D131/OA | 34 | 100 | 49 | 70 |
| SQ2/CA | 13 | 100 | 27 | 49 |
| SQ2/CA+D149/D131/OA | 45 | 100 | 59 | 77 |

Dividing the relative integrated IPCE values by the relative integrated light harvesting efficiency and by the charge collection efficiency then yielded an estimation for the spectrally averaged value of the product $\eta_{inj} \cdot \eta_{reg}$ (***Table 17***), which is identical to the

APCE (eq. (41)) in the present case of $\eta_{cc}$ = 100%. The results confirm and complement the preliminary conclusions drawn in chapter 6.2. In the cell with D149 without coadsorbates, the integrated external quantum efficiency is limited by the light harvesting efficiency and the combined electron injection and dye regeneration efficiency, with $\eta_{lh,int}$ and $\eta_{inj} \cdot \eta_{reg}$ showing nearly identical values of 63 and 64%. For D131 and D149/D131, the electron injection and/or dye regeneration efficiency is higher (77%) than for D149 alone, and light harvesting is clearly the primary limiting factor for the IPCE (and, hence, for $J_{sc}$).

In the cells with SQ2, SQ2+D149, and SQ2+D149/D131, the electron injection and/or dye regeneration efficiency is particularly low (22 – 37%), while the light harvesting efficiency is high (60 – 87%), especially in the co-sensitized samples (87%). For these three cells, $\eta_{inj} \cdot \eta_{reg}$ is thus the primary limiting factor for the IPCE and $J_{sc}$. In the samples with coadsorbates, the integrated light harvesting efficiency was reduced compared to their counterparts without coadsorbates. As for $\eta_{inj} \cdot \eta_{reg}$, it was decreased with respect to the samples without CA/OA for the cells D149/CA and D149/D131/OA, but was strongly increased from 22 to 49% and from 37 to 77% for SQ2/CA and SQ2/CA+D149/D131/OA. The latter effect is likely the consequence of the suppression of aggregation of SQ2 and the resulting decreased probability of radiationless decay of the excited state and/or improved accessibility of oxidized SQ2 for regeneration by the electrolyte, as well as the suppression of potential energy transfer from the indoline dyes to SQ2 in the presence of the coadsorbates. As a result of the effects of the presence of CA and/or OA on light harvesting and electron injection/dye regeneration, $\eta_{lh,int}$ is the main limiting factor for the integrated external quantum efficiency in all four cells with coadsorbates studied in this chapter.

## 6.6 Summary and Conclusions for This chapter

A new method to fabricate panchromatic solar cells based on electrodeposited porous ZnO by co-sensitization with the indoline dyes D149 and D131 and the squaraine dye SQ2 was presented. DSCs with the individual sensitizers were studied along with cells containing different combinations of the three dyes, adsorbed either from a mixed dye bath (D149/D131) or sequentially (SQ2 with D149 or with D149/D131). The influence of the coadsorbates cholic acid (CA) and octanoic acid (OA) was also studied.

UV/Vis absorption spectroscopy of the dye-sensitized films proved successful adsorption of all sensitizers both individually and together with other dyes and showed that the presence of the coadsorbates led to a slight reduction in the dye loading. As desired, ZnO films combining SQ2 with indoline dyes showed very broad absorption extending from 350 nm to ≥ 700 nm. Current-voltage characterization, IPCE measurements, impedance spectroscopy (EIS), intensity-modulated photoelectron spectroscopy (IMPS) and charge extraction were utilized to reveal how the various dyes, dye mixtures and dye-coadsorbate combinations affect device characteristics, charge transport, and charge recombination in the cells. Co-sensitization with SQ2, D149 and D131 in the presence of coadsorbates led to the highest short-circuit photocurrent density among the cells studied in this chapter, exceeding the $J_{sc}$ achieved with any of the three sensitizers individually. Combining results of UV/Vis absorption spectroscopy, EIS, and IMPS, it was found that the charge collection efficiency approached 100% in all samples. The photocurrent efficiency was mostly limited by the integrated light harvesting efficiency, even in the co-sensitized cell SQ2/CA+D149/D131/OA that showed extended light harvesting compared to D149/CA. By contrast, in the cells containing SQ2 without coadsorbate, $J_{sc}$ was limited by the low combined electron injection/dye regeneration efficiency (≤ 37%). The relatively low short-circuit photocurrents of D149/CA and SQ2/CA compared to titania-based devices using the same dyes are concluded to be due to relatively lower injection or regeneration efficiencies ($\eta_{inj} \cdot \eta_{reg}$ = 64% for D149 and $\eta_{inj} \cdot \eta_{reg}$ = 22% for SQ2). Samples with SQ2 exhibited reduced open-circuit photovoltages, which limited the overall efficiency of the SQ2/CA+D149/D131/OA cell to a value just comparable to the cell containing only D149. By use of impedance spectroscopy, the three main origins of variations in $V_{oc}$ – conduction band edge shifts, differences in the short-circuit photocurrent density, and variations in the rate constant of recombination – were quantified based on the $\beta$-recombination model, revealing the detailed influence of the different dyes and dye combinations on the balance between charge injection and charge recombination. For the dye combination SQ2/CA+D149/D131/OA, for example, the loss in photovoltage with respect to D149 as individual sensitizer was due to a relative downward shift of the conduction band edge of ZnO by about 40 mV. The particularly low open-circuit photovoltages and fill factors seen in cells containing the squaraine sensitizer without coadsorbates were connected to the appearance of a local maximum

in the chemical capacitance and a local minimum in the recombination resistance, both located at a quasi-Fermi level of about 0.3 eV (above $E_{redox}$) and indicative of the presence of additional deep electronic states in the dye-sensitized ZnO. Independent measurements of the recombination current (in the dark and under AM1.5G-type white light) corroborated this finding and showed that the additional recombination was only observed under illumination. When coadsorbates were employed, the effect was considerably reduced and open-circuit voltage and fill factor were improved accordingly. The observed influence of illumination and presence of coadsorbates indicated that the additional deep trap states causing the increase in the rate of recombination were formed by aggregated, oxidized SQ2 molecules.

A modified protocol for the determination of conduction band edge shifts from EIS-derived chemical capacitance curves was introduced. Using short-circuit charge extraction, it was demonstrated that the total trap density of the ZnO films, which is commonly assumed to be equal among sets of cells analyzed with respect to $\Delta E_c$, varies systematically depending on the adsorbed dyes and coadsorbates. A newly introduced normalization of the chemical capacitance by relative values of the total trap density – as previously proposed by others for charge density curves – was demonstrated to have a significant effect on the results obtained for the conduction band edge shifts, suggesting that this revised protocol is an important precondition to correctly assess $\Delta E_c$.

As the power conversion efficiency observed for the combination of SQ2, D149, and D131 was chiefly limited by aggregate-promoted recombination as well as a significant relative downward shift of the conduction band edge induced by SQ2, future work should focus on testing alternative red-absorbing dyes for ZnO that show less aggregation and yield high open-circuit photovoltages. Moreover, alternative coadsorbates that cause a higher position of the conduction band edge of the electrodeposited ZnO and are more efficient in preventing the formation of dye aggregates are sought.

# 7 Panchromatic Solar Cells Based on Nanoparticulate ZnO Films

## 7.1 Introductory Remarks

A series of screenprinted nanoparticulate ZnO (np-ZnO) films was sensitized with the dyes D149, D131, or SQ2 in the presence or absence of the coadsorbates cholic acid (CA) or octanoic acid (OA) to test whether the results of chapter 6 are reproduced for this type of nanostructure and to examine general differences between cells based on electrodeposited (edep-ZnO) and nanoparticulate ZnO. Based on BET measurements of similarly fabricated nanoparticulate ZnO films,[161] the inner surface area of the ~10 µm thick films can be estimated at about 0.015 $m^2$, compared to a slightly smaller value of about 0.011 $m^2$ estimated for the electrodeposited films with average thickness of 4.2 µm (cf. ***Figure 33*** and ***Table 30***) using an approximate roughness factor of 400.[25] Thus, the difference in surface area accessible for attachment of dye molecules is expected to be rather small in spite of the significant difference in film thickness. In addition to the dye and dye/coadsorbate combinations studied in chapter 6, a film with D131/OA and a film co-sensitized with all dyes in a three-step sequence (SQ2/CA+D131/OA+D149/D131/OA) were prepared. The additional step of pre-adsorbing D131/OA prior to immersion in D149/D131/OA solution was introduced to test whether the presence of D131 – a dye showing negligible aggregation on ZnO (cf. ***Figure 50***) – may affect the arrangement of subsequently adsorbed D149 and D131 and thereby influence the cell properties.

## 7.2 Optical Absorption

The UV/Vis absorption spectra of the films sensitized with D131, D149, the combination D149/D131, or SQ2 without coadsorbates (***Figure 63*** (a), broken lines) resemble those of the corresponding electrodeposited ZnO films (***Figure 50***), both in shape and height. The spectrum of an additional np-ZnO/SQ2 film with a slightly smaller dye loading (short-dashed blue line in ***Figure 63*** (a)) shows the monomer band (~ 660 nm) together with aggregate-related (cf. ***Figure 49*** (a)) subbands at 600 – 610 nm and ~690

nm, clearly confirming that the broad peak shape observed for SQ2 without CA both on electrodeposited and on nanoparticulate ZnO is due to aggregation.

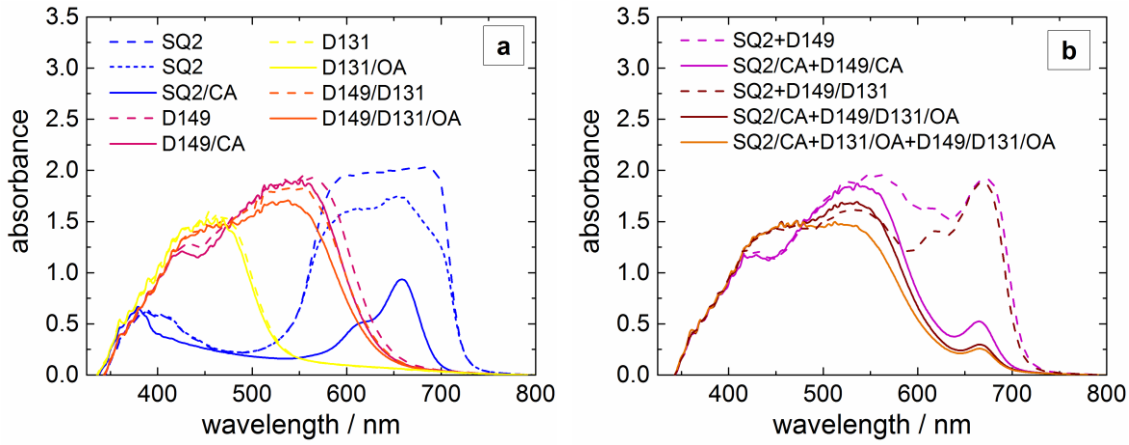


***Figure 63**: UV/Vis absorption spectra of the nanoparticulate ZnO films sensitized with D149, D131, and/or SQ2, in the presence (solid lines) or absence (dashed lines) of the coadsorbates cholic acid or octanoic acid using solutions prepared identically to those employed in chapter 6 (cf. **Figure 49**). The sample with D131 suffered from irreparable damage in the midst of its characterization and will therefore not be part of most of the remaining discussion.*

The three samples SQ2, SQ2/CA, and D131 show an unexpectedly high absorbance of increasing intensity towards decreasing wavelengths in a range in which the dyes are not expected to absorb light (~400 – 550 nm for SQ2 and ~550 – 700 nm for D131, cf. ***Figure 49*** (a)). The effect could be an artifact due to temporal instabilities in the spectral reflectivity of the integrating sphere used in the measurements. Alternatively, it may have been caused by particularly strong Rayleigh scattering of incident light at the nanoparticulate ZnO films, which becomes stronger towards smaller wavelengths ($\propto \lambda^{-4}$)[301] and could have prevented a part of the transmitted light of shorter wavelengths from being detected in spite of the use of the integrating sphere. The IPCE in the corresponding ranges was virtually zero (see ***Figure 66*** in the following section), further supporting that the apparent additional absorbance did not correspond to a real light absorption by the dyes. Combining SQ2 and D149 or SQ2 and D149/D131 (with or without coadsorbate) on np-ZnO films yielded the desired panchromatic absorption (***Figure 63*** (b)), confirming that these dyes can co-exist as adsorbates also on nanopar-

ticulate ZnO. By comparison of the spectra of the films SQ2/CA+D149/D131/OA and SQ2/CA+D131/OA+D149/D131/OA (***Figure 63*** (b)), the additional dipping in D131/OA solution is found to be detrimental, as it did not result in an increased absorbance by D131 but diminished the absorption by the other two sensitizers. As in the previous chapters, addition of CA reduced aggregation of D149 and, in particular, SQ2, as apparent from the reduced widths of the corresponding absorption bands both in the samples with the individual dyes as well as in co-sensitized films. The largely monomeric adsorption of the dye D131 is proven by the near congruence of the spectra of D131 and D131/OA.

Comparing the integrated absorbances $abs_{int}$ of np-ZnO films and edep-ZnO films sensitized with the same dye(s) and coadsorbate(s), ***Table 18***, allows discussing differences in the total dye loading assuming that the molar absorptivity of the individual dyes was constant. For most dyes or dye combinations without coadsorbates, the total dye loading in the np-ZnO films exceeded that in the electrodeposited samples by a factor of 1.1 – 1.2, approximately in line with the estimated increase in surface area by a factor of 1.4 (cf. section 7.1). Among the samples containing coadsorbates, the difference in total dye loading between np-ZnO and edep-ZnO was even more significant (see discussion below), with the $abs_{int}$ values of the former exceeding those of the latter by a factor of 1.4 – 1.8. In contrast, the co-sensitized np-ZnO samples with SQ2+D149 or SQ2+D149/D131 show a lower integrated absorbance than the corresponding edep-ZnO films, which is mainly due to the lower SQ2 loading (see long-wavelength range of dashed lines in ***Figure 63*** (b)). For np-ZnO films, the SQ2 adsorbed in the first step of the sequential co-sensitization thus appears less resistant against replacement by D149 or D131 in the second adsorption step than for electrodeposited ZnO films. This is corroborated by the fact that a blue discoloration of the D149 or D149/D131 solutions was observed after dipping the SQ2-loaded np-ZnO films into these solutions, while no such observation could be made in the sensitization of electrodeposited ZnO. The presence of CA and/or OA in the sensitization of np-ZnO films generally led to a reduction of the total dye loading, as was the case for edep-ZnO films (see ***Table 18***, middle and right column, and ***Figure 50***).

***Table 18**: Integrated absorbance (integration range 350 - 750 nm) of the nanoparticulate ZnO films compared to the corresponding values of their electrodeposited counterparts with the same dyes and coadsorbates.*

| dye(s) and coadsorbate(s) | $abs_{int}$ (np-ZnO) / nm | $abs_{int}$ (edep-ZnO) / nm |
|---|---|---|
| D149 | 380 | 337 |
| D131 | 207 | 168 |
| D149/D131 | 360 | 298 |
| SQ2 | 374 | 336 |
| SQ2+D149 | 512 | 608 |
| SQ2+D149/D131 | 464 | 567 |
| D149/CA | 355 | 202 |
| D149/D131/OA | 333 | 193 |
| SQ2/CA | 132 | 72 |
| SQ2/CA+D149/CA | 359 | 258 |
| SQ2/CA+D149/D131/OA | 338 | 236 |

However, on nanoparticulate ZnO the dyes (particularly D149 and D131) were more stable against replacement by coadsorbates, as apparent from the smaller coadsorbate-induced changes of the height of the absorbance bands (***Figure 63*** vs. ***Figure 50***) and of the integrated absorbances of the films with individual sensitizers (***Table 18***). For example, the relative reductions of $abs_{int}$ upon adding cholic acid to SQ2 or D149 are 78% and 40% for edep-ZnO, but only 65% and 7% for np-ZnO. The increased stability of the dye attachment in the presence of CA and OA explains why the nanoparticulate samples with coadsorbates showed a particularly high dye loading with respect to the edep-ZnO films.

## 7.3 Device Performance and External Quantum Efficiency

The *J-V* characteristics and photovoltaic parameters under AM1.5G illumination of solar cells built from the dye-sensitized np-ZnO films are presented in ***Figure 64*** and ***Table 19***.

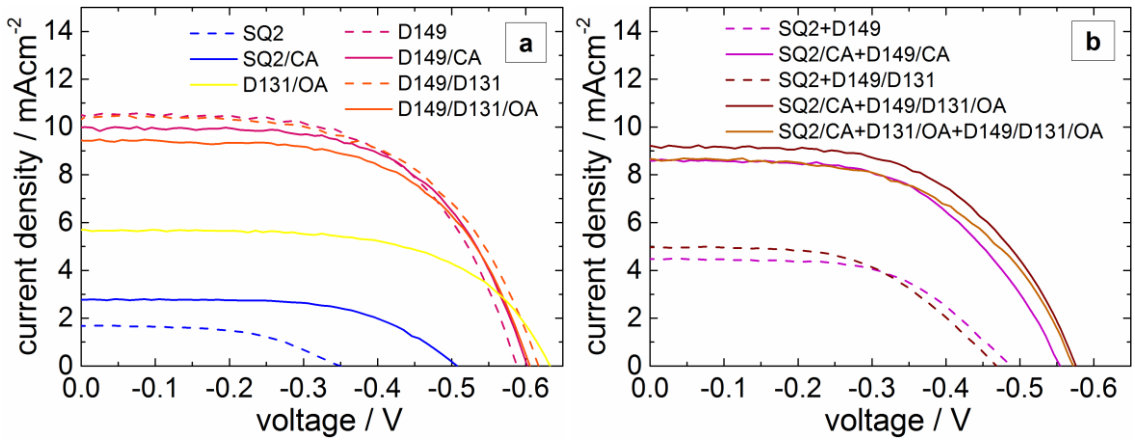


***Figure 64****: Current-voltage characteristics of DSCs based on np-ZnO films sensitized with D149, D131, SQ2, or various combinations of these dyes, in the presence (——) or absence (- - - -) of the coadsorbates CA and/or OA.*

With the exception of the cell with SQ2, the DSCs based on nanoparticulate zinc oxide show better power conversion efficiencies than the corresponding cells based on electrodeposited ZnO (***Table 11***, values repeated in ***Table 19*** for easier comparison). For the cells with one or both indoline dyes (with or without CA/OA), the improvement is caused by considerably enhanced $J_{sc}$ values along with improved $V_{oc}$'s. The cells with SQ2, SQ2+D149, or SQ2+D149/D131 without coadsorbates exhibit higher fill factors and/or higher open-circuit voltages but somewhat lower short-circuit current densities than the corresponding cells based on edep-ZnO, overall resulting in an only slightly improved (or, for SQ2, somewhat smaller) conversion efficiency. In the case of SQ2/CA and the co-sensitized DSC SQ2/CA+D149/D131/OA, the overall performance was improved owing to clearly enhanced voltages and slightly better short-circuit currents. A further discussion of the factors governing the $J_{sc}$ in the nanoparticulate ZnO solar cells with SQ2, D149, and/or D131 will be given below and in section 7.6, and reasons for the different $V_{oc}$ and *FF* will be discussed in 7.7.

***Table 19**: Photovoltaic parameters of the solar cells based on dye-sensitized np-ZnO as well as theoretical short-circuit current densities $J_{sc}^{theo}$ determined from the IPCE spectra. Where possible, the corresponding values of the electrodeposited samples of chapter 6 are given in parentheses for comparison.*

| **sample code** | $J_{sc}$ / mAcm$^{-2}$ | $J_{sc}^{theo}$ / mAcm$^{-2}$ | $V_{oc}$ / mV | *FF* | $\eta$ / % |
|---|---|---|---|---|---|
| NP_D149 | 10.47 (7.8) | 9.16 (7.6) | -0.59 (-0.56) | 0.59 (0.59) | 3.65 (2.57) |
| NP_D149/D131 | 10.41 (6.0) | 8.67 (7.8) | -0.62 (-0.58) | 0.58 (0.59) | 3.73 (2.04) |
| NP_SQ2 | 1.68 (2.6) | 0.79 (2.7) | -0.34 (-0.34) | 0.54 (0.51) | 0.31 (0.45) |
| NP_SQ2+D149 | 4.48 (5.1) | 3.90 (5.2) | -0.49 (-0.40) | 0.57 (0.52) | 1.24 (1.04) |
| NP_SQ2+D149/D131 | 4.97 (6.0) | 4.01 (6.2) | -0.47 (-0.40) | 0.54 (0.49) | 1.24 (1.20) |
| NP_D149/CA | 9.99 (5.8) | 8.77 (5.6) | -0.6 (-0.56) | 0.61 (0.64) | 3.63 (2.06) |
| NP_D131/OA | 5.69 | 4.14 | -0.63 | 0.62 | 2.2 |
| NP_D149/D131/OA | 9.43 (6.7) | 7.74 (6.0) | -0.59 (-0.58) | 0.62 (0.63) | 3.45 (2.42) |
| NP_SQ2/CA | 2.78 (2.7) | 2.35 (2.9) | -0.51 (-0.46) | 0.6 (0.61) | 0.85 (0.74) |
| NP_SQ2/CA+D149/CA | 8.59 | 8.69 | -0.55 | 0.57 | 2.65 |
| NP_SQ2/CA+ D149/D131/OA | 9.19 (8.6) | n.a. (8.7) | -0.57 (-0.54) | 0.57 (0.55) | 2.99 (2.55) |
| NP_SQ2/CA+ D131/OA+ D149/D131/OA | 8.65 | n.a. | -0.57 | 0.55 | 2.71 |

Among the *J-V* curves of the cells based on nanoparticulate ZnO with different dyes and dye combinations in ***Figure 64***, similar trends can be seen as among the cells built from edep-ZnO (***Figure 51***). Most notably, the poor $J_{sc}$, $V_{oc}$, and fill factor of SQ2 are confirmed for this type of ZnO structure. The main difference to the edep-ZnO samples is that the best short-circuit photocurrent densities among the present samples were clearly achieved with D149 and D149/D131 (without coadsorbate)[X] rather than by co-sensitization with SQ2, D149, and D131, as was the case for the edep-ZnO samples. Use of D131/OA resulted in the highest open-circuit photovoltage, but only in a moderate short-circuit photocurrent density. The co-sensitized cells combining SQ2 with indoline dyes all show $J_{sc}$ and $V_{oc}$ values in between those of SQ2 and the indoline dye cells. SQ2/CA+D131/OA+D149/D131/OA delivered the same $V_{oc}$ but a smaller short-circuit current and *FF* with respect to SQ2/CA+D149/D131/OA, demonstrating that the additional adsorption step led to a worsening of the conversion efficiency and was redundant. The best power conversion efficiency among the np-ZnO cells was attained using the indoline dye combination D149/D131 without coadsorbates, which yielded a larger $V_{oc}$ than D149 alone. Concerning the effect of CA and OA on the photovoltaic performance, two major results obtained for the edep-ZnO cells are confirmed: (1) the fill factor is generally increased and, (2) the $J_{sc}$ and $V_{oc}$ of all samples containing SQ2 (individually or in combinations) are considerably improved with respect to the coadsorbate-free counterparts. The decrease of $J_{sc}$ by coadsorption of CA or OA with D149 or D149/D131 is clearly less severe than in the case of electrodeposited samples, which is the result of the dye loading remaining relatively high in the np-ZnO-based cells with coadsorbates (cf. previous section).

Together with the spectral light harvesting efficiencies $\eta_{lh}$ (***Figure 65***), the IPCE spectra of the various dye-sensitized np-ZnO films, ***Figure 66***, further confirm the dye- and coadsorbate-dependent trends observed for electrodeposited ZnO.

[X] Note that the $J_{sc}$ values obtained for D149 and D149/D131 (with or without coadsorbate) on np-ZnO were almost the same, further confirming that the short-circuit currents obtained with D149/CA and D149/D131/OA on edep-ZnO would normally be similar as well.

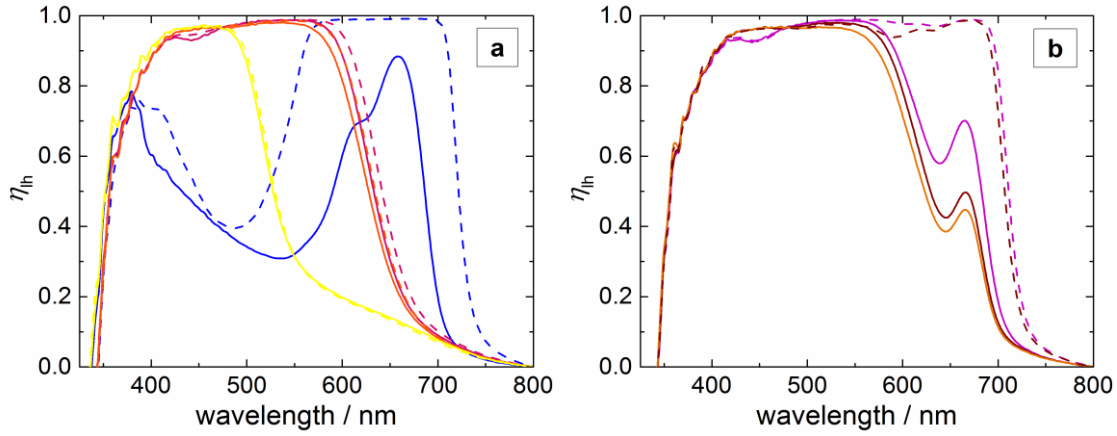


***Figure 65**: Light harvesting efficiency of the various np-ZnO films calculated from the absorbance spectra. Assignment of colors and line styles as in the figure below. The apparent light harvesting in the cells D131, SQ2, and SQ2/CA in the mid-wavelength range is likely due to strong light scattering by the np-ZnO films (cf. **Figure 63** and discussion).*

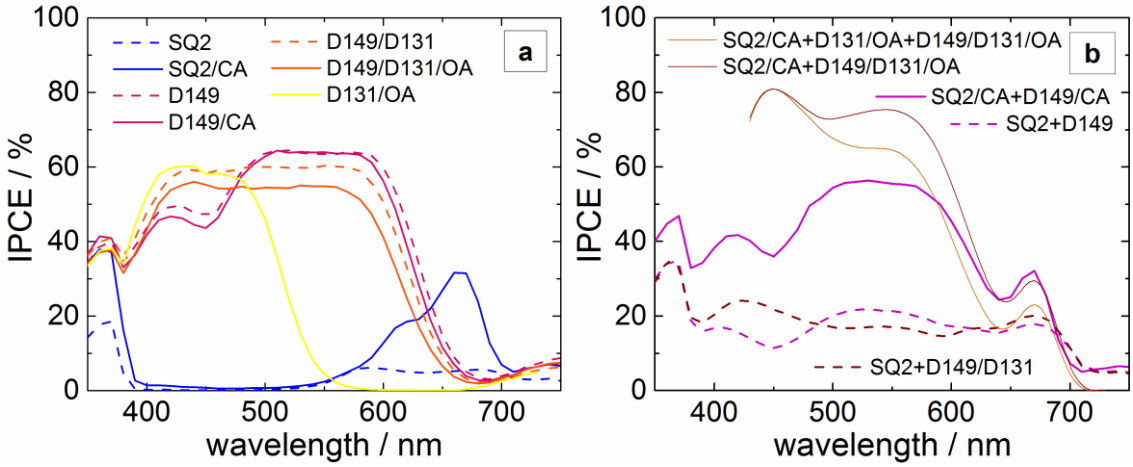


***Figure 66**: External quantum efficiency (IPCE) spectra of np-ZnO DSCs with different sensitizers and sensitizer combinations. The spectra of the samples SQ2/CA+D149/D131/OA and SQ2/CA+D131/OA+D149/D131/OA (thin lines in (b)) were measured by a different experimental setup (Zahner setup, cf. Appendix C) and can only be qualitatively compared to the other spectra presented her.*

Most significantly, the effects of SQ2 as individual sensitizer or co-sensitizer on ZnO are corroborated. As in the case of electrodeposited samples, the very low $J_{sc}$ obtained

with SQ2 was due to hindered electron injection and/or dye regeneration, as indicated by a maximum IPCE much lower than expected based on the high light-harvesting efficiency. Moreover, in co-sensitized samples containing SQ2 without coadsorbates, the short-circuit photocurrent remained low because SQ2 suppressed efficient conversion of absorbed light by D149 and D131, as apparent from the high light-harvesting efficiency but low IPCE in the range 400 – 600 nm. Coadsorption of CA and/or OA again suppressed the undesired dye/dye interactions and enabled a significant improvement of the IPCE over the whole wavelength range. However, unlike in the cells based on electrodeposited ZnO, the combination of SQ2 with indoline dyes in the presence of coadsorbates on np-ZnO yielded inferior $J_{sc}$ values with respect to the cells with indoline dyes only (with or without coadsorbates), because the additional IPCE created by SQ2 in the red part of the spectrum was overcompensated by reduced IPCE values in the absorption range of the indoline dyes, as seen directly in the spectrum of the sample SQ2/CA+D149/CA in ***Figure 66***.[XI]

The theoretical short-circuit current densities $J_{sc}^{theo}$ derived from the IPCE spectra via eq. (36) (***Table 19***) are qualitatively in line with the experimental $J_{sc}$. However, the theoretical values on average amount to only 80% of the experimental values, showing that the measured IPCE tended to be underestimated. A possible reason for this could be strong light scattering by the nanoparticulate ZnO samples, as also suggested the optical absorption (***Figure 63*** and ***Figure 65***), which may have led to an overestimation of the light intensity actually available for absorption and photocurrent generation by the dyes and, in consequence, to an underestimation of the IPCE (see also Appendix C).

## 7.4 Trap Density, Trap Distribution and Conduction Band Edge Shifts

The semilogarithmic capacitance plots of the dye-sensitized np-ZnO solar cells obtained by electrochemical impedance spectroscopy under AM1.5G white light (in the follow-

[XI] While the presented spectra for SQ2/CA+D149/D131/OA and SQ2/CA+D131/OA+D149/D131/OA are not quantitatively comparable to the other spectra (different measurement setup used), a comparison with identically measured spectra of indoline dye cells (cf. ***Figure 103*** in Appendix C) confirms that these cells also suffered from a reduced IPCE in the D149/D131 range that offset the gains in the red part.

ing referred to as EIS$^{AM1.5G}$) (***Figure 67*** (a)) are linear for voltages of about -0.45 V or more negative, confirming that the obtained capacitance constitutes a chemical capacitance determined by an exponential distribution of trap states, as in previous chapters.

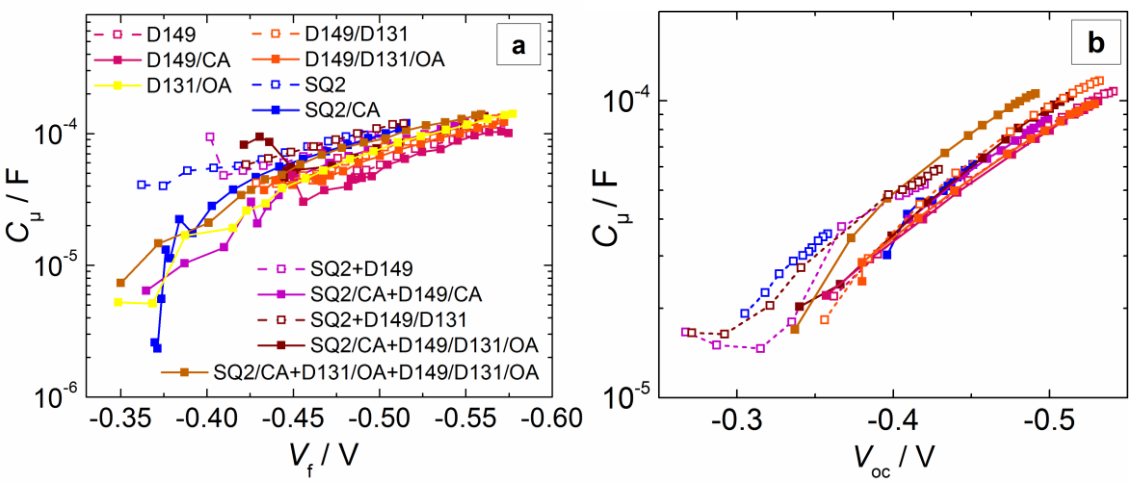


***Figure 67****: Capacitance vs. Fermi-level voltage ($V_f$ or $V_{oc}$) plots of the DSCs based on dye-sensitized np-ZnO films from voltage-dependent EIS under AM1.5G (100 mWcm$^{-2}$) illumination (a) and from EIS at open circuit under illumination by a red LED with varied intensity (b). Legend in (a) refers to both plots. Lines are a guide to the eye only.*

The values shown for voltages less negative than ca -0.45 V cannot be considered reliable, because the fit quality in this voltage range was insufficient due to pronounced scattering of the EIS spectra. However, impedance data measured under varied monochromatic illumination at open circuit (in the following referred to as EIS$^{oc,red}$) allowed to obtain good fits down to less negative voltages, see ***Figure 67*** (b). These curves reveal an onset of a local increase of $C_\mu$ around ca -0.3 V for the cells SQ2+D149 and SQ2+D149/D131, indicating that adsorption of SQ2 without coadsorbates led to the formation of additional deep traps, as was the case (cf. ***Figure 53***) for the corresponding DSCs based on edep-ZnO. (For the np-ZnO cell with SQ2 as individual sensitizer, the EIS data could not be meaningfully evaluated down to the relevant voltage range).

The trap distribution parameters $\alpha$ derived from the exponential part of the $C_\mu$ curves of EIS$^{AM1.5G}$ (fits to eq. (52) shown in the normalized capacitance curves in ***Figure 69*** (b) for better visibility) all showed comparable values of 0.22 +/- 0.03, see ***Table 20***. This is confirmed by the corresponding values from EIS$^{oc,red}$ (see fits in ***Figure 69*** (b) and results in ***Table 20***), which for a given dye or dye combination mostly did not deviate by

more than 0.02 from the $\alpha$ parameters from $EIS^{AM1.5G}$. Somewhat larger differences of 0.04 – 0.06 are found for the cells SQ2, SQ2/CA, SQ2+D149, and D149/CA. For most of them, the $C_\mu$ curves from $EIS^{oc,red}$ did not reach into the negative voltage range beyond -0.45 V, so that the $\alpha$ values were probably not an accurate measure of the exponential trap distribution. Altogether, the trap distribution parameters of 0.16 – 0.28 found here are clearly lower than the $\alpha$ values of 0.32 – 0.44 found for the electrodeposited samples of chapter 6, which shows that the trap distribution in the nanoparticulate ZnO films was significantly steeper than in the electrodeposited ZnO, in line with results of previous studies.[136]

To determine the relative conduction band edge shifts between the different cells, the chemical capacitances from $EIS^{AM1.5G}$ and $EIS^{oc,red}$ were first normalized by the relative total trap densities (see ***Table 20***), determined from the short-circuit charge density under varied illumination by a red LED (***Figure 68***) by use of the same procedure as in chapter 6.3.1.

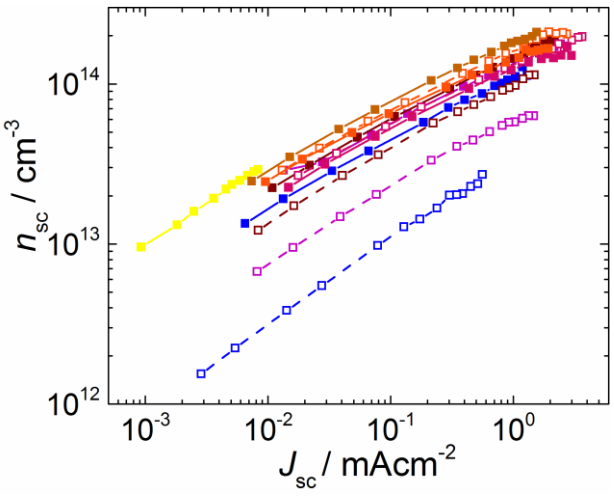


***Figure 68***: *Charge-density under short-circuit conditions for different illumination intensities and resulting short-circuit current densities, used to determine the relative total trap densities of the different cells. See legend in previous figure for the meaning of colors and symbols.*

***Table 20***: *Relative total trap densities $N_t/N_{t,ref}$ (reference sample: NP_D149), as well as relative conduction band edge shifts $\Delta E_c/q$ (reference sample: NP_D149; positive val-*

*ues: downward shifts, negative values: upward shifts) and trap distribution parameters α determined from the $C_\mu$ curves from $EIS^{AM1.5}$ or $EIS^{oc,red}$.*

| **sample code** | $N_t/N_{t,ref}$ | $\Delta E_c/q$ / mV $EIS^{AM1.5}$ | $\Delta E_c/q$ / mV $EIS^{oc,red}$ | $\alpha$ $EIS^{AM1.5}$ | $\alpha$ $EIS^{oc,red}$ |
|---|---|---|---|---|---|
| NP_D149 | 1.0 (ref.) | +/- 0 (ref.) | 0 | 0.23 | 0.21 |
| NP_D149/D131 | 1.2 | +/- 0 | - 7 | 0.22 | 0.20 |
| NP_SQ2 | 0.2 | + 267 | + 237 | 0.21 | 0.26 |
| NP_SQ2+D149 | 0.4 | + 161 | + 150 | 0.22 | 0.16 |
| NP_SQ2+D149/D131 | 0.7 | + 112 | + 74 | 0.21 | 0.22 |
| NP_D149/CA | 0.9 | +/- 0 | + 9 | 0.25 | 0.21 |
| NP_D131/OA | 1.4 | - 20 | n.a. | 0.22 | n.a. |
| NP_D149/D131/OA | 1.2 | - 11 | - 22 | 0.22 | 0.21 |
| NP_SQ2/CA | 0.8 | + 70 | + 34 | 0.24 | 0.28 |
| NP_SQ2/CA+D149/CA | 1.0 | + 28 | + 6 | 0.23 | 0.22 |
| NP_SQ2/CA+ D149/D131/OA | 1.1 | + 16 | +/- 0 | 0.23 | 0.22 |
| NP_SQ2/CA+ D131/OA+ D149/D131/OA | 1.4 | + 3 | +/- 0 | 0.19 | 0.21 |

Comparing the short-circuit charges of the edep-ZnO samples and the np-ZnO samples at a current density of 0.05 $mAcm^{-2}$ (***Figure 54*** vs. ***Figure 68***), lower values are found for the np-ZnO samples than for their edep-ZnO-based counterparts, indicating lower total trap densities in the nanoparticulate zinc oxide.[XII] For example, the $n_{sc}$ ratio and, hence, the relative total trap density of np-ZnO with D149 compared to edep-ZnO with

D149 was estimated at 0.4. This is in line with results of photoluminescence measurements by Pauporté et al. finding higher defect densities in electrodeposited than in nanoparticulate ZnO films.[136] Using the nanoparticulate sample with D149 as a new reference, dye-dependent changes largely comparable to those observed for edep-ZnO are found, ***Table 20***. The cells containing indoline dyes without coadsorbates show very similar trap densities, while SQ2 exhibits a markedly lower $N_t/N_{t,ref}$ and the co-sensitized cells with SQ2+D149 or SQ2+D149/D131 show trap densities in between that of SQ2 and the indoline dyes. With $N_t/N_{t,ref}$ for SQ2 being only one fifth of that for D149, the decrease of the relative total trap density induced by SQ2 is even more pronounced than for the electrodeposited samples, perhaps indicating a reduced (bulk-determined) lower limit of $N_t$ in the nanoparticulate films. The observed effects of coadsorbates on the total trap density, on the other hand, clearly differ from the influence found in chapter 6. No significant influence can be seen for the indoline dyes (compared to a 50% decrease on edep-ZnO), while a significant increase by a factor of 4 is found for SQ2 (compared to no notable change on edep-ZnO). The effect of different surface adsorbates on defect densities is expected to depend on the (relative) surface coverage. The negligible effect of CA and OA on $N_t/N_{t,ref}$ could, thus, be the result of the relatively small influence these coadsorbates had on the amount of adsorbed dyes in the np-ZnO films (cf. ***Figure 63***). Likewise, the fact that the relative trap densities of the three co-sensitized samples containing SQ2 and coadsorbates are closer to those of D149/CA, D131/OA, and D149/D131/OA than to that of SQ2/CA may reflect their relatively small SQ2 loading (***Figure 63***). The pronounced increase of $N_t/N_{t,ref}$ for SQ2/CA compared to SQ2 is roughly in line with the decrease of the SQ2 loading (cf. $abs_{int}$ values in ***Table 18***), i.e., SQ2 seems to lead to a much stronger reduction of the trap density in np-ZnO with respect to CA.

The relative conduction band edge shifts (***Table 20***) obtained from the $N_t/N_{t,ref}$-normalized capacitance curves of the two different EIS measurements (***Figure 69***)

[XII] Note, however, that the slopes of the $n_{sc}$ vs. $J_{sc}$ curves were different for np-ZnO and edep-ZnO as a result of the different trap distributions, which precluded an exact analysis of the difference in trap densities.

showed similar sample-to-sample trends, but $EIS^{oc,red}$ tended to deliver somewhat less positive or more negative values for $\Delta E_c/q$.

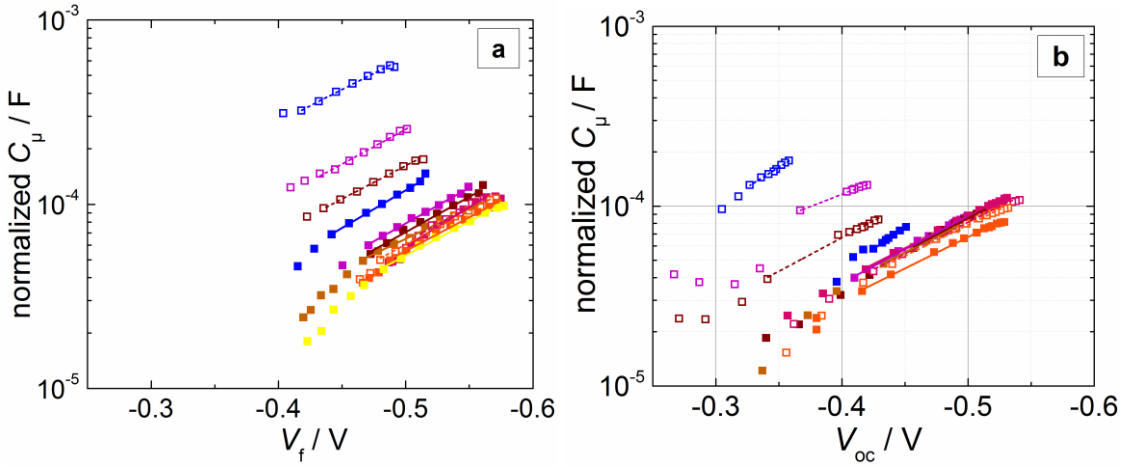


***Figure 69**: Chemical capacitances derived from EIS under varied red illumination at open-circuit (a) or under AM1.5G illumination at varied bias voltages (b) after normalization by the relative total trap densities in **Table 20**. Color and symbol assignment as in **Figure 67**. Lines represent linear fits.*

A separate direct comparison of the normalized capacitance curves from $EIS^{oc,red}$ and $EIS^{AM1.5G}$ of the cell with D149 showed a positive shift by 20 mV along the voltage axis for the curve derived from $EIS^{oc,red}$, which reflects a relative downward shift that may have been caused by the longer light soaking (and possibly aging) the cell had already experienced when the $EIS^{oc,red}$ measurements were performed (about 2 hours and several measurements after $EIS^{AM1.5G}$), cf. chapter 9. The other cells apparently showed somewhat different (time-dependent) changes of the conduction band edge that may have led to the observed variations between the shifts derived from $EIS^{oc,red}$ and $EIS^{AM1.5G}$. The relative conduction band edge shifts between the samples with different dyes and dye combinations qualitatively confirm the results attained for the corresponding edep-ZnO samples. The cells with D149 or D149/D131 showed approximately similar positions of $E_c$ while the sample with SQ2 exhibited a pronounced downward shift by about 270 mV.

Note that previous EIS studies comparing $TiO_2$-based DSCs with a number of different sensitizers reported band edge shifts by up to 400 mV,[128] confirming that the conduction

band edge shifts observed in the present study are in a perfectly reasonable range. The combinations SQ2+D149 and SQ2+D149/D131 again exhibit a slightly smaller relative downward shift of $E_c$ by about 160 mV and about 110 mV, reflecting the combined effect of the presence of SQ2 and indoline dyes on the band edge position. In the presence of coadsorbates the downward shift of $E_c$ observed for the three dye combinations is strongly reduced to 70 mV (SQ2/CA), 28 mV (SQ2/CA+D149/CA), and 16 mV (SQ2/CA+D149/D131/OA). However, the band edge shifts found for the three cells with SQ2 and indoline dyes in the absence of coadsorbates are notably higher than the $\Delta E_c/q$ of ~60 – 110 mV reported for the electrodeposited cells (cf. ***Table 13***), while in the presence of coadsorbates they are smaller than the $\Delta E_c/q$ of ~40 – 90 mV of the edep-ZnO samples. Furthermore, in contrast to the downward shifts of $E_c$ observed for the electrodeposited samples with indoline dyes upon addition of the coadsorbates CA and/or OA in the previous chapter, no shift (D149/CA) or a slight upward shift (D149/D131/OA) are found for the present np-ZnO cells. These different impacts of SQ2 and the coadsorbates on the conduction band edge in np-ZnO and edep-ZnO could have partially been caused by changes in the relative amounts of SQ2 (as well as other dyes) and CA/OA on the inner surface of the films and partially by different initial surface terminations (e.g., -OH groups) of the bare materials without dyes and coadsorbates.

## 7.5 Electron Recombination and Transport

Both voltage-dependent EIS under illumination with simulated solar light and EIS under varied red illumination at open circuit yielded semilogarithmic recombination resistance plots, ***Figure 70***, with the widely linear behavior typical for nanostructured semiconductors with an exponential distribution of trap states. The $R_{rec}$ values obtained by EIS$^{oc,red}$ are quite comparable to those from EIS$^{AM1.5G}$ around a voltage of -0.5 V, but the curves show considerably higher slopes that cause an increasing difference towards smaller voltages (see discussion further below).

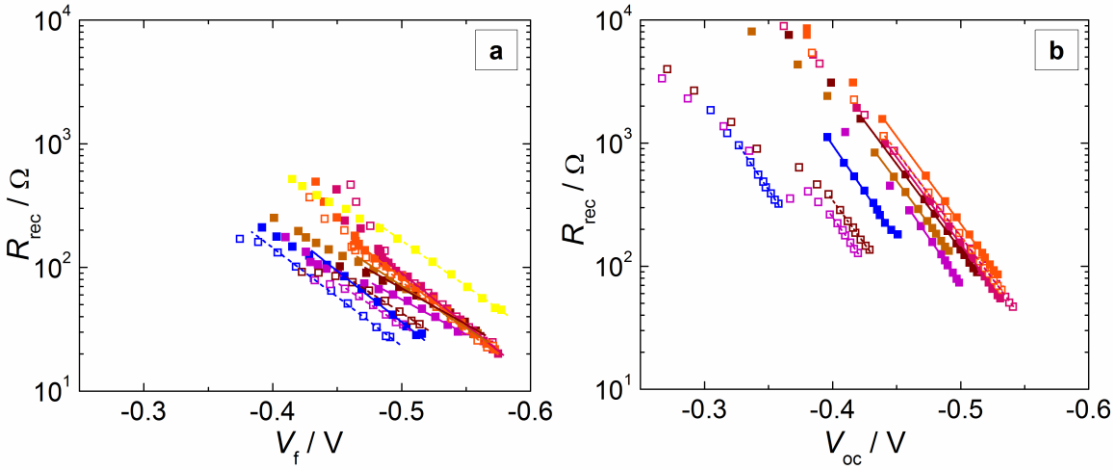


***Figure 70**: Recombination resistance of np-ZnO-based DSCs with different dyes and dye combinations as a function of the Fermi-level voltage ($V_f$ or $V_{oc}$) from voltage-dependent EIS under illumination with AM1.5G white light (a) or EIS under varied illumination with a red LED at open circuit (b). The lines represent linear fits. Legend as in **Figure 67**.*

A similar dye-dependence of the recombination resistance (uncorrected for band edge shifts) is observed for the two different EIS methods, and the trends are roughly in line with the results attained on electrodeposited ZnO (cf. ***Figure 58***). The indoline dyes and indoline dye combinations, both with or without coadsorbates, yielded the highest $R_{rec}$, with D131/OA markedly showing the best results. The cells containing SQ2 without CA/OA showed the overall lowest recombination resistances and among them $R_{rec}$ decreased with increasing amount of SQ2 in the films (cf. ***Figure 63***). The distinction in $R_{rec}$ between the np-ZnO-based cells with SQ2 and those containing only indoline dyes is even more pronounced than among the edep-ZnO cells as a result of the larger conduction band edge shifts. While the presence of coadsorbates in the electrodeposited samples led to higher recombination resistances for all dyes or dye combinations, on nanoparticulate ZnO this improvement was only observed SQ2 or mixtures of SQ2 and indolines. For the edep-ZnO cells with SQ2, SQ2+D149, or SQ2+D149/D131, $R_{rec}$ (***Figure 58***) exhibited a pronounced local minimum at ca -0.3 V as a result of recombination via additional deep traps related to aggregated SQ2 cations. The $R_{rec}$ curves of the present samples show only very faint indications of a locally increased rate of recombination at lower voltages: an onset of a flattening at $V_f \approx$ -0.4 V in the corresponding curves from $EIS^{AM1.5G}$ (best visible in ***Figure 72*** below) and a flattened slope to-

wards smaller voltages with a potential dip around $V_{oc} \approx$ -0.35 V (single data point) for SQ2+D149 and SQ2+D149/D131 in the EIS$^{oc,red}$ measurements. The presence of some additional deep trap states in the cells with SQ2 without CA/OA was, indeed, indicated by their capacitance curves (cf. ***Figure 53***) showing what appears to be an onset of a local increase below Fermi-level voltages of about -0.3 V. Further supporting this, the current-voltage characteristics of the cells with SQ2, SQ2+D149, and SQ2+D149/D131 (re-plotted with extended current density scale in ***Figure 71***), exhibit an S-shape similar to that of the corresponding *J-V* characteristics in chapter 6 (best seen in the representation in ***Figure 59***). Nonetheless, in the case of nanoparticulate ZnO the increase of lower-voltage recombination by (oxidized) SQ2 aggregates appears to be less severe than for the samples based on electrodeposited ZnO.

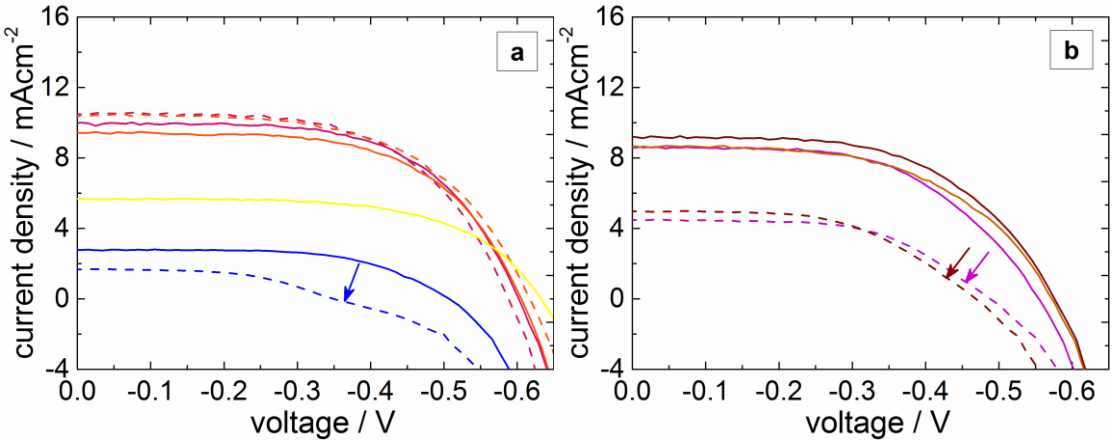


***Figure 71****: Current-voltage curves of the np-ZnO-based solar cells (cf.* ***Figure 64****) with extended current density range to reveal the characteristic shape of some of the curves, as indicated by arrows.*

When plotted against the voltage corrected for conduction band edge shifts $V_f$-$\Delta E_c/q$ or $V_{oc}$-$\Delta E_c/q$ (see ***Figure 72***), most of the recombination resistance curves are moved closer together, suggesting that the differences in their voltage-dependent rate constants of recombination $k_r$ are relatively small.

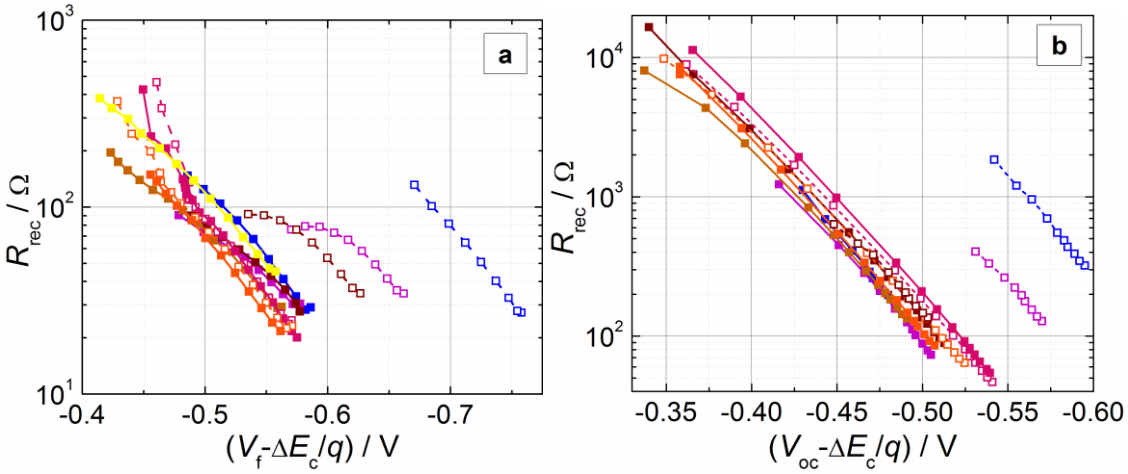


***Figure 72**: $R_{rec}$ from EIS$^{oc,red}$ (a) and from EIS$^{AM1.5G}$ (b) as a function of the band edge-corrected voltage. Lines are a guide to the eye only. Assignment of colors and line/ symbol styles as in **Figure 67**.*

However, SQ2, SQ2+D149, and (based on EIS$^{oc,red}$) SQ2+D149/D131 show conduction band edge-corrected recombination resistances that, at a given corrected voltage, would significantly exceed those of all other samples if the curves were extrapolated to extend over the whole voltage range displayed. This must be caused by the very low total density of trap states in the corresponding samples (***Table 20***). In spite of this, the cells showed the highest rate of recombination at a given (uncorrected) voltage because of the strongly downward shifted conduction band edge. Similar trends were also observed for the electrodeposited counterparts (cf. ***Figure 58***), although they were less pronounced due to a smaller conduction band edge shift and a less significant reduction of the total trap density by SQ2.

The recombination parameters $\beta$ (see ***Table 21***) derived from EIS$^{AM1.5G}$ (cf. linear fits to eq. (54) in ***Figure 70*** (a)) are all relatively similar and the average value of 0.44 (maximum deviation of 0.1) is comparable to the average $\beta$ value of 0.42 determined for the cells based on electrodeposited ZnO with SQ2, D149, and/or D131 (and identical to the average $\beta$ of 0.44 for edep-ZnO cells when a single outlier was excluded). The co-sensitized cells with SQ2+D149 or SQ2+D149/D131 (both with or without coadsorbates) show a tendency towards slightly smaller recombination parameters than the remaining cells (0.34 – 0.41 compared to 0.4 – 0.5), possibly because the corresponding

$R_{rec}$ curves showed only a narrow linear range that could be fitted, making the fits rather inexact.

***Table 21**: Recombination parameters β of the DSCs based on dye-sensitized np-ZnO.*

| sample code | $\beta$ ($EIS^{AM1.5G}$) | $\beta$ ($EIS^{oc,red}$) |
|---|---|---|
| NP_D149 | 0.49 | 0.82 |
| NP_D149/D131 | 0.47 | 0.82 |
| NP_SQ2 | 0.47 | 0.93 |
| NP_SQ2+D149 | 0.41 | 0.88 |
| NP_SQ2+D149/D131 | 0.40 | 0.85 |
| NP_D149/CA | 0.50 | 0.84 |
| NP_D131/OA | 0.44 | n.a. |
| NP_D149/D131/OA | 0.47 | 0.84 |
| NP_SQ2/CA | 0.49 | 0.90 |
| NP_SQ2/CA+D149/CA | 0.34 | 0.90 |
| NP_SQ2/CA+ D149/D131/OA | 0.35 | 0.83 |
| NP_SQ2/CA+ D131/OA+D149/D131/OA | 0.40 | 0.83 |

The recombination parameters determined from $EIS^{oc,red}$ (***Table 21***, cf. linear fits in ***Figure 70*** (b)) confirm that there is no significant trend dependent on the different dyes or coadsorbates. However, with an average value of 0.86 (maximum deviation of 0.07) they are considerably higher than the values derived from $EIS^{AM1.5G}$. This difference is expected based on the different dependence of the conduction band electron density on the voltage under open-circuit conditions vs. when a current flows through the semiconductor. If the applied $V_f$ under AM1.5G illumination takes on the open-circuit value, e.g. $V_f$ = -0.59 V for D149 (cf. ***Table 19***), the electron density is identical to the electron

density that would be achieved under illumination with red light at $V_{oc}$ = -0.59 V (reached by a sufficient increase of the light intensity). On the other hand, at a $V_f$ value under AM1.5G illumination that is further away from open-circuit conditions, say -0.3 V for D149, the quasi-Fermi level will be 0.3 eV above $E_{redox}$ *at the back contact* ($x$ = 0 µm), but will be significantly higher than that *at the semiconductor/electrolyte interface* (cf. 1.2.1),[115] i.e., the electron density would be increased with respect to an open-circuit voltage of $V_{oc}$ = -0.3 V under red illumination (corresponding to a constant quasi-Fermi level of 0.3 eV above $E_{redox}$ at any location in the semiconductor). Based on these differences in the density of conduction band electrons available for recombination reactions, the recombination resistances measured by $EIS^{AM1.5G}$ and $EIS^{oc,red}$ should be equal at the voltage where $V_f$ in $EIS^{AM1.5G}$ corresponds to the AM1.5G open-circuit value, but should be lower for the $EIS^{AM1.5G}$ measurements at any voltage less negative than that. As a result, the recombination resistance from $EIS^{AM1.5G}$ will increase less with decreasing $V_f$ (smaller $\beta$ value) than the $R_{rec}$ from $EIS^{oc,red}$ will do with decreasing $V_{oc}$ (larger $\beta$ value). Since $\beta$ is a phenomenological quantity rather than a fundamental microscopic parameter, neither the $\beta$ value from $EIS^{AM1.5G}$ nor that from $EIS^{oc,red}$ is "more correct" than the other; in comparisons with other studies it should simply be ensured that the recombination parameters are compared for the same measurement condition.

The recombination resistance (***Figure 72***) and chemical capacitance (***Figure 69***) from $EIS^{oc,red}$ were used to determine the effective electron lifetime $\tau_n$ via eq. (47). In addition, $\tau_n$ was obtained independently by intensity-modulated photovoltage spectroscopy at open circuit under red illumination of varied intensity. Based on the identical measurement conditions (open-circuit condition, same light source and light intensities) and the theoretical equivalency of the time constants derived from these two methods (cf. sections 1.4.4 and 1.4.5), it is expected that identical voltage-dependent (cf. eq. (19)) $\tau_n$ curves are obtained for a given sample. ***Figure 73*** shows that this is roughly the case for most of the samples, but the $\tau_n$ values for SQ2 and, to a smaller degree, for combinations of SQ2 and indolines without coadsorbates show quite pronounced differences. This is most likely the result of an overestimation of $R_{rec}$ and/or $C_\mu$ from EIS, because the spectra of these specific cells in part showed $R_{rec}||C_\mu$-related semicircles that were not clearly distinguishable from the other spectral features, see example in ***Figure 105*** in Appendix D. The cells with indoline dyes (with or without coadsorbates) as well as the co-sensitized cells SQ2/CA+D149/D131/OA and SQ2/CA+D131/OA+D149/D131/OA

showed the longest lifetimes, followed by the co-sensitized sample SQ2/CA+D149/CA, then the cell SQ2/CA and lastly the three cells containing SQ2 without coadsorbates with the shortest lifetimes.

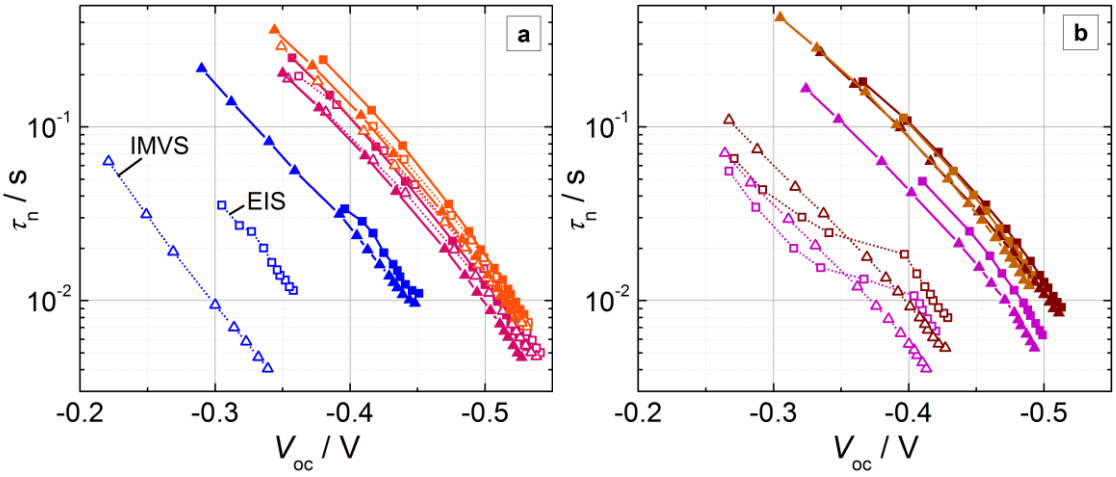


***Figure 73**: Effective electron lifetimes of the np-ZnO solar cells as obtained by IMVS measurements (triangles) and derived from EIS (squares) (see legend in **Figure 67** for the meaning of the different colors).*

The electron transport times $\tau_{tr}$ in the np-ZnO-based solar cells were analyzed in comparison with the $\tau_{tr}$ in the cells based on edep-ZnO using intensity-modulated photocurrent spectroscopy (IMPS) at short circuit under red illumination of varied intensity, see ***Figure 74***. At lower short-circuit currents, the nanoparticulate and electrodeposited ZnO films yielded similar electron transport times, but with increasing $J_{sc}$, the $\tau_{tr}$ difference between the two different types of ZnO structures increased because of the steeper slope observed for the electrodeposited samples. The latter was the result of the flatter trap distribution of these cells (as reflected in their higher $\alpha$ values, cf. ***Figure 55*** and ***Table 20***), which should increase the slope of the electron transport time as a function of the Fermi-level voltage (cf. eq. (15) and eq. (69)) and, in consequence, the slope of $\tau_{tr}$ vs. $J_{sc}$. For both groups of cells, the electron transport time was smallest (i.e., best) for the samples with SQ2, SQ2+D149, or SQ2+D149/D131. To determine to what extent the different transport times observed for different dyes or dye combinations are related to the samples' different total trap densities (eq. (15) and eq. (69)), the $\tau_{tr}$ were normalized by $N_t/N_{t,ref}$ (cf. ***Table 20***), see ***Figure 75***.

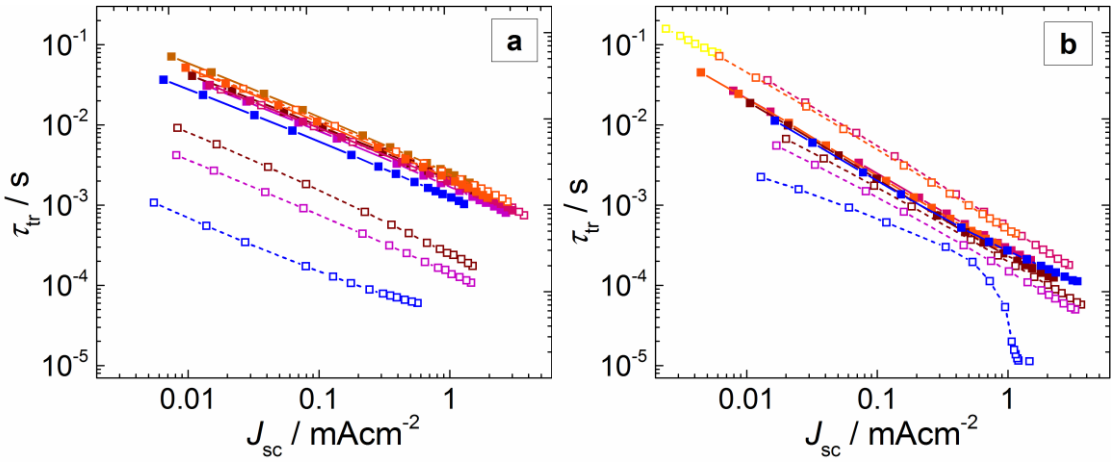


***Figure 74**: Electron transport times from IMPS measurements of DSCs with varied dyes and dye combinations (cf. plot legends in previous sections) based on nanoparticulate ZnO films (a) or based on electrodeposited ZnO films (b) as a function of the constant background value of the short-circuit photocurrent density.*

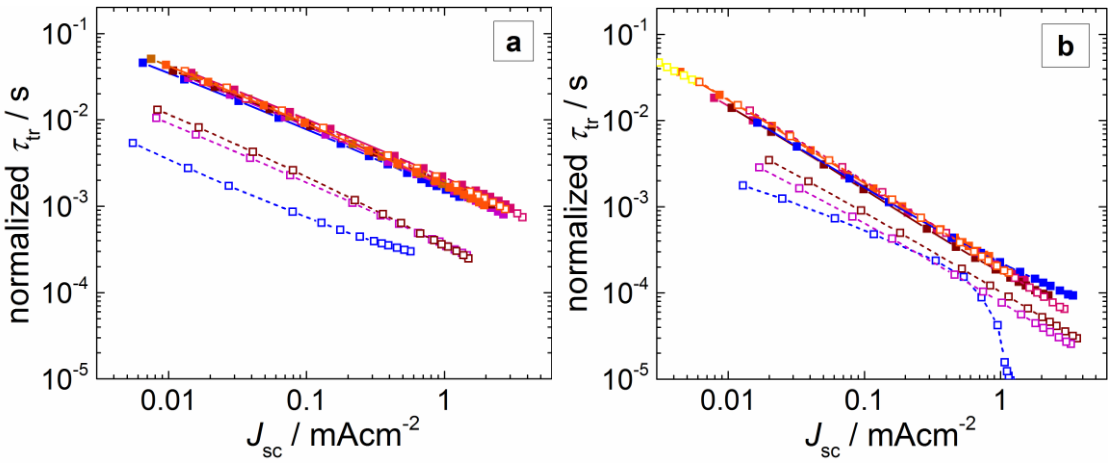


***Figure 75**: IMPS-derived electron transport times of DSCs based on nanoparticulate ZnO films (a) or electrodeposited ZnO films (b) after normalization by the relative total trap density $N_t/N_{t,ref}$ (common reference sample: NP_D149).*

Both in the case of np-ZnO and edep-ZnO, the normalized transport times were virtually identical for the different dyes and dye combinations, indicating that the differences in $\tau_{tr}$ were caused by variations in the total trap density. However, SQ2, SQ2+D149, and SQ2+D149/D131 showed clearly lower transport times than the remaining cells even after normalization, suggesting that these samples, which contained strongly aggregated SQ2 (cf. ***Figure 63***), exhibited an increased apparent electron diffusion coefficient $D_0$

(cf. eq. (15)). It has been previously reported that excited electrons in DSCs can move between oxidized dye molecules via hopping,[290, 302] thus allowing them to move along the film thickness (perpendicular to the substrate) without having to be injected into the semiconductor. Consequently, it is conceivable that in the present case larger amounts of (oxidized) SQ2 aggregates on the ZnO surface allowed for relatively fast hopping of excited electrons, possibly enabling them to reach the substrate on additional pathways. When comparing the normalized electron transport times of the np-ZnO samples and the electrodeposited samples (neglecting the SQ2-containing samples without coadsorbates discussed above), the curves of the latter now generally are below those of the nanoparticulate cells. This could be the result of the smaller film thicknesses compared to np-ZnO and would then indicate a relatively similar diffusion coefficient $D_0$ for the two different types of structures. However, due to the different slopes (trap distribution parameters) found for np-ZnO cells and cells based on electrodeposited ZnO, no final conclusions about the diffusion coefficient can be made on the basis of the present results.

## 7.6 Analysis of the Factors Governing the IPCE

Using the same method as described in section 6.5 of the previous chapter, various measurement results obtained for the DSCs based on nanoparticulate ZnO were combined to further discuss the factors determining the IPCE and short-circuit current densities observed under AM1.5G illumination (cf. section 7.3). For the analysis, the IPCE curves (cf. ***Figure 66***) were corrected for a 30% loss at the conductive glass substrate (i.e., divided by 0.7), as determined from offsets of the absorbance of ~0.15 in the long-wavelength range where none of the dyes absorb. The larger optical loss in the np-ZnO samples is probably the result of the use of thicker, more conductive FTO/glass substrates compared to those used for the edep-ZnO samples (cf. sections 2.2 and 2.3). ***Table 22*** shows the spectrally integrated (integration range 350 – 750 nm) relative[XIII] values of the light harvesting efficiency $\eta_{lh}$ (cf. ***Figure 65***) and of the corrected IPCE. [XIV]

[XIII] referring to a hypothetical ideal cell with $\eta_{lh}$ = IPCE = 1 over the whole wavelength range studied

[XIV] For SQ2/CA+D149/D131/OA (a) and SQ2/CA+D131/OA+D149/D131/OA (b), the IPCE was measured by a Zahner setup as opposed to the Acton/Ivium setup used for the remaining cells. For better comparability, the integrated IPCE for those cells was not determined from the Zahner-based spectra but rather estimated based on the integrated IPCE (Acton/Ivium) of the sample SQ2/CA+D149/CA (c) and the ratio of Zahner-based integrated IPCEs of (a) and (c) and (b) and c.

***Table 22**: Estimated short-circuit electron diffusion lengths $L_{n,sc}$, ratio of $L_{n,sc}$ and the film thickness d =10 µm, relative integrated IPCE (corrected for optical losses), approximate short-circuit charge collection efficiency, relative integrated optical loss-corrected light harvesting efficiency, and calculated product $\eta_{inj} \cdot \eta_{reg}$ for the DSCs based on np-ZnO. Values in parentheses are rough estimates based on assumed $\tau_n$ values.*

| sample code | $L_{n,sc}$ /µm | $L_{n,sc}/d$ | rel. $IPCE_{int}$ (corr.) /% | $\eta_{cc}$ /% | rel. $\eta_{lh,int}$ /% | $\eta_{inj} \cdot \eta_{reg}$ /% |
|---|---|---|---|---|---|---|
| NP_D149 | 17.6 | 1.8 | 57 | 95 | 69 | 87 |
| NP_D149/D131 | 14.8 | 1.5 | 56 | 90 | 67 | 92 |
| NP_SQ2 | (11.2) | (1.1) | 5 | (80) | 71 | (9) |
| NP_SQ2+D149 | (8.3) | (0.8) | 24 | (70) | 85 | (41) |
| NP_SQ2+D149/D131 | 6.5 | 0.7 | 25 | 65 | 83 | 47 |
| NP_D149/CA | 14.5 | 1.5 | 55 | 90 | 67 | 91 |
| NP_D131/OA | 75.4 | 7.5 | 32 | 100 | 47 | 68 |
| NP_D149/D131/OA | 14.9 | 1.5 | 50 | 90 | 66 | 85 |
| NP_SQ2/CA | 5.6 | 0.6 | 14 | 60 | 47 | 51 |
| NP_SQ2/CA+D149/CA | 12.7 | 1.3 | 53 | 85 | 72 | 86 |
| NP_SQ2/CA+ D149/D131/OA | 14.1 | 1.4 | 54 | 90 | 69 | 87 |
| NP_SQ2/CA +D131/OA +D149/D131/OA | 11.2 | 1.1 | 46 | 80 | 67 | 86 |

Conservative estimations of the effective diffusion length $L_n$ under short-circuit conditions were attained by the same procedure as described in chapter 6.5, using the short-circuit electron transport times $\tau_{tr}$ from IMPS at a red light intensity of 25 $mWcm^{-2}$ (cf. ***Figure 74*** (a), serving as a lower estimate for the value under AM1.5G illumination of 100 $mWcm^{-2}$), a factor $\zeta$ of 3.1 (cf. eq. (69)), and the effective electron lifetimes $\tau_n$

$=R_{rec}C_{\mu}$ at an applied voltage $V$ = -0.3 V from EIS$^{AM1.5G}$ (cf. ***Figure 67*** and ***Figure 72***, serving as a lower estimate for the short-circuit value), see ***Table 22***. For the cells with SQ2 or SQ2+D149, the $\tau_n$ value of the sample with SQ2+D149/D131 (which showed a similar voltage-dependent $\tau_n$ at more negative voltages) was used as a rough approximation, because the available EIS fit results did not extend down to applied voltages as small as -0.3 V. Using the ratios of $L_n$ and the np-ZnO film thickness (***Table 22***), the short-circuit charge collection efficiency $\eta_{cc}$ was estimated graphically from the plot of the theoretical correlation between $L_n/d$ and $\eta_{cc}$ reported by Peter (cf. Figure (17) or ref. [87]), see ***Table 22***. The product $\eta_{inj}\cdot\eta_{reg}$ representing the combined effect of electron injection and dye regeneration efficiency, was obtained by dividing the relative integrated IPCE values by the estimated $\eta_{cc}$ values and by $\eta_{lh,int}$, see ***Table 22***.

On the basis of the values listed in ***Table 22***, the factors that determined the integrated IPCE and $J_{sc}$ of the different np-ZnO-based DSCs can now be identified and discussed in comparison with the corresponding results for the edep-ZnO cells (cf. ***Table 17***). While the short-circuit charge collection efficiencies in the DSCs based on electrodeposited ZnO generally approached 100%, nearly all of the np-ZnO samples exhibited $L_n/d$ values below 3 and, accordingly, short-circuit charge collection efficiencies under 100%. Complete collection ($L_n/d > 3$) at short circuit was only attained by the np-ZnO sample with D131/OA. In the np-ZnO cells with SQ2/CA, SQ2+D149, or SQ2+D149/D131, on the other hand, the mean distance electrons could travel before recombining was even smaller than the film thickness ($L_n/d < 1$, $\eta_{cc}$ = 60 – 70%). Comparing the integrated IPCE and partial quantum efficiencies attained for each dye or dye combination on np-ZnO vs. on edep-ZnO (***Table 22*** vs. ***Table 17***), it can be seen that the indoline dye-sensitized np-ZnO-based cells D149, D149/CA, D149/D131, and D149/D131/OA achieved better integrated IPCE and $J_{sc}$ values compared to their electrodeposited counterparts owing to an improvement in the integrated light harvesting efficiency and an increase of the electron injection and/or dye regeneration efficiency: $\eta_{lh,int}$ increased (in the above order) from 63 to 69%, 51 to 67%, 59 to 67%, and 49 to 66%, and $\eta_{inj}\cdot\eta_{reg}$ improved from 64 to 87%, 59 to 91%, 77 to 92%, and 70 to 85%. These increases overcompensated a concomitant decrease of the charge collection efficiency $\eta_{cc}$ in np-ZnO samples with respect to edep-ZnO cells from 100 to 95% (D149) or to 90% (D149/CA and D149/D131/OA), and from 97 to 90% (D149/D131/OA). As for the squaraine sensitizer SQ2 and the dye mixtures SQ2+D149, and

SQ2+D149/D131, the integrated light harvesting efficiency in np-ZnO-based cells increased (SQ2: from 60 to 71%),[XV] or only very slightly decreased (from 87% to 85% for SQ2+D149 and to 83% for SQ2+D149/D131) compared to the electrodeposited counterparts. However, the IPCE and $J_{sc}$ of the np-ZnO-based cells were worsened in all three cases, mainly due to the reduction in charge collection efficiency from 100% to 80% (SQ2), 70% (SQ2+D149), or 65% (SQ2+D149/D131). Although for the dye mixtures SQ2+D149 and SQ2+D149/D131 $\eta_{inj}\cdot\eta_{reg}$ was improved in np-ZnO-based cells compared to electrodeposited ones (from 30 to 41% and from 37 to 47%), this could not compensate the negative effect of the decreased $\eta_{cc}$. SQ2/CA yielded approximately the same $J_{sc}$ on np-ZnO and on electrodeposited ZnO, and the calculated individual quantum efficiencies suggest that this was the case because the $\eta_{cc}$ was strongly reduced (from 100 to 60%) while $\eta_{lh}$ appeared to be increased from 27 to 47%[XV] and $\eta_{inj}\cdot\eta_{reg}$ was slightly improved as well (from 49 to 51%). The co-sensitized np-ZnO sample with SQ2/CA+D149/D131/OA achieved better integrated IPCE and $J_{sc}$ values than the electrodeposited counterpart owing to its integrated light harvesting efficiency being raised from 59 to 69% and its combined electron injection/dye regeneration being increased from 77 to 87%. These changes overcompensated a decrease of $\eta_{cc}$ from 100 to 90%.

Despite being reduced in comparison to the electrodeposited cells, the charge collection efficiency was not the main limiting factor (highlighted by underscores in ***Table 22***) in any of the samples based on np-ZnO. Instead, in all but three (SQ2, SQ2+D149, SQ2+D149/D131) cases it was the integrated light harvesting efficiency that limited the short-circuit current density, as also found for the cells based on electrodeposited ZnO. In the np-ZnO cells with SQ2, SQ2+D149, or SQ2+D149/D131, electron injection and/or dye regeneration ($\eta_{inj}\cdot\eta_{reg}$ of 9, 41, and 47%, respectively) was the clearly dominant limiting factor, also in accordance with the results obtained on electrodeposited ZnO. The low spectrally averaged $\eta_{inj}\cdot\eta_{reg}$ of the co-sensitized samples SQ2+D149 and SQ2+D149/D131 (resulting from hindered injection from SQ2 to ZnO and possibly from energy transfer from D149 and D131 to SQ2) together with their relatively low charge-collection efficiencies < 70% (resulting from additional recombination paths

[XV] Note, however, that the background in the absorbance and light harvesting spectra of the samples D131, SQ2, and SQ2/CA that was not related to light absorption by the dyes likely caused an overestimation of the integrated light harvesting efficiency and, as a result, an underestimation of the corresponding $\eta_{inj}\cdot\eta_{reg}$.

opened up by aggregated SQ2) counteracted the successful increase of the light-harvesting efficiency to 85 and 83% with respect to the cells D149 and D149/D131 ($\eta_{lh}$ = 69 and 67%) and rendered their short-circuit current densities and overall photovoltaic performance much lower than those of the indoline dye cells. In the presence of coadsorbates (cells SQ2/CA+D149/CA and SQ2/CA+D149/D131/OA), the integrated light harvesting efficiencies (72 and 69%) were only slightly improved compared to the corresponding samples without SQ2 (67% for D149/CA and 66% for D149/D131/OA), and the charge collection efficiency and combined electron injection and/or dye regeneration efficiency were also similar or only slightly better ($\eta_{inj} \cdot \eta_{reg}$ of 86 and 87% compared to 91 and 85%, $\eta_{cc}$ of 85 and 90% compared to 90% for D149/CA and D149/D131/OA). While the calculations predict a slight increase of IPCE and $J_{sc}$ (cf. theoretical values in ***Table 19***) at least for SQ2/CA+D149/D131/OA compared to D149/D131/OA, the measured short-circuit current densities of the co-sensitized np-ZnO-based cells with SQ2 and coadsorbates were all lower than those of D149/CA and D149/D131/OA. The incorrect prediction for SQ2/CA+D149/D131/OA may have resulted from temporal variations of the photovoltaic performance (cf. chapter 9). The sample sensitized with SQ2/CA+D131/OA+D149/D131/OA exhibited a smaller $J_{sc}$ than the cell with SQ2/CA+D149/D131/OA (as predicted by the theoretical $J_{sc}$ values) because of its reduced charge collection efficiency (from 90 to 80%) and its slightly reduced light harvesting efficiency (from 69 to 67%), underlining once again the redundancy of the additional step in the sensitization process.

## 7.7 Analysis of the Variation in the Open-Circuit Voltage and Fill Factor

Based on the photovoltaic performance, trap distribution and recombination properties of the DSCs based on nanoparticulate ZnO, the origins of the variations in their $V_{oc}$ and *FF* can now be analyzed quantitatively by a procedure similar to that in chapter 6.4 (electrodeposited ZnO with D149, D131, and/or SQ2). Voltage changes associated with changes in the short-circuit photocurrent density were again calculated by eq. (75) using an average value of the recombination parameter $\beta$. The $\Delta V_{oc}$ originating in differences in the rate constant of recombination (or in the total trap density) in the present case

were determined by a modification of eq. (76) by use of the ratio of the inverse recombination resistances $R_{rec}$ instead of the ratio of recombination currents under illumination, which should be equally valid based on the relationship between $R_{rec}$ and the recombination factor $J_{0k}$ in eq. (54).

***Table 23*** shows the partial contributions to the voltage differences of the various np-ZnO DSCs with respect to the cell with D149 by conduction band edge shifts ($\Delta V_{oc}(\Delta E_c/q)$, cf. ***Table 20***), differences in the short-circuit photocurrent density ($\Delta V_{oc}(\Delta J_{sc})$, cf. ***Table 19***), and differences in the rate of recombination as reflected by changes in $R_{rec}$ at a corrected voltage $V_f$-$\Delta E_c/q$ = -0.55 V ($\Delta V_{oc}(\Delta R_{rec})$, cf. ***Figure 72*** (b)). The calculated total voltage changes $\Delta V_{oc,calc}$ (sum of $\Delta V_{oc}$ ($\Delta E_c/q$), $\Delta V_{oc}$ ($\Delta J_{sc}$) and $\Delta V_{oc}$ ($\Delta R_{rec}$)) largely deliver qualitatively correct predictions of the experimental total voltage changes $\Delta V_{oc}$. Quantitatively, the calculations tended to underestimate the voltage losses observed for the cells containing SQ2 without coadsorbates by 40 – 80 mV, most likely as a result of additional recombination via deep traps (cf. ***Figure 72*** and ***Figure 71*** and discussion) that is not described by the $\beta$-recombination model. This is roughly in line with an additional voltage loss of about 60 mV found for the corresponding edep-ZnO cells as a consequence of the presence of monoenergetic traps located about 0.3 eV above $E_{redox}$ (cf. ***Figure 58*** and ***Table 15***). The calculated origins of the voltage changes between the np-ZnO cells with different dyes and coadsorbates mostly corroborate the results discussed for the corresponding electrodeposited cells (cf. ***Table 15***). Among the cells with indoline dyes only, experimentally a beneficial effect of the presence of D131 on $V_{oc}$ was observed, while coadsorption of CA or OA led to only a slight improvement (D149/CA) or even to a decrease (D149/D131/OA) of $V_{oc}$ with respect to the counterparts without coadsorbates, in agreement with the trends observed among edep-ZnO cells. The calculations in the present case did not precisely predict these changes of $V_{oc}$ among the indoline dye cells. Nevertheless, the different contributions to $\Delta V_{oc}$ determined for D131/OA indicate that an upward shift of the conduction band and a reduction of the rate constant of recombination may have been the reason for the good $V_{oc}$'s attained in the presence of D131.

***Table 23**: Individual contributions $\Delta V_{oc}(...)$ to the total differences of the open-circuit photovoltages ($\Delta V_{oc,calc}$: theoretical total change, $\Delta V_{oc}$: experimental change) among the DSCs based on np-ZnO with different dyes or dye combinations, resulting from shifts in the conduction band edge $\Delta E_c/q$ (positive: downward shift, negative: upward shift), differences in the short-circuit photocurrent density $\Delta J_{sc}$, and changes $\Delta R_{rec}$ of the recombination resistance at a corrected voltage $V_f$-$\Delta E_c/q$ of -0.55 V. Calculations were performed using the average β parameter of 0.44.*

| sample code | $\Delta V_{oc}(\Delta E_c/q)$ /mV | $\Delta V_{oc}$ ($\Delta J_{sc}$) /mV | $\Delta V_{oc}$ ($\Delta R_{rec}$) /mV | $\Delta V_{oc,calc}$ /mV | $\Delta V_{oc}$ /mV |
|---|---|---|---|---|---|
| NP_D149 | +/- 0 (ref.) | +/- 0 (ref.) | +/- 0 (ref.) | +/- 0 (ref.) | +/- 0 (ref.) |
| NP_D149/D131 | +/- 0 | +/- 0 | + 6 | + 6 | - 30 |
| NP_SQ2 | + 267 | + 109 | - 208 | + 167 | + 250 |
| NP_SQ2+D149 | + 161 | + 50 | - 110 | + 101 | + 100 |
| NP_SQ2+D149/D131 | + 112 | + 44 | - 76 | + 80 | + 120 |
| NP_D149/CA | +/- 0 | + 3 | +/- 0 | + 3 | - 10 |
| NP_D131/OA | - 20 | + 36 | - 22 | - 5 | - 40 |
| NP_D149/D131/OA | - 11 | + 6 | + 15 | + 10 | +/- 0 |
| NP_SQ2/CA | + 70 | + 79 | - 28 | + 121 | + 80 |
| NP_SQ2/CA+D149/CA | + 28 | + 12 | - 12 | + 27 | + 40 |
| NP_SQ2/CA +D149/D131/OA | + 16 | + 8 | - 16 | + 7 | + 20 |
| NP_SQ2/CA+D131/OA +D149/D131/OA | + 3 | + 11 | + 1 | + 16 | + 20 |

The coadsorbates CA and OA did not seem to have a significant effect on any of the individual quantities contributing to voltage changes, which presents a difference compared to the effects of CA/OA on the conduction band edge and rate constant of recombination observed on edep-ZnO. For nanoparticulate ZnO the indoline dye molecules

were more stable against replacement by CA/OA, so that D149/CA and D149/D131/OA likely contained relatively small amounts of coadsorbates, decreasing the influence of CA or OA on microscopic processes in the cells. Most notably, the present results confirm that sensitization of np-ZnO with the squaraine dye SQ2, as in the case of edep-ZnO, led to a very strong voltage loss with respect to D149 due to a large conduction band edge downward shift and a very limited short-circuit photocurrent. The effects of these factors were not fully compensated by the strong $V_{oc}$-enhancing effect of the low total trap density indicated for SQ2. When CA was coadsorbed with SQ2, the significant reduction of the downward conduction band edge shift and the increase of $J_{sc}$ enabled a large gain of $V_{oc}$ with respect to the coadsorbate-free sample, also in line with the results found on edep-ZnO. The co-sensitized cells containing SQ2 together with indoline dyes again showed improved $V_{oc}$'s compared to SQ2 and SQ2/CA because both the losses related to $J_{sc}$ as well as the conduction band edge downward shifts were clearly decreased. However, compared to the cells with indoline dyes only, lower $J_{sc}$ values and downward shifts of the conduction band edge – albeit reduced compared to SQ2 or SQ2/CA – still caused a lower $V_{oc}$. In the cell SQ2/CA+D131/OA+D149/D131/OA, the downward shift of the conduction band edge was somewhat reduced compared to the cell SQ2/CA+D149/D131/OA, but the $J_{sc}$-related voltage loss was larger and the recombination-related voltage gain was reduced, so that the net effect was a constant experimental $V_{oc}$, which contributed to the fact that the 3-step co-sensitization procedure did not bring about any advantages over the 2-step process.

In a second step, the origins of the differences in $V_{oc}$ between the cells based on nanoparticulate ZnO and the corresponding electrodeposited samples were investigated. Approximate conduction band edge shifts $\Delta E_c/q$ were determined between each np-ZnO sample and its edep-ZnO counterpart neglecting their different trap distribution parameters (cf. ***Figure 55*** and ***Figure 69*** (a), ***Table 12*** and ***Table 20***), see ***Table 24***. The voltage differences originating in the differences of $J_{sc}$ and $R_{rec}$ (at $V_f$-$\Delta E_c/q$ = -0.55 V) between the np-ZnO cells and the edep-ZnO cells (cf. ***Table 11*** and ***Figure 58*** (b)) were calculated via eq. (75) and the modified eq. (76) using the edep-ZnO films as references and a $\beta$ parameter of 0.44 (average value both among edep-ZnO cells and among np-ZnO cells), see ***Table 24***. The calculated total voltage changes $\Delta V_{oc,calc}$ (see ***Table 24***) largely confirm the experimental changes $\Delta V_{oc}$, which in all but one case (SQ2) constituted increases for np-ZnO with respect to edep-ZnO. However, the $\Delta V_{oc,calc}$ values dif-

fer from the experimental changes $\Delta V_{oc}$ by up to 80 mV, which could be due to inexact values of $\Delta E_c/q$ as a result of the different trap distributions in np-ZnO and edep-ZnO as well as to different additional losses by recombination via deep-lying monoenergetic trap states. The calculated individual contributions in ***Table 24*** reveal that the higher voltages of np-ZnO cells with respect to edep-ZnO cells were caused by their much lower rate constants of recombination and their mostly higher short-circuit photocurrent densities, which overcompensated the mostly positive (downward) relative shifts of the conduction band edge.

***Table 24****: Different contributions $\Delta V_{oc}$(...) to the change of the open-circuit photovoltage for DSCs based on nanoparticulate ZnO (this chapter) with respect to the corresponding DSCs fabricated from electrodeposited ZnO (previous chapter).*

| $\Delta V_{oc}$ (np-ZnO vs. e- ZnO) / dye | $\Delta V_{oc}$ ($\Delta E_c/q$) /mV | $\Delta V_{oc}$ ($\Delta J_{sc}$) /mV | $\Delta V_{oc}$ ($\Delta R_{rec}$) /mV | $\Delta V_{oc,calc}$ /mV | $\Delta V_{oc}$ /mV |
|---|---|---|---|---|---|
| D149 | 40 | -17 | -134 | -111 | -30 |
| D149/D131 | 34 | -33 | -92 | -91 | -40 |
| SQ2 | 199 | 26 | -264 | -39 | 0 |
| SQ2+D149 | 145 | 8 | -212 | -59 | -90 |
| SQ2 +D149/D131 | 88 | 11 | -159 | -60 | -60 |
| D149/CA | -19 | -32 | -49 | -100 | -40 |
| D149/D131/OA | -36 | -20 | -6 | -62 | -10 |
| SQ2/CA | 22 | -2 | -45 | -24 | -60 |
| SQ2/CA +D149/D131/OA | 14 | -4 | -23 | -13 | -30 |

The np-ZnO cell with SQ2 showed a $V_{oc}$ identical to that of its electrodeposited counterpart even though its short-circuit photocurrent was somewhat higher than the $J_{sc}$ of

the latter and the conduction band edge position was much lower, because the related losses were offset by a gain associated with a significantly smaller rate constant of recombination. To take a closer look at the variations of the fill factors between the different np-ZnO-based solar cells, the internal (i.e., series resistance-corrected) values of *FF* were determined by plotting the cell current density (of the *J-V* curves, cf. ***Figure 64***) against the Fermi-level voltage $V_f$, as derived from EIS under AM1.5G type illumination. The results are plotted together with the external fill factors (cf. ***Table 19***) as a function of the open-circuit voltage in ***Figure 76***. In addition, values of *FF* that were calculated by inserting the experimental $V_{oc}$ and $\beta$ values of the individual cells into eq. (35) as well as a simulated curve based on eq. (35) under the assumption of a constant $\beta$ parameter of 0.44 are presented. The simulated curve and the individual calculated values are well in line, indicating that the differences in the fill factors were mainly determined (via $V_{oc}$, cf. eq. (34) and eq. (35)) by the changes of the parameters $J_{sc}$, $E_c$, and $J_{0k}$ (cf. ***Table 23***) and were not significantly influenced by the small variations of the recombination parameter $\beta$. The internal fill factors determined from the $J$-$V_f$ curves strongly deviate from the simulated curve and the calculated data, showing a steeper increase with more negative $V_{oc}$ and, as a result, clearly higher values in the range -0.55 V – -0.65 V. The external fill factors, on the other hand, closely follow the trend of the calculated data but are generally somewhat lower. It is likely that the determination of the internal FF from the $J$-$V_f$ characteristics was flawed because of the fact that the EIS-based $V_f$ in the lower voltage range was generally inexact, since the $R_{rec}$ data that was used to derive $V_f$ was not reliable anymore in this range. In a few cases (SQ2, SQ2+D149, SQ2+D149/D131, and SQ2/CA), $V_f$ did not even reach the internal maximum power point, so that extrapolations had to be used to determine the internal *FF*. Comparison between the external *FF* values and the calculated internal *FF* suggests that the series resistance causes a quantitatively similar decrease of the fill factor for all samples and corresponding open-circuit voltages instead of changing the slope of *FF* with respect to $V_{oc}$.

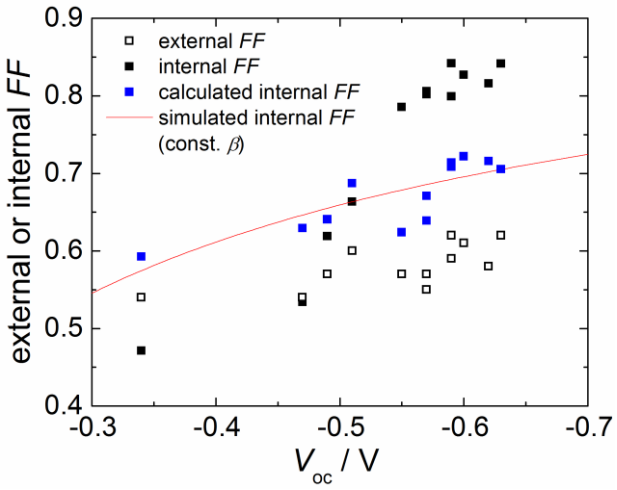


***Figure 76**: External (open symbols) or internal (filled symbols and line) fill factors of the DSCs based on nanoparticulate ZnO as a function of the experimental open-circuit photovoltage $V_{oc}$. The data represented by filled black symbols was determined from experimental J-Vf curves, the data shown as blue symbols was calculated analytically based on the open-circuit voltages and β values of the samples, and the simulated curve was calculated under the assumption of a constant β.*

## 7.8 Summary and Conclusions for This Chapter

This chapter presented an investigation of DSCs based on screenprinted nanoparticulate ZnO films and the photosensitizers D149, D131, SQ2, or mixtures thereof, partly combined with the coadsorbates cholic acid and/or octanoic acid. The variations of the cell properties depending on the dye or dye/coadsorbate combinations were studied and the influence of the type of ZnO structure was elucidated by comparison with the properties of the analogously sensitized cells based on electrodeposited ZnO of the previous chapter.

The UV/Vis absorption and light harvesting efficiency spectra of the DSCs based on np-ZnO generally resembled those of the electrodeposited ZnO films with the same dyes, and the films co-sensitized with SQ2 and indoline dyes again showed the desired panchromatic absorption. As in the edep-ZnO films, D149 and, in particular, SQ2 exhibited signs of aggregation that were considerably reduced in the presence of CA. An estimated slight increase in inner surface area of the np-ZnO films by a factor of 1.4 with respect to the edep-ZnO films enabled a higher dye loading. While the presence of CA

and/or OA during the adsorption led to reduced dye loadings with respect to films without coadsorbates, the decrease was clearly less pronounced when compared to electrodeposited ZnO films, especially for D149 and D131.

The power conversion efficiencies of the solar cells based on nanoparticulate ZnO were generally better than those of their counterparts based on electrodeposited ZnO owing to mostly enhanced short-circuit photocurrent densities and generally higher open-circuit photovoltages. The improvement of $J_{sc}$ was observed for the indoline dye cells with or without coadsorbates as well as for SQ2/CA+D149/D131/OA as a result of the higher integrated light harvesting efficiencies and of higher spectrally averaged combined electron injection and dye regeneration efficiencies. The increased $V_{oc}$ were mainly the consequence of reduced recombination independent of the conduction band edge position (and for some cells higher short-circuit photocurrent densities). Albeit not presenting the main factor limiting $J_{sc}$, the short-circuit charge collection efficiencies of the cells based on the ~ 10 µm thick np-ZnO films were all lower than those of the cells based on the thinner electrodeposited films. Due to the presence of additional recombination paths at lower quasi-Fermi levels, $\eta_{cc}$ was particularly low for SQ2, SQ2/CA, SQ2+D149, and SQ2+D149/D131, effecting lower short-circuit current densities with respect to the corresponding electrodeposited samples. The dye- and coadsorbate-dependent trends of the photovoltaic parameters observed among the various sensitized np-ZnO cells largely confirmed the results found for the electrodeposited cells. The open-circuit voltages and short-circuit photocurrents were highest for indoline dyes without coadsorbates, lowest for SQ2 as individual sensitizer without CA, and in between for combinations of SQ2 and D149 or D149/D131. As observed on edep-ZnO, the $J_{sc}$ values of the three cells SQ2, SQ2+D149, and SQ2+D149/D131 were considerably lower than expected based on their light harvesting efficiency, which was due to, (1) the particularly low combined electron injection and dye regeneration efficiency ($\eta_{inj} \cdot \eta_{reg}$) of the squaraine sensitizer also on nanoparticulate ZnO and, (2) a clearly hindered activity of D149 and D131 in the presence of SQ2, indicating undesired energy transfer from the indoline dyes to poorly injecting SQ2. The low photovoltages of the np-ZnO cells with SQ2 were again the result of their small $J_{sc}$'s, of strong downward shifts of the conduction band edge, and of the presence of additional recombination pathways through deep monoenergetic traps related to oxidized aggregated SQ2, as suggested by subtle indications in the chemical capacitance and recombination resistance curves from EIS and, more clearly,

by the S-shape of the *J-V* curves of the corresponding cells. The presence of the coadsorbates CA or OA in the np-ZnO solar cells tended to increase the $V_{oc}$ and the fill factor. As in the case of edep-ZnO, the improvement was particularly pronounced for SQ2, SQ2+D149, and SQ2+D149/D131, where it originated in a strong reduction of downward shift of the conduction band edge compared to the cells without coadsorbates. As for the short-circuit photocurrent density, CA/OA led to a minor decrease for the indoline dye cells (reduced light harvesting efficiency) but to a considerable improvement for SQ2 and the mixtures SQ2+D149 and SQ2+D149/D131. This was the consequence of a strong improvement of the electron injection and/or dye regeneration efficiency and of an increase of the charge collection efficiency, indicating that the coadsorbates hindered energy transfer between the dyes and prevented the formation of additional recombination pathways related to oxidized SQ2 aggregates. However, whereas the co-sensitized cell with SQ2/CA+D149/D131/OA had shown the best $J_{sc}$ among the electrodeposited samples, in the present group of np-ZnO-based cells D149 and D149/D131 produced a higher short-circuit photocurrent density both with or without coadsorbates due to their higher combined electron injection and dye regeneration efficiency.

In conclusion, the DSCs based on 10 µm thick nanoparticulate ZnO films with SQ2, D149, and/or D131 showed decreased short-circuit charge collection efficiencies but nevertheless yielded somewhat higher power conversion efficiencies than analogous cells based on ~ 4 µm thick electrodeposited ZnO, mainly as a result of increased light harvesting efficiencies and/or lower rate constants of recombination. The goal of enhancing the conversion efficiency compared to indoline-sensitized ZnO solar cells by using the squaraine sensitizer SQ2 to extend the light harvesting efficiency into the red part of the spectrum was confounded by the small electron injection and/or dye regeneration efficiency of SQ2 as well as by the strong downward shift of the conduction band edge caused by this sensitizer, as also observed when SQ2 was combined with electrodeposited ZnO. Although these two issues could be partially counteracted by the use of the coadsorbates cholic acid and octanoic acid, the improvement was not significant enough to render the co-sensitized cells more efficient than the cells with indoline dyes only. Thus, the experiments on nanoparticulate ZnO confirmed the poor suitability of the squaraine dye SQ2 as co-sensitizer that was already observed on electrodeposited ZnO, indicating that this dye is not compatible with ZnO as a semiconductor in general.

In the following chapter, a sulfonated Zn phthalocyanine will therefore be investigated as an alternative red-absorbing co-sensitizer in combination with D149.

# 8 Panchromatic Dye-Sensitized Solar Cells Based on Electrodeposited ZnO with D149 and Sulfonated Zinc Phthalocyanine

## 8.1 UV/Vis Absorption of Dye Solutions and Sensitized Films

Sensitization of electrodeposited porous ZnO films with a mixture of the indoline dye D149 and the phthalocyanine $S_{1.15}$PcZn was achieved by dipping the films into an ethanolic solution containing both dyes together with the coadsorbate cholic acid (CA) at a molar ratio of 1:1.5:2 (D149:$S_{1.15}$PcZn:CA). Comparison samples containing only D149/CA or $S_{1.15}$PcZn/CA were prepared using ethanolic solutions of the individual dyes. The UV/Vis absorption spectra of the latter (***Figure 77***, solid pink and cyan curves) show absorption bands at 387 nm (HOMO → LUMO+1 transition)[303] and at 527 nm (HOMO → LUMO)[303] for D149 and at 363 nm (Soret band; HOMO → LUMO+1)[304, 305] and 669 nm (Q band; HOMO → LUMO)[304, 305] for $S_{1.15}$PcZn.

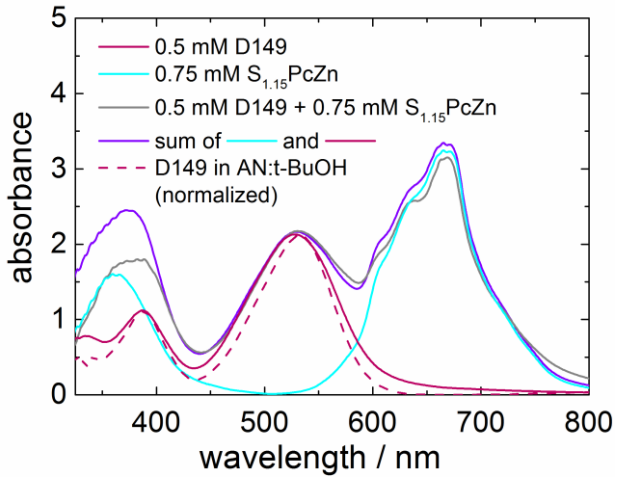


***Figure 77:*** *UV/Vis absorption spectra of the ethanolic dye solutions (all containing 1 mM CA) used to sensitize porous electrodeposited ZnO films with D149, $S_{1.15}$PcZn, or both, together with a spectrum of 0.5 mM D149/1 mM CA in its standard solvent mixture (normalized to the same peak height as the ethanolic D149 solution) and a superposition of the spectra of D149 or $S_{1.15}$PcZn in ethanol.*

D149/CA in ethanol shows nearly identical absorbance peak positions but slightly broader peaks compared to D149/CA in the typically used acetonitrile:*tert*-butanol (1:1) solvent mixture (dashed pink curve in ***Figure 77***), indicating a somewhat higher degree of aggregation in the ethanolic solution. The broad Q band of the phthalocyanine with shoulders at around 637 and 611 nm indicates the presence of a large number of H-aggregates (coplanar associated molecules).[304] In the spectrum of the mixed dye solution (grey curve in ***Figure 77***), the positions of the main peaks of D149 and $S_{1.15}$PcZn are largely maintained, and the low wavelength maxima are merged into one peak at 384 nm. A superposition of the individual spectra (violet curve in ***Figure 77***) reflects the characteristics of the mixed dye solution very well in the main absorption range of D149 (400 – 600 nm), demonstrating that the HOMO → LUMO transition of D149 is neither affected by the presence of $S_{1.15}$PcZn nor by the smaller amount of CA per mole of dyes in the mixed solution (0.8) compared to the individual dye solutions (1.3 for the $S_{1.15}$PcZn solution and 2 for the D149 solution). At wavelengths below and above the range 400 – 600 nm, the spectrum of the D149/$S_{1.15}$PcZn/CA solution shows lower absorbance values and more pronounced peak shoulders at 637 and 611 nm than the calculated spectrum, indicating an increased tendency of aggregation of $S_{1.15}$PcZn molecules in the mixed solution that was likely the result of the lower molar ratio of CA to $S_{1.15}$PcZn. The differently sensitized ZnO films were characterized by solid-state UV/Vis absorption spectroscopy, see ***Figure 78***.

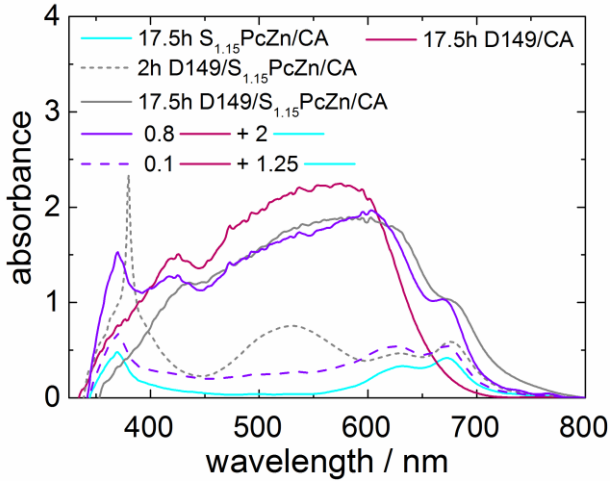


***Figure 78:*** *Optical absorption (and linear combinations thereof) of electrodeposited ZnO sensitized with D149 and/or $S_{1.15}$PcZn together with CA. The spike in the dashed grey line is an artifact.*

The film sensitized with D149/CA for 17.5 h showed a very broad and high absorption feature in the wavelength range from about 350 to 650 nm, with an asymmetric, red-shifted main absorption peak at around 575 nm and a shoulder located at around 425 nm. By comparison with the spectra of D149-sensitized electrodeposited ZnO of previous chapters (adsorption from *tert*-butanol:acetonitrile solution for 2 h, cf. ***Figure 37*** and ***Figure 50***), these absorption characteristics clearly resemble those of films containing D149 *without* CA rather than those of films with D149/CA, indicating strong aggregation of D149 in the dye-loaded film. This could be due to the increase of the adsorption time from 2 h to 17.5 h,[XVI] which led to a strongly increased D149 loading, as reflected in the higher integrated absorbance (integration range 350 – 800 nm) of $abs_{int}$ = 494 nm compared to $abs_{int}$ = 337 nm and 202 nm for the D149- and D149/CA-sensitized films of chapter 6 (prepared using the same synthesis batch of D149). The sample sensitized with $S_{1.15}$PcZn/CA for 17.5 h exhibited much smaller and narrower absorption peaks compared to D149/CA, with the pronounced shoulder of the Q band at 633 nm indicating a high extent of aggregation. While the molar absorptivity of $S_{1.15}$PcZn is smaller than that of D149 (for a mixed sulfonated ZnPc with unspecified degree of sulfonation, $\varepsilon \approx 45{,}000\ M^{-1}cm^{-1}$ at 675 nm in dimethyl sulfoxide,[306] compared to ε (D149) = $72{,}350\ M^{-1}cm^{-1}$ at 530 nm in DMF[136]), the difference does not fully explain the difference in peak height by a factor of more than 5, thus indicating a notably smaller amount of dye. Dipping the ZnO films into the mixed dye solution for 17.5 h led to successful adsorption of both dyes (cf. solid grey spectrum in ***Figure 78***). For the resulting co-sensitized film the absorption peak caused by D149 was smaller but showed the same type of asymmetry as in the present film with D149/CA only. The additional absorption by $S_{1.15}$PcZn appeared as a shoulder at approximately 680 nm, i.e., slightly red-shifted compared to the films with $S_{1.15}$PcZn only. The shape of the spectrum of the co-sensitized film closely resembled that of a calculated spectrum (solid violet curve in ***Figure 78***) corresponding to the weighted sum of the spectra of D149/CA (weighting factor 0.8) and $S_{1.15}$PcZn/CA (weighting factor 2), indicating a comparable degree of dye aggregation as in the samples D149/CA and $S_{1.15}$PcZn/CA.

[XVI] Chosen because shorter adsorption (e.g. for 2 h) from ethanolic solution in test experiments resulted in weak coloration of the ZnO films compared to adsorption from *tert*-butanol:acetonitrile for 2 h.

Based on the above molar absorptivities of the dyes in solution, the height ratio of the absorption peaks associated with the two different dyes of approximately 2:1 (D149:$S_{1.15}$PcZn) corresponds to a molar D149:$S_{1.15}$PcZn ratio of ~1:1 on the ZnO surface. This presents a coarse approximation, because in dye-sensitized films with strong dye aggregation the peak height is not an exact measure for the dye loading (cf. chapter 5.1). When the soaking time in the mixed dye solution was decreased from 17.5 h to 2 h (see dashed grey spectrum in ***Figure 78***), the absorption caused by $S_{1.15}$PcZn still showed a strong contribution by aggregates (peak at around 630 nm), but D149 was significantly less aggregated (narrower, symmetric absorption peak without red-shift with respect to the solution spectrum). As a result of its different peak positions and shapes, the spectrum could not be accurately described by weighted sums of the spectra of the samples D149/CA and $S_{1.15}$PcZn/CA (see example shown as dashed violet curve in ***Figure 78***), further supporting that aggregation was clearly reduced. However, this came at the cost of a much smaller absorption compared to the film co-sensitized for 17.5 h over virtually the whole range of absorbed wavelengths. The peak height ratio for D149:$S_{1.15}$PcZn (main peak) of 0.75:0.42 suggests that the molar ratio of the two dyes in the film was again approximately 1:1. Interestingly, the amount of $S_{1.15}$PcZn in the co-sensitized films is increased with respect to the sample $S_{1.15}$PcZn/CA, indicating that the presence of D149 assists the adsorption of the phthalocyanine dye.

***Figure 79*** shows the light harvesting efficiency $\eta_{lh}$ of the four samples. The film with D149/CA and the one sensitized with D149/$S_{1.15}$PcZn/CA for 17.5 h both show a light harvesting efficiency of close to 1 over a broad range from about 425 nm to 650 nm (D149/CA) or 670 nm (D149/$S_{1.15}$PcZn/CA), respectively. The other two samples show narrower peaks with maximum values of $\eta_{lh}$ of about 0.6 ($S_{1.15}$PcZn/CA) or 0.8 (2 h D149/$S_{1.15}$PcZn/CA).

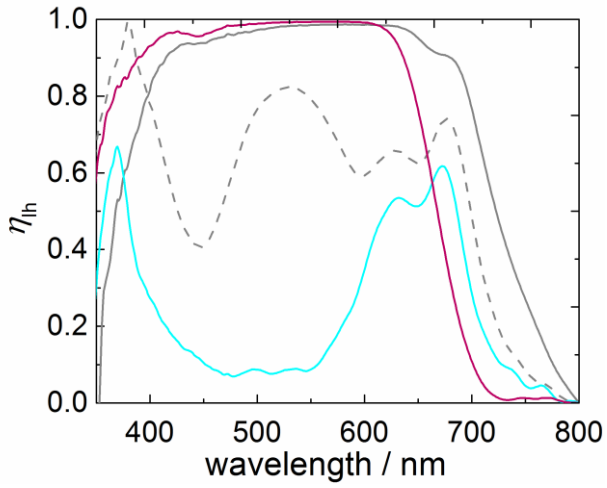


***Figure 79:*** *Light harvesting efficiency of D149- and/or $S_{1.15}$PcZn-sensitized porous ZnO films (legend as in previous plot) calculated from the absorbance.*

## 8.2 Photovoltaic Performance and Steady-State Quantum Efficiency

The current-voltage characteristics of the cells built from the porous ZnO electrodes with D149/CA, $S_{1.15}$PcZn/CA or D149/ $S_{1.15}$PcZn/CA showed a short-term variation under illumination (approaching a saturation value) and depended on the age of the cell, which will be discussed separately in chapter 9. For the sake of comparability with the results presented in the following sections, the present section will mainly focus on the saturation *J-V* characteristics of each cell measured on the day of its analysis by time- and frequency-dependent methods, see ***Figure 80***. D149/CA achieved the best performance among the present cells, roughly similar to that of the indoline dye-sensitized cells in chapter 6 (***Figure 51***), while the cell with $S_{1.15}$PcZn/CA showed almost no photovoltaic activity. The co-sensitized samples performed better than $S_{1.15}$PcZn/CA, but were clearly less efficient than D149/CA despite their extended spectral absorption range.

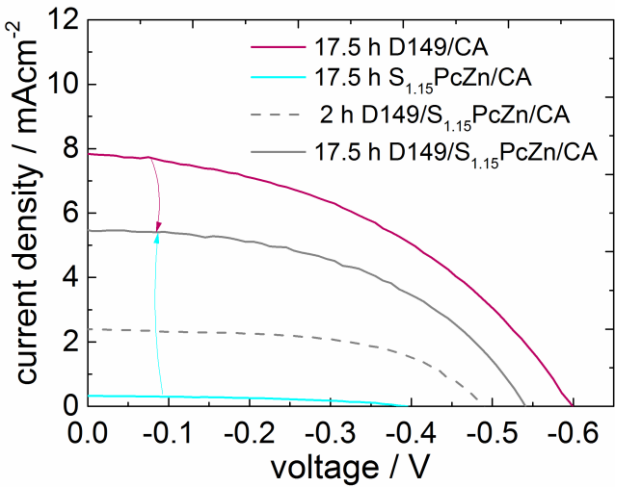


***Figure 80:*** *Stabilized current-voltage characteristics under AM1.5G-type illumination of DSCs with D149- and/or $S_{1.15}$PcZn-sensitized ZnO photoelectrodes.*

The sample-to-sample trends among the $J_{sc}$ values in ***Figure 80*** are well in line with the IPCE (measured on freshly prepared cells) in ***Figure 81***, which was largest for D149/CA, extremely small for $S_{1.15}$PcZn/CA, and in between that of the cells with individual sensitizers for the co-sensitized samples, with D149/$S_{1.15}$PcZn/CA (17.5 h) showing a slightly larger area under the IPCE curve than D149/$S_{1.15}$PcZn/CA (2 h).

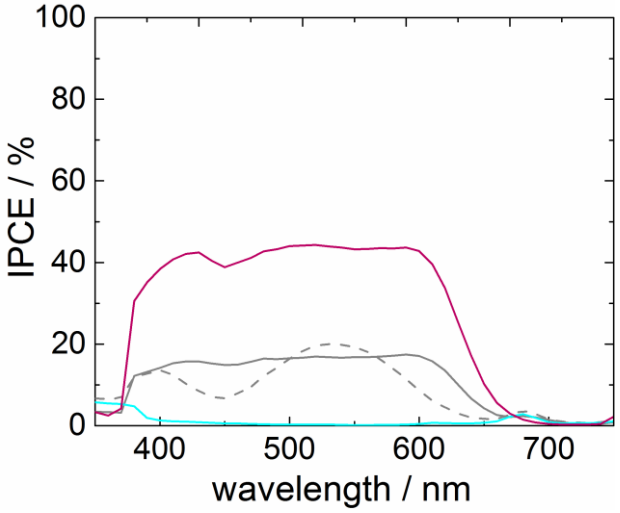


***Figure 81:*** *IPCE spectra of the freshly prepared DSCs with D149 and/or $S_{1.15}$PcZn (legend as in the previous figure).*

The theoretical short-circuit current densities derived from the IPCE spectra by eq. (36) largely present good estimates of the experimental short-circuit photocurrent densities of the freshly prepared cells, see ***Table 25***. The $J_{sc}$ of the freshly prepared sample D149/$S_{1.15}$PcZn/CA (2 h), however, was clearly underestimated by the calculations, possibly as a result of a change in the photovoltaic characteristics between IPCE measurement and *J-V* characterization (cf. short-term development in ***Figure 90*** of chapter 9.1).

***Table 25:*** *Maximum incident photon-to-electron conversion efficiency values $IPCE_{max}$ (with corresponding wavelengths), theoretical short-circuit photocurrent densities $J_{sc}^{theo}$ calculated from the IPCE curves, and experimental $J_{sc}$ of the freshly prepared cells.*

| **sample** | **$IPCE_{max}$ / %** | **$J_{sc}^{theo}$ / mAcm$^{-2}$** | **$J_{sc}$ / mAcm$^{-2}$** |
|---|---|---|---|
| D149/$S_{1.15}$PcZn/CA (2h) | 20 @ 530 nm | 2.03 | 3.19 |
| D149/$S_{1.15}$PcZn/CA (17.5 h) | 18 @ 590 nm | 2.65 | 2.86 |
| $S_{1.15}$PcZn/CA | 3 @ 680 nm | 0.21 | 0.26 |
| D149/CA | 44 @ 520 nm | 6.40 | 6.52 |

The overall efficiency of $\eta$ = 2% of the present cell with D149/CA (see ***Figure 80***) was equivalent to that reached by D149/CA cell in chapter 6, but the fill factor was strongly decreased (from 0.64 to 0.44), while the short-circuit photocurrent density and open-circuit photovoltage were increased (from 5.8 mAcm$^{-2}$ to 7.8 mAcm$^{-2}$ and from -0.56 V to -0.6 V). The higher $J_{sc}$ and $V_{oc}$ were most likely the result of the higher dye loading in the present cell (cf. section 8.1). The open-circuit photovoltages and fill factors will be addressed in more detail as part of the impedance spectroscopic analysis in section 8.3. Given the high and broad light harvesting efficiency of the cell with D149/CA (cf. ***Figure 79***), the IPCE and $J_{sc}$ (eq. (39) and eq. (40)) were limited by the efficiency of electron injection, dye regeneration, or charge collection, as also apparent from the internal quantum efficiency (APCE, cf. eq. (41)) plots in ***Figure 82***.

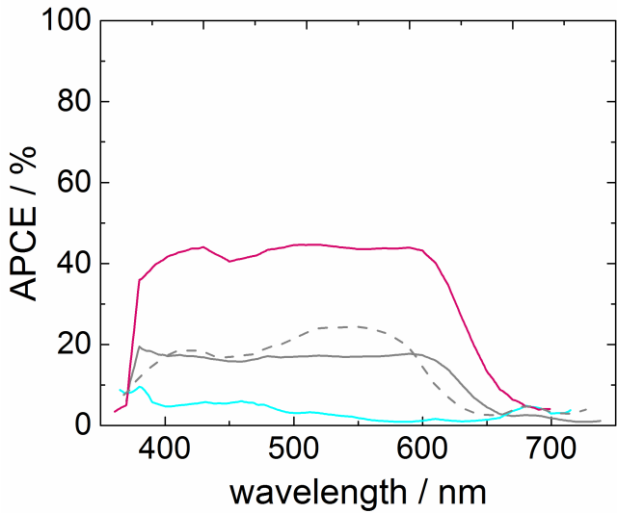


***Figure 82:*** *Absorbed photon-to-electron conversion efficiencies (APCE) spectra of the cells with D149 and/or $S_{1.15}$PcZn (color assignment as above), determined by dividing the spectral IPCE (**Figure 81**) by the spectral light harvesting efficiency (**Figure 79**).*

The charge collection efficiency could be excluded as a limiting factor for the cells D149/CA and D149/$S_{1.15}$PcZn/CA (17.5 h) by an estimation as in chapter 6.5, which showed that the ratio between short-circuit diffusion length and film thickness (***Table 26***) was clearly larger than 3, demonstrating that the charge collection efficiency was ~100%.

***Table 26****: Film thickness, short-circuit electron diffusion length and ratio of the two parameters for two of the four cells. $L_{n,sc}$ values are lower estimates determined from the effective electron lifetime from EIS (AM1.5G) at an applied voltage of -0.2 V and the short-circuit electron transport time from IMPS at a red LED intensity of 25 mWcm$^{-2}$.*

| **sample code** | ***d* / µm** | ***$L_{n,sc}$* / µm** | ***$L_{n,sc}/d$*** |
|---|---|---|---|
| D149/CA | 4.6 | 36 | 8 |
| D149/$S_{1.15}$PcZn/CA (17.5 h) | 4.7 | 51 | 11 |

While no charge transport data was available for D149/$S_{1.15}$PcZn/CA (2 h) and $S_{1.15}$PcZn/CA (2 h), the conclusion of unproblematic charge collection can likely be

extended to these cells by analogy with the electrodeposited samples in chapter 6 (which also included a poor sensitizer, SQ2), cf. ***Table 17***, and based on the independence of the electron transport time of changes to the semiconductor surface (cf. ***Figure 74***) together with the fact that the effective electron lifetime for D149/$S_{1.15}$PcZn/CA (2 h) was comparable to that of D149/$S_{1.15}$PcZn/CA with 17.5 h adsorption time (see ***Figure 85***).

The sample containing only $S_{1.15}$PcZn/CA showed the poorest performance of $\eta$ = 0.06 % among the cells of this chapter, with $J_{sc}$ = 0.32 mAcm$^{-2}$, $V_{oc}$ = -0.39 V, and $FF$ = 0.45 (***Figure 80***). The very small short-circuit photocurrent was partially explained by the relatively low and narrow light harvesting efficiency (***Figure 79***). Nevertheless, the very small APCE values (***Figure 82***) clearly show that there is a strong additional limitation of the IPCE by electron injection and/or dye regeneration. Electrochemical studies of $S_{1.15}$PcZn[307] yielded an oxidation potential of 1.03 V vs. NHE (normal hydrogen electrode), which can be converted to the absolute energy scale[74, 77] to yield a Fermi level $E^0(S^+/S)$ of the ground state (cf. ***Figure 3***) at about -5.5 eV. Together with an optical gap of 1.8 eV (estimated from the onset of the Q-band in the UV/Vis absorption spectrum),[307] the energy of the Fermi level $E^0(S^+/S^*)$ of excited $S_{1.15}$PcZn can be approximated at about -3.7 eV. This indicates that electron injection into ZnO (conduction band edge at -3.9 – -4.5 eV)[42, 292] and regeneration by an $I^-/I_3^-$ electrolyte ($E_{redox}$ = -4.85 eV)[35] are thermodynamically feasible for $S_{1.15}$PcZn, so that a weak bond between $S_{1.15}$PcZn and ZnO and/or the strong aggregation of the phthalocyanine (cf. ***Figure 78***) must have caused the small electron injection and/or dye regeneration efficiency.

Among the two co-sensitized cells, the $J_{sc}$ for the cell D149/$S_{1.15}$PcZn/CA (2 h) was smaller than that of D149/$S_{1.15}$PcZn/CA (17.5 h) in the saturation *J-V* curves measured directly before the detailed photoelectrochemical characterization (2.39 mAcm$^{-2}$ vs. 5.46 mAcm$^{-2}$, cf. ***Figure 80***), while the opposite was observed in the measurements on the freshly prepared cells (3.19 mAcm$^{-2}$ vs. 2.86 mAcm$^{-2}$, see ***Table 25***). The discrepancy was due to the fact that the samples showed a different long-term development of their photovoltaic characteristics (cf. ***Figure 95*** of chapter 9.2). In the *J-V* curves in ***Figure 80*** (relevant for the following sections), D149/$S_{1.15}$PcZn/CA (17.5 h) also showed a superior $V_{oc}$ (-0.54 V) compared to the cell with 2 h adsorption time (-0.49 V), which, together with the increased short-circuit photocurrent, overcompensated a de-

creased fill factor (0.5 vs. 0.56) to yield a higher power conversion efficiency of 1.47 % (compared to $\eta$ = 0.66 for D149/$S_{1.15}$PcZn/CA (2 h)). Although in the sample D149/$S_{1.15}$PcZn/CA (2 h) the low light harvesting efficiency contributed to the poor IPCE and $J_{sc}$ with respect to D149/CA, both of the co-sensitized samples also displayed poor APCE values over the whole spectrum, reflecting low electron injection and/or dye regeneration efficiencies for both sensitizers. The maximum internal quantum efficiency in the absorption range of D149 was slightly better for D149/$S_{1.15}$PcZn/CA (2 h) than for D149/$S_{1.15}$PcZn/CA (17.5 h), but did not come close to that measured for the reference cell D149/CA. Similar to what was discussed for the squaraine co-sensitizer SQ2 in the previous chapters, this could indicate undesired energy transfer from D149 to inefficiently working $S_{1.15}$PcZn. Unlike in the cells with SQ2, however, in the present case coadsorption of cholic acid and strong reduction of the amount of dyes in the ZnO films did not prevent such detrimental dye-dye interactions. For D149/$S_{1.15}$PcZn/CA (17.5h), the APCE is also lowered in the absorption range of $S_{1.15}$PcZn with respect to the cell $S_{1.15}$PcZn/CA, suggesting that the presence of both dyes in larger amounts and in a strongly aggregated state on the ZnO surface leads to a mutually negative effect on the efficiency of electron injection and/or dye regeneration.

Because the sample $S_{1.15}$PcZn/CA was damaged during the IPCE measurements, the results obtained in the subsequent impedance and photoelectrochemical measurements are not considered reliable and will therefore be omitted in the following discussion.

## 8.3 Recombination and Origins of Variations in $V_{oc}$ and *FF*

***Figure 83*** (a) shows the recombination resistance $R_{rec}$ as a function of the Fermi-level voltage. In the high-voltage range, all three samples exhibit the exponential behavior characteristic of recombination under the influence of an exponential distribution of surface traps in the semiconductor (eq. (53)). In the $R_{rec}$ curves of the cells D149/CA and D149/$S_{1.15}$PcZn/CA (17.5 h), a clearly reduced slope is observed at voltages less negative than about -0.5 V, which usually indicates that the measured resistance is governed by recombination events at the substrate/electrolyte interface rather than by $R_{rec}$.[128] On the other hand, a depression of the low-voltage recombination resistance over a wider range can also be caused by an abundance of recombination-promoting dye ag-

gregates on the ZnO surface, as observed for D149 in chapter 5 (***Figure 44***). However, the fact that the two differently sensitized cells both show an equivalent slope of $R_{rec}$ in the low-voltage range speaks against the assumption that recombination via dye aggregates caused the flattening of $R_{rec}$, leaving recombination via the substrate as a more likely explanation (cf. further discussion in section 8.4). In the present samples, the low-voltage slope of the $R_{rec}$ curve is much smaller and appears to extend to more negative voltages compared to $R_{rec}$ curves of previous chapters (see for example ***Figure 58***), indicating a stronger and more extended influence of recombination via the substrate.

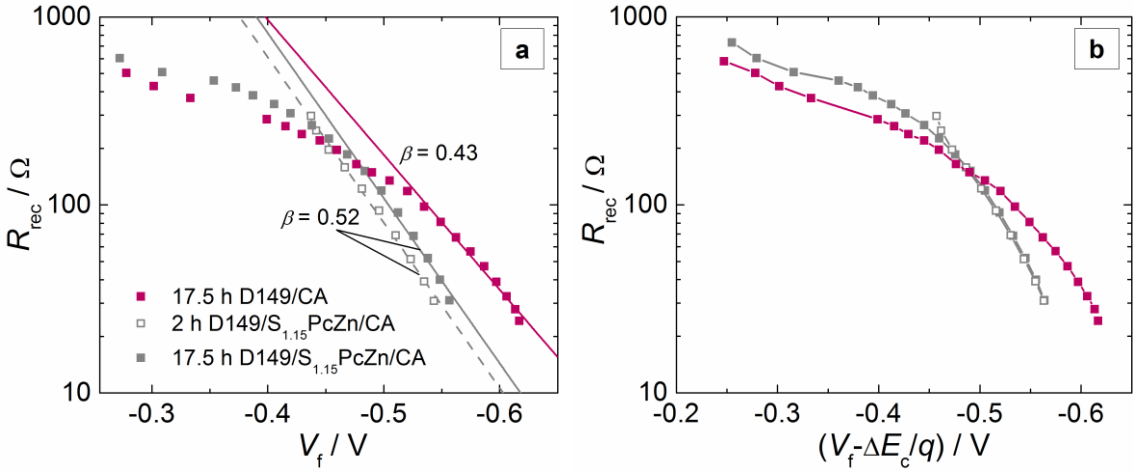


***Figure 83***: *Recombination resistance of ZnO-based DSCs sensitized with D149/CA or with D149/$S_{1.15}$PcZn/ CA for 2 or 17.5 hours against the Fermi-level voltage $V_f$ (a) and against $V_f$ corrected by conduction band edge shifts (b). Lines in (a) represent fits to the high-voltage part of the curves, lines in (b) are a guide to the eye.*

Focusing on the high-voltage sections of the $R_{rec}$ curves, the recombination parameter $\beta$ (see fits to eq. (54) in ***Figure 83*** (a)) of D149/CA was identical (0.43) to the value observed for D149/CA in chapter 6, showing that neither the use of ethanol as a solvent of the dye solution nor the increase of the adsorption time from 2 h to 17.5 h affected the energetic distribution of surface trap states or of oxidized D149 molecules involved in recombination reactions (cf. chapter 5). The $\beta$ parameters of the co-sensitized cells were equal (0.52) for both adsorption times and were increased compared to the value for D149/CA, pointing towards a shift of the energy levels of oxidized dye molecules that act as recombination pathways or targets in the presence of $S_{1.15}$PcZn.

In the plots of the recombination resistance against the corrected voltage $V_f$-$\Delta E_c/q$ (cf. $\Delta E_c/q$ values in ***Table 29***), see ***Figure 83*** (b), the co-sensitized cells with D149/$S_{1.15}$PcZn/CA showed identical recombination resistances independent of the adsorption time, representative of equal rate constants of recombination. In the range of higher corrected voltages ($V_f$-$\Delta E_c/q$ = -0.5 V and more negative), these cells showed lower $R_{rec}$ values than D149/CA, suggesting that charge transfer from ZnO to the electrolyte was less efficiently blocked by adsorbed $S_{1.15}$PcZn molecules compared to D149 molecules. However, in the lower voltage range the recombination resistance of the co-sensitized cells exceeded that of D149/CA, possibly as a result of more pronounced recombination via the substrate.

The three different origins of the differences in $V_{oc}$ and *FF* (i.e., differences in $J_{sc}$, conduction band edge shifts, and differences in the rate constant of recombination) between the cells of this chapter have been studied quantitatively by the same protocol as in chapter 7.7, see ***Table 27***. For a comparison of the results obtained by the present cell with D149/CA, the calculations were also performed for the sample D149/CA of chapter 6.

***Table 27****: Calculated voltage changes with respect to the reference sample D149/CA due to differences in the short-circuit photocurrent, the conduction band edge position, and the recombination resistance. The total voltage changes based on calculation ($\Delta V_{oc,calc}$) and experiment ($\Delta V_{oc}$) are given as well.*

| **sample code** | $\Delta V_{oc}$ ($\Delta J_{sc}$) /mV | $\Delta V_{oc}$ ($\Delta E_c/q$) /mV | $\Delta V_{oc}$ ($\Delta R_{rec}$) /mV | $\Delta V_{oc,calc}$ /mV | $\Delta V_{oc}$ /mV |
|---|---|---|---|---|---|
| D149/CA | +/- 0 (ref.) | +/- 0 (ref.) | +/- 0 (ref.) | +/- 0 (ref.) | +/- 0 (ref.) |
| $S_{1.15}$PcZn/CA | + 174 | n.a. | n.a. | n.a. | + 210 |
| D149/$S_{1.15}$PcZn /CA (2h) | + 65 | + 20 | + 33 | + 118 | + 70 |
| D149/$S_{1.15}$PcZn /CA (17.5h) | + 19 | + 7 | + 30 | + 56 | + 60 |
| D149/CA (chapter 6) | + 18 | - 64 | + 104 | + 58 | + 40 |

For the cell with $S_{1.15}$PcZn, only the influence of the smaller $J_{sc}$ on the voltage difference compared to the reference cell D149/CA could be determined (a loss by 174 mV), which explained more than 80% of the observed voltage loss $\Delta V_{oc}$ of 210 mV**.** The remaining voltage loss of 40 mV must have been caused by a downward shift of the conduction band edge and/or an increase in the rate constant of recombination. The calculations very accurately predicted the experimental voltage difference ($\Delta V_{oc}$ = 60 mV) between D149/CA and the co-sensitized cell with 17.5 h adsorption time. The reduced $J_{sc}$ and increased rate constant of recombination here led to voltage losses of ~20 mV and 30 mV, and the small conduction band edge shift downwards delivered the remaining contribution. The total voltage loss of the co-sensitized cell with 2 h adsorption time with respect to D149/CA was overestimated by almost 50 mV. The difference in $J_{sc}$ already explained nearly the whole experimental voltage difference, but the calculations predicted an additional loss of ~50 mV due to a positive conduction band edge shift and a higher rate constant of recombination, which may have been an overestimation as a result of the approximated conduction band edge shift (see previous chapter). Comparing the cell D149/CA of this chapter and the corresponding sample of chapter 6, a reasonable theoretical prediction of the experimental $\Delta V_{oc}$ was attained. The total voltage gain of 40 mV for the present sample was the result of its higher $J_{sc}$ and lower rate constant of recombination, which may both have been caused by the higher dye loading (cf. section 8.1). These gains overcompensated a relative downward shift of the conduction band edge with respect to the cell of chapter 6. This downward shift of $E_c$ must have been the result of the long sensitization time of 17.5 h in ethanolic dye solution (compared to 2 h adsorption from *tert*-butanol:acetonitrile solution). The use of an ethanolic dye solution is not expected to be responsible for the relative shift, because *all* of the dye-sensitized films in this work were thoroughly rinsed with this solvent after sensitization, independent of the solvent used in the adsorption solution. Rather, the long exposure to the (acidic) dye solution could have changed the surface chemistry of the ZnO towards a more positive surface charge.

***Table 28*** shows the external (from ***Figure 80***) and internal (from plots of $J$ vs. $V_f$) fill factors of the cells with D149 and/or $S_{1.15}$PcZn as well as their theoretical internal fill factors calculated from the experimental $V_{oc}$ and $\beta$ values by eq. (35).

***Table 28**: External fill factors (FF), internal fill factors, and theoretical internal fill factors for DSCs with D149 and/or $S_{1.15}$PcZn. For D149/S1.15PcZn/CA (2h), no internal fill factor could be determined because EIS data for the determination of $V_f$ was not available for voltages as small as the maximum power point. Values in parentheses were calculated based on hypothetical β values as specified in the footnotes.*

| sample code | *FF* | internal *FF* | calculated internal *FF* | |
|---|---|---|---|---|
| | | | with high-$V_f$ $\beta$ | with low-$V_f$ $\beta$ |
| D149/CA | 0.44 | 0.52 | 0.69 | 0.42 |
| $S_{1.15}$PcZn/CA | 0.45 | 0.45 | (0.68)[a] | (0.33)[b] |
| D149/$S_{1.15}$PcZn/CA (2h) | 0.56 | n.a. | 0.71 | (0.39)[b] |
| D149/$S_{1.15}$PcZn/CA (17.5h) | 0.50 | 0.55 | 0.71 | 0.40 |

[a] $\beta$ = 0.61 (based on the assumption that the $\beta$ value of the co-sensitized samples was the average of the $\beta$ values of D149/CA and $S_{1.15}$PcZn/CA); [b] $\beta$ = 0.13 (assumed to be equal to the low-voltage $\beta$ values of the two other cells)

The fill factors in D149/CA and D149/S1.15PcZn/CA (17.5 h) were significantly reduced by 10 – 15% due to a high series resistance, in accordance with the results of chapter 5 (cf. ***Table 10***), which showed that for cells with high dye loadings desorbed D149 molecules in the electrolyte solution and on the counter electrode caused the high series resistance. For $S_{1.15}$PcZn/CA, internal and external fill factors were equal, demonstrating that the effect of the series resistance on the *J-V* curve was negligible compared to other detrimental processes in this sample. The calculated values of the internal fill factor are qualitatively in line with the actual internal *FF*, but are clearly overestimated. This is because the calculations used the high-voltage (ca -0.5 V and more negative) $\beta$ values and, thus, did not account for the influence of recombination via the substrate, which was detected in the recombination resistance around the maximum power point (-0.26 – -0.4 V for the present cells) and most likely limited the fill factor. While the theoretical internal fill factors estimated using the lower-voltage $\beta$ value of 0.13 were somewhat closer to the actual internal fill factors (see ***Table 10*** (right column)), they

clearly represented underestimations. This suggests that the experimental internal *FF* was controlled by recombination both via the substrate and via the porous ZnO film.

## 8.4 Distribution of Trap States

The EIS-derived capacitance of the DSCs based on electrodeposited ZnO with D149/CA or D149/$S_{1.15}$PcZn/CA, ***Figure 84*** (a), showed the exponential behavior typical of a chemical capacitance in nanostructured semiconductors (eq. (52)), in accordance with the results of previous chapters.

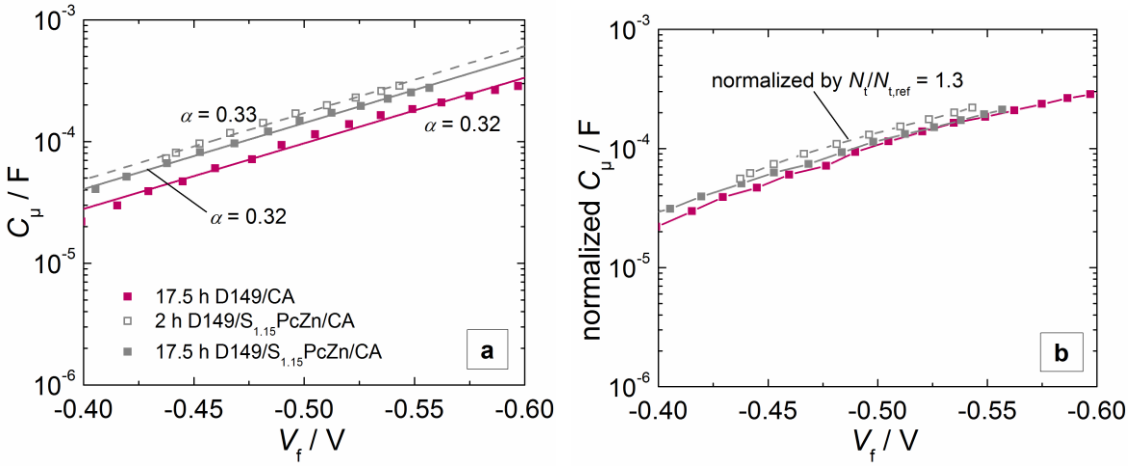


***Figure 84:*** *Chemical capacitance of ZnO-based DSCs with D149/CA or D149/$S_{1.15}$PcZn/CA as a function of the Fermi-level voltage before (a) and after (b) normalization of some of the curves (as indicated) by the relative total trap density. Lines in (a) are linear fits, lines in (b) are a guide to the eye only.*

The trap distribution parameters $\alpha$ of 0.32 to 0.33 determined from the slopes of the $C_\mu$ curves (cf. fits to eq. (52) in ***Figure 84*** (a)) were nearly constant for D149/CA and D149/$S_{1.15}$PcZn/CA (both adsorption times) and were comparable to the $\alpha$ value of 0.35 obtained for D149/CA in chapter 6. For the determination of relative conduction band edge shifts, the chemical capacitance was normalized (***Figure 84*** (b)) by the relative differences in the total trap density $N_t$ obtained by short-circuit charge extraction (see ***Table 29***), as introduced in chapter 6.3.

***Table 29**: Relative total trap densities and relative conduction band edge shifts of the cells sensitized with D149 or D149 and $S_{1.15}$PcZn in the presence of cholic acid. The positive values of $\Delta E_c/q$ indicate downward shifts towards $E_{redox}$.*

| sample code | $N_t/N_{t,ref}$ | $\Delta E_c/q$ / mV |
|---|---|---|
| D149/CA | 1 (ref.) | +/- 0 (ref.) |
| D149/S1.15PcZn/CA (2h) | (30) | + 20 |
| D149/S1.15PcZn/CA (17.5h) | 1.3 | + 7 |

The co-sensitized cell D149/$S_{1.15}$PcZn/CA (17.5 h) showed a slight increase of the total trap density by a factor of 1.3 with respect to D149/CA. The relative $N_t$ of 30 determined for the sample D149/$S_{1.15}$PcZn/CA (2 h) appears unreasonably high given the fact that the same surface adsorbates as in D149/$S_{1.15}$PcZn/CA (17.5 h) were present. Since the corresponding sample showed strong bleaching of the ZnO/dye film after the full photoelectrochemical characterization (including short-circuit charge extraction to determine $N_t/N_{t,ref}$), the faulty result was most likely due to cell degradation.[XVII] On the basis of the identical molar ratio of D149:$S_{1.15}$PcZn of 1:1 in the two co-sensitized ZnO films (cf. section 8.1), an approximation of the normalized capacitance for the sample D149/$S_{1.15}$PcZn/CA (2 h) was determined by assuming that the relative total trap density was equivalent to that of D149/$S_{1.15}$PcZn/CA (17.5 h). In this estimation, both samples co-sensitized with D149 and the phthalocyanine show a small downward shift of $E_c$ with respect to the cell with D149 only, see ***Table 29***, indicating that adsorption of $S_{1.15}$PcZn leads to a more positive surface charge of the ZnO film. This is reasonable based on the slightly higher number (on average 1.15) of acidic –$SO_3H$ anchoring groups on $S_{1.15}$PcZn (compared to a single –COOH group on D149), which can release protons that are adsorbed to the ZnO surface in parallel with the dyes.[67]

[XVII] Note that the cell did not yet show any signs of degradation after the EIS measurements, so that the results of those are considered reliable.

## 8.5 Open-Circuit Voltage Decay and Lifetime Measurements

As an alternative route to analyze recombination kinetics, the time-dependent decay of the open-circuit photovoltage following illumination with light of a red ($\lambda_{max}$ = 632 nm) LED was measured, see ***Figure 85*** (a).[XVIII]

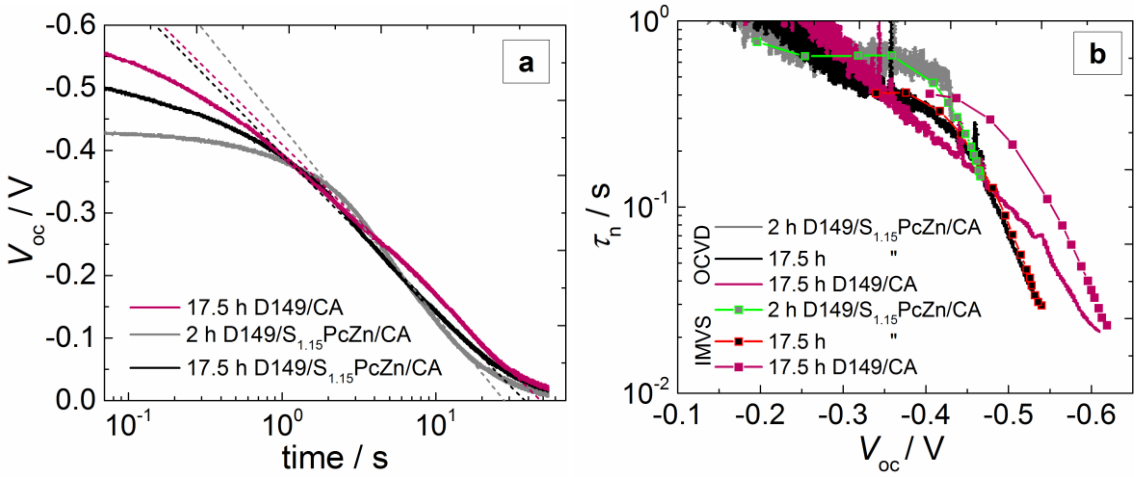


***Figure 85:*** *Time-dependent decay of $V_{oc}$ (OCVD) after illumination with red light (intensity of 25 mWcm$^{-2}$) (a) and voltage-dependent effective electron lifetime calculated from the OCVD or measured by IMVS (b) for DSCs sensitized with D149 and/or D149/S$_{1.15}$PcZn/CA. Dashed lines in (a) are linear fits to small sections of the curves in the time range t ≈ 2 – 20 s, lines in (b) are a guide to the eye.*

All curves show only small linear regions in the semilogarithmic plot and, as a whole, resemble typical voltage decays of cells without blocking layer more than decays of samples with properly functioning blocking layers, for which a linear shape of such plots is observed at times $t > 0.1$ s (with $t = 0$ being the time at which the light is turned off).[266] This confirms that the electrodeposited blocking layer in the present samples did not sufficiently hinder recombination via the FTO/glass substrate. The films were the only ones out of deposition batch no. 5 that were employed in this work and it is possible that this batch showed defects in the compact ZnO blocking layer.

[XVIII] Note that the results presented for D149/S$_{1.15}$PcZn/CA (2h) must be interpreted with reservations, because the cell showed signs of degradation after the detailed photoelectrochemical characterization that included the measurements discussed in this section.

The electron lifetimes $\tau_n$ calculated from the open-circuit voltage decays using eq. (70), see ***Figure 85*** (b), indicated a similar trend with respect to recombination as observed in the $R_{rec}$ curves (cf. ***Figure 83***). (Note that this was still true when the curves were plotted against $V_{oc}$ corrected by the conduction band edge shifts in ***Table 29***.) At $V_{oc}$'s more negative than -0.45 V, co-sensitization with D149 and $S_{1.15}$PcZn yielded a shorter lifetime than use of D149 as individual sensitizer, indicating a higher probability of recombination events, while at voltages between about -0.3 and -0.45 V, the co-sensitized cells showed longer lifetimes than D149/CA. The lifetime data at open-circuit voltages less negative than -0.3 V was not reliable because of the small change of $V_{oc}$ per time compared to the resolution of the measurement. The effective electron lifetimes obtained by intensity-modulated photovoltage spectroscopy (IMVS), ***Figure 85*** (b), also largely confirmed that D149/CA showed the least pronounced recombination in the higher-voltage range but became inferior to the co-sensitized samples at lower voltages. The IMVS results exactly reproduced the lifetimes obtained from the voltage decay except in the case of D149/CA, for which IMVS (measured about 90 minutes after OCVD) yielded considerably higher lifetimes, possibly as a result of a reduction of recombination over time (cf. chapter 9.1).

## 8.6 Summary and Conclusions for This Chapter

Coadsorption of D149 and the phthalocyanine $S_{1.15}$PcZn was achieved by dipping electrodeposited ZnO films into ethanolic solutions containing both dyes together with cholic acid (CA) at a molar ratio of 1:1.5:2 (D149:$S_{1.15}$PcZn:CA) for 2 h or 17.5 h. Characteristic peaks or peak shifts and broadening in the UV/Vis absorption spectra showed that the two dyes were strongly aggregated both in solution and when adsorbed to ZnO. Only in the co-sensitized film with 2 h adsorption time, a reduced degree of aggregation was attained, albeit in connection with a significantly smaller optical absorption. Although the dye loading in a reference film sensitized with $S_{1.15}$PcZn/CA only was much smaller than in a reference film with D149/CA, the absorption spectra indicated a D149:$S_{1.15}$PcZn ratio of approximately 1:1 in the samples containing both sensitizers, suggesting that the presence of D149 assisted in the adsorption of the phthalocyanine.

The highest power conversion efficiency among the cells studied in this chapter ($\eta$ = 2%) was yielded by the solar cell sensitized with D149/CA from ethanolic solution for 17.5 h, while the cell with $S_{1.15}$PcZn as individual sensitizer showed the poorest performance ($\eta$ = 0.06 %). The poor result obtained with the phthalocyanine was partially caused by the small dye loading, but the major limiting factor was a very small internal quantum efficiency, which suggested that there was a fundamental problem in the sensitization of ZnO with $S_{1.15}$PcZn, such as hindered electron injection due to a weak bond between dye and semiconductor. Co-sensitization with D149 and the phthalocyanine for either 2 h or 17.5 h resulted in photovoltaic performance superior to that of the cell with $S_{1.15}$PcZn, but clearly inferior to that of the DSC with D149/CA. The APCE of both co-sensitized cells in the absorption range of D149 was significantly lower than in samples with D149 as individual sensitizer, which indicates undesired energy transfer from the indoline dye to the inefficient phthalocyanine dye, as observed for the squaraine dye SQ2 in previous chapters.

The cell with D149/CA and the samples with D149/$S_{1.15}$PcZn/CA displayed nearly identical trap distributions, but the co-sensitized samples showed a slightly higher total trap density and a relative downward shift of the conduction band edge by ~10 – 20 mV, indicating additional positive surface charges introduced by adsorption of the more acidic phthalocyanine. Combination of D149 and $S_{1.15}$PcZn also led to increased recombination in the high-voltage range compared to D149/CA, as confirmed by impedance spectroscopy, open-circuit voltage decay measurements as well as intensity-modulated photovoltage spectroscopy. All of the cells studied in the present chapter exhibited non-linear semilogarithmic plots of the open-circuit photovoltage decay as well as strongly flattened sections of the voltage-dependent recombination resistance that extended to relatively negative voltages of about -0.5 V. This strongly suggested that the blocking layers of the ZnO film batch used in this chapter insufficiently blocked recombination via the substrate, which, in consequence, influenced the photovoltaic performance up to the range of the maximum power point of the cells and thus contributed to their unusually low fill factors. An analysis of the origins of the sample-to-sample differences in $V_{oc}$ showed that less efficient injection as seen in the smaller short-circuit photocurrents of the cell with $S_{1.15}$PcZn and the co-sensitized samples presented a major source of voltage loss with respect to the sample with D149/CA. The downward shift of the con-

duction band edge and the smaller recombination resistances led to additional losses of ca 10 – 30 mV each.

In conclusion, the sulfonated phthalocyanine $S_{1.15}$PcZn was found to be even less suitable as sensitizer for ZnO than the squaraine dye SQ2 discussed in the previous chapters. In future experiments, it is therefore vital to explore other types of red-absorbing dyes with respect to their compatibility with ZnO. Choosing molecules with large bulky substituents could contribute to minimize dye aggregation, which was detected as a major problem both for SQ2 and $S_{1.15}$PcZn in the present work.

# 9 Stability Aspects of DSCs Sensitized with Organic Dyes and Coadsorbates

## 9.1 Short-Term Stability of Photovoltaic Characteristics and Role of Cell Temperature

In the current-voltage characterization of the DSCs based on D149-sensitized electrodeposited ZnO of chapter 5, a decrease of the open-circuit photovoltage was observed when multiple measurements under illumination were performed in succession. In the example in ***Figure 86*** (left), the $V_{oc}$ measured after light soaking for 5 min was 27 mV smaller than the value measured initially after storage in the dark and the corresponding dark current showed an earlier onset than the dark current measured after dark storage. To investigate whether the changes might have been caused by a temperature increase, the temperature development on the illuminated glass surface of the cell (working electrode side) was monitored over time after turning on the solar simulator (100 $mWcm^{-2}$). Within about 30 minutes, a large change from an initial temperature of 26°C to a final temperature of ~51°C had occurred. Exposure (following dark storage) to a stream of 70°C warm air supplied by a blow dryer led to a very similar effect on the *J-V* curves as the light soaking, see ***Figure 86*** (right): the $V_{oc}$ decreased by 17 mV compared to measurements performed at room temperature after dark storage and the onset of the dark current shifted to less negative voltages. Simulated current-voltage characteristics under illumination (***Figure 87***), calculated based on eq. (31) and (32), predict a 25 mV decrease in $V_{oc}$ upon increasing the temperature from 26°C to 50°C, further confirming that the change by 27 mV observed in ***Figure 86*** (left) is temperature-related. As theoretical dark current and current under illumination only differ by a constant offset equal to $J_{sc}$, the simulations also predict a positive shift of the dark current onset. The fact that the exposure to 70°C warm air did not lead to an even larger decrease in $V_{oc}$, as predicted by the calculations (green curve in ***Figure 87***), could indicate that the temperature in the active layer was smaller than 70°C.

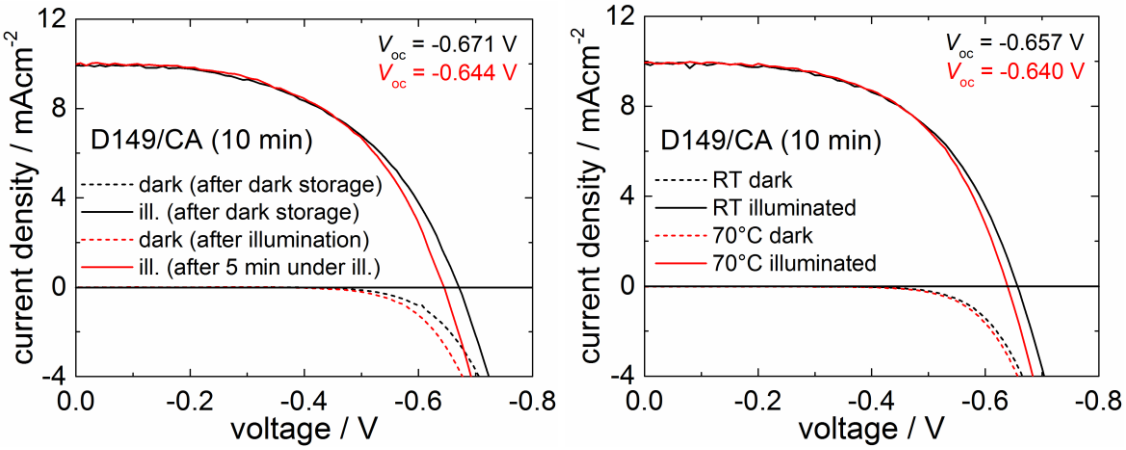


***Figure 86**: Influence of pre-soaking of a DSC with D149/CA (adsorption time of 10 minutes) in AM1.5G type light for 5 min (left) or heating the same cell to 70°C (right) on the current-voltage characteristics in the dark and under AM1.5G illumination.*

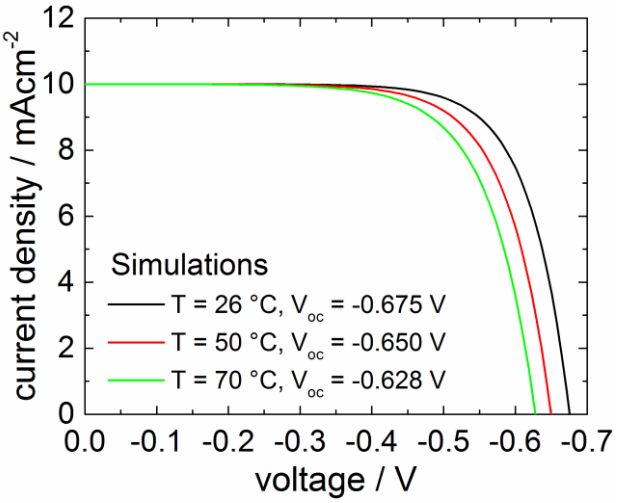


***Figure 87**: Simulated current-voltage curves (under illumination) illustrating the influence of increased cell temperatures on the open-circuit photovoltage. Simulation parameters were $J_{sc}$ = 10 mAcm$^{-2}$, d = 4.1 µm, and β = 0.46 (experimental averages for cells sensitized with D149/CA for 10 minutes), and $k_r = 10^{14}$ s$^{-1}$, $N_c = 4 \cdot 10^{18}$ cm$^{-3}$, and ($E_c$-$E_{redox}$) = 1 eV (values given in ref. [267] for ZnO-based DSCs).*

The current-voltage characteristics of the dye-sensitized solar cells analyzed in chapter 6 (with the dyes D149, D131, and/or Sq2) showed similar changes during continuous illumination by the solar simulator as discussed above for the cells of chapter 5, but the decrease of the open-circuit photovoltage was accompanied by a minor increase of the

short-circuit photocurrent density, see examples in ***Figure 88***. A saturation of $J_{sc}$ and $V_{oc}$ was typically approached in about 10 minutes or less. A possible reason for the slight gain in $J_{sc}$, which is not expected to result from the increase of the cell temperature (cf. ***Figure 87***), could be a downward shift of the conduction band edge of the semiconductor film under illumination, as has been reported for $TiO_2$-based cells.[308] This would also be expected to lead to a decrease in $V_{oc}$, which would have added to the temperature-induced decrease of the open-circuit voltage. Another possible factor that could have influenced $J_{sc}$ is a rearrangement of surface-adsorbed dye molecules during cell operation, which may have involved desorption of inefficient weakly attached sensitizer molecules or aggregates and thereby improved the electron injection efficiency (cf. ***Table 17***).

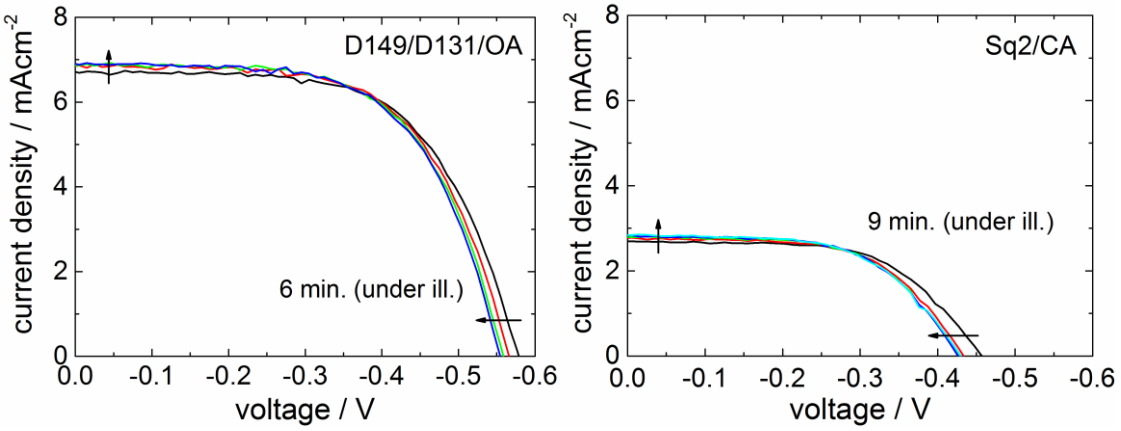


***Figure 88****: Representative examples of the short-term development of the current-voltage characteristics of DSCs based on electrodeposited ZnO with indoline dyes, squaraine dye, or combinations of both (chapter 6) under continuous illumination with AM1.5G-type light.*

For the dye-sensitized solar cells based on nanoparticulate ZnO (cf. chapter 7), the development of the *J-V* characteristics during light soaking, see examples in ***Figure 89***, again showed a temperature-related decrease in $V_{oc}$, which was, however, accompanied by a minor decrease (instead of a small increase) in $J_{sc}$. Assuming that the change in current is again related to desorption of a part of the dye molecules, possible improvements in the (already relatively high, cf. ***Table 22***) electron injection efficiency in this case seemed to have been outweighed by the negative effect of the reduction of the light harvesting efficiency resulting from partial dye desorption.

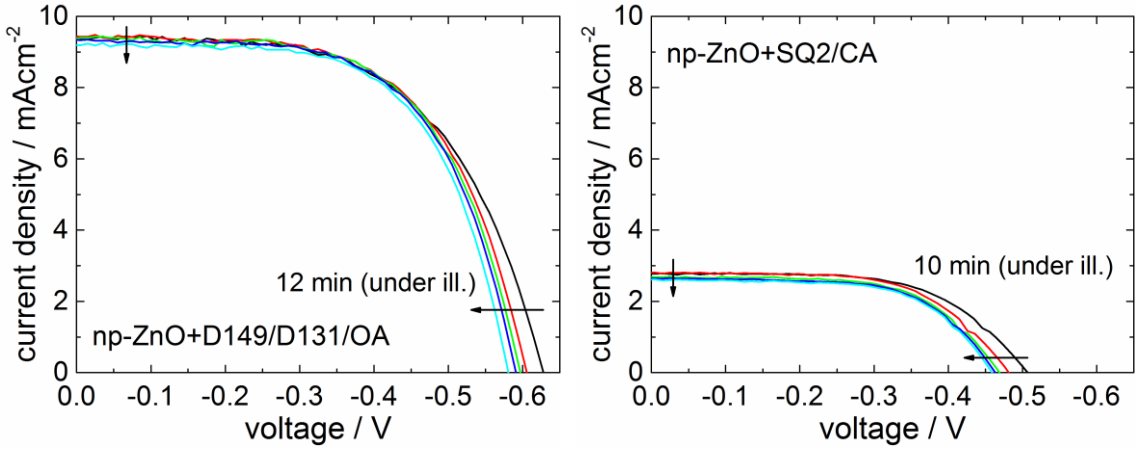


***Figure 89**: Short-term development of the J-V characteristics (representative examples) of solar cells based on nanoparticulate ZnO (chapter 7) under continuous illumination with AM1.5G-type light.*

As for the *J-V* curves of the cells sensitized with D149 and/or $S_{1.15}$PcZn from ethanolic solution (chapter 8), only the samples $S_{1.15}$PcZn/CA (17.5 h) and D149/$S_{1.15}$PcZn/CA (2 h) (***Figure 90*** top row) presented a development under illumination similar to that described above, with a temperature-related decrease of $V_{oc}$ and a small increase or decrease in $J_{sc}$ that was presumably again related to changes in the light harvesting efficiency and/or electron injection efficiency as a result of partial dye desorption. For the cells sensitized for 17.5 h with D149/CA or D149/$S_{1.15}$PcZn/CA, the initial *J-V* curves showed a pronounced "S-shape" that is reminiscent of – albeit more pronounced than – the shape of the current-voltage characteristics found in chapters 6 and 7 for strong recombination at lower energies via oxidized dye aggregates (cf. ***Figure 71***). Illumination for 20 – 25 min led to a drastic increase of $J_{sc}$ (from 3.8 and 0.5 mAcm$^{-2}$ to 7.6 and 3.2 mAcm$^{-2}$), *FF* (from 0.36 and 0.18 to 0.49 and 0.44), and, in one case, $V_{oc}$ (from 0.37 to 0.52 V). This is particularly surprising in the case of the cell containing only D149/CA, for which a constant $J_{sc}$ along with a temperature-related decrease of $V_{oc}$ would be expected based on the results in ***Figure 86***. A possible explanation for such a finding may be a significant rearrangement of the dye/coadsorbate layer under illumination and photovoltaic operation in these two cells that contained very large dye loadings and showed pronounced signs of dye aggregation (cf. ***Figure 78***). This may involve break-up or desorption of the recombination-promoting and injection-hindering sensitizer aggregates.

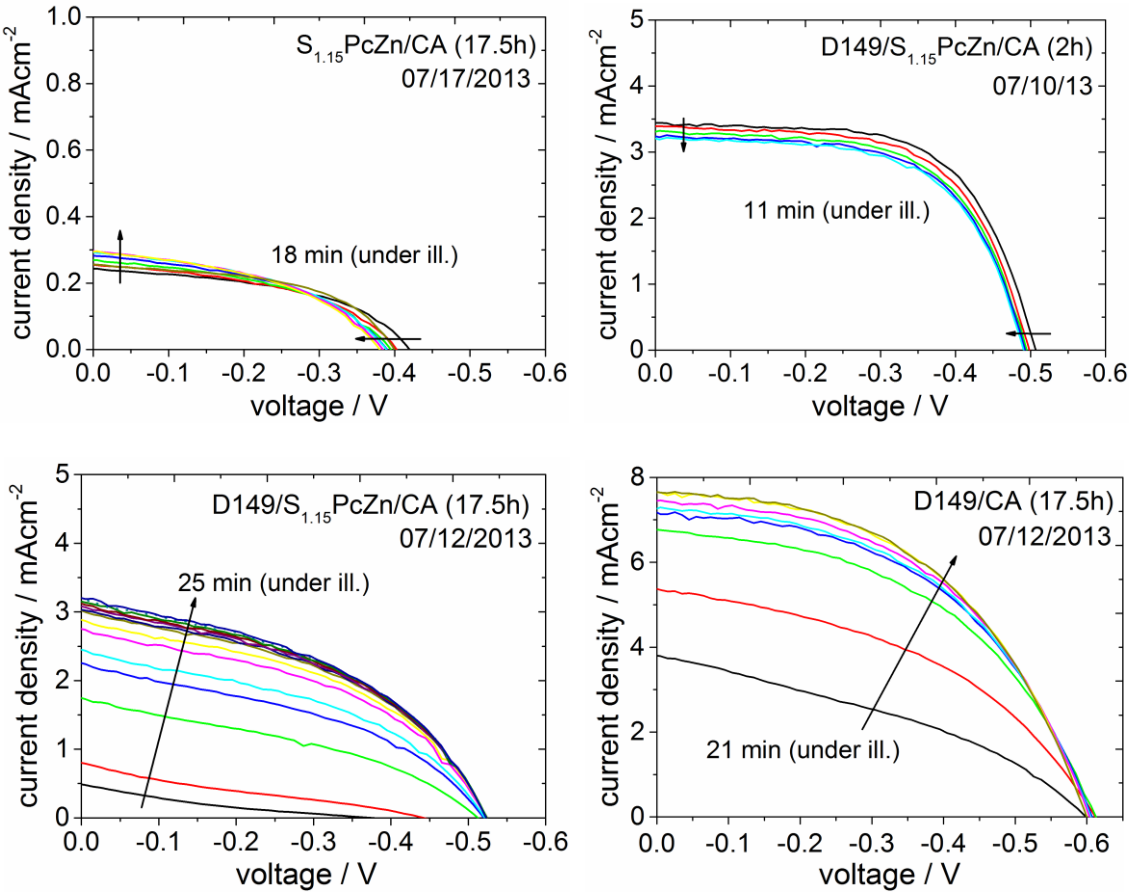


***Figure 90**: Short-term change of the J-V characteristics of solar cells with D149 and/or the phthalocyanine dye $S_{1.15}$PcZn (see chapter 7) under continuous AM1.5G illumination.*

## 9.2 Long-Term Development of Cell Properties

The current-voltage characteristics of the ZnO-based dye-sensitized solar cells with varied amounts of D149 with cholic acid (cf. chapter 5) were monitored over a period of 4.5 months. The first two measurements for each cell were performed at Gifu University and the remaining three at University of Gießen. In both cases AM1.5G illumination of a solar simulator was employed, and the illumination intensity was set with silicon diode based detectors, thus making the experiments in the two different laboratories as comparable as possible. In the first two as well as the last current-voltage measurement a black shadow mask with an aperture of 5 mm was used, while this was not the case in the third and fourth measurements. A comparison of the *J-V* curves of an example cell measured subsequently with and without the mask (***Figure 91***) shows almost no differ-

ence, indicating that, unlike in a previous report studying $TiO_2$-based cells on 4 mm thick FTO/glass substrates,[309] the use of a mask with an aperture size comparable to the cell area for the present cells on thinner (1.1 mm) glass substrates did not lead to significant changes in the cell performance.

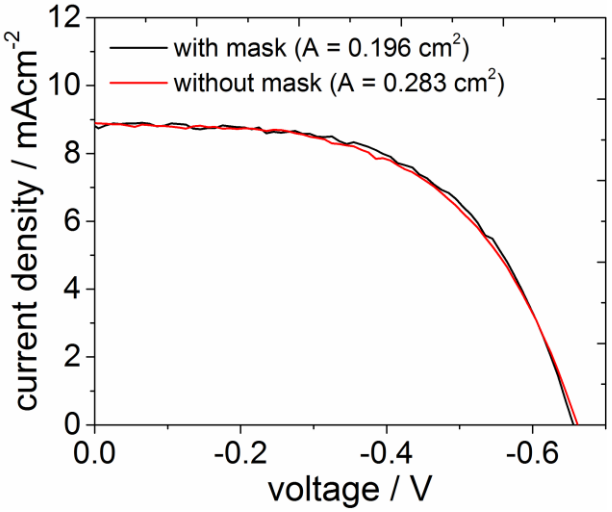


***Figure 91**: Comparison of J-V curves of a DSC with D149/CA (adsorption time of 120 min) measured with and without a shadow mask limiting the illuminated cell area to 0.196 $cm^2$. The current densities were calculated using the illuminated cell areas given in the legend.*

The $J_{sc}$, $V_{oc}$, *FF*, and $\eta$ values determined from the repeated *J-V* measurements are plotted as a function of time in ***Figure 92***. The short-circuit photocurrent for the cells prepared with 1 or 2 min adsorption time showed a minor increase in the first few days, which was followed by a steady decrease over several weeks. The cells with 10 or 120 min adsorption time displayed a more significant trend to increase over the first month, before they decreased in a similar way as the samples with smaller dye loadings. In a previous study investigating cells based on D149-sensitized electrodeposited ZnO with coadsorbate lithocholic acid (adsorption time of 15 min), a slow, steady increase of $J_{sc}$ from about 13.5 to 14.5 $mAcm^{-2}$ over a period of 4 weeks was observed with a high time resolution.[280] The present low-resolution data for 10 min adsorption time is roughly consistent with such a behavior. On the other hand, all four groups of data (with 4 different adsorption times) would also be compatible with a peak function centered at

approximately 20 days. The limited time resolution does not allow for final conclusions on the development of $J_{sc}$ over the first month.

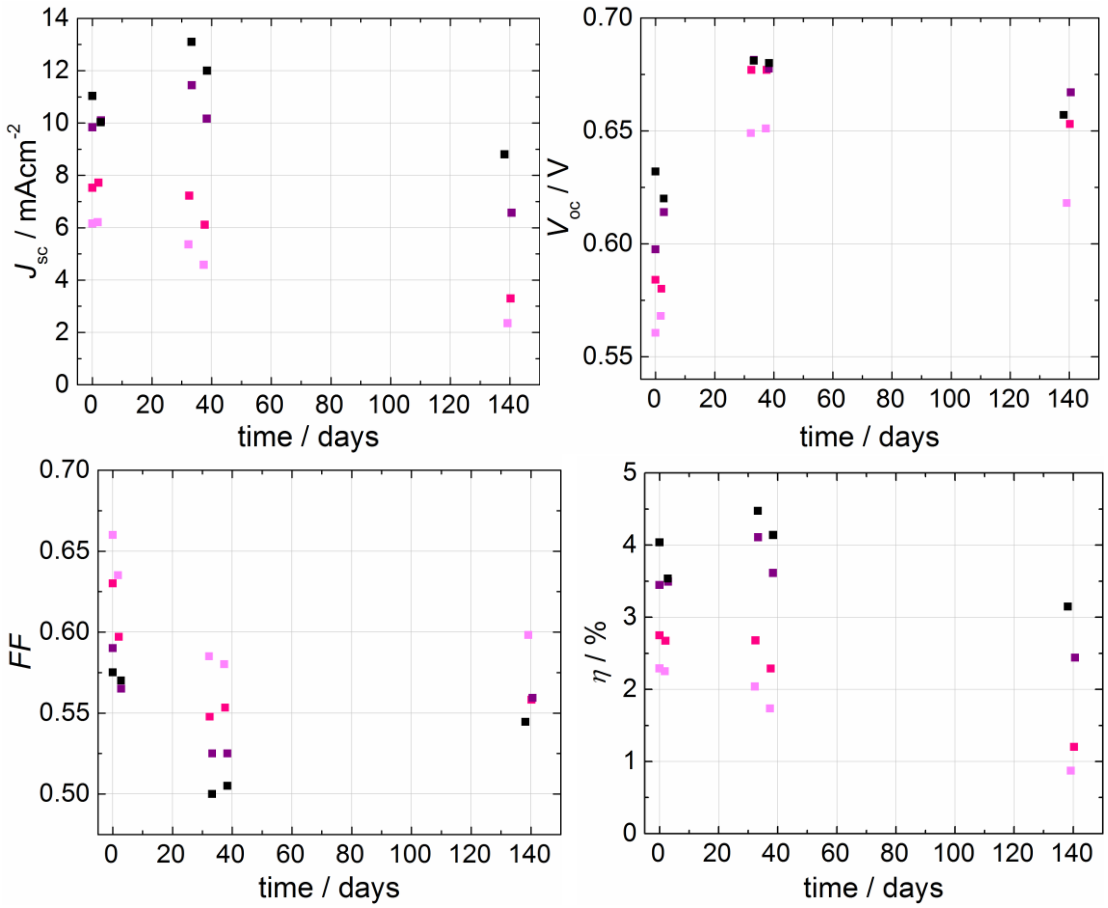


***Figure 92**: Change of photovoltaic characteristics of the DSCs with varied amounts of D149 (with CA; cf. chapter 5) over a period of 4.5 months. Adsorption times were 1 min (light magenta), 2 min (pink), 10 min (purple) or 120 min (black). Values shown in the plot are averages of the characteristics of one to three cells prepared for each adsorption time. In between measurements, the cells were stored in plastic sample cases in the dark.*

In general, a long-term decrease of $J_{sc}$ is most likely caused by a reduction of the dye loading (desorption or decomposition of sensitizer molecules)[280, 286] or by surface degradation leading to a decreased electron injection efficiency.[168, 310] A possible increase in the first 2 – 3 weeks could have resulted from an initial beneficial dye rearrangement to reduce the degree of dye aggregation on the semiconductor surface. The open-circuit voltage shows a similar development for all four groups of cells: over the first 40 days

there is a strong increase, followed by a moderate decrease. This differs from the results of the above-mentioned previous study on the stability of ZnO/D149 solar cells, in which $V_{oc}$ remained constant over 30 days. A constant $V_{oc}$ (at reduced $J_{sc}$) was also observed in the present work in cells containing only D149 without coadsorbate, which will be discussed below. The significantly increased $V_{oc}$ of the 4-month old cells with D149/CA points to an upward shift of the conduction band edge, because the $J_{sc}$ after 4 weeks is notably smaller than in the initial measurement and a reduction in the rate constant of recombination is considered unlikely (cf. eq. (34)). A shift of $E_c$ could generally be related to changes in the relative amounts of dyes and coadsorbates on the surface. The time dependence of the fill factors appears largely like an inversion of the trend observed in the present study for $V_{oc}$: for all adsorption times, *FF* steeply decreases between day 0 and day 40 and afterwards stabilizes (low adsorption times) or increases again (high adsorption times). A decrease followed by a stabilization was also found in the previous investigation and, according to the results observed in connection with dye desorption and dissolution in the electrolyte solution in chapter 5.3.5, indicates an increase of the series resistance of the complete cell. Since the time dependences of $V_{oc}$ and *FF* are nearly diametrical, the development of the power conversion efficiency $\eta$ is mainly determined by the changes in $J_{sc}$.

For DSCs containing varied amounts of D149 in the absence of any coadsorbate (cf. chapter 5), the current-voltage characteristics were measured on the day of preparation and after 4 weeks (***Figure 93*** (left)). Here, a significant decrease in $J_{sc}$ (from 2.4 – 11.2 $mAcm^{-2}$ down to 1.3 – 8.2 $mAcm^{-2}$) and *FF* (from 0.52 – 0.7 down to 0.43 – 0.69) at maintained or in some cases very slightly increased $V_{oc}$ values of 0.52 – 0.59 V was observed for cells with all adsorption times. Based on electrochemical impedance measurements in chapter 5.3.5 it was inferred that D149 may have been less stably bound to ZnO in films without CA with respect to films with D149/CA, which might explain the observed clear decrease of $J_{sc}$ in ***Figure 93*** over 3 weeks, while an initial increase over 4 weeks was seen for the cells with coadsorbate. As a result, the power conversion efficiency was significantly reduced for all samples after four weeks (0.9 – 3.6% to 0.4 – 2.2%). As discussed above for cells with D149/CA, the long-term decrease of $J_{sc}$ was most likely mainly the result of a reduced amount of light-absorbing and electron-injecting dye molecules on the ZnO surface. The reduction of *FF* again indicates an enlarged series resistance due to dye molecules dissolving in the electrolyte. ***Figure 93***

(right) shows the change of the *J-V* curve over time in more detail for a selected cell with 10 min adsorption time, with an additional measurement performed three weeks after cell preparation.

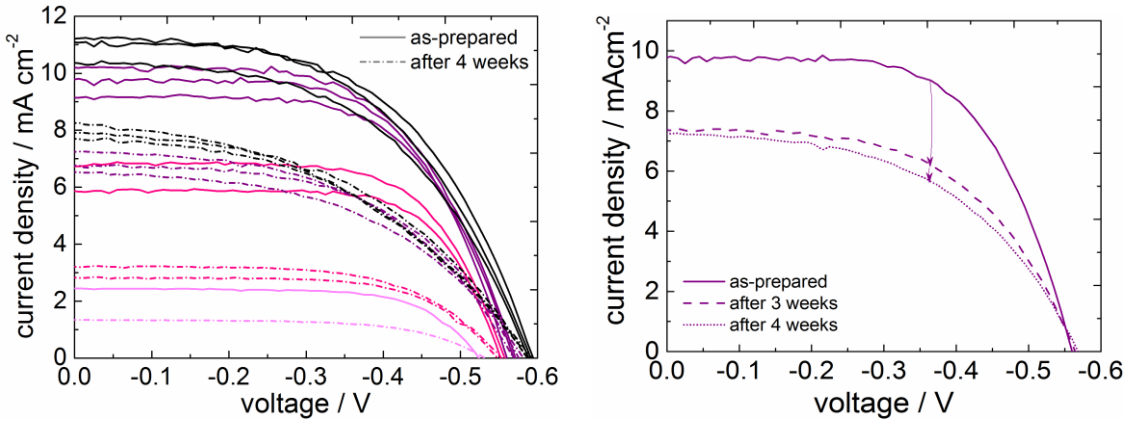


***Figure 93**: Current-voltage characteristics on the day of preparation (——) and after 4 weeks (-·-·-·) of ZnO-based DSCs (cf. chapter 5) with the indoline dye D149 without CA (left). Adsorption times were 1 min (light magenta), 2 min (pink), 10 min (purple) or 120 min (black). For one of the cells with 10 min adsorption time, an additional measurement after 3 weeks was performed (right), along with a detailed analysis as discussed below.*

This data demonstrates that the current had already decayed to the lower value of ca 7.3 $mAcm^{-2}$ after three weeks, and that between the second and third measurement only the fill factor showed a further decrease. To attempt an investigation of the reasons for the nearly constant $V_{oc}$ at lowered $J_{sc}$ for this cell, intensity-modulated photovoltage spectroscopy and charge extraction measurements were performed on the day of preparation and after 3 weeks. The effective electron lifetime, ***Figure 94*** (left), maintained the same slope but was increased by a factor of 3 for the 3-weeks-old cell. The constant slope in the two measurements indicates that the energetic distribution of bulk and surface traps did not change (eq. (19)). The increase of the effective electron lifetime over the whole voltage range may in principle be the result of a decrease in the rate constant of recombination, of an upward shift of the conduction band edge, and/or of an increase in the total trap density $N_t$ (cf. eq. (19) and corresponding text). To further investigate changes in $N_t$ and possible conduction band edge shifts that could have resulted from changes in

the amount or arrangement of the dye molecules on the ZnO surface, the charge density vs. $V_{oc}$ curves are shown in ***Figure 94*** (right).

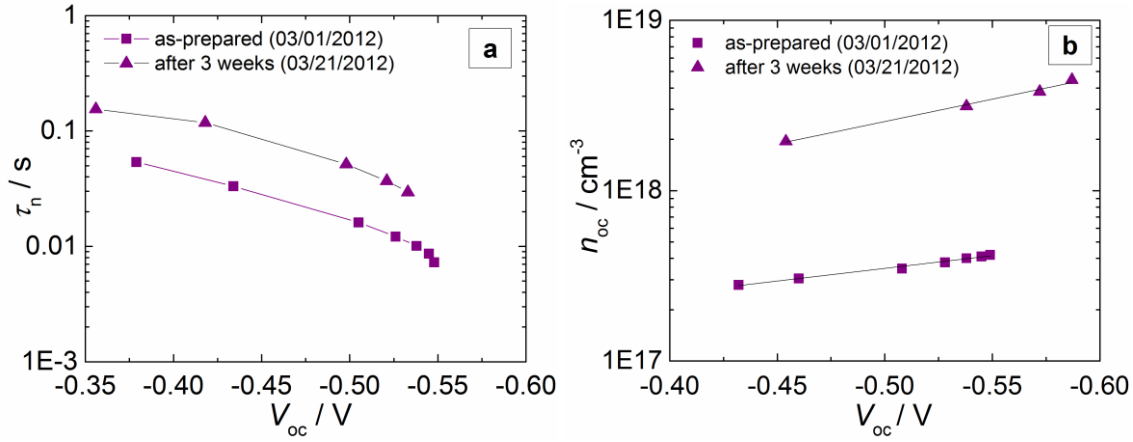


***Figure 94****: IMPS-derived open-circuit effective electron lifetime $\tau_n$ (a; lines are a guide to the eye only) and extracted open-circuit charge density (b; lines are linear fits) of a DSC based on electrodeposited porous ZnO with the photosensitizer D149 (adsorption time of 10 min; cf. chapter 5) on the day of cell preparation and three weeks later. Measurements were performed with a red (IMVS and charge extraction on 03/01/2012) or cyan (charge extraction on 03/21/2012) LED.*[XIX]

A strong displacement of the $n_{oc}$ vs. $V_{oc}$ curve to higher $n_{oc}$ values without a significant change in slope is observed compared to the data of the freshly prepared cell. Although this could, in principle, be interpreted as a tremendous conduction band edge shift *downwards* by ~400 mV for the 3-week old cell, such shift appears almost impossible in view of the nearly constant $V_{oc}$ (cf. ***Figure 93*** (right)), since it would have to be compensated by a remarkable decrease in the rate constant of recombination by a factor of 1000, as estimated by eq. (34). Hence, the observed shift of the charge density curve must be dominated by a significantly increased total trap density, possibly superimposed onto smaller shifts of the conduction band edge. (No further distinction between changes in $N_t$ and/or $E_c$ can be made based on the available data.) Consequently, the observed increase in the electron lifetime most likely was largely the result of an increase in $N_t$, while a small upward shift of the conduction band edge could have delivered an addi-

[XIX] Charge extraction measurements using the red or cyan LED are comparable provided that the trap distribution did not vary significantly along the thickness of the porous film, which is expected based on the homogeneous nanostructure of the electrodeposited porous ZnO films and the constant current density measured over the course of the film deposition (cf. chapter 4).

tional contribution. The combined effect of changes in the recombination-related parameters must have been an increase of $V_{oc}$ by about 25 mV, since the decrease of $J_{sc}$ from 9.79 to 7.35 $mAcm^{-2}$ should, according to eq. (75), have entailed a decrease of $V_{oc}$ by 17 mV, while the actual open-circuit voltage showed a minor *increase* by 8 mV between the day of preparation and the measurement after 3 weeks.

For the DSCs sensitized with D149 and/or sulfonated Zn phthalocyanine, *J-V* curves were repeatedly measured over the course of 1 – 2 weeks, see ***Figure 95***. As discussed in the previous section, the current-voltage characteristics of these cells showed significant changes when measured repeatedly over 5 – 20 minutes under continuous illumination. These short-term changes were observed each time the cells were characterized during the 1 – 2 weeks, indicating that the partial desorption of (aggregated) dye molecules discussed in the previous section was reversible and the initial condition of the semiconductor/dye interface was restored when the cells were stored in the dark. The curves displayed here all represented the state of saturation achieved under illumination on a particular day.

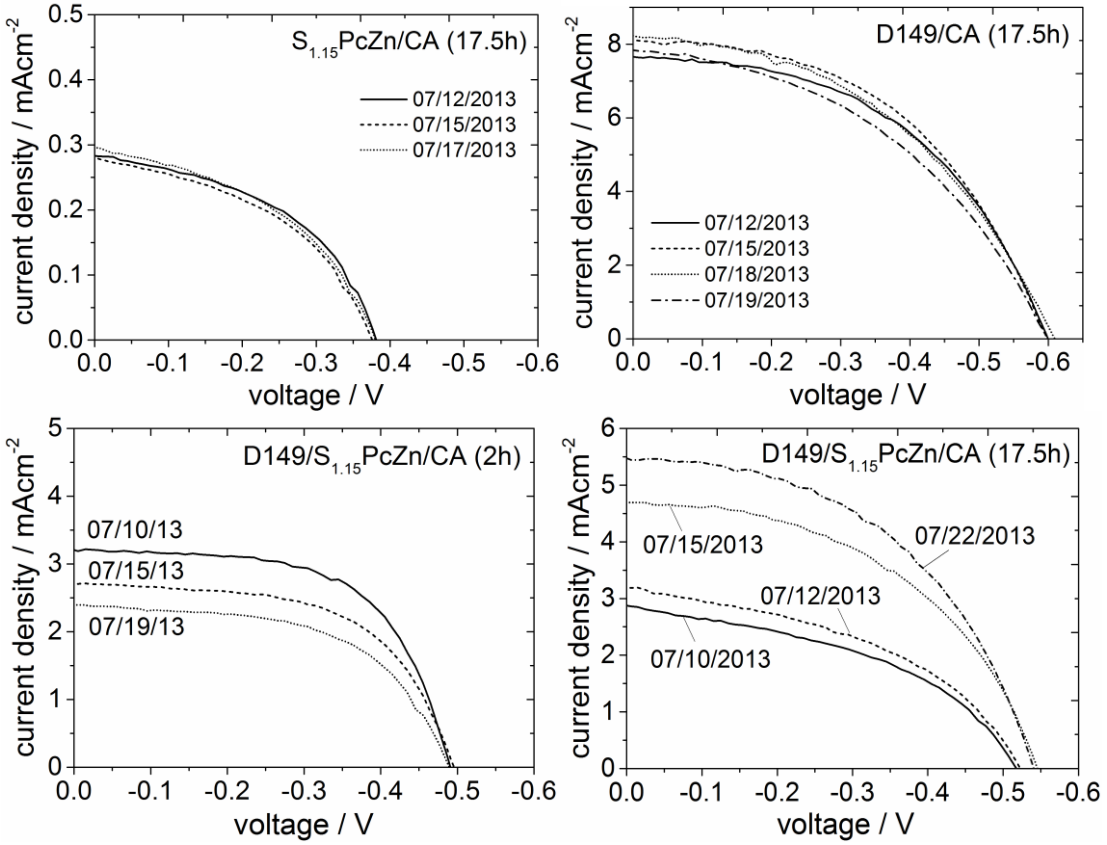


***Figure 95**: Saturation J-V curves of DSCs sensitized with D149 and/or $S_{1.15}$PcZn measured at different times between 7 and 12 days after the day of preparation (07/10/13), as specified by the dates given in the plots.*

The current-voltage characteristics of this group of DSCs showed a variety of time dependences. For the cell with the shorter adsorption time of 2 h, sensitized with both dyes in the presence of CA, the $J_{sc}$ decreased from 3.2 to 2.4 mAcm$^{-2}$, the fill factor decreased from 0.62 to 0.56, and the open-circuit voltage stayed constant. The two cells with either D149 or $S_{1.15}$PcZn as individual sensitizer presented relatively stable current-voltage characteristics over about a week. The measurement performed for the sample with D149/CA after a week (07/19/2013) showed a somewhat decreased $J_{sc}$ and *FF*, which suggests a beginning decay of the performance, albeit much less pronounced than in the case of the co-sensitized cell with 2 h adsorption time. It is conceivable that the large dye loading in the cell D149/CA resulted in a relatively high local concentration of dye molecules in the electrolyte in the pores due to desorption. This could have prevented the photocurrent from decreasing due to excessive desorption of efficiently injecting non-aggregated dyes. The DSC containing only the phthalocyanine contained

a small amount of dye, so that the present results indicate that the dye layer did not undergo significant changes within the first week after cell preparation. The co-sensitized sample fabricated with an adsorption time of 17.5 h exhibited an improvement of all photovoltaic parameters over the 12 days it was monitored. The development of the saturation *J*-*V* curves of this cell (cf. ***Figure 90***) is consistent with the changes found for D149/CA cells with varied dye loadings and, hence, also possibly reflects a beneficial rearrangement of the dye molecules over a longer period of time. For D149/S1.15PcZn/CA (17.5 h), the improvement occurring over ~1 week was superimposed onto a short-term improvement observed on each day of measurement (***Figure 90***). This indicates that two different processes may be responsible for the short-term and long-term improvement, respectively. One possibility is that in addition to the desorption/aggregate-dissolving processes indicated above, D149 molecules may over time replace phthalocyanine molecules on the surface, which should lead to an improvement of the photovoltaic properties.

## 9.3 Summary and Conclusions for This Chapter

The different sets of cells analyzed in this work showed largely similar, reversible short-term (< 30 minutes) developments of their current-voltage characteristics under continued AM1.5G-type illumination, characterized by a decrease of $V_{oc}$ by typically 20 – 50 mV that was, at least in part, attributed to an increase of the cell temperature to ca 50°C. In most cases, the decrease of $V_{oc}$ was accompanied by slight changes in $J_{sc}$ thought to be mainly caused by a partial desorption of adsorbed dye molecules. Much more significant short-term changes were observed for cells fabricated with a very long adsorption time of 17.5 h (D149/CA and D149/$S_{1.15}$PcZn/CA): strong aggregation in the dye layer here led to a very limited initial photovoltaic performance, but $J_{sc}$, $V_{oc}$, and *FF* displayed a remarkable reversible increase under continuous illumination for ~20 minutes, indicating a beneficial break-up/desorption of dye aggregates.

The long-term development of the photovoltaic characteristics was monitored over several weeks for cells with varied amounts of D149 without CA and for the co-sensitization series with D149 and/or $S_{1.15}$PcZn, and over 4.5 months for cells with varied amounts of D149 with cholic acid. For D149/CA with varied dye loading, the short-circuit photocurrent density first increased, indicating beneficial changes in the dye lay-

er such as a reduction of the number of aggregated inefficient sensitizers, before it decreased for all samples over several months to arrive at values clearly below the initial $J_{sc}$, suggesting a long-term decrease of the amount of efficiently injecting dye molecules on the ZnO surface by desorption or degradation. The open-circuit photovoltage showed a substantial increase over the monitoring period of 4.5 months, which pointed towards an upward shift of the conduction band edge. For DSCs with varied amounts of D149 without coadsorbate, a repeated *J-V* characterization performed 3 – 4 weeks after cell preparation showed a pronounced decay of the short-circuit photocurrents and fill factors, which was largely comparable to the findings for D149/CA cells if one neglects the initial $J_{sc}$ improvements for the latter. The open-circuit voltages of the D149 cells without CA retained their initial values or were slightly increased. Intensity-modulated photovoltage spectroscopy and charge extraction measurements on the day of preparation and after 3 weeks indicated a constant distribution of trap states and an increase of the total trap density after 3 weeks, and were compatible with a slight upward shift of the conduction band edge that may explain the fact that $V_{oc}$ remained constant in spite of the decrease of $J_{sc}$. For the cells sensitized with D149 and/or $S_{1.15}$PcZn, the development of the *J-V* characteristics over the course of 1 – 2 weeks varied between the samples with different sensitizers or sensitizer combinations, ranging from a decay of $J_{sc}$ and *FF* (D149/$S_{1.15}$PcZn/CA with 2 h adsorption time) to largely stable performance (D149/CA and $S_{1.15}$PcZn/CA with 17.5 h adsorption time) to a pronounced improvement (D149/$S_{1.15}$PcZn/CA with 17.5 h adsorption time). These results underlined that changes in the dye/coadsorbate layer (such as dye desorption or the break-up of aggregates), which were proposed to have contributed to variations in the photovoltaic performance of all cells, depend on detailed conditions of the photosensitization, such as dye adsorption times and choice of dye combinations, and the dyes' tendency for aggregation under these conditions.

# 10 Final Conclusions and Outlook

In this work, several aspects of the operation of dye-sensitized solar cells based on electrodeposited porous ZnO were investigated. Starting from standard cells using the organic indoline dye D149 as photosensitizer, the role of the dye layer at the interface between ZnO and a liquid $I^-/I_3^-$ electrolyte in limiting the performance was examined by studying the effects of deliberate modifications to this interface. These included variation of the D149 loading, use of coadsorbates, and co-sensitization with red-absorbing dyes.

With standard cells based on electrodeposited ZnO sensitized with D149 in the presence of cholic acid for 2 h, maximum short-circuit photocurrents of 11 $mAcm^{-2}$, open-circuit photovoltages of -0.63 V, fill factors of 0.57 and power conversion efficiencies of about 4% were achieved. This compares to $J_{sc}$ = 18.5 $mAcm^{-2}$, $V_{oc}$ = -0.69 V, $FF$ = 0.62, and $\eta$ = 8% reported for $TiO_2$-based cells with D149/CA.[202] Optical and photoelectrochemical characterization of the present cells based on electrodeposited ZnO indicated that $J_{sc}$ was limited by the spectrally integrated light-harvesting efficiency $\eta_{lh}$ and by the combined electron injection and dye regeneration efficiency. The charge-collection efficiency $\eta_{cc}$ under short-circuit conditions, on the other hand, approached 100% and therefore did not affect $J_{sc}$. The optical absorption of the optimized D149/CA samples (***Figure 37***) compared favorably with that of $TiO_2$-based cells with D149/CA (Figure 2 in ref. [202]), thus excluding $\eta_{lh}$ as possible origin of the different currents. Since the regeneration efficiency is generally determined by the properties of dye and electrolyte rather than the semiconductor,[100, 102] it is concluded that the smaller short-circuit photocurrent density of the ZnO/D149 solar cells is the consequence of a lower electron injection efficiency compared to $TiO_2$/D149 cells. This finding is in agreement with recent results of a laser spectroscopic study,[311] which indicated that efficient charge separation in ZnO/D149 cells was hindered by stronger interactions between injected electrons and dye cations compared to $TiO_2$. On the basis of the $\beta$-recombination model (eq. (75) with $\beta$ = 0.42 estimated to be equal for both types of cells), the lowered rate of electron injection in the present ZnO/D149 cells ($J_{sc}$ of 11 $mAcm^{-2}$ vs. 18.5 $mAcm^{-2}$ on $TiO_2$) explains approximately half (30 mV) of the observed loss in $V_{oc}$. Given that the reference cell based on $TiO_2$ contained the electrolyte additive *tert*-butylpyridine to cause an up-

ward shift of the $TiO_2$ conduction band edge,[202, 312] the additional voltage loss by about 30 mV is explained by a relative downward shift of the semiconductor conduction band edge (cf. eq. (34)) in the present cells without additive. Note that the addition of *tert*-butylpyridine to the electrolyte compromises the long-term stability of D149-sensitized DSCs both based on $TiO_2$ or ZnO,[170, 171] so that it does not present a technologically feasible pathway to improve the voltage in such cells. Finally, the observed total decrease of $V_{oc}$ by 60 mV explains, according to the $\beta$-recombination model (eq. (35) with $\beta = 0.42$), a decrease of the fill factor by 0.02. The additional loss of 0.03 must have resulted from a higher series resistance in the present cells, most likely as a result of using a higher-viscosity electrolyte containing ethylene carbonate as opposed to an electrolyte based on low-viscosity 3-methoxypropionitrile.[202, 313] Consequently, future work on this type of DSCs should include an optimization of the electrolyte with respect to the series resistance. The importance of coadsorbing cholic acid in cells containing the high amounts of D149 required for sufficient light harvesting was clearly confirmed in the present work by a significant improvement of the fill factor compared to cells without CA. Electrochemical impedance spectroscopy demonstrated that the reduced fill factor in cells with aggregated D149 was caused by an increased rate of recombination in the range of lower bias voltages. In cells based on electrodeposited ZnO using the squaraine sensitizer SQ2 (see below), an even stronger influence of (oxidized) aggregates on recombination at low voltages was reflected in a pronounced local minimum of the EIS-derived recombination resistance that was removed when cholic acid was coadsorbed with SQ2. An increase in the rate of recombination in a limited voltage range generally can be due to an increase in the density of states in the semiconductor or in an increase in the density of acceptor states,[86] which are either unoccupied states in the redox electrolyte or unoccupied states in oxidized dye molecules. For the DSCs with SQ2, the minimum in the recombination resistance was accompanied by a local maximum of the chemical capacitance $C_\mu$ from impedance spectroscopy, corresponding to an increased density of states (cf. eq. (44)). In the case of samples with D149, on the other hand, no such increase of $C_\mu$ was detected. Although $C_\mu$ is usually thought of as reflecting only the density of states in the semiconductor,[114] it can be expected that the electronic states of adsorbed dye molecules will contribute to the measured chemical capacitance.[294] Therefore, it can generally not be concluded whether an increase of $C_\mu$, as measured at low voltages on ZnO films with strongly aggregated SQ2, is caused by an

increase of the trap density in the semiconductor due to adsorption of dye molecules or reflects electronic states in dye molecules themselves. (The same is true for the density of states of dye-sensitized semiconductors measured by alternative methods, such as photoelectron spectroscopy.)[70] In consequence, no final conclusion can be drawn as to whether the increased recombination in SQ2 cells was the result of an increased density of semiconductor trap states able to donate electrons or whether it was due to an increased concentration of oxidized SQ2 molecules acting as electron acceptors. However, based on the fact that the recombination reactions associated with this additional density of states in SQ2 cells only occurred under illumination and that energetic position of the increased density of states at 0.3 eV above $E_{redox}$ was consistent with the Fermi level $E^0(S/S^+)$ of the oxidation potential of ground-state SQ2, the second possibility appears more likely. For D149-sensitized cells, the question arises why the aggregate-related increase in recombination was not accompanied by corresponding changes in the density of states (i.e., in $C_\mu$). One possible explanation could be that aggregates of D149 offer more favorable binding sites for acceptors in the electrolyte ($I_3^-$ or $I_2$)[151] than monomeric D149, thus increasing the concentration of acceptors near the surface rather than changing the density of donor states in ZnO or the density of oxidized dye molecules participating in recombination. On the other hand, such a mechanism is normally not expected to affect the energy-dependence of the rate of recombination but rather to enhance recombination independent of the applied voltage.[151] To further clarify this question, experiments on ZnO/D149 cells with varied degree of D149 aggregation could be performed using a different test redox shuttle such as ferrocene/ferrocenium.[314] Furthermore, it could be useful to compare recombination measurements (EIS, *J*-*V* curves) in the dark and under illumination, as was realized for the cells with SQ2.

Since D149 shows a relatively narrow absorption range (~350 – 650 nm) compared to top-efficiency ruthenium(II) polypyridyl[19, 29, 45-47] or donor-π-acceptor porphyrin[15, 34] sensitizers (which are both not suitable for ZnO),[167, 168, 315] there is room to improve the integrated light harvesting efficiency with respect to cells with D149/CA. While it is very important to continue the search for broad-wavelength absorbers suitable for ZnO, co-sensitization with multiple dyes with narrower absorption spectra is an attractive alternative approach that allows for facile extension of the absorption without the need to develop new synthesis strategies to achieve compatible broad-wavelength sensitizers.[34, 222-227] In the present thesis, the optical absorption of dye-sensitized ZnO films

was successfully extended into the longer-wavelength range (up to ~ 700 – 720 nm) of the solar spectrum by sequential co-sensitization of ZnO with the squaraine dye SQ2 and (in the second step) with D149. Additional light harvesting around 450 nm, where D149 shows a minimum in its absorbance, was achieved when D149 was adsorbed from a dye cocktail together with the indoline dye D131. Coadsorbing cholic acid and/or octanoic acid was found to be crucial to achieve functioning co-sensitized cells with increased (factor of 1.5) $J_{sc}$ values with respect to a D149/CA reference, because the presence of SQ2 otherwise prevented efficient photocurrent generation in the absorption range of the indoline dyes. This phenomenon may be explained by energy transfer from D149 and D131 to SQ2, which showed poor photosensitizing properties on ZnO ($\eta$ < 1% as individual sensitizer). Förster resonance energy transfer (FRET) between dyes has been studied in the context of energy relay dyes added to the electrolyte of DSCs to transfer absorbed energy to efficiently operating red-absorbing acceptor dyes attached to the semiconductor (an alternative approach to extending the spectral absorption range of DSCs).[316-318] Efficient FRET in such systems requires a large fluorescence decay rate (short fluorescence lifetime) of the energy relay dye, a large overlap of the absorbance spectrum of the acceptor dye with the fluorescence spectrum of the energy relay dye, and close proximity of the two dyes of not more than a few nanometers.[316, 317] The fluorescence peak of D149 (in ethanol) is centered at a wavelength of about 650 nm and extends from about 550 to about 750 nm,[213] indicating a large overlap with the absorption spectrum of SQ2, which showed its peak around 650 nm (extending from at least 550 nm to at least 700 nm, cf. ***Figure 49*** and ***Figure 50***). Moreover, the fluorescence lifetime of D149 was reported to be around 3.2 ns (D131: 5.0 ns),[213] which is very close to the lifetime given for an efficient energy relay dye by Hardin et al..[316] For fluorescence lifetimes in this range and for close proximity of donor (energy relay dye) and acceptor molecules, FRET rates are the picosecond range,[316] so that energy transfer competes with electron injection from the donor to the semiconductor. Thus, it is feasible that, in the presence of SQ2 (without coadsorbates), D149 and/or D131 may have transferred their excitation to SQ2 instead of injecting efficiently into ZnO. This is further supported by the fact that highly efficient energy transfer has been reported from 4-dicyanomethylene-2-methyl-6-*p*-dimethylamino-styryl-4*H*-pyran (DCM) as energy-relay dye to $TiO_2$-bound SQ1, a squaraine dye with a molecular structure very similar to SQ2.[317] The use of coadsorbates might have reduced the probability of energy transfer

simply by increasing the distance between the dye molecules. From a thermodynamic point of view, the higher position of the LUMO in the indoline dyes compared to SQ2 (see ***Figure 96***) would also allow for transfer of holes from SQ2 to the indoline dyes. Hole transfer from near-infrared absorbing (NIR) dyes to other dyes in their proximity has, in fact, been reported in the context of DSCs with energy relay dyes as well, and was shown to decrease the quantum efficiency of the NIR dye.[316] Hence, intermolecular hole transfer from SQ2 to D131 or D149 might have constituted an additional loss process in the present co-sensitized cells without coadsorbates. However, as the time constant of intermolecular charge transfer should be in the range of µs,[316] this process alone cannot explain why D149 and D131 showed drastically reduced electron injection efficiencies in the presence of SQ2.

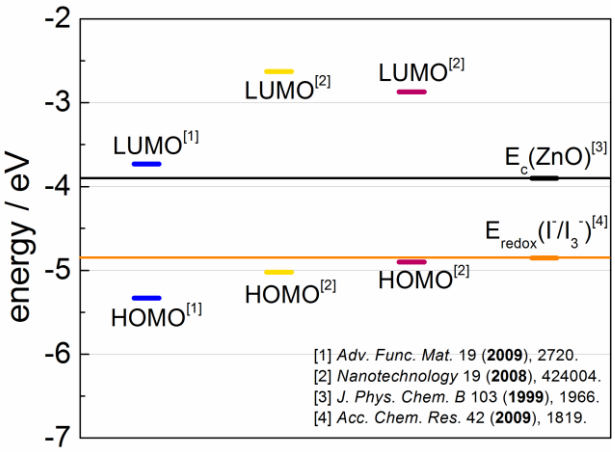


***Figure 96****: Scheme of the positions of highest occupied molecular orbitals (HOMOs) and lowest unoccupied molecular orbitals (LUMOs) of SQ2 (blue), D131 (yellow), and D149 (pink) based on literature values, all determined by electrochemical measurements. The redox level of the electrolyte (electrochemically measured) and the conduction band edge in ZnO (computed) are shown for comparison.*

Even when undesired dye/dye interactions were suppressed by using coadsorbates, the overall efficiency of the co-sensitized ZnO-based DSCs remained below that achieved with D149/CA due to losses in $V_{oc}$ and *FF*. These losses resulted from a pronounced downward shift of the ZnO conduction band edge (relative to D149/CA cells) as well as from the presence of additional recombination paths formed by oxidized aggregates of SQ2. Using the sulfonated Zn phthalocyanine $S_{1.15}$PcZn as co-sensitizer with D149/CA

(adsorption from dye cocktail), similarly poor results were obtained, with $S_{1.15}$PcZn showing poor injection into ZnO and hindering efficient photocurrent generation by D149 even in the presence of a coadsorbate. On the basis of the present results on SQ2 and $S_{1.15}$PcZn, the following possible approaches for future co-sensitization studies aiming at obtaining electrodeposited ZnO-based DSCs with increased light harvesting efficiency are suggested.

(1) Alternative red-absorbing sensitizers with optimized properties for application on electrodeposited ZnO should be selected or synthesized and subsequently studied in cells. These dyes should neither cause the ZnO conduction band edge to be shifted downwards relative to D149/CA-sensitized ZnO nor form significant amounts of aggregates that enhance recombination. Based on theoretical work by De Angelis et al.,[67] a relatively high position of the conduction band edge is achieved for dyes that adsorb to the semiconductor (in their case, $TiO_2$) in the bridged bidentate mode, i.e., with both oxygen atoms of the carboxylic acid anchoring group forming bonds to surface metal atoms. Furthermore, a strong upward shift of the conduction band edge is promoted by choice of organic donor-π-acceptor dyes with strong donor groups (pronounced electron density shift towards the anchoring group and the semiconductor). The adsorption mode of a dye on ZnO is difficult to predict based on the molecular structure but rather requires theoretical calculations or experimental studies such as attenuated total reflectance Fourier transform infrared spectroscopy (ATR-FTIR) or Raman spectroscopy.[281, 296, 297] The strength of different donor groups, on the other hand, is well known based on a large number of dyes investigated in experimental studies (see, for example, reviews in ref. [51], [80], and [38]). Efficient donor groups include triphenylamine, indoline (cf. D149 and D131), and carbazole.[80] Unfortunately, the thus-far reported dyes containing these donors generally do not efficiently absorb light in the red and near-infrared part of the spectrum.[80] An key step towards more efficient red-absorbing sensitizers for ZnO would therefore be to find new synthesis strategies to combine near-IR-absorbing dye skeletons, such as squaraines or phthalocyanines, with strong donor groups. The use of sensitizers with inherently low tendency of aggregation, such as dyes with bulky side groups like tert-butyl groups,[222] may contribute to preventing aggregation and the formation of undesired additional recombination paths. Introduction of bulky side groups in the co-sensitizer may also present an alternative approach to preventing undesired energy transfer between dyes by increasing the distance between their $\pi$-electron systems.

However, if D149 is used as the main sensitizer, coadsorption of cholic acid will likely still be required to prevent a decrease of the fill factor. The good suitability of D131 as co-sensitizer for D149, which has already been reported before,[31] was confirmed in the present experiments, which underlines that D131 should be included as a third absorber in further co-sensitization studies on electrodeposited ZnO that involve D149.

(2) An investigation of ZnO-based DSCs with multiple spatially separated sensitizers could be worthwhile, as it would allow the complementary absorption spectra of multiple dyes to be exploited while avoiding negative dye/dye interactions. For example, a tandem-like DSC structure in which two different dyes are employed in two cell compartments (each containing a dye-sensitized photoelectrode, electrolyte, and counter electrode) and externally connected in parallel has been proposed by Dürr et al..[319] The tandem cell showed a broad absorption over the range 300 – 800 nm and produced a high total $J_{sc}$ of ca. 20 mAcm$^{-2}$ (sum of the current produced by the two compartments). The parallel connection of the two subcells in such a structure implies that the total voltage should adjust to that of the lower-voltage compartment. Therefore, the feasibility of this approach for combining D149/CA or other shorter-wavelength absorbers with a red-absorbing sensitizer on electrodeposited ZnO will only be given once a red absorber is found that produces significantly higher $V_{oc}$ values on ZnO than SQ2 (with CA: -0.46 V) or $S_{1.15}$PcZn (with CA: -0.39 V). Assuming that one of the optimized D149/CA cells of this work was combined with a ZnO-based red-absorbing cell that yielded the same $V_{oc}$ and *FF* (-0.63 V and 0.57) as D149/CA and produced a conservative photocurrent of 6 mAcm$^{-2}$, a tandem cell would be expected to achieve $J_{sc}$ = 17 mAcm$^{-2}$, $V_{oc}$ = -0.63 V, *FF* = 0.57 and a power conversion efficiency of 6.1%. An alternative structure in which two dyes are combined in a spatially separated fashion is a double dye-layer structure as introduced by Noma et al..[320] In this approach, two sensitizers with different absorption spectra (the Ru(II) dye Z907 and the coumarin sensitizer NK3705) were combined in two layers of one porous semiconductor film to achieve co-sensitization while avoiding undesired dye/dye interactions. In the case of Z907 and NK3705, the layered structure formed automatically when the films were dipped in a dye cocktail solution over a period of several days as a result of the differing molecule sizes and adsorption strengths on $TiO_2$. Perhaps this strategy could be transferred to electrodeposited ZnO using D149 (with CA) as smaller, fast-adsorbing dye together with a very bulky long-wavelength absorber, such as a metal phthalocyanine chosen

according to the criteria further above. For sensitization processes that require adsorption times as long as several days, however, it must be ensured that no undesired dissolution of the ZnO surface by the dye solution[160, 167] occurs. To avoid photovoltaic losses compared to cells with D149/CA due to a reduced amount of D149, the film thickness could be slightly increased to allow producing a sample with a D149/CA-sensitized layer of identical thickness as in the best cells in this work (4 – 5 µm) plus a thin additional layer containing only the red-absorbing dye. Electrodeposition studies have shown that the film thickness of electrodeposited ZnO can be increased up to about 8 µm.[321] The charge collection efficiency analysis in the present work showed that the effective diffusion length at short circuit for indoline dye-sensitized cells with coadsorbates was 4 – 5 times the film thickness. (The lower limit for complete collection is 3 times the film thickness).[87] Thus, a slight increase of the film thickness should be possible without collection losses.

Even though there is evidence that the use of porous ZnO photoelectrodes in DSCs may generally not allow to attain short-circuit photocurrent densities as high as those yielded with $TiO_2$, ZnO films offer an important technological advantage over $TiO_2$ electrodes: They can be fabricated with good electron transport properties (complete charge collection) at low temperatures (100 – 150°C).[28] For nanoparticulate $TiO_2$ films, on the other hand, lowering the sintering temperature from the commonly used 450 – 500°C[19, 86] down to 100°C decreases the power conversion efficiency to values as low as < 0.5%,[20] which is clearly inferior to the performance achieved with electrodeposited ZnO ($\eta$ = 4% in the present work, $\eta$ up to 5.6% in the literature[25]). Preparation at low temperatures is an essential requirement for the production of solar cells on temperature-sensitive flexible substrates such as plastic foil or textiles, which in turn is crucial to lower the costs of production (roll-to-roll fabrication) and transport[23] and, furthermore, is relevant for emerging specialized applications such as textile-based or textile-compatible photovoltaics.[41, 322] The screen printed dye-sensitized nanoparticulate ZnO films investigated for comparative purposes in this thesis were fabricated at low temperatures (up to 80°C) as well. However, compared to the optimized cells based on electrodeposited ZnO with D149/CA, their performance remained inferior (for D149/CA on np-ZnO, $J_{sc}$ = 10 mAcm$^{-2}$, $V_{oc}$ = -0.60 V, $FF$ = 0.61, and $\eta$ = 3.6%). In conclusion, further work aiming at an improvement of DSCs based on electrodeposited ZnO is clearly desirable and relevant from a technological point of view.

# Acknowledgements

I would like to thank Prof. Derck Schlettwein for offering me the possibility to perform my doctoral research in his group and for being an excellent mentor throughout my undergraduate and graduate studies. I much appreciate the variety and depth of academic experience I was able to gain through the work under his supervision.

Thanks to Prof. Jürgen Janek for serving as a second referee for this thesis and for supporting me in my applications for postdoctoral positions.

I am grateful to Prof. Tsukasa Yoshida for kindly supporting and supervising me as a guest student in his group at Gifu University, Japan, and for giving me the opportunity to do interesting research while getting to know the beautiful culture of Japan.

Furthermore, I would like to thank the following people:

- Shigeo Hori for the kind preparation of electrodeposited porous ZnO films, for his help in using the experimental setups at Gifu University, and for fruitful discussions.
- Hayato Kurotaki for kindly preparing screenprinted nanoparticulate ZnO films and Pt-coated FTO/glass.
- Dr. Hidetoshi Miura (Chemicrea) for kindly providing the dyes D149 and D131.
- André Dragässer for the time and energy he put into developing the AutoHotkey routine for automated measurements with the Zahner CIMPS setup and the OriginPro scripts for automated data analysis, for introducing me to the routines and allowing me to utilize them for my research.
- Christoph Richter, Jane Falgenhauer, and Max Beu for many fruitful discussions.
- Silvia Schmandt for providing the materials for my experiments and her relentless efforts to keep the laboratory structured, which are very much appreciated.
- The staff at the electronics workshop and the two mechanics workshops of the Department of Physics for the fabrication and modification of various parts and instruments and helpful discussions.
- Ursula Hermann-Lippert, Doris Kirschbaum, Alexandra Gabriel and Birgit Reichhardt for their kind assistance in administrative and photography-related questions.
- Dr. Michael Multerer (ZAHNER-elektrik) for his detailed help in technical questions related to the Zahner CIMPS measurement system.

- All current and former members of the Schlettwein group for the supportive and pleasant atmosphere in the group.

Funding of this work by the Bundesministerium für Bildung und Forschung (BMBF) as part of the project “KorTeSo” as well as through a scholarship by the University of Gießen (Doktorandinnenprogramm) is gratefully acknowledged.

I thank my family for supporting my university education with their love, patience and financial assistance and for always being supportive and understanding of the paths I am choosing to take in my life.

To my husband Peter: Words can hardly express how deeply I appreciate your generous, unconditional support, especially during this last part of my PhD journey. Thank you for giving me a tremendous amount of flexibility and for standing by me with your love and patient commitment all the way to the finish line.

# Appendix A: Full List of Samples

***Table 30:*** *Samples studied in this work, with ZnO film code, date of film preparation, film thickness d, dyes and coadsorbates with adsorption time, date of sensitization, and date of first characterization of the corresponding solar cell. The final step of cell assembly of inserting the electrolyte took place on the day of their first characterization, except for the cells D149/CA of chapter 5 (built complete with electrolyte on 11/14/11).*

| film code (deposition batch-film number) | film preparation (mm/dd/yy) | d /µm | dye(s), coadsorbate(s) (adsorption time) | sensitization (mm/dd/yy) | 1st cell characterization (mm/dd/yy) |
|---|---|---|---|---|---|
| **Series D149 with CA and D149 without CA, chapter 5** | | | | | |
| 03/11/11-1-1 | 11/03/11 | 4.1 | D149/CA (1 min) | 11/13/11 | 11/15/11 |
| 02/11/11-1-1 | 11/02/11 | 4.3 | D149/CA (1 min) | 11/13/11 | 11/16/11 |
| 02/11/11-2-6 | 11/02/11 | 4.1 | D149/CA (1 min) | 11/13/11 | 11/16/11 |
| 03/11/11-1-7 | 11/03/11 | 4.1 | D149/CA (2 min) | 11/13/11 | 11/15/11 |
| 02/11/11-1-5 | 11/02/11 | 4.4 | D149/CA (2 min) | 11/13/11 | 11/17/11 |
| 02/11/11-2-7 | 11/02/11 | 4.2 | D149/CA (2 min) | 11/13/11 | 11/16/11 |
| 03/11/11-1-5 | 11/03/11 | 4.3 | D149/CA (10 min) | 11/13/11 | cell broken |
| 02/11/11-1-8 | 11/02/11 | 4.1 | D149/CA (10 min) | 11/13/11 | 11/15/11 |
| 02/11/11-2-8 | 11/02/11 | 4.1 | D149/CA (10 min) | 11/13/11 | 11/15/11 |
| 03/11/11-1-3 | 11/03/11 | 4.1 | D149/CA (2 h) | 11/13/11 | cell broken |
| 03/11/11-1-6 | 11/03/11 | 4.1 | D149/CA (2 h) | 11/13/11 | 11/16/11 |
| 03/11/11-1-8 | 11/03/11 | 4.3 | D149/CA (2 h) | 11/13/11 | 11/14/11 |
| 4-02 | 12/02/11 | 4.3 | D149 (1 min) | 04/18/12 | 04/23/12 |
| 4-05 | 12/02/11 | 4.3 | D149 (1 min) | 04/18/12 | 04/24/12 |
| 6-05 | 12/09/11 | 4.2 | D149 (1 min) | 02/26/12 | 03/03/12 |
| 6-06 | 12/09/11 | 4.2 | D149 (2 min) | 02/26/12 | 03/03/12 |
| 6-02 | 12/09/11 | 4.2 | D149 (2 min) | 02/26/12 | 02/29/12 |
| 2-06 | 12/02/11 | 4.3 | D149 (2 min) | 02/26/12 | 03/02/12 |
| 2-07 | 12/02/11 | 4.2 | D149 (10 min) | 02/26/12 | 03/01/12 |
| 6-03 | 11/03/11 | 4.3 | D149 (10 min) | 02/26/12 | 03/02/12 |
| 6-07 | 12/09/11 | 4.3 | D149 (10 min) | 02/26/12 | 03/03/12 |
| 6-08 | 12/09/11 | 4.3 | D149 (2 h) | 02/26/12 | 03/01/12 |
| 6-04 | 12/09/11 | 4.2 | D149 (2 h) | 02/26/12 | 03/02/12 |
| 2-08 | 12/02/11 | 4.2 | D149 (2 h) | 02/26/12 | 03/03/12 |

| | | | | | |
|---|---|---|---|---|---|
| **Series D149+D131+SQ2, chapter 6** (adsorption times: see ***Table 6***) | | | | | |
| 3-04 | 12/02/11 | 4.1 | D149/CA | 09/30/13 | 10/02/13 |
| 4-01 | 12/02/11 | 4.6 | D149/D131/OA | 09/30/13 | 10/04/13 |
| 4-03 | 12/02/11 | 4.3 | SQ2/CA+D149/CA | 10/01/13 | 10/03/13 |
| 4-07 | 12/02/11 | 4.5 | SQ2/CA+ D149/D131/OA | 10/01/13 | 10/06/13 |
| 4-08 | 12/02/11 | 4.4 | SQ2/CA | 09/30/13 | 10/22/13 |
| 7-01 | 12/09/11 | 4.2 | D149 | 08/28/13 | 09/03/13 |
| 7-02 | 12/09/11 | 4.3 | D131 | 08/28/13 | 09/18/13 |
| 7-03 | 12/09/11 | 4.2 | D149/D131 | 08/28/13 | 09/04/13 |
| 7-04 | 12/09/11 | 4.2 | SQ2 | 08/28/13 | 09/11/13 |
| 7-06 | 12/09/11 | 4.3 | SQ2+D149/D131 | 08/30/13 | 09/07/13 |
| 7-07 | 12/09/11 | 4.2 | SQ2+D149 | 08/29/13 | 09/06/13 |
| **Series np-ZnO+D149+D131+SQ2, chapter 7** (adsorption times: see ***Table 7***) | | | | | |
| NP-01 | 08/07/13 | 10 | SQ2 | 11/06/13 | 11/12/13 |
| NP-02 | 08/07/13 | 10 | SQ2+D149 | 11/07/13 | 11/13/13 |
| NP-04 | 08/07/13 | 10 | SQ2/CA | 11/06/13 | 11/14/13 |
| NP-05 | 08/07/13 | 10 | SQ2/CA+D149/CA | 11/07/13 | 11/15/13 |
| NP-06 | 08/07/13 | 10 | SQ2/CA+ D149/D131/OA | 11/07/13 | 11/16/13 |
| NP-07 | 08/07/13 | 10 | SQ2/CA+D131/OA +D149/D131/OA | 11/07/13 | 11/17/13 |
| NP-08 | 08/07/13 | 10 | D149 | 11/06/13 | 11/18/13 |
| NP-09 | 08/07/13 | 10 | D149/CA | 11/06/13 | 11/19/13 |
| NP-11 | 08/07/13 | 10 | D149/D131 | 11/06/13 | 11/20/13 |
| NP-12 | 08/07/13 | 10 | D149/D131/OA | 11/06/13 | 11/21/13 |
| NP-13 | 08/07/13 | 10 | SQ2+D149/D131 | 11/11/13 | 11/22/13 |
| NP-15 | 08/07/13 | 10 | D131/OA | 11/07/13 | 11/23/13 |
| **Series D149+$S_{1.15}$PcZn, chapter 8** | | | | | |
| 5-02 | 12/02/11 | 4.5 | D149/$S_{1.15}$PcZn/CA (2 h) | 07/05/13 | *J-V*, IPCE: 07/10/13 rest: 07/19/13 |
| 5-05 | 12/02/11 | 4.7 | D149/$S_{1.15}$PcZn/CA (17.5 h) | 07/09/13 | *J-V*, IPCE: 07/10/13 rest: 07/22/13 |
| 5-06 | 12/02/11 | 4.5 | $S_{1.15}$PcZn/CA (17.5 h) | 07/09/13 | *J-V*, IPCE: 07/10/13 rest: 07/17/13 |
| 5-07 | 12/02/11 | 4.6 | D149/CA (17.5 h) | 07/09/13 | *J-V*, IPCE: 07/10/13 rest: 07/18/13 |

# Appendix B: Customized Zahner CIMPS Measurement Setup

Most of the photovoltaic and photoelectrochemical characterizations discussed in this thesis were performed using a ZAHNER-elektrik CIMPS (controlled intensity-modulated photocurrent and photovoltage spectroscopy) system (see ***Figure 97***) consisting of IM6 workstation, PP211 slave potentiostat, optical bench, LED housing, various LEDs, light sensor (Si photodiode) and sensor holder, sample holder base, the add-ons CIMPS-pcs and for IPCE measurements (see Appendix C) and CIMPS-fit for the recording of fast photocurrent or photovoltage transients with time resolution down to the ns range, as well as the software Thales with CIMPS, CIMPS-pcs, and CIMPS-fit extensions. The IM6 main potentiostat is responsible for controlling and measuring cell currents and voltages, while the additional PP211 slave potentiostat drives the light source (Zahner LED) and regulates the light intensity incident on the solar cell. This occurs via in-situ measurement of the light intensity by a photodetector positioned in the vicinity of the sample and controlling the light intensity by comparison of the set value with the actual value via a feedback loop, cf. arrows in ***Figure 97***.

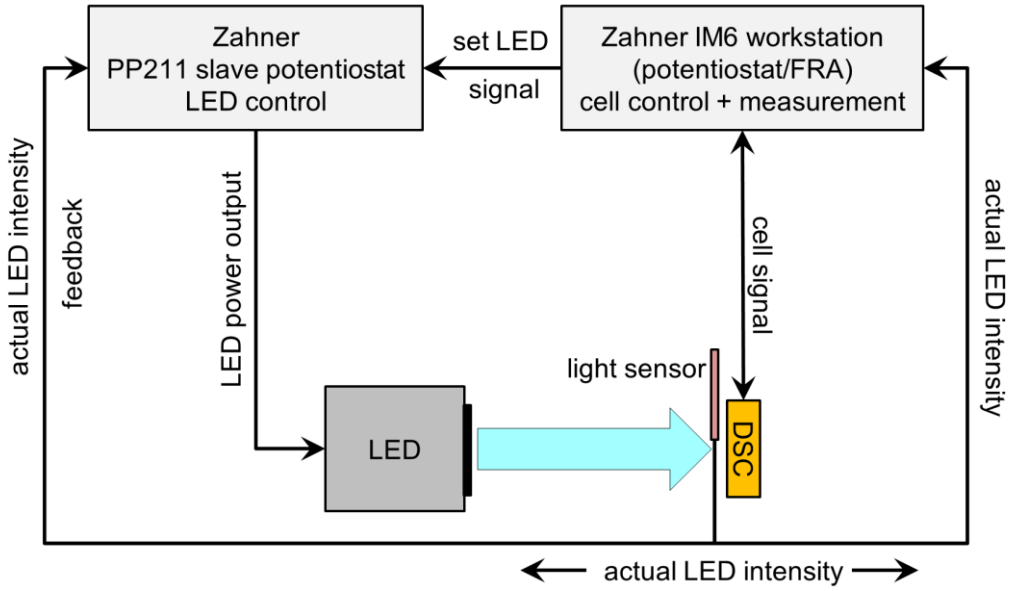


***Figure 97**: Scheme showing the basic components and principle of the Zahner CIMPS measurement setup used to characterize the DSCs in this work.*

The light sensor is delivered with calibration data for each of the light sources, allowing the system to automatically determine the actual light intensity at the location of the sample center based on a geometric calibration factor and the intensity measured at a defined location in the vicinity of the sample. For an accurate knowledge of the light intensity incident on the cell it is, therefore, important to position the sensor exactly as instructed in the CIMPS manual and to choose the correct calibration file via the Thales software. The actual light intensity determined by the system is recorded in most measurements and automatically used by the Thales software in the determination of solar cell parameters that depend on the light intensity, such as the IMPS and IMVS transfer functions (cf. chapter 1.4.5) and the IPCE.

The spectral intensity distributions of the three Zahner light sources used in this work are shown in ***Figure 98***. RTR01 and CYR01 are a red and cyan LED with narrow Gauss type intensity distributions and peak intensities at the wavelengths $\lambda_{max}$ = 632 nm and $\lambda_{max}$ = 513 nm. TLS02 is a tunable light source used (exclusively) for IPCE measurements that consists of multiple LEDs and a Zahner monochromator, see Appendix C. The spectrum shown in ***Figure 98*** (right) is a plot of the maxima of the Gauss-shaped intensity distributions that the TLS02 outputs at different set wavelengths.

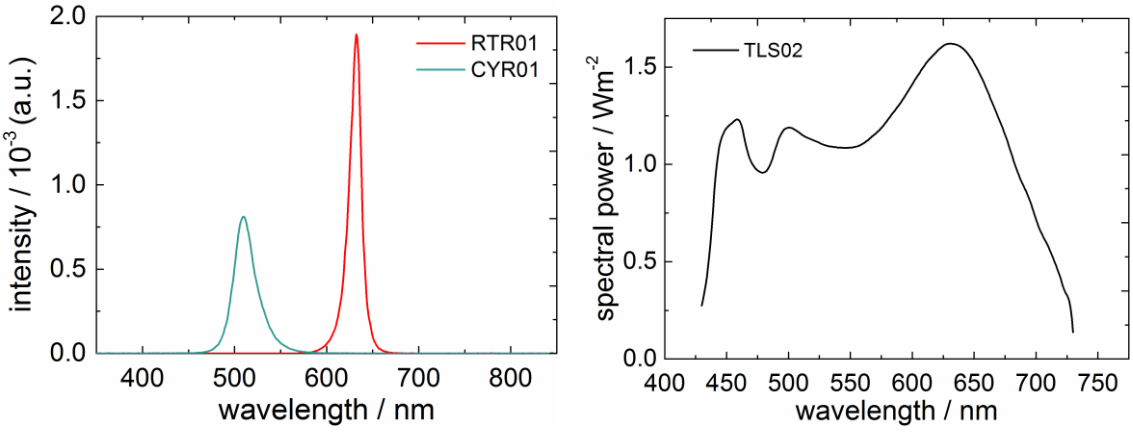


***Figure 98****: Spectral intensity distribution of the three Zahner light sources used in the present work.*

The Zahner CIMPS system (as-delivered) does not include a dark box to exclude ambient light during the measurements and, furthermore, does not allow for solar cell characterization under realistic AM1.5G illumination conditions. Therefore, the system was extended and customized as part of this PhD work, see ***Figure 99***.

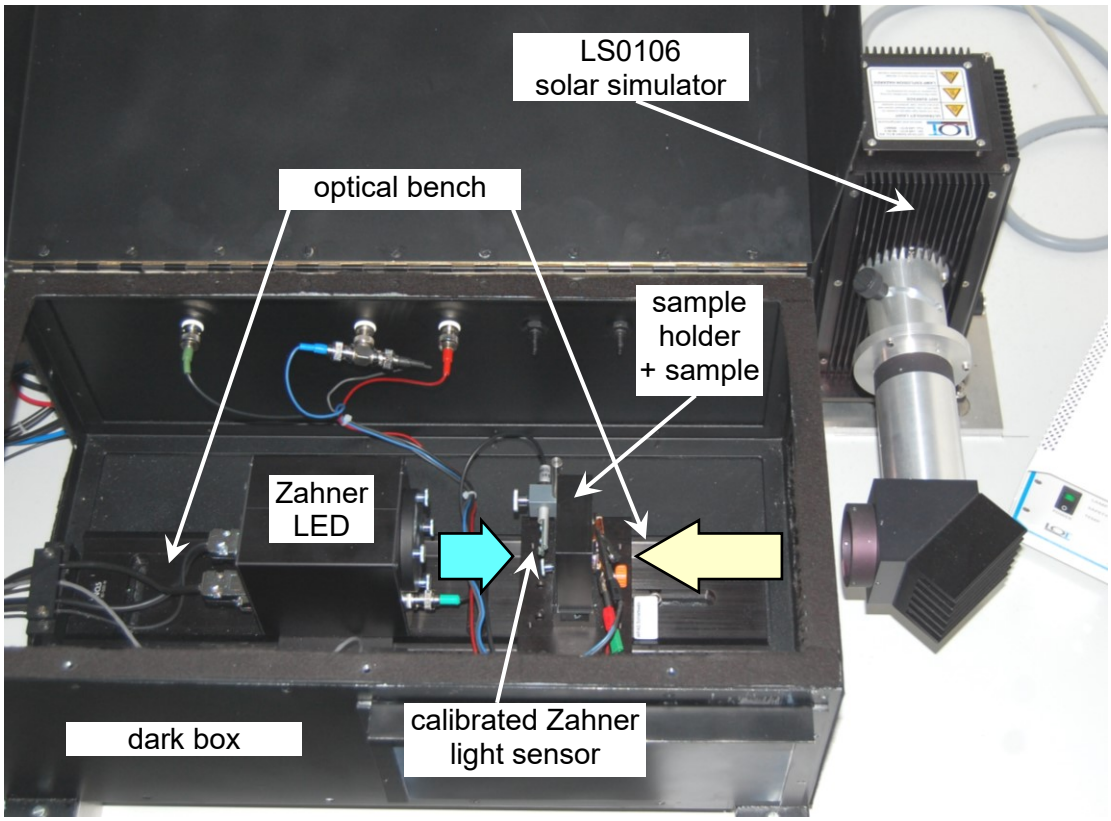


***Figure 99**: Photograph of the custom-built combination of Zahner CIMPS setup (potentiostats not shown) with LOT Oriel LS0106 solar simulator and dark box. The green and light yellow arrows indicate the light paths of the Zahner LED and the external solar simulator.*

In this customized setup, an LOT Oriel solar simulator LS0106 with AM1.5G filter LSZ189 is integrated with the Zahner system. The Zahner optical bench is fixed on the bottom of a dark box custom-built by the mechanics workshop of the Institute of Applied Physics. Zahner LED housing (or TLS02 light source with monochromator) as well as sample holder base are positioned at a variable distance to each other on the optical bench. The cell is fixed on a black sample holder (on the plane perpendicular to the light path), also custom-built by the workshop, and the latter is fastened to the Zahner sample holder base. Two openings in the side walls of the dark box (which can be closed by manual shutters) allow to shine the light of the solar simulator into the dark box and to insert samples without having to open the screw-fixed main lid of the box. To set the solar simulator intensity incident on the cell to 100 $mWcm^{-2}$, the correct position of the sample holder base is determined via a light intensity measurement with a

pyranometer (EKO Instruments ML-020VM), fixed on a custom-built holder that replaces the sample holder during this calibration. When the sample holder is positioned with the sample facing the solar simulator, the thus-customized measurement system allows performing current-voltage characterization as well as electrochemical impedance spectroscopy (EIS) under AM1.5G conditions using the IM6 potentiostat and software of the CIMPS system. To use the additional LED-based characterization methods offered by the CIMPS setup (intensity- and time-dependent photocurrent and photovoltage measurements, IMPS and IMVS, EIS under varied illumination intensities, and charge extraction), the sample holder simply needs to be rotated by 180°C to face the LED.

# Appendix C: Comparison of Two Setups Used to Measure the IPCE

The characterization of the external quantum efficiency (IPCE) was performed using two different measurements setups, referred to as Acton/Ivium system and Zahner system (Zahner CIMPS with CIMPS-pcs add-on), see ***Table 31***.

***Table 31****: Comparison of setups for the measurement of the IPCE*

| | **Zahner setup** | **Acton/Ivium setup** |
|---|---|---|
| **light source** | Zahner TLS02 (combination of LEDs and Zahner monochromator) | Oriel 1000 W Xe arc lamp combined with Acton SpectraPro 2300i monochromator |
| **size and homogeneity of light beam** | circular area with diameter of about 4 cm, homogeneous to the eye | rectangular area of $\leq 1$ cm$^2$, less intense in peripheral areas compared to central area |
| **type of light signal** | sinusoidal signal ($v$ = 1 Hz, amplitude = 1/3 of background signal) superimposed on constant background signal | illumination constant over time |
| **photon flux density (order of magnitude)** | $\sim 10^{14}$ cm$^{-2}$s$^{-1}$ | $\sim 10^{15}$ - $10^{16}$ cm$^{-2}$s$^{-1}$ |
| **wavelength range** | 430 – 730 nm | 350 – 1100 nm |
| **wavelength increment** | 5 nm | 10 nm |
| **light intensity measurement** | Zahner-integrated Si photodiode, intensity measured during IPCE measurement in peripheral position in light beam while sample is positioned in center of light beam; system calculates intensity at position of sample using geometric factor | Thorlabs FDS-100 Si photodiode, light intensity measured before IPCE measurement at position of active cell area; position of sensor in x-y plane (perpendicular to light beam) well defined, position of cell in x-y plane less well defined (adjusted manually) |

The spectral intensity distribution of the light source/monochromator combination of the Acton/Ivium system is shown in ***Figure 100*** (left)) and the spectrum of the Zahner TLS02 tunable light source was presented in Appendix B (***Figure 98***). As neither the Acton/Ivium setup nor the Zahner setup kept the photon flux density constant for each wavelength, the measurements relied on the IPCE being independent of the photon flux, which was confirmed at a wavelength of 632 nm (Zahner LED RTR01) for all cells by the linearity of the intensity-dependent short-circuit photocurrent density in the range of photon fluxes used for the IPCE measurements (see example in ***Figure 100*** (right)).

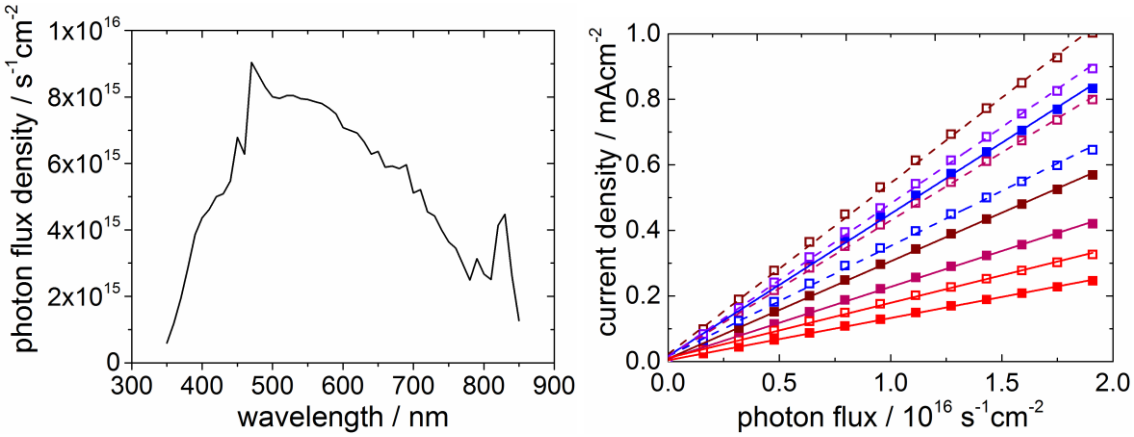


***Figure 100****: Spectral photon flux output of the combination of Xe arc lamp and Acton monochromator at the position of the specimen (left) and photon flux-dependent short-circuit photocurrent density of the differently sensitized DSCs based on electrodeposited ZnO of chapter 6 (right).*

The Zahner setup generally yielded much higher IPCE values compared to the Acton/Ivium system, as demonstrated for the example of D149/$S_{1.15}$PcZn/CA-sensitized DSCs (chapter 8) in ***Figure 101*** and ***Table 32***. For instance, a maximum IPCE of 98% was obtained for the D149/CA-sensitized cell, compared to $IPCE_{max}$ = 44% measured by the Acton/Ivium system. Considering the optical losses at the FTO-coated glass substrate of about 20% (cf. chapter 6.5), it is obvious that an IPCE of 98 % is not realistic. In other experiments in the Schlettwein group, the Zahner system even delivered IPCE peak values significantly above 100 % for cells based on electrodeposited ZnO and organic dyes, strongly corroborating that it generally overestimated the IPCE for the type of samples analyzed in this thesis.

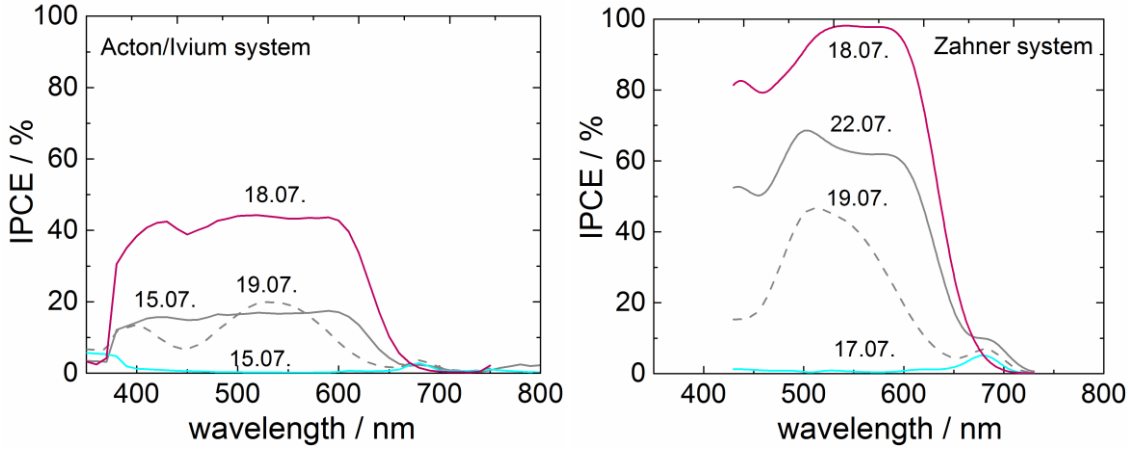


***Figure 101:*** *IPCE spectra of the dye-sensitized solar cells of chapter 8, measured with the Acton/Ivium setup (left) or the Zahner system (right). Curve labels correspond to the dates of the measurements (dd.mm).*

***Table 32:*** *Maximum IPCE values (with corresponding wavelengths), theoretical short-circuit photocurrent densities $J_{sc}^{theo}$ determined from the IPCE spectra using eq. (36) and the AM1.5G spectrum, experimental $J_{sc}$ under AM1.5G illumination, and ratio of $J_{sc}^{theo}$ and $J_{sc}$ for the cells of chapter 8.*

| **sample** | **IPCE$_{max}$** | **$J_{sc}^{theo}$ / mAcm$^{-2}$** | **$J_{sc}$ / mAcm$^{-2}$** | **$J_{sc}^{theo}$ / $J_{sc}$** |
|---|---|---|---|---|
| **Acton/Ivium system** | | | | |
| 2 h D149/S$_{1.15}$PcZn/CA | 0.2 @ 530 nm | 2.03 | 2.37 | 0.9 |
| 17.5 h D149/S$_{1.15}$PcZn/CA | 0.18 @ 590 nm | 2.65 | 4.69 | 0.6 |
| 17.5 h S$_{1.15}$PcZn/CA | 0.03 @ 680 nm | 0.21 | 0.32 | 0.7 |
| 17.5 h D149/CA | 0.44 @ 520 nm | 6.40 | 8.09 | 0.8 |
| **Zahner system** | | | | |
| 2 h D149/S$_{1.15}$PcZn/CA | 0.47 @ 511 nm | 4.19 | 2.37 | 1.8 |
| 17.5 h D149/S$_{1.15}$PcZn/CA | 0.69 @ 503 nm | 8.39 | 5.46 | 1.5 |
| 17.5 h S$_{1.15}$PcZn/CA | 0.05 @ 679 nm | 0.27 | 0.32 | 0.8 |
| 17.5 h D149/CA | 0.98 @ 542 nm | 12.44 | 8.09 | 1.5 |

The overestimation of the IPCE by the Zahner system is further supported by the fact that the theoretical short-circuit photocurrent densities $J_{sc}^{theo}$ of the example cells were mostly much higher than the actually measured $J_{sc}$ (cf. ***Table 32***). The difference between IPCE-derived and measured $J_{sc}$ would become even greater if the measurement range of the Zahner system was wide enough to cover the full absorption range of the dyes. In addition to the differences in peak heights, the spectra obtained with the two setups also tend to exhibit different shapes. While the curves measured for the cells with D149/CA or with D149/$S_{1.15}$PcZn/CA (17.5 h adsorption time) using the Acton/Ivium system show broader plateaus, reflecting the nearly saturated light harvesting efficiency of these samples (cf. ***Figure 79***), the Zahner-based IPCE shows narrower peaks and different peak-to-peak height ratios. IPCE curves of D149-sensitized ZnO with high light harvesting efficiency obtained as part of the present work by means of a third system at Gifu University for which $J_{sc}^{theo}/J_{sc} \approx 1$ (cf. example in ***Figure 102***) resemble the corresponding result of the Acton/Ivium system more than the spectrum obtained by the Zahner system, indicating that the Acton/Ivium system delivered more accurate results.

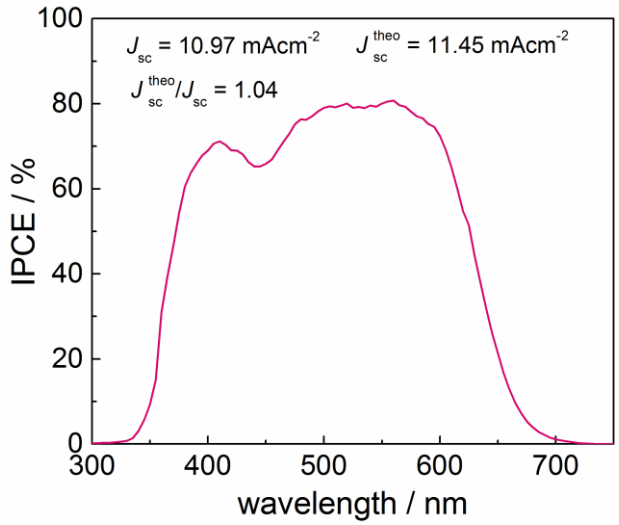


***Figure 102****: IPCE spectrum of a DSC based on electrodeposited porous ZnO sensitized with D149/CA for 2 hours (cf. chapter 5), measured at Gifu University.*

The $J_{sc}^{theo}$ values based on the Acton/Ivium measurements of the sample cells were somewhat smaller than the experimental $J_{sc}$ values (cf. ***Table 32***), showing that this system tended to underestimate the IPCE by 10 – 40%. However, considering the results for all 30 cells characterized by the two different IPCE measurement setups in the pre-

sent work, the average ratio of IPCE-derived theoretical and experimental short-circuit current $J_{sc}^{theo}/J_{sc}$ was 0.9 for the Acton/Ivium system and 1.2 for the Zahner system, demonstrating that the Acton/Ivium system presented a more accurate measure of the actual external quantum efficiency of the DSCs. Therefore, the discussion of the IPCE throughout this thesis focused on the spectra obtained with the Acton/Ivium setup. Note, however, that the Acton/Ivium system led to a slightly more pronounced underestimation of $J_{sc}$ for the cells based on nanoparticulate ZnO in chapter 7 (average $J_{sc}^{theo}/J_{sc}$ = 0.81 for this set of samples, cf. ***Figure 66***) compared to those based on electrodeposited ZnO. The Zahner spectra for the np-ZnO cells, on the other hand, delivered $J_{sc}^{theo}$ values closer to the experimental $J_{sc}$ (average $J_{sc}^{theo}/J_{sc}$ = 0.96) and are therefore provided as supplementary information for comparison in ***Figure 103***.

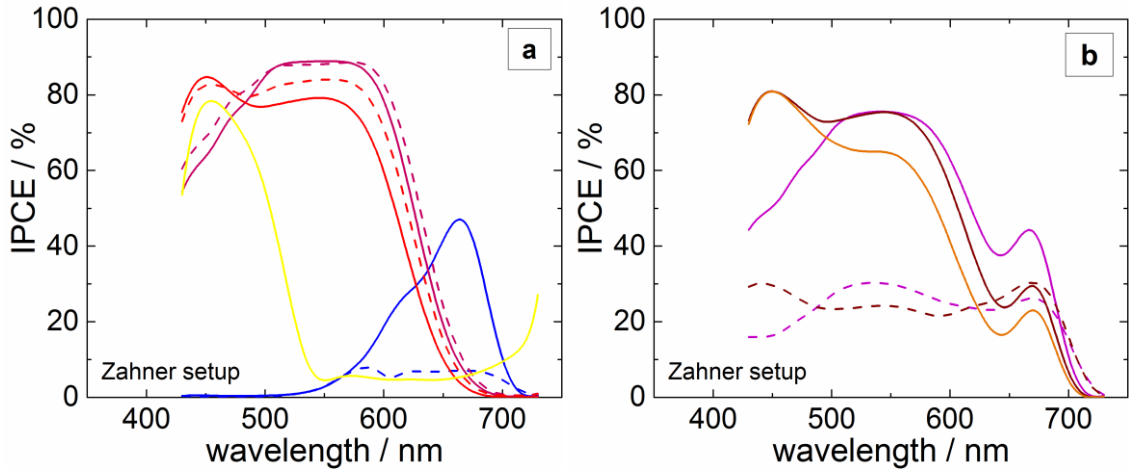


***Figure 103****: IPCE spectra of np-ZnO DSCs of chapter 7 containing SQ2 and/or indoline dyes, measured with the Zahner measurement system. Legend as in* ***Figure 66****.*

Over- or underestimations of the IPCE by the two systems considered here must be due (cf. eq. (39)) to over-/underestimations of the measured wavelength-dependent photocurrent, the measured wavelength-dependent incident photon flux density, or the active cell area. On the basis of the specifications in ***Table 31*** it is likely that, for the Acton/Ivium system, the small size and the inhomogeneity of the illumination spot, together with the relatively poorly defined position of the solar cell, led to an incomplete illumination of the active cell area or to a smaller light intensity incident on the cell compared to the intensity incident on the sensor. This would have caused an overestimation of the incident photon flux and/or the illuminated cell area and would thereby have led

to an underestimation of the IPCE, in line with the above observations. Moreover, several cells showed an increase of the $J_{sc}$ with illumination time (cf. chapter 9). Comparing saturated $J_{sc}$ values from the *J-V* measurements with presumably less-than-saturated values from the relatively fast IPCE measurements, as done in the present study, might be another explanation of the apparent underestimation of $J_{sc}$ based on the IPCE curves. For the Zahner setup, on the other hand, it is possible that the large size of the illumination spot (larger than the whole solar cell) led to a situation where light reflection and/or scattering, for example at the edges of the cell's glass substrates, increased the light intensity incident on the active cell area compared to that incident on the sensor. The fact that both setups yielded generally lower $J_{sc}^{theo}/J_{sc}$ ratios for the cells based on nanoparticulate ZnO compared to the electrodeposited samples may be related to the larger optical losses (reflection/absorption) at the thicker, more conductive glass substrate used for these cells (cf. chapter 7).

# Appendix D: Additional Information on Impedance Spectroscopy Measurements

***Table 33:*** *Overview of parameters in impedance spectroscopic measurements.*

| sample group | illumination | voltage range (step width) /V | $\hat{V}^{a}$ /mV | frequency range /Hz |
|---|---|---|---|---|
| D149 with CA | AM1.5G (60 mWcm$^{-2}$) | -0.1 – -0.8 | 10 | 0.1 – $10^5$ |
| D149 without CA | AM1.5G (100 mWcm$^{-2}$) | -0.21 – -0.77 (0.07) | 10 | 0.1 – $10^5$ |
| D149+$S_{1.15}$PcZn (5-06, 5-07) | AM1.5G (100 mWcm$^{-2}$) | 0.00 – -0.25 (0.05) | 20 | 1 – $10^5$ |
| | | -0.30 – -0.66 (0.02) | 10 | 0.1 – $10^5$ |
| D149+$S_{1.15}$PcZn (5-02, 5-05)<br>D149+D131+SQ2<br>np-ZnO+D149+D131+SQ2 | AM1.5G (100 mWcm$^{-2}$) | -0.15 – -0.25 (0.05) | 20 | 1 – $10^5$ |
| | | -0.30 – -0.58 (0.02) | 10 | 0.1 – $10^5$ |
| D149+$S_{1.15}$PcZn (5-05, 5-07)<br>D149+D131+SQ2<br>np-ZnO+D149+D131+SQ2 | red LED (varied: 0.1 – 25 mWcm$^{-2}$) | n.a. [open circuit] | 10 | 0.1 – $10^5$ |

[a] amplitude of voltage modulation.

Typical EIS spectra of DSCs based on electrodeposited ZnO are shown in ***Figure 104*** for a range of bias voltages. The spectra displayed two or three semicircles, as expected (cf. ***Figure 13*** and ***Figure 14*** and discussion). The impedance spectra of most of the screenprinted nanoparticulate ZnO samples also showed the voltage-dependent behavior as presented in ***Figure 104***. However, for the np-ZnO cells with SQ2, SQ2+D149, or SQ2+D149/D131 (see example in ***Figure 105***), the spectra at low voltages showed a transition to the case in which transport resistance and recombination resistance were similar and could not be distinguished anymore (Gerischer impedance),[128] see for example the spectrum at -0.36 V in ***Figure 105***. This case corresponds to a low charge collection efficiency (cf. ***Table 22***) and does not allow extracting recombination re-

sistances and chemical capacitances based on fits using the typical equivalent circuit (see below) anymore.

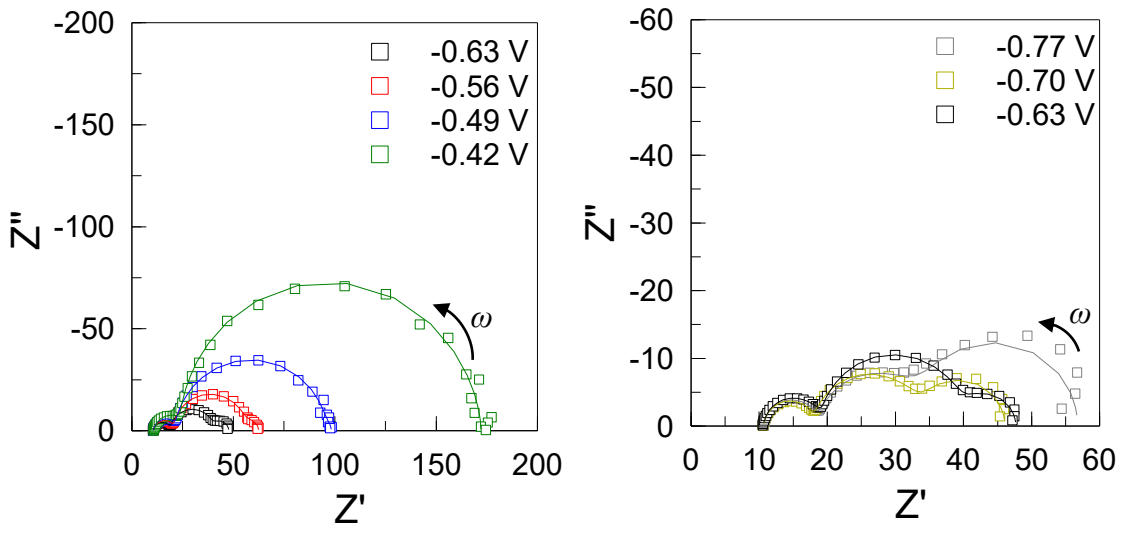


***Figure 104:*** *Typical voltage-dependent EIS spectra (symbols: measured data; lines: fits) of dye-sensitized solar cells based on electrodeposited ZnO. The example cell (2-08) was prepared with a D149 adsorption time of 120 minutes without cholic acid.*

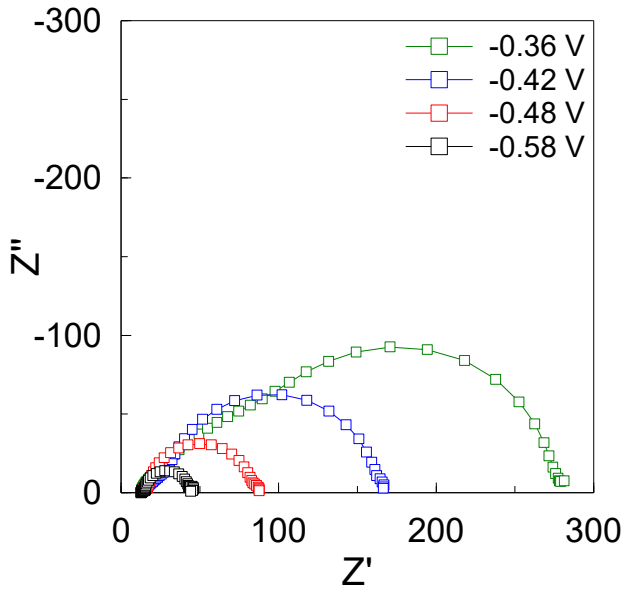


***Figure 105****: Example (sample NP-01, 4h SQ2) of voltage-dependent EIS spectra of DSCs based on screenprinted nanoparticulate ZnO containing the sensitizer SQ2 alone or in combinations without coadsorbate.*

The equivalent circuit used for all EIS fits in the present work is presented in ***Figure 106***.


***Figure 106:*** *Equivalent circuit used to fit the EIS spectra of the DSCs in this work, cf.* ***Figure 12****.*[128, 141] *Rs, Rpt: resistances of the FTO-coated glass substrate and Pt-coated counter electrode, Zd: finite-length Warburg element (short-circuit terminus) describing transport in the electrolyte, cf. eq. (51), CPEpt: constant phase element describing the (non-ideal) capacitance of the counter electrode, DX1: transmission line reflecting charge transport, accumulation and recombination in the porous film, cf. eq. (50).*

# Publications and Presentations

The original research presented in this thesis has partially been published in the following peer-reviewed journal articles:

- "Improvement of Light Harvesting by Addition of a Long-Wavelength Absorber in Dye-Sensitized Solar Cells Based on ZnO and Indoline Dyes," Rudolph, M.; Yoshida, T.; Miura, H.; and Schlettwein, D., *J. Phys. Chem. C* 119 (**2015**), 1298-1311.
- "Influence of Indoline Dye and Coadsorbate Molecules on Photovoltaic Performance and Recombination in Dye-Sensitized Solar Cells Based on Electrodeposited ZnO," Rudolph, M.; Yoshida, T.; and Schlettwein, D., *J. Electroanal. Chem.* 709 (**2013**), 10-18.

Further contributions related to the discussion in this work can be found in:

- "Photovoltaic Characteristics and Dye Regeneration Kinetics in D149-sensitized ZnO with Varied Dye Loading and Film Thickness," Tefashe, U.M.; Rudolph, M.; Miura, H.; Schlettwein, D.; and Wittstock, G. *Phys. Chem. Chem. Phys.* 14 (**2012**), 7533-7542.
- "Electrospun Antimony Doped Tin Oxide (ATO) Nanofibers as a Versatile Conducting Matrix," Ostermann, R.; Zieba, R.; Rudolph, M.; Schlettwein, D.; and Smarsly, B.M. *Chem. Commun.* 47 (**2011**), 12119-12121.
- "Textile-Compatible Substrate Electrodes with Electrodeposited ZnO - a New Pathway to Textile-Based Photovoltaics," Loewenstein, T.; Rudolph, M.; Mingebach, M.; Strauch, K.; Zimmermann, Y.; Neudeck, A.; Sensfuss, S.; and Schlettwein, D. *Chem. Phys. Chem.* 11 (**2010**), 783-788.
- "Pulsed Electrodeposition of Porous ZnO on Ag-coated Polyamide Filaments", Rudolph, M.; Loewenstein, T.; Arndt, E.; Zimmermann, Y.; Neudeck, A.; and Schlettwein, D. *Phys. Chem. Chem. Phys.* 11 (**2009**), 3313-3319.

Parts of the results have been discussed on scientific meetings:

- "Interfacial Charge Transfer and Charge Transport in Dye-Sensitized Solar Cells Based on Porous Zinc Oxide and Combinations of Organic Dyes," Rudolph, M., MRS Fall Meeting, Dec 2014, Boston, USA (C).

- “Photoelectrochemical Characterization of Dye-Sensitized Solar Cells,” Rudolph, M., Workshop “Dynamics of Excited-States and Electron Transfer in Dye-Sensitized Solar Cells Based on Electrodeposited ZnO”, Dec 2013, Gießen, Germany (Oral Contribution).
- “Effect of Indoline Dyes on Recombination in Dye-Sensitized Solar Cells Based on Electrodeposited ZnO,” Rudolph, M., E-MRS 2013 Spring Meeting, May 2013, Strasbourg, France (Poster).
- “Effect of Indoline Dyes on Recombination in Dye-Sensitized Solar Cells Based on Electrodeposited ZnO,” Rudolph, M., 19th International Conference on Photochemical Conversion and Storage of Solar Energy (IPS-19), July 2012, Pasadena, USA (Oral Contribution).
- “Photoelectrochemical Investigation of D149-sensitized ZnO Electrodes,” Rudolph, M., Workshop “Nanostructured Dye-Sensitized Solar Cells”, Mar 2012, Delmenhorst, Germany (Oral Contribution).
- “Electron Transport and Recombination in Electrodeposited, Dye-Modified Nano-ZnO,” Rudolph, M., MRS Fall Meeting, Dec 2011, Boston, USA (Oral Contribution).
- “Influence of Dye Adsorption Conditions on the Properties of Electrodeposited, Dye-Sensitized Zinc Oxide Films,” Rudolph, M., MRS Fall Meeting, Dec 2011, Boston, USA (Poster).
- “Photovoltaic and Photoelectrochemical Properties of Electrodeposited, Dye-Sensitized Zinc Oxide Films Depending on Dye Loading,” Rudolph, M., 15th International Conference on Thin Films, Nov 2011, Kyoto, Japan (Poster).
- “Influence of Dye Adsorption Conditions on the Properties of Electrodeposited, Dye-Sensitized Zinc Oxide Films,” Rudolph, M., 6th Aceanian Conference on Dye-Sensitized and Organic Solar Cells, Oct 2011, Oita, Japan (Poster).
- “Light-Induced Electron Transfer and Charge Transport in Mesoporous ZnO/D149 Hybrid Films,” Rudolph, M., Annual Meeting of the German Physical Society (DPG), Mar 2011, Dresden, Germany (Oral Contribution).
- “Photoelectrochemical Kinetics of D149-sensitized ZnO Films Depending on the Dye Content,” Rudolph, M., 2nd “Cormorant” Workshop on Innovative Solar Cells, Feb 2011, Gifu, Japan (Oral Contribution).

# List of Abbreviations

| | |
|---|---|
| $A$ | projected film area |
| $\tilde{A}$ | RC attenuation factor in IMPS |
| $abs$ | absorbance |
| $abs_{\mathrm{int}}$ | spectrally integrated absorbance |
| APCE | absorbed photon-to-electron conversion efficiency |
| $c$ | concentration |
| $C$ | capacitance |
| CA | cholic acid |
| $C_{\mathrm{BL}}$ | capacitance of interface between blocking layer and electrolyte |
| $c_{\mu}$ | chemical capacitance per unit volume |
| $C_{\mu}$ | total chemical capacitance |
| $C_{\mu}^{\mathrm{t}}$ | chemical capacitance associated with trapped electron density |
| $C_{\mathrm{Pt}}$ | capacitance of interface between Pt counter electrode and electrolyte |
| $d$ | film thickness or optical path length |
| $D_0$ | diffusion coefficient of electrons in semiconductor in the absence of traps |
| $D_{\mathrm{n}}$ | effective diffusion coefficient of electrons in semiconductor |
| DSC | dye-sensitized solar cell |
| $E$ | energy |
| $E_{0\text{-}0}$ | transition energy between lowest vibrational levels in ground and excited states of dye |
| $E^0(S^+/S^*)$ | Fermi level corresponding to oxidation potential of dye in excited state |
| $E^0(S^+/S)$ | Fermi level corresponding to oxidation potential of dye in ground state |
| $E^0_{\mathrm{ox}}$ | maximum of distribution of unoccupied states in dye or electrolyte |
| $E^0_{\mathrm{red}}$ | maximum of distribution of occupied states in dye or electrolyte |
| $^*E^0_{\mathrm{ox}}$ | maximum of distribution of unoccupied states in excited dye |
| $^*E^0_{\mathrm{red}}$ | maximum of distribution of occupied states in excited dye |
| $E_{\mathrm{c}}$ | energy of the conduction band edge (or mobility edge) |
| $\Delta E_{\mathrm{c}}$ | conduction band edge (or mobility edge) shift |
| $E_{\mathrm{HOMO}}$ | energy of the highest occupied molecular orbital |
| EIS | electrochemical impedance spectroscopy |

| | |
|---|---|
| $E_{LUMO}$ | energy of the lowest unoccupied molecular orbital |
| $E_{fn}$ | quasi-Fermi level of electrons in the semiconductor |
| $E_{redox}$ | redox level of the electrolyte |
| $FF$ | fill factor |
| $FF_{int}$ | internal fill factor |
| FTO | fluorine-doped tin oxide |
| $\Delta G^0$ | reaction free energy |
| $\Delta G^*$ | activation energy |
| $G_n$ | electron generation rate |
| $g(E)$ | density of states |
| $g^t(E)$ | density of states of traps in the band gap |
| $g^{cb}(E)$ | density of states in the conduction band |
| $h$ | Planck's constant, or abbreviation for "hour(s)" |
| $\hbar$ | Planck's constant divided by $2\pi$ |
| $H_{AB}$ | perturbation in the quantum-mechanical treatment of electron transfer |
| $\overline{\lvert H_{AB}\rvert}^2$ | absolute square of perturbation matrix element averaged over final states |
| HOMO | highest occupied molecular orbital |
| $i$ | current |
| $\hat{i}$ | amplitude of sinusoidal current signal |
| Im or Imag | imaginary part of a complex quantity |
| IMPS | intensity-modulated photocurrent spectroscopy |
| IMVS | intensity-modulated photovoltage spectroscopy |
| IPCE | incident photon-to-electron conversion efficiency |
| $IPCE_{int}$ | spectrally integrated IPCE |
| $IPCE_{max}$ | maximum value of the spectral IPCE |
| $I_{sc}$ | short-circuit photocurrent |
| $J$ | current density |
| $J_0$ | exchange current density of recombination |
| $J_{0k}$ | factor describing the dependence of $J_0$ on $k_r$ independent of $E_c$ |
| $\hat{J}$ | amplitude of sinusoidal current density signal |
| $J_{mpp}$ | current density at the maximum power point |
| $J_{sc}^{theo}$ | theoretical short-circuit photocurrent density estimated from IPCE spectrum |

| | |
|---|---|
| $J_{rec}^{light}$ | recombination current density under illumination |
| $J_{rec}^{dark}$ | recombination current density in the dark |
| $J_{sc}$ | short-circuit photocurrent density |
| $k$ | Boltzmann constant |
| $k_{decay}$ | rate constant of excited state decay of the dye |
| $k_{el}$ | rate constant of recombination |
| $k_{inj}$ | rate constant of electron injection from dye to semiconductor |
| $k_r$ | rate constant of recombination containing concentration of acceptor species |
| $k_{rec,dye}$ | rate constant of recombination with the oxidized dye |
| $k_{reg}$ | rate constant of dye regeneration |
| $L_0$ | steady-state diffusion length of electrons in the semiconductor |
| $L_n$ | effective diffusion length of electrons in the semiconductor |
| LUMO | lowest unoccupied molecular orbital |
| $M$ | scaling factor in analytical expression for the IMVS response |
| $n$ | total electron density |
| $n_c$ | density of conduction band electrons |
| $N_c$ | effective density of states at the conduction band edge |
| $n_{oc}$ | total electron density in the semiconductor under open-circuit conditions |
| $n_{sc}$ | total electron density in the semiconductor under short-circuit conditions |
| $n_t$ | density of trapped electrons |
| $N_t$ | total density of trap states |
| OA | octanoic acid |
| OCVD | open-circuit photovoltage decay |
| $p$ | porosity |
| $P_{in}$ | power density of incident light |
| $P_{max}$ | maximum power density |
| $q$ | electron charge |
| $Q_{oc}$ | charge in the semiconductor under open-circuit conditions |
| $Q_{sc}$ | charge in the semiconductor under short-circuit conditions |
| $R$ | resistance |
| $R_{refl}$ | reflectance |
| $R_{BL}$ | resistance of interface between blocking layer and electrolyte |
| $R_d$ | (ohmic) diffusion resistance of ions in the electrolyte |

| | |
|---|---|
| Re or Real | real part of a complex quantity |
| $R_{film}$ | total (ohmic) resistance of dye-sensitized semiconductor film |
| $R_{Pt}$ | resistance of interface between Pt counter electrode and electrolyte |
| $r_{rec}$ | recombination resistance per unit volume |
| $R_{rec}$ | recombination resistance |
| $R_s$ | resistance of the conductively coated glass substrate |
| $R_{series}$ | total series resistance |
| $r_{tr}$ | transport resistance per unit length per area |
| $R_{tr}$ | transport resistance |
| SDA | structure-directing agent |
| SEM | scanning electron microscopy |
| SLIM-PCV | stepped light-induced transient measurements of photocurrent and -voltage |
| $t$ | time |
| $T$ | temperature |
| $T_{trans}$ | transmittance |
| $t_{ads}$ | dye adsorption time |
| TCO | transparent conductive oxide |
| $U_n$ | volume rate of electron recombination |
| $V$ | applied voltage |
| $\hat{V}$ | amplitude of sinusoidal voltage signal |
| $V_f$ | Fermi-level voltage |
| $V_{mpp}$ | voltage at the maximum power point |
| $V_{oc}$ | open-circuit photovoltage |
| $V_{series}$ | voltage drop at the series resistance |
| $x$ | position along the x-axis |
| $Z$ | impedance |
| $Z'$ | real part of the impedance |
| $Z''$ | imaginary part of the impedance |
| $Z_d$ | impedance of diffusion in the electrolyte |
| $Z_{TL}$ | impedance of transmission line |
| $\alpha$ | trap distribution parameter |
| $\alpha_{abs}$ | absorption coefficient |
| $\alpha_{bulk}$ | trap distribution parameter of bulk trap states |

| | |
|---|---|
| $\alpha_{ss}$ | trap distribution parameter of surface trap states |
| $\beta$ | recombination parameter |
| $\varepsilon$ | molar absorptivity |
| $\varepsilon_{max}$ | maximum of the molar absorptivity |
| $\zeta$ | numerical factor in formal description of IMPS response |
| $\eta$ | power conversion efficiency |
| $\eta_{cc}$ | charge collection efficiency |
| $\eta_{inj}$ | electron injection efficiency |
| $\eta_{lh}$ | light harvesting efficiency |
| $\eta_{lh,int}$ | spectrally integrated light harvesting efficiency |
| $\eta_{reg}$ | dye regeneration efficiency |
| $\theta$ | phase shift between excitation signal and response |
| $\lambda$ | reorganization energy, or wavelength |
| $\lambda_{max}$ | wavelength of the absorption or emission maximum |
| $\nu$ | frequency |
| $\tau_0$ | lifetime of conduction band electrons in the absence of surface traps |
| $\tau_f$ | lifetime of conduction band electrons in the presence of surface traps |
| $\tau_{IMPS}$ | characteristic time constant of the IMPS response |
| $\tau_n$ | effective electron lifetime |
| $\tau_{tr}$ | transport time (for transport of electrons through the semiconductor) |
| $\phi$ | photon flux density |
| $\phi_0$ | initial or time-independent background photon flux density |
| $\hat{\phi}$ | amplitude of sinusoidal photon flux density signal |
| $\Phi(\omega)$ | IMPS or IMVS (as indicated by index) transfer function |
| $\omega$ | angular frequency |
| $\omega_d^p$ | characteristic frequency of diffusion in the electrolyte |
| $\omega_{min,IMPS}$ | angular frequency at minimum of imaginary part of IMPS response |
| $\omega_{min,IMVS}$ | angular frequency at minimum of imaginary part of IMVS response |
| $\omega_{rec}$ | characteristic frequency of recombination |

# References


1. Funk, M., The Wreck of the Kulluk. *The New York Times* 2014.

2. http://www.shell.com/global/aboutshell/lets-go-tpkg/campaign.html.

3. Crowley, T. J., Causes of climate change over the past 1000 years. *Science* **2000,** *289* (5477), 270-277; Solomon, S.; Plattner, G. K.; Knutti, R.; Friedlingstein, P., Irreversible climate change due to carbon dioxide emissions. *Proceedings of the National Academy of Sciences of the United States of America* **2009,** *106* (6), 1704-1709.

4. *World Energy Scenarios: Composing energy futures to 2050*; World Energy Council: 2013.

5. Swarup, R.; Mishra, S. N.; Jauhari, V. P., *Encyclopaedia of Ecology, Environment and Pollution Control - Energy and the Environment (Vol. 11)*. Mittal Publications: 1992.

6. *New Lens Scenarios - A Shift in Perspective for a World in Transition*; Shell International BV: 2013.

7. http://www.schott.com/csp/english/index.html.

8. http://www.sharp-world.com/solar/en/.

9. http://eu-solar.panasonic.net/en/.

10. Miller, D., *Selling Solar: The Diffusion of Renewable Energy in Emerging Markets*. Earthscan: 2012; Flynn, A., BP to Exit Solar Business After 40 Years. *The Wall Street Journal* 2011.

11. Quaschning, V., *Renewable Energy and Climate Change*. John Wiley & Sons, Ltd: Chichester, UK, 2010.

12. Epstein, P. R.; Buonocore, J. J.; Eckerle, K.; Hendryx, M.; Stout, B. M., III; Heinberg, R.; Clapp, R. W.; May, B.; Reinhart, N. L.; Ahern, M. M.; Doshi, S. K.; Glustrom, L., Full cost accounting for the life cycle of coal. *Ecological Economics Reviews* **2011,** *1219*, 73-98.

13. *Photovoltaics Report*; Fraunhofer ISE: 2014.

14. Goodrich, A.; Hacke, P.; Wang, Q.; Sopori, B.; Margolis, R.; James, T. L.; Woodhouse, M., A wafer-based monocrystalline silicon photovoltaics road map: Utilizing known technology improvement opportunities for further reductions in manufacturing costs. *Solar Energy Materials and Solar Cells* **2013,** *114*, 110-135.

15. Mathew, S.; Yella, A.; Gao, P.; Humphry-Baker, R.; Curchod, B. F. E.; Ashari-Astani, N.; Tavernelli, I.; Rothlisberger, U.; Nazeeruddin, M. K.; Grätzel, M., Dye-sensitized solar cells with 13% efficiency achieved through the molecular engineering of porphyrin sensitizers. *Nature Chemistry* **2014,** *6* (3), 242-247.

16. Parisi, M. L.; Maranghi, S.; Basosi, R., The evolution of the dye sensitized solar cells from Grätzel prototype to up-scaled solar applications: A life cycle assessment approach. *Renewable & Sustainable Energy Reviews* **2014,** *39*, 124-138.

17. http://www.nrel.gov/ncpv/images/efficiency_chart.jpg.

18. Boix, P. P.; Agarwala, S.; Koh, T. M.; Mathews, N.; Mhaisalkar, S. G., Perovskite Solar Cells: Beyond Methylammonium Lead Iodide. *Journal of Physical Chemistry Letters* **2015,** *6* (5), 898-907.

19. O'Regan, B.; Grätzel, M., A low-cost, high-efficiency solar cell based on dye-sensitized colloidal $TiO_2$ films. *Nature* **1991,** *353* (6346), 737-740.

20. Park, N. G.; Schlichthörl, G.; van de Lagemaat, J.; Cheong, H. M.; Mascarenhas, A.; Frank, A. J., Dye-sensitized $TiO_2$ solar cells: Structural and photoelectrochemical characterization of nanocrystalline electrodes formed from the hydrolysis of $TiCl_4$. *Journal of Physical Chemistry B* **1999,** *103* (17), 3308-3314.

21. Zhang, Q.; Dandeneau, C. S.; Zhou, X.; Cao, G., ZnO Nanostructures for Dye-Sensitized Solar Cells. *Advanced Materials* **2009,** *21* (41), 4087-4108.

22. Jiang, C. Y.; Sun, X. W.; Tan, K. W.; Lo, G. Q.; Kyaw, A. K. K.; Kwong, D. L., High-bendability flexible dye-sensitized solar cell with a nanoparticle-modified ZnO-nanowire electrode. *Applied Physics Letters* **2008,** *92*, 143101.

23. Toivola, M.; Halme, J.; Miettunen, K.; Aitola, K.; Lund, P. D., Nanostructured dye solar cells on flexible substrates-Review. *International Journal of Energy Research* **2009,** *33* (13), 1145-1160.

24. Chen, H. W.; Lin, C. Y.; Lai, Y. H.; Chen, J. G.; Wang, C. C.; Hu, C. W.; Hsu, C. Y.; Vittal, R.; Ho, K. C., Electrophoretic deposition of ZnO film and its compression for a plastic based flexible dye-sensitized solar cell. *Journal of Power Sources* **2011,** *196* (10), 4859-4864.

25. Yoshida, T.; Zhang, J. B.; Komatsu, D.; Sawatani, S.; Minoura, H.; Pauporté, T.; Lincot, D.; Oekermann, T.; Schlettwein, D.; Tada, H.; Wöhrle, D.; Funabiki, K.; Matsui, M.; Miura, H.; Yanagi, H., Electrodeposition of Inorganic/Organic Hybrid Thin Films. *Advanced Functional Materials* **2009,** *19* (1), 17-43.

26. Yoshida, T.; Pauporté, T.; Lincot, D.; Oekermann, T.; Minoura, H., Cathodic electrodeposition of ZnO/eosin Y hybrid thin films from oxygen-saturated aqueous solution of $ZnCl_2$ and eosin Y. *Journal of the Electrochemical Society* **2003,** *150* (9), C608-C615.

27. Pauporté, T.; Yoshida, T.; Cortes, R.; Froment, M.; Lincot, A., Electrochemical growth of epitaxial eosin/ZnO hybrid films. *Journal of Physical Chemistry B* **2003,** *107* (37), 10077-10082.

28. Oekermann, T.; Yoshida, T.; Minoura, H.; Wijayantha, K. G. U.; Peter, L. M., Electron transport and back reaction in electrochemically self-assembled nanoporous ZnO/dye hybrid films. *Journal of Physical Chemistry B* **2004,** *108* (24), 8364-8370.

29. Nazeeruddin, M. K.; Kay, A.; Rodicio, I.; Humphrybaker, R.; Muller, E.; Liska, P.; Vlachopoulos, N.; Grätzel, M., Conversion of light to electricity by cis-X2bis(2,2'-bipyridyl-4,4'-dicarboxylate)ruthenium(II) charge-transfer sensitizers (X = $Cl^-$, $Br^-$, $I^-$, $CN^-$, and $SCN^-$) on nanocrystalline $TiO_2$ electrodes. *Journal of the American Chemical Society* **1993,** *115* (14), 6382-6390.

30. Zeng, W.; Cao, Y.; Bai, Y.; Wang, Y.; Shi, Y.; Zhang, M.; Wang, F.; Pan, C.; Wang, P., Efficient Dye-Sensitized Solar Cells with an Organic Photosensitizer

Featuring Orderly Conjugated Ethylenedioxythiophene and Dithienosilole Blocks. *Chemistry of Materials* **2010,** *22* (5), 1915-1925.

31. Magne, C.; Urien, M.; Pauporté, T., Enhancement of photovoltaic performances in dye-sensitized solar cells by co-sensitization with metal-free organic dyes. *Rsc Advances* **2013,** *3* (18), 6315-6318.

32. Geiger, T.; Kuster, S.; Yum, J. H.; Moon, S. J.; Nazeeruddin, M. K.; Grätzel, M.; Nüesch, F., Molecular Design of Unsymmetrical Squaraine Dyes for High Efficiency Conversion of Low Energy Photons into Electrons Using $TiO_2$ Nanocrystalline Films. *Advanced Functional Materials* **2009,** *19* (17), 2720-2727.

33. Chang, J.; Lee, C. P.; Kumar, D.; Chen, P. W.; Lin, L. Y.; Thomas, K. R. J.; Ho, K. C., Co-sensitization promoted light harvesting for organic dye-sensitized solar cells using unsymmetrical squaraine dye and novel pyrenoimidazole-based dye. *Journal of Power Sources* **2013,** *240*, 779-785.

34. Yella, A.; Lee, H.-W.; Tsao, H. N.; Yi, C.; Chandiran, A. K.; Nazeeruddin, M. K.; Diau, E. W.-G.; Yeh, C.-Y.; Zakeeruddin, S. M.; Grätzel, M., Porphyrin-Sensitized Solar Cells with Cobalt (II/III)-Based Redox Electrolyte Exceed 12 Percent Efficiency. *Science* **2011,** *334* (6056), 629-634.

35. Boschloo, G.; Hagfeldt, A., Characteristics of the iodide/triiodide redox mediator in dye-sensitized solar cells. *Acc Chem Res* **2009,** *42* (11), 1819-26.

36. Hauch, A.; Georg, A., Diffusion in the electrolyte and charge-transfer reaction at the platinum electrode in dye-sensitized solar cells. *Electrochimica Acta* **2001,** *46* (22), 3457-3466.

37. Zistler, M.; Wachter, P.; Wasserscheid, P.; Gerhard, D.; Hinsch, A.; Sastrawan, R.; Gores, H. J., Comparison of electrochemical methods for triiodide diffusion coefficient measurements and observation of non-Stokesian diffusion behaviour in binary mixtures of two ionic liquids. *Electrochimica Acta* **2006,** *52* (1), 161-169.

38. Hagfeldt, A.; Boschloo, G.; Sun, L. C.; Kloo, L.; Pettersson, H., Dye-Sensitized Solar Cells. *Chemical Reviews* **2010,** *110* (11), 6595-6663.

39. Ye, M.; Wen, X.; Wang, M.; Iocozzia, J.; Zhang, N.; Lin, C.; Lin, Z., Recent advances in dye-sensitized solar cells: from photoanodes, sensitizers and electrolytes to counter electrodes. *Materials Today* **2015,** *18* (3), 155-162.

40. Keis, K.; Bauer, C.; Boschloo, G.; Hagfeldt, A.; Westermark, K.; Rensmo, H.; Siegbahn, H., Nanostructured ZnO electrodes for dye-sensitized solar cell applications. *Journal of Photochemistry and Photobiology a-Chemistry* **2002,** *148* (1-3), 57-64; Kyaw, A. K. K.; Sun, X. W.; Zhao, J. L.; Wang, J. X.; Zhao, D. W.; Wei, X. F.; Liu, X. W.; Demir, H. V.; Wu, T., Top-illuminated dye-sensitized solar cells with a room-temperature-processed ZnO photoanode on metal substrates and a Pt-coated Ga-doped ZnO counter electrode. *Journal of Physics D-Applied Physics* **2011,** *44*, 045102; Sayama, K.; Sugihara, H.; Arakawa, H., Photoelectrochemical properties of a porous $Nb_2O_5$ electrode sensitized by a ruthenium dye. *Chemistry of Materials* **1998,** *10* (12), 3825-3832; Park, N. G.; Kang, M. G.; Kim, K. M.; Ryu, K. S.; Chang, S. H.; Kim, D. K.; van de Lagemaat, J.; Benkstein, K. D.; Frank, A. J., Morphological and photoelectrochemical characterization of core-shell nanoparticle films for dye-sensitized solar cells: Zn-O type shell on $SnO_2$ and $TiO_2$ cores. *Langmuir* **2004,** *20* (10), 4246-4253; Turkovic, A.; Orel, Z. C., Dye-sensitized solar cell with $CeO_2$ and mixed

$CeO_2/SnO_2$ photoanodes. *Solar Energy Materials and Solar Cells* **1997,** *45* (3), 275-281; Guo, P.; Aegerter, M. A., Ru(II) sensitized $Nb_2O_5$ solar cell made by the sol-gel process. *Thin Solid Films* **1999,** *351* (1-2), 290-294.

41. Loewenstein, T.; Rudolph, M.; Mingebach, M.; Strauch, K.; Zimmermann, Y.; Neudeck, A.; Sensfuss, S.; Schlettwein, D., Textile-Compatible Substrate Electrodes with Electrodeposited ZnO-A New Pathway to Textile-Based Photovoltaics. *Chemphyschem* **2010,** *11* (4), 783-788.

42. Katoh, R.; Furube, A.; Yoshihara, T.; Hara, K.; Fujihashi, G.; Takano, S.; Murata, S.; Arakawa, H.; Tachiya, M., Efficiencies of electron injection from excited N3 dye into nanocrystalline semiconductor ($ZrO_2$, $TiO_2$, ZnO, $Nb_2O_5$, $SnO_2$, $In_2O_3$) films. *Journal of Physical Chemistry B* **2004,** *108* (15), 4818-4822.

43. Anta, J. A.; Guillén, E.; Tena-Zaera, R., ZnO-Based Dye-Sensitized Solar Cells. *Journal of Physical Chemistry C* **2012,** *116* (21), 11413-11425.

44. Elias, J.; Lévy-Clément, C.; Bechelany, M.; Michler, J.; Wang, G. Y.; Wang, Z.; Philippe, L., Hollow Urchin-like ZnO thin Films by Electrochemical Deposition. *Advanced Materials* **2010,** *22* (14), 1607-1612.

45. Hagfeldt, A.; Grätzel, M., Molecular Photovoltaics. *Acc. Chem. Res.* **2000,** *33* (5), 269-277.

46. Nazeeruddin, M. K.; De Angelis, F.; Fantacci, S.; Selloni, A.; Viscardi, G.; Liska, P.; Ito, S.; Bessho, T.; Grätzel, M., Combined experimental and DFT-TDDFT computational study of photoelectrochemical cell ruthenium sensitizers. *Journal of the American Chemical Society* **2005,** *127* (48), 16835-16847.

47. Chiba, Y.; Islam, A.; Watanabe, Y.; Komiya, R.; Koide, N.; Han, L., Dye-sensitized solar cells with conversion efficiency of 11.1%. *Japanese Journal of Applied Physics Part 2-Letters & Express Letters* **2006,** *45* (24-28), L638-L640; Chen, C. Y.; Wang, M. K.; Li, J. Y.; Pootrakulchote, N.; Alibabaei, L.; Ngoc-le, C. H.; Decoppet, J. D.; Tsai, J. H.; Grätzel, C.; Wu, C. G.; Zakeeruddin, S. M.; Grätzel, M., Highly Efficient Light-Harvesting Ruthenium Sensitizer for Thin-Film Dye-Sensitized Solar Cells. *Acs Nano* **2009,** *3* (10), 3103-3109.

48. Horiuchi, T.; Miura, H.; Uchida, S., Highly efficient metal-free organic dyes for dye-sensitized solar cells. *Journal of Photochemistry and Photobiology a-Chemistry* **2004,** *164* (1-3), 29-32.

49. Hwang, S.; Lee, J. H.; Park, C.; Lee, H.; Kim, C.; Lee, M. H.; Lee, W.; Park, J.; Kim, K.; Park, N. G., A highly efficient organic sensitizer for dye-sensitized solar cells. *Chemical Communications* **2007,** (46), 4887-4889; Kitamura, T.; Ikeda, M.; Shigaki, K.; Inoue, T.; Anderson, N. A.; Ai, X.; Lian, T. Q.; Yanagida, S., Phenyl-conjugated oligoene sensitizers for $TiO_2$ solar cells. *Chemistry of Materials* **2004,** *16* (9), 1806-1812; Hara, K.; Kurashige, M.; Ito, S.; Shinpo, A.; Suga, S.; Sayama, K.; Arakawa, H., Novel polyene dyes for highly efficient dye-sensitized solar cells. *Chemical Communications* **2003,** (2), 252-253; Choi, H.; Baik, C.; Kang, S. O.; Ko, J.; Kang, M. S.; Nazeeruddin, M. K.; Grätzel, M., Highly efficient and thermally stable organic sensitizers for solvent-free dye-sensitized solar cells. *Angewandte Chemie-International Edition* **2008,** *47* (2), 327-330.

50. Wang, Z.-S.; Cui, Y.; Dan-oh, Y.; Kasada, C.; Shinpo, A.; Hara, K., Thiophene-functionalized coumarin dye for efficient dye-sensitized solar cells: Electron lifetime

improved by coadsorption of deoxycholic acid. *Journal of Physical Chemistry C* **2007,** *111* (19), 7224-7230.

51. Mishra, A.; Fischer, M. K. R.; Bäuerle, P., Metal-Free Organic Dyes for Dye-Sensitized Solar Cells: From Structure: Property Relationships to Design Rules. *Angewandte Chemie-International Edition* **2009,** *48* (14), 2474-2499.

52. Horiuchi, T.; Miura, H.; Uchida, S., Highly-efficient metal-free organic dyes for dye-sensitized solar cells. *Chemical Communications* **2003,** 3036-3037.

53. Peter, L. M.; Duffy, N. W.; Wang, R. L.; Wijayantha, K. G. U., Transport and interfacial transfer of electrons in dye-sensitized nanocrystalline solar cells. *Journal of Electroanalytical Chemistry* **2002,** *524*, 127-136; Joly, D.; Pellejà, L.; Narbey, S.; Oswald, F.; Chiron, J.; Clifford, J. N.; Palomares, E.; Demadrille, R., A Robust Organic Dye for Dye Sensitized Solar Cells Based on Iodine/Iodide Electrolytes Combining High Efficiency and Outstanding Stability. *Scientific Reports* **2014,** *4* (4033), 1-7.

54. Gregg, B. A.; Pichot, F.; Ferrere, S.; Fields, C. L., Interfacial recombination processes in dye-sensitized solar cells and methods to passivate the interfaces. *Journal of Physical Chemistry B* **2001,** *105* (7), 1422-1429.

55. Wang, X. G.; Stanbury, D. M., Oxidation of iodide by a series of Fe(III) complexes in acetonitrile. *Inorganic Chemistry* **2006,** *45* (8), 3415-3423.

56. Olsen, E.; Hagen, G.; Lindquist, S. E., Dissolution of platinum in methoxy propionitrile containing LiI/$I_2$. *Solar Energy Materials and Solar Cells* **2000,** *63* (3), 267-273.

57. Ben Aribia, K.; Moehl, T.; Zakeeruddin, S. M.; Grätzel, M., Tridentate cobalt complexes as alternative redox couples for high-efficiency dye-sensitized solar cells. *Chemical Science* **2013,** *4* (1), 454-459.

58. Oskam, G.; Bergeron, B. V.; Meyer, G. J.; Searson, P. C., Pseudohalogens for dye-sensitized $TiO_2$ photoelectrochemical cells. *Journal of Physical Chemistry B* **2001,** *105* (29), 6867-6873; Hattori, S.; Wada, Y.; Yanagida, S.; Fukuzumi, S., Blue copper model complexes with distorted tetragonal geometry acting as effective electron-transfer mediators in dye-sensitized solar cells. *Journal of the American Chemical Society* **2005,** *127* (26), 9648-9654.

59. Liu, Y. R.; Jennings, J. R.; Huang, Y.; Wang, Q.; Zakeeruddin, S. M.; Grätzel, M., Cobalt Redox Mediators for Ruthenium-Based Dye-Sensitized Solar Cells: A Combined Impedance Spectroscopy and Near-IR Transmittance Study. *Journal of Physical Chemistry C* **2011,** *115* (38), 18847-18855.

60. Schmidt-Mende, L.; Bach, U.; Humphry-Baker, R.; Horiuchi, T.; Miura, H.; Ito, S.; Uchida, S.; Grätzel, M., Organic dye for highly efficient solid-state dye-sensitized solar cells. *Advanced Materials* **2005,** *17* (7), 813-815; Wei, D.; Unalan, H. E.; Han, D. X.; Zhang, Q. X.; Niu, L.; Amaratunga, G.; Ryhanen, T., A solid-state dye-sensitized solar cell based on a novel ionic liquid gel and ZnO nanoparticles on a flexible polymer substrate. *Nanotechnology* **2008,** *19*, 424006; Wang, P.; Zakeeruddin, S. M.; Moser, J. E.; Nazeeruddin, M. K.; Sekiguchi, T.; Grätzel, M., A stable quasi-solid-state dye-sensitized solar cell with an amphiphilic ruthenium sensitizer and polymer gel electrolyte. *Nature Materials* **2003,** *2* (6), 402-407; Bach, U.; Lupo, D.; Comte, P.; Moser, J. E.; Weissörtel, F.; Salbeck, J.; Spreitzer, H.; Grätzel, M., Solid-state dye-

sensitized mesoporous $TiO_2$ solar cells with high photon-to-electron conversion efficiencies. *Nature* **1998,** *395* (6702), 583-585.

61. Ding, I. K.; Tétreault, N.; Brillet, J.; Hardin, B. E.; Smith, E. H.; Rosenthal, S. J.; Sauvage, F.; Grätzel, M.; McGehee, M. D., Pore-Filling of Spiro-OMeTAD in Solid-State Dye Sensitized Solar Cells: Quantification, Mechanism, and Consequences for Device Performance. *Advanced Functional Materials* **2009,** *19* (15), 2431-2436; Burschka, J.; Dualeh, A.; Kessler, F.; Baranoff, E.; Cevey-Ha, N.-L.; Yi, C.; Nazeeruddin, M. K.; Grätzel, M., Tris(2-(1H-pyrazol-1-yl)pyridine)cobalt(III) as p-Type Dopant for Organic Semiconductors and Its Application in Highly Efficient Solid-State Dye-Sensitized Solar Cells. *Journal of the American Chemical Society* **2011,** *133* (45), 18042-18045.

62. Fabregat-Santiago, F.; Bisquert, J.; Cevey, L.; Chen, P.; Wang, M.; Zakeeruddin, S. M.; Grätzel, M., Electron Transport and Recombination in Solid-State Dye Solar Cell with Spiro-OMeTAD as Hole Conductor. *Journal of the American Chemical Society* **2009,** *131* (2), 558-562.

63. Ibach, H. L., Hans, *Solid-State Physics*. Springer-Verlag: Berlin Heidelberg, 2003.

64. Sze, S. M.; Kwok, K. N., *Physics of Semiconductor Devices*. 3 ed.; John Wiley & Sons, Inc.: Hoboken, New Jersey, 2007.

65. Mott, N., The mobility edge since 1967. *Journal of Physics C-Solid State Physics* **1987,** *20* (21), 3075-3102.

66. Kay, A.; Humphrybaker, R.; Grätzel, M., Artificial Photosynthesis .2. Investigations on the mechanism of photosensitization of nancrystalline $TiO_2$ solar-cells by chlorophyll derivatives. *Journal of Physical Chemistry* **1994,** *98* (3), 952-959; Bisquert, J.; Marcus, R. A., Device modeling of dye-sensitized solar cells. *Topics in current chemistry* **2014,** *352*, 325-396; O'Regan, B. C.; Durrant, J. R., Kinetic and Energetic Paradigms for Dye-Sensitized Solar Cells: Moving from the Ideal to the Real. *Accounts of Chemical Research* **2009,** *42* (11), 1799-1808.

67. Ronca, E.; Pastore, M.; Belpassi, L.; Tarantelli, F.; De Angelis, F., Influence of the dye molecular structure on the $TiO_2$ conduction band in dye-sensitized solar cells: disentangling charge transfer and electrostatic effects. *Energy & Environmental Science* **2013,** *6* (1), 183-193.

68. Schwanitz, K.; Weiler, U.; Hunger, R.; Mayer, T.; Jaegermann, W., Synchrotron-induced photoelectron spectroscopy of the dye-sensitized nanocrystalline $TiO_2$/electrolyte interface: Band gap states and their interaction with dye and solvent molecules. *Journal of Physical Chemistry C* **2007,** *111* (2), 849-854; Dimitrijevic, N. M.; Saponjic, Z. V.; Bartels, D. M.; Thurnauer, M. C.; Tiede, D. M.; Rajh, T., Revealing the nature of trapping sites in nanocrystalline titanium dioxide by selective surface modification. *Journal of Physical Chemistry B* **2003,** *107* (30), 7368-7375.

69. Nunzi, F.; Mosconi, E.; Storchi, L.; Ronca, E.; Selloni, A.; Grätzel, M.; De Angelis, F., Inherent electronic trap states in $TiO_2$ nanocrystals: effect of saturation and sintering. *Energy & Environmental Science* **2013,** *6* (4), 1221-1229.

70. Westermark, K.; Henningsson, A.; Rensmo, H.; Södergren, S.; Siegbahn, H.; Hagfeldt, A., Determination of the electronic density of states at a nanostructured $TiO_2$/Ru-dye/electrolyte interface by means of photoelectron spectroscopy. *Chemical Physics* **2002,** *285* (1), 157-165.

71. Memming, R., *Semiconductor Electrochemistry*. Wiley-VCH: Weinheim, 2001.

72. Hamann, C. H.; Vielstich, W., *Elektrochemie*. 4 ed.; Wiley-VCH: Weinheim, 2005.

73. Gerischer, H., Charge transfer processes at semiconductor-electrolyte interfaces in connection with problems of catalysis. *Surface Science* **1969,** *18* (1), 97-122.

74. Bard, A. J.; Faulkner, L. R., *Electrochemical Methods: Fundamentals and Applications*. 2 ed.; John Wiley & Sons: 2001.

75. Braslavsky, S. E., Glossary of terms used in Photochemistry 3rd Edition (IUPAC Recommendations 2006). *Pure and Applied Chemistry* **2007,** *79* (3), 293-465.

76. D'Andrade, B. W.; Datta, S.; Forrest, S. R.; Djurovich, P.; Polikarpov, E.; Thompson, M. E., Relationship between the ionization and oxidation potentials of molecular organic semiconductors. *Organic Electronics* **2005,** *6* (1), 11-20.

77. Memming, R., Electron-transfer process with excited molecules at semiconductor electrodes. *Progress in Surface Science* **1984,** *17* (1), 7-73.

78. Tachibana, Y.; Hara, K.; Sayama, K.; Arakawa, H., Quantitative analysis of light-harvesting efficiency and electron-transfer yield in ruthenium-dye-sensitized nanocrystalline $TiO_2$ solar cells. *Chemistry of Materials* **2002,** *14* (6), 2527-2535.

79. Ardo, S.; Meyer, G. J., Photodriven heterogeneous charge transfer with transition-metal compounds anchored to $TiO_2$ semiconductor surfaces. *Chemical Society Reviews* **2009,** *38* (1), 115-164.

80. Ooyama, Y.; Harima, Y., Photophysical and Electrochemical Properties, and Molecular Structures of Organic Dyes for Dye-Sensitized Solar Cells. *Chemphyschem* **2012,** *13* (18), 4032-4080.

81. Wu, S.-L.; Lu, H.-P.; Yu, H.-T.; Chuang, S.-H.; Chiu, C.-L.; Lee, C.-W.; Diau, E. W.-G.; Yeh, C.-Y., Design and characterization of porphyrin sensitizers with a push-pull framework for highly efficient dye-sensitized solar cells. *Energy & Environmental Science* **2010,** *3* (7), 949-955.

82. Tachibana, Y.; Moser, J. E.; Grätzel, M.; Klug, D. R.; Durrant, J. R., Subpicosecond interfacial charge separation in dye-sensitized nanocrystalline titanium dioxide films. *Journal of Physical Chemistry* **1996,** *100* (51), 20056-20062.

83. Asbury, J. B.; Hao, E.; Wang, Y. Q.; Ghosh, H. N.; Lian, T. Q., Ultrafast electron transfer dynamics from molecular adsorbates to semiconductor nanocrystalline thin films. *Journal of Physical Chemistry B* **2001,** *105* (20), 4545-4557; Pelet, S.; Grätzel, M.; Moser, J. E., Femtosecond dynamics of interfacial and intermolecular electron transfer at eosin-sensitized metal oxide nanoparticles. *Journal of Physical Chemistry B* **2003,** *107* (14), 3215-3224.

84. Peter, L. M.; Wijayantha, K. G. U., Electron transport and back reaction in dye sensitised nanocrystalline photovoltaic cells. *Electrochimica Acta* **2000,** *45* (28), 4543-4551.

85. Bisquert, J.; Vikhrenko, V. S., Interpretation of the time constants measured by kinetic techniques in nanostructured semiconductor electrodes and dye-sensitized solar cells. *Journal of Physical Chemistry B* **2004,** *108* (7), 2313-2322.

86. Wang, Q.; Ito, S.; Grätzel, M.; Fabregat-Santiago, F.; Mora-Seró, I.; Bisquert, J.; Bessho, T.; Imai, H., Characteristics of high efficiency dye-sensitized solar cells. *Journal of Physical Chemistry B* **2006,** *110* (50), 25210-25221.

87. Peter, L. M., Characterization and modeling of dye-sensitized solar cells. *Journal of Physical Chemistry C* **2007,** *111* (18), 6601-6612.

88. Dloczik, L.; Ileperuma, O.; Lauermann, I.; Peter, L. M.; Ponomarev, E. A.; Redmond, G.; Shaw, N. J.; Uhlendorf, I., Dynamic response of dye-sensitized nanocrystalline solar cells: Characterization by intensity-modulated photocurrent spectroscopy. *Journal of Physical Chemistry B* **1997,** *101* (49), 10281-10289.

89. Cao, F.; Oskam, G.; Meyer, G. J.; Searson, P. C., Electron transport in porous nanocrystalline $TiO_2$ photoelectrochemical cells. *Journal of Physical Chemistry* **1996,** *100* (42), 17021-17027.

90. Bisquert, J.; Fabregat-Santiago, F.; Mora-Seró, I.; Garcia-Belmonte, G.; Gimenez, S., Electron Lifetime in Dye-Sensitized Solar Cells: Theory and Interpretation of Measurements. *Journal of Physical Chemistry C* **2009,** *113* (40), 17278-17290.

91. Cameron, P. J.; Peter, L. M.; Hore, S., How important is the back reaction of electrons via the substrate in dye-sensitized nanocrystalline solar cells? *Journal of Physical Chemistry B* **2005,** *109* (2), 930-936.

92. Cameron, P. J.; Peter, L. M., Characterization of titanium dioxide blocking layers in dye-sensitized nanocrystalline solar cells. *Journal of Physical Chemistry B* **2003,** *107* (51), 14394-14400.

93. Haque, S. A.; Tachibana, Y.; Klug, D. R.; Durrant, J. R., Charge recombination kinetics in dye-sensitized nanocrystalline titanium dioxide films under externally applied bias. *Journal of Physical Chemistry B* **1998,** *102* (10), 1745-1749.

94. Barnes, P. R. F.; Anderson, A. Y.; Durrant, J. R.; O'Regan, B. C., Simulation and measurement of complete dye sensitised solar cells: including the influence of trapping, electrolyte, oxidised dyes and light intensity on steady state and transient device behaviour. *Physical Chemistry Chemical Physics* **2011,** *13* (13), 5798-5816.

95. Barnes, P. R. F.; Anderson, A. Y.; Juozapavicius, M.; Liu, L. X.; Li, X. E.; Palomares, E.; Forneli, A.; O'Regan, B. C., Factors controlling charge recombination under dark and light conditions in dye sensitised solar cells. *Physical Chemistry Chemical Physics* **2011,** *13* (8), 3547-3558.

96. Clifford, J. N.; Palomares, E.; Nazeeruddin, M. K.; Grätzel, M.; Nelson, J.; Li, X.; Long, N. J.; Durrant, J. R., Molecular control of recombination dynamics in dye-sensitized nanocrystalline $TiO_2$ films: Free energy vs distance dependence. *Journal of the American Chemical Society* **2004,** *126* (16), 5225-5233.

97. Peter, L. M., Dye-sensitized nanocrystalline solar cells. *Physical Chemistry Chemical Physics* **2007,** *9* (21), 2630-2642.

98. Schlichthörl, G.; Park, N. G.; Frank, A. J., Evaluation of the charge-collection efficiency of dye-sensitized nanocrystalline $TiO_2$ solar cells. *Journal of Physical Chemistry B* **1999,** *103* (5), 782-791.

99. Dunn, H. K.; Peter, L. M., How Efficient Is Electron Collection in Dye-Sensitized Solar Cells? Comparison of Different Dynamic Methods for the Determination of the Electron Diffusion Length. *Journal of Physical Chemistry C* **2009,** *113* (11), 4726-4731.

100. Clifford, J. N.; Palomares, E.; Nazeeruddin, M. K.; Grätzel, M.; Durrant, J. R., Dye dependent regeneration dynamics in dye sensitized nanocrystalline solar cells: Evidence for the formation of a ruthenium bipyridyl cation/iodide intermediate. *Journal of Physical Chemistry C* **2007,** *111* (17), 6561-6567.

101. Nyhlen, J.; Boschloo, G.; Hagfeldt, A.; Kloo, L.; Privalov, T., Regeneration of Oxidized Organic Photo-Sensitizers in Grätzel Solar Cells: Quantum-Chemical Portrait of a General Mechanism. *Chemphyschem* **2010,** *11* (9), 1858-1862.

102. Pelet, S.; Moser, J. E.; Grätzel, M., Cooperative effect of adsorbed cations and iodide on the interception of back electron transfer in the dye sensitization of nanocrystalline $TiO_2$. *Journal of Physical Chemistry B* **2000,** *104* (8), 1791-1795.

103. Kuciauskas, D.; Freund, M. S.; Gray, H. B.; Winkler, J. R.; Lewis, N. S., Electron transfer dynamics in nanocrystalline titanium dioxide solar cells sensitized with ruthenium or osmium polypyridyl complexes. *Journal of Physical Chemistry B* **2001,** *105* (2), 392-403.

104. Tefashe, U. M.; Loewenstein, T.; Miura, H.; Schlettwein, D.; Wittstock, G., Scanning electrochemical microscope studies of dye regeneration in indoline (D149)-sensitized ZnO photoelectrochemical cells. *Journal of Electroanalytical Chemistry* **2010,** *650* (1), 24-30; Tefashe, U. M.; Nonomura, K.; Vlachopoulos, N.; Hagfeldt, A.; Wittstock, G., Effect of Cation on Dye Regeneration Kinetics of N719-Sensitized $TiO_2$ Films in Acetonitrile-Based and Ionic-Liquid-Based Electrolytes Investigated by Scanning Electrochemical Microscopy. *Journal of Physical Chemistry C* **2012,** *116* (6), 4316-4323.

105. Shen, Y.; Nonomura, K.; Schlettwein, D.; Zhao, C.; Wittstock, G., Photoelectrochemical kinetics of eosin Y-sensitized zinc oxide films investigated by scanning electrochemical microscopy. *Chemistry-a European Journal* **2006,** *12* (22), 5832-5839.

106. Li, F.; Jennings, J. R.; Wang, Q., Determination of Sensitizer Regeneration Efficiency in Dye-Sensitized Solar Cells. *Acs Nano* **2013,** *7* (9), 8233-8242.

107. Jennings, J. R.; Liu, Y.; Wang, Q., Efficiency Limitations in Dye-Sensitized Solar Cells Caused by Inefficient Sensitizer Regeneration. *Journal of Physical Chemistry C* **2011,** *115* (30), 15109-15120.

108. Nelson, J., *The Physics of Solar Cells*. Imperial College Press: London, 2003.

109. Bisquert, J.; Mora-Seró, I., Simulation of Steady-State Characteristics of Dye-Sensitized Solar Cells and the Interpretation of the Diffusion Length. *Journal of Physical Chemistry Letters* **2010,** *1* (1), 450-456.

110. Kopidakis, N.; Schiff, E. A.; Park, N. G.; van de Lagemaat, J.; Frank, A. J., Ambipolar diffusion of photocarriers in electrolyte-filled, nanoporous $TiO_2$. *Journal of Physical Chemistry B* **2000,** *104* (16), 3930-3936.

111. Peter, L., "Sticky Electrons" Transport and Interfacial Transfer. of Electrons in the Dye-Sensitized Solar Cell. *Accounts of Chemical Research* **2009,** *42* (11), 1839-1847.

112. Södergren, S.; Hagfeldt, A.; Olsson, J.; Lindquist, S. E., Theoretical models for the action spectrum and the current-voltage characteristics of microporous semiconductor-films in photoelectrochemical cells. *Journal of Physical Chemistry* **1994,** *98* (21), 5552-5556.

113. Duffy, N. W.; Peter, L. M.; Rajapakse, R. M. G.; Wijayantha, K. G. U., A novel charge extraction method for the study of electron transport and interfacial transfer in dye sensitised nanocrystalline solar cells. *Electrochemistry Communications* **2000,** *2* (9), 658-662.

114. Bisquert, J., Chemical capacitance of nanostructured semiconductors: its origin and significance for nanocomposite solar cells. *Physical Chemistry Chemical Physics* **2003,** *5* (24), 5360-5364.

115. Peter, L., Transport, trapping and interfacial transfer of electrons in dye-sensitized nanocrystalline solar cells. *Journal of Electroanalytical Chemistry* **2007,** *599* (2), 233-240.

116. de Jongh, P. E.; Vanmaekelbergh, D., Investigation of the electronic transport properties of nanocrystalline particulate $TiO_2$ electrodes by intensity-modulated photocurrent spectroscopy. *Journal of Physical Chemistry B* **1997,** *101* (14), 2716-2722.

117. Tiedje, T.; Rose, A., A physical interpretation of dispersive transport in disordered semiconductors. *Solid State Communications* **1981,** *37* (1), 49-52.

118. Fisher, A. C.; Peter, L. M.; Ponomarev, E. A.; Walker, A. B.; Wijayantha, K. G. U., Intensity dependence of the back reaction and transport of electrons in dye-sensitized nanacrystalline $TiO_2$ solar cells. *Journal of Physical Chemistry B* **2000,** *104* (5), 949-958.

119. Bisquert, J.; Zaban, A.; Greenshtein, M.; Mora-Seró, I., Determination of rate constants for charge transfer and the distribution of semiconductor and electrolyte electronic energy levels in dye-sensitized solar cells by open-circuit photovoltage decay method. *Journal of the American Chemical Society* **2004,** *126* (41), 13550-13559.

120. Walker, A. B.; Peter, L. M.; Lobato, K.; Cameron, P. J., Analysis of photovoltage decay transients in dye-sensitized solar cells. *Journal of Physical Chemistry B* **2006,** *110* (50), 25504-25507.

121. Barnes, P. R. F.; Miettunen, K.; Li, X.; Anderson, A. Y.; Bessho, T.; Grätzel, M.; O'Regan, B. C., Interpretation of Optoelectronic Transient and Charge Extraction Measurements in Dye-Sensitized Solar Cells. *Advanced Materials* **2013,** *25* (13), 1881-1922.

122. Zaban, A.; Meier, A.; Gregg, B. A., Electric potential distribution and short-range screening in nanoporous $TiO_2$ electrodes. *Journal of Physical Chemistry B* **1997,** *101* (40), 7985-7990.

123. Oekermann, T.; Yoshida, T.; Boeckler, C.; Caro, J.; Minoura, H., Capacitance and field-driven electron transport in electrochemically self-assembled nanoporous ZnO/Dye hybrid films. *Journal of Physical Chemistry B* **2005,** *109* (25), 12560-12566.

124. Nakade, S.; Kanzaki, T.; Kubo, W.; Kitamura, T.; Wada, Y.; Yanagida, S., Role of electrolytes on charge recombination in dye-sensitized $TiO_2$ solar cell (1): The case of solar cells using the $I^-/I_3^-$ redox couple. *Journal of Physical Chemistry B* **2005,** *109* (8), 3480-3487.

125. Nister, D.; Keis, K.; Lindquist, S. E.; Hagfeldt, A., A detailed analysis of ambipolar diffusion in nanostructured metal oxide films. *Solar Energy Materials and Solar Cells* **2002,** *73* (4), 411-423; Nakade, S.; Kambe, S.; Kitamura, T.; Wada, Y.; Yanagida, S., Effects of lithium ion density on electron transport in nanoporous $TiO_2$ electrodes. *Journal of Physical Chemistry B* **2001,** *105* (38), 9150-9152.

126. Bisquert, J.; Cahen, D.; Hodes, G.; Ruhle, S.; Zaban, A., Physical chemical principles of photovoltaic conversion with nanoparticulate, mesoporous dye-sensitized solar cells. *Journal of Physical Chemistry B* **2004,** *108* (24), 8106-8118.

127. Bailes, M.; Cameron, P. J.; Lobato, K.; Peter, L. M., Determination of the density and energetic distribution of electron traps in dye-sensitized nanocrystalline solar cells. *Journal of Physical Chemistry B* **2005,** *109* (32), 15429-15435.

128. Fabregat-Santiago, F.; Garcia-Belmonte, G.; Mora-Seró, I.; Bisquert, J., Characterization of nanostructured hybrid and organic solar cells by impedance spectroscopy. *Physical Chemistry Chemical Physics* **2011,** *13* (20), 9083-9118.

129. Boschloo, G.; Fitzmaurice, D., Spectroelectrochemical investigation of surface states in nanostructured $TiO_2$ electrodes. *Journal of Physical Chemistry B* **1999,** *103* (12), 2228-2231.

130. Bertoluzzi, L.; Herraiz-Cardona, I.; Gottesman, R.; Zaban, A.; Bisquert, J., Relaxation of Electron Carriers in the Density of States of Nanocrystalline $TiO_2$. *Journal of Physical Chemistry Letters* **2014,** *5* (4), 689-694.

131. *Dye-sensitized Solar Cells*. EPFL Press: Lausanne, 2010.

132. Barzykin, A. V.; Tachiya, M., Mechanism of molecular control of recombination dynamics in dye-sensitized nanocrystalline semiconductor films. *Journal of Physical Chemistry B* **2004,** *108* (24), 8385-8389.

133. Waita, S. M.; Aduda, B. O.; Mwabora, J. M.; Niklasson, G. A.; Granqvist, C. G.; Boschloo, G., Electrochemical characterization of $TiO_2$ blocking layers prepared by reactive DC magnetron sputtering. *Journal of Electroanalytical Chemistry* **2009,** *637* (1-2), 79-83.

134. Jang, K.-I.; Hong, E.; Kim, J. H., Effect of an electrodeposited $TiO_2$ blocking layer on efficiency improvement of dye-sensitized solar cell. *Korean Journal of Chemical Engineering* **2012,** *29* (3), 356-361.

135. Peulon, S.; Lincot, D., Cathodic electrodeposition from aqueous solution of dense or open-structured zinc oxide films. *Advanced Materials* **1996,** *8* (2), 166-170.

136. Magne, C.; Moehl, T.; Urien, M.; Grätzel, M.; Pauporté, T., Effects of ZnO film growth route and nanostructure on electron transport and recombination in dye-sensitized solar cells. *Journal of Materials Chemistry A* **2013,** *1* (6), 2079-2088.

137. Sakuragi, Y.; Wang, X. F.; Miura, H.; Matsui, M.; Yoshida, T., Aggregation of indoline dyes as sensitizers for ZnO solar cells. *Journal of Photochemistry and Photobiology a-Chemistry* **2010,** *216* (1), 1-7.

138. Richter, C.; Beu, M.; Schlettwein, D., Influence of counter-anions during electrochemical deposition of ZnO on the charge transport dynamics in dye-sensitized solar cells. *Physical Chemistry Chemical Physics* **2015,** *17* (3), 1883-1890.

139. Green, A. N. M.; Chandler, R. E.; Haque, S. A.; Nelson, J.; Durrant, J. R., Transient absorption studies and numerical modeling of iodine photoreduction by nanocrystalline $TiO_2$ films. *Journal of Physical Chemistry B* **2005,** *109* (1), 142-150.

140. Barnes, P. R. F.; Liu, L. X.; Li, X. E.; Anderson, A. Y.; Kisserwan, H.; Ghaddar, T. H.; Durrant, J. R.; O'Regan, B. C., Re-evaluation of Recombination Losses in Dye-Sensitized Cells: The Failure of Dynamic Relaxation Methods to Correctly Predict Diffusion Length in Nanoporous Photoelectrodes. *Nano Letters* **2009,** *9* (10), 3532-3538.

141. Guillén, E.; Peter, L. M.; Anta, J. A., Electron Transport and Recombination in ZnO-Based Dye-Sensitized Solar Cells. *Journal of Physical Chemistry C* **2011,** *115* (45), 22622-22632.

142. Zaban, A.; Greenshtein, M.; Bisquert, J., Determination of the electron lifetime in nanocrystalline dye solar cells by open-circuit voltage decay measurements. *Chemphyschem* **2003,** *4* (8), 859-864.

143. Marcus, R. A.; Sutin, N., Electron transfers in chemistry and biology. *Biochimica Et Biophysica Acta* **1985,** *811* (3), 265-322; Gao, Y. Q.; Georgievskii, Y.; Marcus, R. A., On the theory of electron transfer reactions at semiconductor electrode/liquid interfaces. *Journal of Chemical Physics* **2000,** *112* (7), 3358-3369.

144. Gao, Y. Q.; Marcus, R. A., On the theory of electron transfer reactions at semiconductor/liquid interfaces. II. A free electron model. *Journal of Chemical Physics* **2000,** *113* (15), 6351-6360.

145. O'Regan, B. C.; López-Duarte, I.; Martínez-Díaz, M. V.; Forneli, A.; Albero, J.; Morandeira, A.; Palomares, E.; Torres, T.; Durrant, J. R., Catalysis of recombination and its limitation on open circuit voltage for dye sensitized photovoltaic cells using phthalocyanine dyes. *Journal of the American Chemical Society* **2008,** *130* (10), 2906-2907.

146. Ren, X.; Feng, Q.; Zhou, G.; Huang, C.-H.; Wang, Z.-S., Effect of Cations in Coadsorbate on Charge Recombination and Conduction Band Edge Movement in Dye-Sensitized Solar Cells. *Journal of Physical Chemistry C* **2010,** *114* (15), 7190-7195.

147. Kopidakis, N.; Neale, N. R.; Frank, A. J., Effect of an adsorbent on recombination and band-edge movement in dye-sensitized $TiO_2$ solar cells: Evidence for surface passivation. *Journal of Physical Chemistry B* **2006,** *110* (25), 12485-12489.

148. Miyashita, M.; Sunahara, K.; Nishikawa, T.; Uemura, Y.; Koumura, N.; Hara, K.; Mori, A.; Abe, T.; Suzuki, E.; Mori, S., Interfacial Electron-Transfer Kinetics in Metal-Free Organic Dye-Sensitized Solar Cells: Combined Effects of Molecular Structure of Dyes and Electrolytes. *Journal of the American Chemical Society* **2008,** *130* (52), 17874-17881.

149. Neale, N. R.; Kopidakis, N.; van de Lagemaat, J.; Grätzel, M.; Frank, A. J., Effect of a coadsorbent on the performance of dye-sensitized $TiO_2$ solar cells: Shielding versus band-edge movement. *Journal of Physical Chemistry B* **2005,** *109* (49), 23183-23189.

150. Jena, A. K.; Bhargava, P., Effect of amount of dye in the $TiO_2$ photoanode on electron transport, recombination, $J_{sc}$ and $V_{oc}$ of dye-sensitized solar cells. *Rsc Advances* **2013,** *3* (8), 2655-2661; Fillinger, A.; Parkinson, B. A., The adsorption behavior of a

rutheninm-based sensitizing dye to nanocrystalline $TiO_2$ - Coverage effects on the external and internal sensitization quantum yields. *Journal of the Electrochemical Society* **1999,** *146* (12), 4559-4564; Marinado, T.; Nonomura, K.; Nissfolk, J.; Karlsson, M. K.; Hagberg, D. P.; Sun, L. C.; Mori, S.; Hagfeldt, A., How the Nature of Triphenylamine-Polyene Dyes in Dye-Sensitized Solar Cells Affects the Open-Circuit Voltage and Electron Lifetimes. *Langmuir* **2010,** *26* (4), 2592-2598.

151. O'Regan, B. C.; Walley, K.; Juozapavicius, M.; Anderson, A.; Matar, F.; Ghaddar, T.; Zakeeruddin, S. M.; Klein, C.; Durrant, J. R., Structure/Function Relationships in Dyes for Solar Energy Conversion: A Two-Atom Change in Dye Structure and the Mechanism for Its Effect on Cell Voltage. *Journal of the American Chemical Society* **2009,** *131* (10), 3541-3548.

152. Chen, P.; Yum, J. H.; De Angelis, F.; Mosconi, E.; Fantacci, S.; Moon, S.-J.; Baker, R. H.; Ko, J.; Nazeeruddin, M. K.; Grätzel, M., High Open-Circuit Voltage Solid-State Dye-Sensitized Solar Cells with Organic Dye. *Nano Letters* **2009,** *9* (6), 2487-2492.

153. Look, D. C., Recent advances in ZnO materials and devices. *Materials Science and Engineering B-Solid State Materials for Advanced Technology* **2001,** *80* (1-3), 383-387.

154. Janotti, A.; Van de Walle, C. G., Fundamentals of zinc oxide as a semiconductor. *Reports on Progress in Physics* **2009,** *72*, 126501.

155. Harrison, S. E., Conductivity and Hall effect of ZnO at low temperatures. *Physical Review* **1954,** *93* (1), 52-62; Hoffmann, K.; Hahn, D., Electron-spin resonance of lattice-defects in zinc-oxide. *Physica Status Solidi a-Applied Research* **1974,** *24* (2), 637-648; Hagemark, K. I., Defect structure of Zn-doped ZnO. *Journal of Solid State Chemistry* **1976,** *16* (3-4), 293-299.

156. Van de Walle, C. G., Hydrogen as a cause of doping in zinc oxide. *Physical Review Letters* **2000,** *85* (5), 1012-1015; Janotti, A.; Van de Walle, C. G., Hydrogen multicentre bonds. *Nature Materials* **2007,** *6* (1), 44-47; Hofmann, D. M.; Hofstaetter, A.; Leiter, F.; Zhou, H. J.; Henecker, F.; Meyer, B. K.; Orlinskii, S. B.; Schmidt, J.; Baranov, P. G., Hydrogen: A relevant shallow donor in zinc oxide. *Physical Review Letters* **2002,** *88* (4), 045504.

157. Forro, L.; Chauvet, O.; Emin, D.; Zuppiroli, L.; Berger, H.; Lévy, F., High-mobility n-type charge-carriers in large single-crystals of anatase ($TiO_2$). *Journal of Applied Physics* **1994,** *75* (1), 633-635.

158. Look, D. C.; Reynolds, D. C.; Sizelove, J. R.; Jones, R. L.; Litton, C. W.; Cantwell, G.; Harsch, W. C., Electrical properties of bulk ZnO. *Solid State Communications* **1998,** *105* (6), 399-401.

159. Pal, B.; Sharon, M., Enhanced photocatalytic activity of highly porous ZnO thin films prepared by sol-gel process. *Materials Chemistry and Physics* **2002,** *76* (1), 82-87.

160. Keis, K.; Magnusson, E.; Lindström, H.; Lindquist, S. E.; Hagfeldt, A., A 5% efficient photo electrochemical solar cell based on nanostructured ZnO electrodes. *Solar Energy Materials and Solar Cells* **2002,** *73* (1), 51-58.

161. Matsui, M.; Ono, M.; Kubota, Y.; Funabiki, K.; Yoshida, T.; Kim, H. J.; Hong, C. K.; Higashijima, S.; Miura, H., Survey of co-adsorbent for DN350 in zinc oxide dye-sensitized solar cell. *Dyes and Pigments* **2013,** *99* (3), 829-832.

162. Yi, S.-H.; Choi, S.-K.; Jang, J.-M.; Kim, J.-A.; Jung, W.-G., Low-temperature growth of ZnO nanorods by chemical bath deposition. *Journal of Colloid and Interface Science* **2007,** *313* (2), 705-710.

163. Secu, C. E.; Sima, M., Photoluminescence and thermoluminescence of ZnO nano-needle arrays and films. *Optical Materials* **2009,** *31* (6), 876-880.

164. Pradhan, B.; Batabyal, S. K.; Pal, A. J., Vertically aligned ZnO nanowire arrays in Rose Bengal-based dye-sensitized solar cells. *Solar Energy Materials and Solar Cells* **2007,** *91* (9), 769-773.

165. Memarian, N.; Concina, I.; Braga, A.; Rozati, S. M.; Vomiero, A.; Sberveglieri, G., Hierarchically Assembled ZnO Nanocrystallites for High-Efficiency Dye-Sensitized Solar Cells. *Angewandte Chemie-International Edition* **2011,** *50* (51), 12321-12325.

166. Loewenstein, T.; Nonomura, K.; Yoshida, T.; Michaelis, E.; Wöhrle, D.; Rathousky, J.; Wark, M.; Schlettwein, D., Efficient sensitization of mesoporous electrodeposited zinc oxide by cis-bis(isothiocyanato)bis(2,2 '-bipyridyl-4,4 '-dicarboxylato)-ruthenium(II). *Journal of the Electrochemical Society* **2006,** *153* (4), A699-A704.

167. Bauer, C.; Boschloo, G.; Mukhtar, E.; Hagfeldt, A., Electron injection and recombination in $Ru(dcbpy)_2(NCS)_2$ sensitized nanostructured ZnO. *Journal of Physical Chemistry B* **2001,** *105* (24), 5585-5588.

168. Katoh, R.; Furube, A.; Tamaki, Y.; Yoshihara, T.; Murai, M.; Hara, K.; Murata, S.; Arakawa, H.; Tachiya, M., Microscopic imaging of the efficiency of electron injection from excited sensitizer dye into nanocrystalline ZnO film. *Journal of Photochemistry and Photobiology a-Chemistry* **2004,** *166* (1-3), 69-74.

169. Parks, G. A., The Isoelectric Points of Solid Oxides, Solid Hydroxides, and Aqueous Hydroxo Complex Systems. *Chemical Reviews* **1965,** *65* (2), 177-198.

170. Guillén, E.; Idígoras, J.; Berger, T.; Anta, J. A.; Fernández-Lorenzo, C.; Alcántara, R.; Navas, J.; Martín-Calleja, J., ZnO-based dye solar cell with pure ionic-liquid electrolyte and organic sensitizer: the relevance of the dye-oxide interaction in an ionic-liquid medium. *Physical Chemistry Chemical Physics* **2011,** *13* (1), 207-213.

171. Le Bahers, T.; Labat, F.; Pauporté, T.; Ciofini, I., Effect of solvent and additives on the open-circuit voltage of ZnO-based dye-sensitized solar cells: a combined theoretical and experimental study. *Physical Chemistry Chemical Physics* **2010,** *12* (44), 14710-14719.

172. Furube, A.; Katoh, R.; Hara, K.; Murata, S.; Arakawa, H.; Tachiya, M., Ultrafast stepwise electron injection from photoexcited Ru-complex into nanocrystalline ZnO film via intermediates at the surface. *Journal of Physical Chemistry B* **2003,** *107* (17), 4162-4166; Stockwell, D.; Yang, Y.; Huang, J.; Anfuso, C.; Huang, Z.; Lian, T., Comparison of Electron-Transfer Dynamics from Coumarin 343 to $TiO_2$, $SnO_2$, and ZnO Nanocrystalline Thin Films: Role of Interface-Bound Charge-Separated Pairs. *Journal of Physical Chemistry C* **2010,** *114* (14), 6560-6566.

173. Furube, A.; Katoh, R.; Yoshihara, T.; Hara, K.; Murata, S.; Arakawa, H.; Tachiya, M., Ultrafast direct and indirect electron-injection processes in a photoexcited dye-sensitized nanocrystalline zinc oxide film: The importance of exciplex intermediates at the surface. *Journal of Physical Chemistry B* **2004,** *108* (33), 12583-12592.

174. Nemec, H.; Rochford, J.; Taratula, O.; Galoppini, E.; Kuzel, P.; Polívka, T.; Yartsev, A.; Sundström, V., Influence of the Electron-Cation Interaction on Electron Mobility in Dye-Sensitized ZnO and $TiO_2$ Nanocrystals: A Study Using Ultrafast Terahertz Spectroscopy. *Physical Review Letters* **2010,** *104*, 197401.

175. Izaki, M.; Omi, T., Transparent zinc oxide films prepared by electrochemical reaction. *Applied Physics Letters* **1996,** *68* (17), 2439-2440.

176. Pauporté, T.; Lincot, D., Hydrogen peroxide oxygen precursor for zinc oxide electrodeposition I. Deposition in perchlorate medium. *Journal of the Electrochemical Society* **2001,** *148* (4), C310-C314.

177. Peulon, S.; Lincot, D., Mechanistic study of cathodic electrodeposition of zinc oxide and zinc hydroxychloride films from oxygenated aqueous zinc chloride solutions. *Journal of the Electrochemical Society* **1998,** *145* (3), 864-874.

178. Roth, A. P.; Webb, J. B.; Williams, D. F., Absorption-edge shift in ZnO thin-films at high carrier densities. *Solid State Communications* **1981,** *39* (12), 1269-1271; Burstein, E., Anomalous optical absorption limit in InSb. *Physical Review* **1954,** *93* (3), 632-633.

179. Lupan, O.; Guérin, V. M.; Tiginyanu, I. M.; Ursaki, V. V.; Chow, L.; Heinrich, H.; Pauporté, T., Well-aligned arrays of vertically oriented ZnO nanowires electrodeposited on ITO-coated glass and their integration in dye sensitized solar cells. *Journal of Photochemistry and Photobiology a-Chemistry* **2010,** *211* (1), 65-73.

180. Lupan, O.; Pauporté, T.; Chow, L.; Viana, B.; Pellé, F.; Ono, L. K.; Cuenya, B. R.; Heinrich, H., Effects of annealing on properties of ZnO thin films prepared by electrochemical deposition in chloride medium. *Applied Surface Science* **2010,** *256* (6), 1895-1907.

181. Marrani, A. G.; Caprioli, F.; Boccia, A.; Zanoni, R.; Decker, F., Electrochemically deposited ZnO films: an XPS study on the evolution of their surface hydroxide and defect composition upon thermal annealing. *Journal of Solid State Electrochemistry* **2014,** *18* (2), 505-513.

182. Nonomura, K.; Komatsu, D.; Yoshida, T.; Minoura, H.; Schlettwein, D., Dependence of the photoelectrochemical performance of sensitised ZnO on the crystalline orientation in electrodeposited ZnO thin films. *Physical Chemistry Chemical Physics* **2007,** *9* (15), 1843-1849.

183. Yoshida, T.; Iwaya, M.; Ando, H.; Oekermann, T.; Nonomura, K.; Schlettwein, D.; Wöhrle, D.; Minoura, H., Improved photoelectrochemical performance of electrodeposited ZnO/EosinY hybrid thin films by dye re-adsorption. *Chemical Communications* **2004,** 400-401.

184. Yoshida, T.; Tochimoto, M.; Schlettwein, D.; Wöhrle, D.; Sugiura, T.; Minoura, H., Self-assembly of zinc oxide thin films modified with tetrasulfonated

metallophthalocyanines by one-step electrodeposition. *Chemistry of Materials* **1999,** *11* (10), 2657-2667.

185. Goux, A.; Pauporté, T.; Yoshida, T.; Lincot, D., Mechanistic study of the electrodeposition of nanoporous self-assembled ZnO/eosin Y hybrid thin films: Effect of eosin concentration. *Langmuir* **2006,** *22* (25), 10545-10553.

186. Guérin, V. M.; Magne, C.; Pauporté, T.; Le Bahers, T.; Rathousky, J., Electrodeposited Nanoporous versus Nanoparticulate ZnO Films of Similar Roughness for Dye-Sensitized Solar Cell Applications. *Acs Applied Materials & Interfaces* **2010,** *2* (12), 3677-3685.

187. Pauporté, T.; Rathousky, J., Electrodeposited mesoporous ZnO thin films as efficient photocatalysts for the degradation of dye pollutants. *Journal of Physical Chemistry C* **2007,** *111* (21), 7639-7644.

188. Uboldi, D.; Ronchini, F. Screen Printing: Changing The Rules Of The Game 2014; Adanur, S., *Wellington Sears Handbook of Industrial Textiles*. Technomic Publishing Company, Inc.: Lancaster, Pennsylvania, 1995.

189. DuPont http://www.dupont.com/products-and-services/electronic-electrical-materials/printed-electronics.html.

190. Krebs, F. C., Fabrication and processing of polymer solar cells: A review of printing and coating techniques. *Solar Energy Materials and Solar Cells* **2009,** *93* (4), 394-412.

191. Ito, S.; Chen, P.; Comte, P.; Nazeeruddin, M. K.; Liska, P.; Péchy, P.; Grätzel, M., Fabrication of screen-printing pastes from $TiO_2$ powders for dye-sensitised solar cells. *Progress in Photovoltaics* **2007,** *15* (7), 603-612.

192. Ito, S.; Murakami, T. N.; Comte, P.; Liska, P.; Grätzel, C.; Nazeeruddin, M. K.; Grätzel, M., Fabrication of thin film dye sensitized solar cells with solar to electric power conversion efficiency over 10%. *Thin Solid Films* **2008,** *516* (14), 4613-4619.

193. Zeng, L. Y.; Dai, S. Y.; Xu, W. W.; Wang, K. J., Dye-sensitized solar cells based on ZnO films. *Plasma Science & Technology* **2006,** *8* (2), 172-175.

194. Hara, K.; Horiguchi, T.; Kinoshita, T.; Sayama, K.; Sugihara, H.; Arakawa, H., Highly efficient photon-to-electron conversion with mercurochrome-sensitized nanoporous oxide semiconductor solar cells. *Solar Energy Materials and Solar Cells* **2000,** *64* (2), 115-134.

195. Tsoukleris, D. S.; Arabatzis, I. M.; Chatzivasilogiou, E.; Kontos, A. I.; Belessi, V.; Bernard, M. C.; Falaras, P., 2-Ethyl-1-hexanol based screen-printed titania thin films for dye-sensitized solar cells. *Solar Energy* **2005,** *79* (4), 422-430.

196. Hobby, A. Screen Printing for the Industrial User 1997.

197. Gemici, Z.; Shimomura, H.; Cohen, R. E.; Rubner, M. F., Hydrothermal treatment of nanoparticle thin films for enhanced mechanical durability. *Langmuir* **2008,** *24* (5), 2168-2177; Oekermann, T.; Zhang, D.; Yoshida, T.; Minoura, H., Electron transport and back reaction in nanocrystalline $TiO_2$ films prepared by hydrothermal crystallization. *Journal of Physical Chemistry B* **2004,** *108* (7), 2227-2235.

198. Koops, S. E.; Barnes, P. R. F.; O'Regan, B. C.; Durrant, J. R., Kinetic Competition in a Coumarin Dye-Sensitized Solar Cell: Injection and Recombination

Limitations upon Device Performance. *Journal of Physical Chemistry C* **2010,** *114* (17), 8054-8061.

199. Hara, K.; Sato, T.; Katoh, R.; Furube, A.; Ohga, Y.; Shinpo, A.; Suga, S.; Sayama, K.; Sugihara, H.; Arakawa, H., Molecular design of coumarin dyes for efficient dye-sensitized solar cells. *Journal of Physical Chemistry B* **2003,** *107* (2), 597-606.

200. Chen, R.; Yang, X.; Tian, H.; Wang, X.; Hagfeldt, A.; Sun, L., Effect of tetrahydroquinoline dyes structure on the performance of organic dye-sensitized solar cells. *Chemistry of Materials* **2007,** *19* (16), 4007-4015.

201. Hao, Y.; Yang, X.; Cong, J.; Tian, H.; Hagfeldt, A.; Sun, L., Efficient near infrared D-pi-A sensitizers with lateral anchoring group for dye-sensitized solar cells. *Chemical Communications* **2009,** 4031-4033.

202. Horiuchi, T.; Miura, H.; Sumioka, K.; Uchida, S., High efficiency of dye-sensitized solar cells based on metal-free indoline dyes. *Journal of the American Chemical Society* **2004,** *126* (39), 12218-12219.

203. Ito, S.; Miura, H.; Uchida, S.; Takata, M.; Sumioka, K.; Liska, P.; Comte, P.; Péchy, P.; Grätzel, M., High-conversion-efficiency organic dye-sensitized solar cells with a novel indoline dye. *Chemical Communications* **2008,** 5194-5196.

204. Zhang, G.; Bala, H.; Cheng, Y.; Shi, D.; Lv, X.; Yu, Q.; Wang, P., High efficiency and stable dye-sensitized solar cells with an organic chromophore featuring a binary pi-conjugated spacer. *Chemical Communications* **2009,** 2198-2200.

205. Marinado, T.; Hagberg, D. P.; Hedlund, M.; Edvinsson, T.; Johansson, E. M. J.; Boschloo, G.; Rensmo, H.; Brinck, T.; Sun, L. C.; Hagfeldt, A., Rhodanine dyes for dye-sensitized solar cells: spectroscopy, energy levels and photovoltaic performance. *Physical Chemistry Chemical Physics* **2009,** *11* (1), 133-141.

206. Zhang, G.; Bai, Y.; Li, R.; Shi, D.; Wenger, S.; Zakeeruddin, S. M.; Grätzel, M.; Wang, P., Employ a bisthienothiophene linker to construct an organic chromophore for efficient and stable dye-sensitized solar cells. *Energy & Environmental Science* **2009,** *2* (1), 92-95.

207. Sayama, K.; Hara, K.; Mori, N.; Satsuki, M.; Suga, S.; Tsukagoshi, S.; Abe, Y.; Sugihara, H.; Arakawa, H., Photosensitization of a porous $TiO_2$ electrode with merocyanine dyes containing a carboxyl group and a long alkyl chain. *Chemical Communications* **2000,** (13), 1173-1174.

208. Sayama, K.; Tsukagoshi, S.; Mori, T.; Hara, K.; Ohga, Y.; Shinpou, A.; Abe, Y.; Suga, S.; Arakawa, H., Efficient sensitization of nanocrystalline $TiO_2$ films with cyanine and merocyanine organic dyes. *Solar Energy Materials and Solar Cells* **2003,** *80* (1), 47-71.

209. Yum, J. H.; Walter, P.; Huber, S.; Rentsch, D.; Geiger, T.; Nüesch, F.; De Angelis, F.; Grätzel, M.; Nazeeruddin, M. K., Efficient far red sensitization of nanocrystalline $TiO_2$ films by an unsymmetrical squaraine dye. *Journal of the American Chemical Society* **2007,** *129* (34), 10320-10321.

210. Thomas, K. R. J.; Hsu, Y.-C.; Lin, J. T.; Lee, K.-M.; Ho, K.-C.; Lai, C.-H.; Cheng, Y.-M.; Chou, P.-T., 2,3-disubstituted thiophene-based organic dyes for solar cells. *Chemistry of Materials* **2008,** *20* (5), 1830-1840; Xu, M.; Li, R.; Pootrakulchote,

N.; Shi, D.; Guo, J.; Yi, Z.; Zakeeruddin, S. M.; Grätzel, M.; Wang, P., Energy-Level and Molecular Engineering of Organic D-pi-A Sensitizers in Dye-Sensitized Solar Cells. *Journal of Physical Chemistry C* **2008,** *112* (49), 19770-19776.

211. Grätzel, M., Dye-sensitized solar cells. *Journal of Photochemistry and Photobiology C-Photochemistry Reviews* **2003,** *4* (2), 145-153.

212. Lin, C.-Y.; Lai, Y.-H.; Chen, H.-W.; Chen, J.-G.; Kung, C.-W.; Vittal, R.; Ho, K.-C., Highly efficient dye-sensitized solar cell with a ZnO nanosheet-based photoanode. *Energy & Environmental Science* **2011,** *4* (9), 3448-3455.

213. Le Bahers, T.; Pauporté, T.; Scalmani, G.; Adamo, C.; Ciofini, I., A TD-DFT investigation of ground and excited state properties in indoline dyes used for dye-sensitized solar cells. *Physical Chemistry Chemical Physics* **2009,** *11* (47), 11276-11284.

214. Jose, R.; Kumar, A.; Thavasi, V.; Ramakrishna, S., Conversion efficiency versus sensitizer for electrospun $TiO_2$ nanorod electrodes in dye-sensitized solar cells. *Nanotechnology* **2008,** *19*, 424004.

215. Ogura, R. Y.; Nakane, S.; Morooka, M.; Orihashi, M.; Suzuki, Y.; Noda, K., High-performance dye-sensitized solar cell with a multiple dye system. *Applied Physics Letters* **2009,** *94*, 073308.

216. Dentani, T.; Kubota, Y.; Funabiki, K.; Jin, J.; Yoshida, T.; Minoura, H.; Miura, H.; Matsui, M., Novel thiophene-conjugated indoline dyes for zinc oxide solar cells. *New Journal of Chemistry* **2009,** *33* (1), 93-101.

217. Jose, R.; Kumar, A.; Thavasi, V.; Fujihara, K.; Uchida, S.; Ramakrishna, S., Relationship between the molecular orbital structure of the dyes and photocurrent density in the dye-sensitized solar cells. *Applied Physics Letters* **2008,** *93*, 023125.

218. Lu, H. P.; Tsai, C. Y.; Yen, W. N.; Hsieh, C. P.; Lee, C. W.; Yeh, C. Y.; Diau, E. W. G., Control of Dye Aggregation and Electron Injection for Highly Efficient Porphyrin Sensitizers Adsorbed on Semiconductor Films with Varying Ratios of Coadsorbate. *Journal of Physical Chemistry C* **2009,** *113* (49), 20990-20997.

219. Magne, C.; Urien, M.; Ciofini, I.; Tugsuz, T.; Pauporté, T., Amphiphilic acids as co-adsorbents of metal-free organic dyes for the efficient sensitization of nanostructured photoelectrode. *Rsc Advances* **2012,** *2* (31), 11836-11842.

220. Tatay, S.; Haque, S. A.; O'Regan, B.; Durrant, J. R.; Verhees, W. J. H.; Kroon, J. M.; Vidal-Ferran, A.; Gaviña, P.; Palomares, E., Kinetic competition in liquid electrolyte and solid-state cyanine dye sensitized solar cells. *Journal of Materials Chemistry* **2007,** *17* (29), 3037-3044.

221. Matsuzaki, H.; Murakami, T. N.; Masaki, N.; Furube, A.; Kimura, M.; Mori, S., Dye Aggregation Effect on Interfacial Electron-Transfer Dynamics in Zinc Phthalocyanine-Sensitized Solar Cells. *Journal of Physical Chemistry C* **2014,** *118* (31), 17205-17212.

222. Cid, J. J.; Yum, J. H.; Jang, S. R.; Nazeeruddin, M. K.; Ferrero, E. M.; Palomares, E.; Ko, J.; Grätzel, M.; Torres, T., Molecular cosensitization for efficient panchromatic dye-sensitized solar cells. *Angewandte Chemie-International Edition* **2007,** *46* (44), 8358-8362.

223. Lin, L. Y.; Yeh, M. H.; Lee, C. P.; Chang, J.; Baheti, A.; Vittal, R.; Thomas, K. R. J.; Ho, K. C., Insights into the co-sensitizer adsorption kinetics for complementary organic dye-sensitized solar cells. *Journal of Power Sources* **2014,** *247*, 906-914.

224. Yum, J.-H.; Baranoff, E.; Wenger, S.; Nazeeruddin, M. K.; Grätzel, M., Panchromatic engineering for dye-sensitized solar cells. *Energy & Environmental Science* **2011,** *4* (3), 842-857.

225. Xue, Z.; Wang, L.; Liu, B., Facile fabrication of co-sensitized plastic dye-sensitized solar cells using multiple electrophoretic deposition. *Nanoscale* **2013,** *5* (6), 2269-2273.

226. Kuang, D.; Walter, P.; Nüesch, F.; Kim, S.; Ko, J.; Comte, P.; Zakeeruddin, S. M.; Nazeeruddin, M. K.; Grätzel, M., Co-sensitization of organic dyes for efficient ionic liquid electrolyte-based dye-sensitized solar cells. *Langmuir* **2007,** *23* (22), 10906-10909.

227. Kimura, M.; Nomoto, H.; Masaki, N.; Mori, S., Dye Molecules for Simple Co-Sensitization Process: Fabrication of Mixed-Dye-Sensitized Solar Cells. *Angewandte Chemie-International Edition* **2012,** *51* (18), 4371-4374.

228. Kim, S.; Lee, J. K.; Kang, S. O.; Ko, J.; Yum, J. H.; Fantacci, S.; De Angelis, F.; Di Censo, D.; Nazeeruddin, M. K.; Grätzel, M., Molecular engineering of organic sensitizers for solar cell applications. *Journal of the American Chemical Society* **2006,** *128* (51), 16701-16707; Yum, J.-H.; Baranoff, E.; Kessler, F.; Moehl, T.; Ahmad, S.; Bessho, T.; Marchioro, A.; Ghadiri, E.; Moser, J.-E.; Yi, C.; Nazeeruddin, M. K.; Grätzel, M., A cobalt complex redox shuttle for dye-sensitized solar cells with high open-circuit potentials. *Nature Communications* **2012,** *3* (631), 1-8.

229. Kimura, M.; Nomoto, H.; Suzuki, H.; Ikeuchi, T.; Matsuzaki, H.; Murakami, T. N.; Furube, A.; Masaki, N.; Griffith, M. J.; Mori, S., Molecular Design Rule of Phthalocyanine Dyes for Highly Efficient Near-IR Performance in Dye-Sensitized Solar Cells. *Chemistry-a European Journal* **2013,** *19* (23), 7496-7502.

230. Nazeeruddin, M. K.; Humphry-Baker, R.; Grätzel, M.; Wöhrle, D.; Schnurpfeil, G.; Schneider, G.; Hirth, A.; Trombach, N., Efficient near-IR sensitization of nanocrystalline $TiO_2$ films by zinc and aluminum phthalocyanines. *Journal of Porphyrins and Phthalocyanines* **1999,** *3* (3), 230-237.

231. Laqua, K.; Melhuish, W. H.; Zander, M., Nomenclature, symbols, units and their usage in spectrochemical analysis .7. Molecular absorption-spectroscopy, ultraviolet and visible (UV Vis) - (Recommendations 1988). *Pure and Applied Chemistry* **1988,** *60* (9), 1449-1460.

232. Hollas, J. M., *Modern Spectroscopy*. 4 ed.; Wiley: 2004.

233. Morton, S. M.; Jensen, L., A discrete interaction model/quantum mechanical method for describing response properties of molecules adsorbed on metal nanoparticles. *Journal of Chemical Physics* **2010,** *133*, 074103.

234. Myers, A. B.; Birge, R. R., The effect of solvent environment on molecular electronic oscillator-strengths. *Journal of Chemical Physics* **1980,** *73* (10), 5314-5321.

235. Lasser, L.; Ronca, E.; Pastore, M.; De Angelis, F.; Cornil, J.; Lazzaroni, R.; Beljonne, D., Energy Level Alignment at Titanium Oxide-Dye Interfaces: Implications

for Electron Injection and Light Harvesting. *Journal of Physical Chemistry C* **2015,** *119* (18), 9899-9909.

236. tec5 http://www.tec5.com/products/72/en/multispec%C2%AE-systems.html.

237. Ionita, I., *Condensed Matter Optical Spectroscopy : An Illustrated Introduction*. CRC Press: 2014.

238. PerkinElmer. Transmission Measurements Using Integrating Spheres - Application note for the LAMBDA 950/850/650 UV/Vis/NIR and UV/Vis Spectrophotometers 2004.

239. Masilela, N.; Nombona, N.; Loewenstein, T.; Nyokong, T.; Schlettwein, D., Symmetrically and unsymmetrically substituted carboxy phthalocyanines as sensitizers for nanoporous ZnO films. *Journal of Porphyrins and Phthalocyanines* **2010,** *14* (11), 985-992.

240. Myers Kelley, A., *Condensed-Phase Molecular Spectroscopy and Photophysics*. John Wiley & Sons, Inc.: Hoboken, New Jersey, 2013.

241. Green, M. A., Solar Cells: Operating Principles, Technology, and System Applications. Prentice Hall: 1981.

242. Jennings, J. R.; Ghicov, A.; Peter, L. M.; Schmuki, P.; Walker, A. B., Dye-sensitized solar cells based on oriented $TiO_2$ nanotube arrays: Transport, trapping, and transfer of electrons. *Journal of the American Chemical Society* **2008,** *130* (40), 13364-13372.

243. Burke, A.; Ito, S.; Snaith, H.; Bach, U.; Kwiatkowski, J.; Grätzel, M., The function of a $TiO_2$ compact layer in dye-sensitized solar cells incorporating "Planar" organic dyes. *Nano Letters* **2008,** *8* (4), 977-981.

244. Smestad, G. P.; Krebs, F. C.; Lampert, C. M.; Granqvist, C. G.; Chopra, K. L.; Mathew, X.; Takakura, H., Reporting solar cell efficiencies in solar energy materials and solar cells. *Solar Energy Materials and Solar Cells* **2008,** *92* (4), 371-373.

245. *Impedance Spectroscopy: Theory, Experiment, and Applications*. John Wiley & Sons, Inc.: Hoboken, New Jersey., 2005.

246. Zahner-Elektrik, Manual for Thales Software, Chapter 2: "Basics and Applications". 2008.

247. Fabregat-Santiago, F.; Bisquert, J.; Garcia-Belmonte, G.; Boschloo, G.; Hagfeldt, A., Influence of electrolyte in transport and recombination in dye-sensitized solar cells studied by impedance spectroscopy. *Solar Energy Materials and Solar Cells* **2005,** *87* (1-4), 117-131.

248. Halme, J.; Vahermaa, P.; Miettunen, K.; Lund, P., Device Physics of Dye Solar Cells. *Advanced Materials* **2010,** *22* (35), E210-E234.

249. Fabregat-Santiago, F.; Bisquert, J.; Palomares, E.; Otero, L.; Kuang, D.; Zakeeruddin, S. M.; Grätzel, M., Correlation between photovoltaic performance and impedance spectroscopy of dye-sensitized solar cells based on ionic liquids. *Journal of Physical Chemistry C* **2007,** *111* (17), 6550-6560.

250. Bisquert, J.; Garcia-Belmonte, G.; Fabregat-Santiago, F.; Ferriols, N. S.; Bogdanoff, P.; Pereira, E. C., Doubling exponent models for the analysis of porous film

electrodes by impedance. Relaxation of $TiO_2$ nanoporous in aqueous solution. *Journal of Physical Chemistry B* **2000,** *104* (10), 2287-2298.

251. Guillén, E.; Azaceta, E.; Peter, L. M.; Zukal, A.; Tena-Zaera, R.; Anta, J. A., ZnO solar cells with an indoline sensitizer: a comparison between nanoparticulate films and electrodeposited nanowire arrays. *Energy & Environmental Science* **2011,** *4* (9), 3400-3407.

252. O'Regan, B.; Li, X.; Ghaddar, T., Dye adsorption, desorption, and distribution in mesoporous $TiO_2$ films, and its effects on recombination losses in dye sensitized solar cells. *Energy & Environmental Science* **2012,** *5* (5), 7203-7215.

253. Docampo, P.; Guldin, S.; Steiner, U.; Snaith, H. J., Charge Transport Limitations in Self-Assembled $TiO_2$ Photoanodes for Dye-Sensitized Solar Cells. *Journal of Physical Chemistry Letters* **2013,** *4* (5), 698-703.

254. Wang, M.; Chen, P.; Humphry-Baker, R.; Zakeeruddin, S. M.; Grätzel, M., The Influence of Charge Transport and Recombination on the Performance of Dye-Sensitized Solar Cells. *Chemphyschem* **2009,** *10* (1), 290-299; Ripolles-Sanchis, T.; Guo, B. C.; Wu, H. P.; Pan, T. Y.; Lee, H. W.; Raga, S. R.; Fabregat-Santiago, F.; Bisquert, J.; Yeh, C. Y.; Diau, E. W. G., Design and characterization of alkoxy-wrapped push-pull porphyrins for dye-sensitized solar cells. *Chemical Communications* **2012,** *48* (36), 4368-4370; Raga, S. R.; Fabregat-Santiago, F., Temperature effects in dye-sensitized solar cells. *Physical Chemistry Chemical Physics* **2013,** *15* (7), 2328-2336.

255. Bisquert, J.; Palomares, E.; Quinones, C. A., Effect of energy disorder in interfacial kinetics of dye-sensitized solar cells with organic hole transport material. *Journal of Physical Chemistry B* **2006,** *110* (39), 19406-19411.

256. Schlichthörl, G.; Huang, S. Y.; Sprague, J.; Frank, A. J., Band edge movement and recombination kinetics in dye-sensitized nanocrystalline $TiO_2$ solar cells: A study by intensity modulated photovoltage spectroscopy. *Journal of Physical Chemistry B* **1997,** *101* (41), 8141-8155.

257. Peter, L. M.; Vanmaekelbergh, D., *Time and Frequency Resolved Studies of Photoelectrochemical Kinetics*. WILEY-VCH: Weinheim, 1999; Vol. 6.

258. Halme, J.; Miettunen, K.; Lund, P., Effect of Nonuniform Generation and Inefficient Collection of Electrons on the Dynamic Photocurrent and Photovoltage Response of Nanostructured Photoelectrodes. *Journal of Physical Chemistry C* **2008,** *112* (51), 20491-20504.

259. Halme, J., Linking optical and electrical small amplitude perturbation techniques for dynamic performance characterization of dye solar cells. *Physical Chemistry Chemical Physics* **2011,** *13* (27), 12435-12446.

260. Franco, G.; Peter, L. M.; Ponomarev, E. A., Detection of inhomogeneous dye distribution in dye sensitised nanocrystalline solar cells by intensity modulated photocurrent spectroscopy (IMPS). *Electrochemistry Communications* **1999,** *1* (2), 61-64.

261. van de Lagemaat, J.; Park, N. G.; Frank, A. J., Influence of electrical potential distribution, charge transport, and recombination on the photopotential and photocurrent conversion efficiency of dye-sensitized nanocrystalline $TiO_2$ solar cells: A study by

electrical impedance and optical modulation techniques. *Journal of Physical Chemistry B* **2000,** *104* (9), 2044-2052.

262. Frank, A. J.; Kopidakis, N.; van de Lagemaat, J., Electrons in nanostructured $TiO_2$ solar cells: transport, recombination and photovoltaic properties. *Coordination Chemistry Reviews* **2004,** *248* (13-14), 1165-1179.

263. van de Lagemaat, J.; Frank, A. J., Nonthermalized electron transport in dye-sensitized nanocrystalline $TiO_2$ films: Transient photocurrent and random-walk modeling studies. *Journal of Physical Chemistry B* **2001,** *105* (45), 11194-11205.

264. Nakade, S.; Kanzaki, T.; Wada, Y.; Yanagida, S., Stepped light-induced transient measurements of photocurrent and voltage in dye-sensitized solar cells: Application for highly viscous electrolyte systems. *Langmuir* **2005,** *21* (23), 10803-10807.

265. O'Regan, B. C.; Bakker, K.; Kroeze, J.; Smit, H.; Sommeling, P.; Durrant, J. R., Measuring charge transport from transient photovoltage rise times. A new tool to investigate electron transport in nanoparticle films. *Journal of Physical Chemistry B* **2006,** *110* (34), 17155-17160.

266. Cameron, P. J.; Peter, L. M., How does back-reaction at the conducting glass substrate influence the dynamic photovoltage response of nanocrystalline dye-sensitized solar cells? *Journal of Physical Chemistry B* **2005,** *109* (15), 7392-7398.

267. Quintana, M.; Edvinsson, T.; Hagfeldt, A.; Boschloo, G., Comparison of dye-sensitized ZnO and $TiO_2$ solar cells: Studies of charge transport and carrier lifetime. *Journal of Physical Chemistry C* **2007,** *111* (2), 1035-1041.

268. Yane, T.; Koyama, A.; Hiramatsu, K.; Isogai, Y.; Ichinose, K.; Yoshida, T., Development of Electrodeposition System Employing 8 Rotating Disc Electrodes for Highly Reproducible Synthesis of Zinc Oxide Thin Films. *Electrochemistry* **2012,** *80* (11), 891-897.

269. Ichinose, K.; Kimikado, Y.; Yoshida, T., The Effect of Pre-treatments of F-Doped $SnO_2$ Substrates for Cathodic Nucleation of ZnO Crystals in Aqueous $ZnCl_2$ Solution with Dissolved $O_2$. *Electrochemistry* **2011,** *79* (3), 146-155.

270. Yoshida, T., Personal Communication.

271. Yum, J. H.; Moon, S. J.; Humphry-Baker, R.; Walter, P.; Geiger, T.; Nüesch, F.; Grätzel, M.; Nazeeruddin, M. d. K., Effect of coadsorbent on the photovoltaic performance of squaraine sensitized nanocrystalline solar cells. *Nanotechnology* **2008,** *19*, 424005.

272. Dragässer, A., Untersuchung und Kontrolle der Ladungsträgerrekombination in organischen Solarzellen aus Kupferphthalocyanin und Buckminsterfulleren. *Dissertation, Justus-Liebig-Universität Gießen* **2014**.

273. Birkenstock, J. Bachelor's Thesis: "Optimierung eines Aufbaus zur Messung der Quantenausbeute von Solarzellen". Justus-Liebig-Universität Gießen, 2012.

274. Zahner-Elektrik, Manual for CIMPS Software, Chapter 5: "Charge Extraction after N.W. Duffy, L.M. Peter et al.". 2014.

275. Komatsu, D.; Zhang, J.; Yoshida, T.; Minoura, H., *Trans. Mater. Res. Soc. Jpn.* **2006,** *32*, 417-420.

276. Komatsu, D. Dissertation. Gifu University, 2008.

277. Yoshida, T.; Zhang, J. B.; Komatsu, D.; Sawatani, S.; Minoura, H.; Pauporté, T.; Lincot, D.; Oekermann, T.; Schlettwein, D.; Tada, H.; Wöhrle, D.; Funabiki, K.; Matsui, M.; Miura, H.; Yanagi, H., Electrodeposition of Inorganic/Organic Hybrid Thin Films. *Advanced Functional Materials* **2009,** *19* (1), 17-43.

278. Rudolph, M.; Yoshida, T.; Schlettwein, D., Influence of indoline dye and coadsorbate molecules on photovoltaic performance and recombination in dye-sensitized solar cells based on electrodeposited ZnO. *Journal of Electroanalytical Chemistry* **2013,** *709*, 10-18.

279. Beu, M., Nutzung von Zinkoxid-Schichten in farbstoffsensibilisierten Festkörpersolarzellen. *Dissertation, Justus-Liebig-Universität Gießen* **2014**.

280. Fiehler, F. Master's Thesis: "Einfluss der chemischen Verankerung von Farbstoffen auf die Sensibilisierung von ZnO". Justus-Liebig-Universität Gießen, 2013.

281. Pastore, M.; De Angelis, F., Aggregation of Organic Dyes on $TiO_2$ in Dye-Sensitized Solar Cells Models: An Ab Initio Investigation. *Acs Nano* **2010,** *4* (1), 556-562.

282. Rohwer, E.; Richter, C.; Heming, N.; Strauch, K.; Litwinski, C.; Nyokong, T.; Schlettwein, D.; Schwoerer, H., Ultrafast Photodynamics of the Indoline Dye D149 Adsorbed to Porous ZnO in Dye-Sensitized Solar Cells. *Chemphyschem : a European journal of chemical physics and physical chemistry* **2013,** *14* (1), 132-139.

283. Marotta, G.; Lobello, M. G.; Anselmi, C.; Consiglio, G. B.; Calamante, M.; Mordini, A.; Pastore, M.; De Angelis, F., An Integrated Experimental and Theoretical Approach to the Spectroscopy of Organic-Dye-Sensitized $TiO_2$ Heterointerfaces: Disentangling the Effects of Aggregation, Solvation, and Surface Protonation. *Chemphyschem* **2014,** *15* (6), 1116-1125.

284. Hagberg, D. P.; Edvinsson, T.; Marinado, T.; Boschloo, G.; Hagfeldt, A.; Sun, L., A novel organic chromophore for dye-sensitized nanostructured solar cells. *Chemical Communications* **2006,** (21), 2245-2247.

285. Valeur, B.; Berberan-Santos, M. N., *Molecular Fluorescence: Principles and Applications*. 2 ed.; Wiley-VCH: Weinheim, 2013.

286. Falgenhauer, J.; Richter, C.; Miura, H.; Schlettwein, D., Stable Sensitization of ZnO by Improved Anchoring of Indoline Dyes. *Chemphyschem* **2012,** *13* (12), 2893-2897.

287. Schmidt, J.-A., Einfluss gelöster Farbstoffmoleküle auf den Ladungstransport in einem $I^-/I_3^-$-Redoxelektrolyten und den Ladungstransfer an der Grenzfläche $I^-/I_3^-$-Elektrolyt/Platin. *Praktikumsbericht, Justus-Liebig-Universität Gießen* **2013**.

288. Rudolph, M.; Yoshida, T.; Miura, H.; Schlettwein, D., Improvement of Light Harvesting by Addition of a Long-Wavelength Absorber in Dye-Sensitized Solar Cells Based on ZnO and Indoline Dyes. *Journal of Physical Chemistry C* **2015,** *119* (3), 1298-1311.

289. Tanaka, H.; Takeichi, A.; Higuchi, K.; Motohiro, T.; Takata, M.; Hirota, N.; Nakajima, J.; Toyoda, T., Long-term durability and degradation mechanism of dye-

sensitized solar cells sensitized with indoline dyes. *Solar Energy Materials and Solar Cells* **2009,** *93* (6-7), 1143-1148.

290. Fattori, A.; Peter, L. M.; Wang, H.; Miura, H.; Marken, F., Fast Hole Surface Conduction Observed for Indoline Sensitizer Dyes Immobilized at Fluorine-Doped Tin Oxide-$TiO_2$ Surfaces. *Journal of Physical Chemistry C* **2010,** *114* (27), 11822-11828.

291. Borrelli, R.; Ellena, S.; Barolo, C., Theoretical and experimental determination of the absorption and emission spectra of a prototypical indolenine-based squaraine dye. *Physical Chemistry Chemical Physics* **2014,** *16* (6), 2390-2398.

292. Hagfeldt, A.; Grätzel, M., Light-induced redox reactions in nanocrystalline systems. *Chemical Reviews* **1995,** *95* (1), 49-68; Rodriguez, J. A.; Jirsak, T.; Hrbek, J., Reaction of $SO_2$ with cesium and cesium-promoted ZnO and $MoO_2$. *Journal of Physical Chemistry B* **1999,** *103* (11), 1966-1976.

293. Mora-Seró, I.; Bisquert, J., Fermi level of surface states in $TiO_2$ nanoparticles. *Nano Letters* **2003,** *3* (7), 945-949.

294. Bisquert, J.; Fabregat-Santiago, F.; Mora-Seró, I.; Garcia-Belmonte, G.; Barea, E. M.; Palomares, E., A review of recent results on electrochemical determination of the density of electronic states of nanostructured metal-oxide semiconductors and organic hole conductors. *Inorganica Chimica Acta* **2008,** *361* (3), 684-698.

295. Nazeeruddin, M. K.; Zakeeruddin, S. M.; Humphry-Baker, R.; Jirousek, M.; Liska, P.; Vlachopoulos, N.; Shklover, V.; Fischer, C. H.; Grätzel, M., Acid-base equilibria of (2,2 '-bipyridyl-4,4 '-dicarboxylic acid)ruthenium(II) complexes and the effect of protonation on charge-transfer sensitization of nanocrystalline titania. *Inorganic Chemistry* **1999,** *38* (26), 6298-6305.

296. De Angelis, F.; Fantacci, S.; Selloni, A.; Grätzel, M.; Nazeeruddin, M. K., Influence of the sensitizer adsorption mode on the open-circuit potential of dye-sensitized solar cells. *Nano Letters* **2007,** *7* (10), 3189-3195.

297. Lee, K. E.; Gomez, M. A.; Elouatik, S.; Demopoulos, G. P., Further Understanding of the Adsorption Mechanism of N719 Sensitizer on Anatase $TiO_2$ Films for DSSC Applications Using Vibrational Spectroscopy and Confocal Raman Imaging. *Langmuir* **2010,** *26* (12), 9575-9583.

298. Kay, A.; Grätzel, M., Artificial photosynthesis .1. Photosensitization of $TiO_2$ solar-cells with Chlorophyll derivatives and related natural porphyrins. *Journal of Physical Chemistry* **1993,** *97* (23), 6272-6277.

299. Boschloo, G.; Lindström, J.; Magnusson, E.; Holmberg, A.; Hagfeldt, A., Optimization of dye-sensitized solar cells prepared by compression method. *Journal of Photochemistry and Photobiology a-Chemistry* **2002,** *148* (1-3), 11-15.

300. Tefashe, U. M.; Rudolph, M.; Miura, H.; Schlettwein, D.; Wittstock, G., Photovoltaic characteristics and dye regeneration kinetics in D149-sensitized ZnO with varied dye loading and film thickness. *Physical Chemistry Chemical Physics* **2012,** *14* (20), 7533-7542.

301. Barnett, C. E., Some Applications of Wave-length Turbidimetry in the Infrared. *The Journal of Physical Chemistry* **1942,** *46* (1), 69-75; Young, A. T., Rayleigh-scattering. *Physics Today* **1982,** *35* (1), 42-48.

302. Wang, Q.; Zakeeruddin, S. M.; Nazeeruddin, M. K.; Humphry-Baker, R.; Grätzel, M., Molecular wiring of nanocrystals: NCS-Enhanced cross-surface charge transfer in self-assembled Ru-complex monolayer on mesoscopic oxide films. *Journal of the American Chemical Society* **2006,** *128* (13), 4446-4452.

303. Lohse, P. W.; Kuhnt, J.; Druzhinin, S. I.; Scholz, M.; Ekimova, M.; Oekermann, T.; Lenzer, T.; Oum, K., Ultrafast photoinduced relaxation dynamics of the indoline dye D149 in organic solvents. *Physical Chemistry Chemical Physics* **2011,** *13* (43), 19632-19640.

304. Masilela, N.; Idowu, M.; Nyokong, T., Photophysical, photochemical and electrochemical properties of water soluble silicon, titanium and zinc phthalocyanines. *Journal of Photochemistry and Photobiology A: Chemistry* **2009,** *201* (2–3), 91-97.

305. *Phthalocyanines, Properties and Applications, Volume 1*. Wiley-VCH: Weinheim, 1989.

306. Ogunsipe, A.; Chen, J. Y.; Nyokong, T., Photophysical and photochemical studies of zinc(II) phthalocyanine derivatives - effects of substituents and solvents. *New Journal of Chemistry* **2004,** *28* (7), 822-827.

307. Falgenhauer, J. Bericht zum Vertiefungsmodul MatWiss-MV 04 und zum Spezialisierungsmodul MatWiss-MS 04: "Charakterisierung von sulfonierten Phthalocyaninen mittels Spektroelektrochemie, Elektrochemie und Photoelektrochemie". Justus-Liebig-Universität Gießen, 2011.

308. Listorti, A.; Creager, C.; Sommeling, P.; Kroon, J.; Palomares, E.; Fornelli, A.; Breen, B.; Barnes, P. R. F.; Durrant, J. R.; Law, C.; O'Regan, B., The mechanism behind the beneficial effect of light soaking on injection efficiency and photocurrent in dye sensitized solar cells. *Energy & Environmental Science* **2011,** *4* (9), 3494-3501.

309. Ito, S.; Nazeeruddin, M. K.; Liska, P.; Comte, P.; Charvet, R.; Péchy, P.; Jirousek, M.; Kay, A.; Zakeeruddin, S. M.; Grätzel, M., Photovoltaic characterization of dye-sensitized solar cells: Effect of device masking on conversion efficiency. *Progress in Photovoltaics* **2006,** *14* (7), 589-601.

310. Palacios-Lidón, E.; Pickup, D. F.; Johnson, P. S.; Ruther, R. E.; Tena-Zaera, R.; Hamers, R. J.; Colchero, J.; Himpsel, F. J.; Ortega, J. E.; Rogero, C., Face-Selective Etching of ZnO during Attachment of Dyes. *Journal of Physical Chemistry C* **2013,** *117* (36), 18414-18422; Keis, K.; Lindgren, J.; Lindquist, S. E.; Hagfeldt, A., Studies of the adsorption process of Ru complexes in nanoporous ZnO electrodes. *Langmuir* **2000,** *16* (10), 4688-4694.

311. Sobus, J.; Burdzinski, G.; Karolczak, J.; Idígoras, J.; Anta, J. A.; Ziolek, M., Comparison of $TiO_2$ and ZnO Solar Cells Sensitized with an Indoline Dye: Time-Resolved Laser Spectroscopy Studies of Partial Charge Separation Processes. *Langmuir* **2014,** *30* (9), 2505-2512.

312. Boschloo, G.; Haggman, L.; Hagfeldt, A., Quantification of the effect of 4-tert-butylpyridine addition to $I^-/I_3^-$ redox electrolytes in dye-sensitized nanostructured $TiO_2$ solar cells. *Journal of Physical Chemistry B* **2006,** *110* (26), 13144-13150; Katoh, R.; Kasuya, M.; Kodate, S.; Furube, A.; Fuke, N.; Koide, N., Effects of 4-tert-Butylpyridine and Li Ions on Photoinduced Electron Injection Efficiency in Black-Dye-Sensitized Nanocrystalline $TiO_2$ Films. *Journal of Physical Chemistry C* **2009,** *113* (48), 20738-20744.

313. Richter, C., Dissertation. *Dissertation, Justus-Liebig-Universität Gießen* **2015**.

314. Daeneke, T.; Kwon, T.-H.; Holmes, A. B.; Duffy, N. W.; Bach, U.; Spiccia, L., High-efficiency dye-sensitized solar cells with ferrocene-based electrolytes. *Nature Chemistry* **2011,** *3* (3), 211-215.

315. Fan, J.; Hao, Y.; Cabot, A.; Johansson, E. M. J.; Boschloo, G.; Hagfeldt, A., Cobalt(II/III) Redox Electrolyte in ZnO Nanowire-Based Dye-Sensitized Solar Cells. *Acs Applied Materials & Interfaces* **2013,** *5* (6), 1902-1906.

316. Hardin, B. E.; Sellinger, A.; Moehl, T.; Humphry-Baker, R.; Moser, J.-E.; Wang, P.; Zakeeruddin, S. M.; Grätzel, M.; McGehee, M. D., Energy and Hole Transfer between Dyes Attached to Titania in Cosensitized Dye-Sensitized Solar Cells. *Journal of the American Chemical Society* **2011,** *133* (27), 10662-10667.

317. Basham, J. I.; Mor, G. K.; Grimes, C. A., Förster Resonance Energy Transfer in Dye-Sensitized Solar Cells. *Acs Nano* **2010,** *4* (3), 1253-1258.

318. Hardin, B. E.; Hoke, E. T.; Armstrong, P. B.; Yum, J.-H.; Comte, P.; Torres, T.; Fréchet, J. M. J.; Nazeeruddin, M. K.; Grätzel, M.; McGehee, M. D., Increased light harvesting in dye-sensitized solar cells with energy relay dyes. *Nature Photonics* **2009,** *3* (7), 406-411.

319. Dürr, M.; Bamedi, A.; Yasuda, A.; Nelles, G., Tandem dye-sensitized solar cell for improved power conversion efficiencies. *Applied Physics Letters* **2004,** *84* (17), 3397-3399.

320. Noma, Y.; Iizuka, K.; Ogomi, Y.; Pandey, S. S.; Hayase, S., Preparation of Double Dye-Layer Structure of Dye-Sensitized Solar Cells from Cocktail Solutions for Harvesting Light in Wide Range of Wavelengths. *Japanese Journal of Applied Physics* **2009,** *48*, 020213.

321. Künze, S., Electroless deposition of porous zinc oxide on aluminium. *Dissertation, Justus-Liebig-Universität Gießen* **2014**.

322. Loewenstein, T.; Hastall, A.; Mingebach, M.; Zimmermann, Y.; Neudeck, A.; Schlettwein, D., Textile electrodes as substrates for the electrodeposition of porous ZnO. *Physical Chemistry Chemical Physics* **2008,** *10* (14), 1844-1847; Rudolph, M.; Loewenstein, T.; Arndt, E.; Zimmermann, Y.; Neudeck, A.; Schlettwein, D., Pulsed electrodeposition of porous ZnO on Ag-coated polyamide filaments. *Physical Chemistry Chemical Physics* **2009,** *11* (17), 3313-3319; Schubert, M. B.; Werner, J. H., Flexible solar cells for clothing. *Materials Today* **2006,** *9* (6), 42-50.

# Erklärung

Ich erkläre: Ich habe die vorgelegte Dissertation selbständig und ohne unerlaubte fremde Hilfe und nur mit den Hilfen angefertigt, die ich in der Dissertation angegeben habe. Alle Textstellen, die wörtlich oder sinngemäß aus veröffentlichten Schriften entnommen sind, und alle Angaben, die auf mündlichen Auskünften beruhen, sind als solche kenntlich gemacht. Bei den von mir durchgeführten und in der Dissertation erwähnten Untersuchungen habe ich die Grundsätze guter wissenschaftlicher Praxis, wie sie in der „Satzung der Justus-Liebig-Universität Gießen zur Sicherung guter wissenschaftlicher Praxis“ niedergelegt sind, eingehalten.

| | |
|---|---|
| Ort, Datum | Unterschrift |